Dissertation for the Degree of Doctor

Dynamical Behaviors of Coupled Chaotic Systems and Quasiperiodically Forced Systems: Synchronization and Strange Nonchaotic Attractors

by
Woochang Lim
Department of Physics

Graduate School
Kangwon National University

August, 2005

Under the Guidance of
Professor Sang-Yoon Kim

Dynamical Behaviors of Coupled Chaotic Systems and Quasiperiodically Forced Systems: Synchronization and Strange Nonchaotic Attractors

A DISSERTATION

Submitted to the Graduate School of
Kangwon National University in Partial
Fulfillment of the Requirements
for the Degree of

Doctor of Science

Woochang Lim

Department of Physics

August, 2005

Approved by Committee of the Graduate School of Kangwon National University in Partial Fulfillment of the Requirements for the Degree of Doctor of Science

Woochang Lim

June, 2005

Dissertation Committee;

Sang-Yoon Kim	(signature)
(Chairman of Committee)	
Jaegu Kim	(signature)
(Committeeman)	
Sun-Mok Paik	(signature)
(Committeeman)	
Youngtae Kim	(signature)
(Committeeman)	
Sang-Rak Kim	(signature)
(Committeeman)	

Dynamical Behaviors of Coupled Chaotic Systems and Quasiperiodically Forced Systems: Synchronization and Strange Nonchaotic Attractors

Abstract

Synchronization in coupled chaotic systems has become a current topic of intensive study because of its potential applications such as secure communication. Much attention has also been paid to the study of quasiperiodically forced systems, since they generically may have strange nonchaotic attractors (SNAs). In this thesis, we study both the chaos synchronization and the dynamical routes to SNAs.

First, we are concerned about loss of synchronization in two coupled chaotic systems without symmetry. By varying a coupling parameter, we investigate the stability of the synchronized chaotic attractor (SCA) with respect to a perturbation transverse to the synchronization subspace. If all periodic saddles embedded in the SCA are transversely stable, we have a high-quality "strong synchronization" without any burstings from the synchronization subspace. As the coupling parameter varies and passes a threshold value, a saddle fixed point is found to first become transversely unstable through a transcritical bifurcation. Then, burstings from the synchronization subspace occur, and we have a low-quality "weak synchronization." For this case, the basin of the SCA becomes riddled with a dense set of "holes," belonging to the basin of another attractor (or infinity), and the riddled basin is also characterized in terms of the divergence and uncertainty exponents. This kind of weakly stable SCA is very sensitive with respect to the parameter mismatching and the noise which are unavoidable in real situation. To quantitatively measure the degree of such sensitivity, we introduce the parameter and noise sensitivity exponents. In terms of these exponents, we characterize the effect of the parameter mismatch and noise on the intermittent bursting and basin riddling occurring in the regime of weak synchronization. As the coupling parameter is further varied, the SCA becomes more and more weakly stable, and eventually it becomes transversely unstable through a blowout bifurcation when passing another threshold value. Consequently, a complete desynchronization occurs. Thus, an asynchronous hyperchaotic or chaotic attractor with a positive or negative second Lyapunov exponent appears through

a supercritical blowout bifurcation. The type of the newly-born asynchronous attractor, exhibiting on-off intermittency, is found to be determined through competition between its laminar and bursting components. However, for three or more coupled systems, in addition to the complete desynchronization, partial synchronization, where some of the subsystems synchronize while others do not, may also occur via a blowout bifurcation of the SCA. We investigate the dynamical mechanism for the occurrence of partial synchronization in three coupled chaotic systems. For this case, a two-cluster state, exhibiting on-off intermittency, appears on an invariant plane through a supercritical blowout bifurcation. If the newly-born two-cluster state is transversely stable, then partial synchronization occurs on the invariant plane. It is shown that the transverse stability of the intermittent two-cluster state may also be determined via competition between its laminar and bursting components.

Second, we study the dynamical behaviors of the quasiperiodically forced systems. In particular, we are interested in the birth of SNAs which are strange in the geometrical sense but nonchaotic in the dynamical sense. Using the rational approximation to a quasiperiodic forcing, we investigate the mechanism for the appearance of SNAs. It is thus found that a smooth torus transforms into an intermittent SNA through the mechanism of intermittency or band merging when it collides with a new kind of unstable ring-shaped set which has no counterpart in the unforced case. Characterization of the intermittent SNAs is made in terms of the average time between bursts and the local Lyapunov exponents. Furthermore, when an attractor (torus, SNA, chaotic attractor) collides with the ring-shaped unstable set on a basin boundary, it suddenly disappears through a new type of boundary crisis.

Contents

1 Introduction **1**

2 Synchronization in Coupled Chaotic Systems **13**

2.1 Bifurcation Mechanism for the Loss of Chaos Synchronization 14

2.1.1 Transcritical Transition to Basin Riddling 15

2.1.2 Characterization of the Riddled Basin 22

2.1.3 Effect of Asymmetry on the Loss of Chaos Synchronization 24

2.2 Effect of Parameter Mismatching and Noise on Weak Synchronization 47

2.2.1 Characterization of the Parameter Sensitivity 48

2.2.2 Characterization of the Bubbling Attractor and the Chaotic Transient 57

2.2.3 Characterization of the Noise Sensitivity 59

2.2.4 Universality for the Parameter-Mismatching and Noise Effect 70

2.3 Dynamical Consequence of Blowout Bifurcations 83

2.3.1 Consequence of Blowout Bifurcations in Two Coupled 1D Maps . . . 83

2.3.2 Consequence of Blowout Bifurcations in High-Dimensional Invertible Systems 94

2.4 Partial Synchronization in Three Coupled Chaotic Systems 99

2.4.1 Partial Synchronization in Three Coupled 1D Maps 99

2.4.2 Partial Synchronization in Multi-Dimensional Invertible Systems . . . 110

3 Dynamical Transitions in Quasiperiodically Forced Systems **117**

3.1 Intermittent Route to Strange Nonchaotic Attractors 118

3.1.1 Intermittent Transition to Strange Nonchaotic Attractors in the Quasiperiodically Forced Logistic Map 118

3.1.2 Universality for the Intermittent Route to Strange Nonchaotic Attractors 126
3.2 Band-Merging Route to Strange Nonchaotic Attractors 139
3.2.1 Band-Merging Transitions in the Quasiperiodically Forced Logistic Map 141
3.2.2 Universality for the Band-Merging Route to Strange Nonchaotic Attractors 155
3.3 Boundary Crises in Quasiperiodically Forced Systems 163
3.3.1 Boundary Crises in the Quasiperiodically Forced Logistic Map 164
3.3.2 Universality for the Boundary Crises 174

4 Conclusion **179**

List of Figures

1.1 Chaos synchronization and application 3
1.2 Appearance of the strange nonchaotic attractor 9

2.1 Stability diagram for the chaos synchronization 17
2.2 Global effects of supercritical riddling and blowout bifurcations 19
2.3 Disappearance of the absorbing area via a transcritical bifurcation 20
2.4 Characterization of the riddled basin 21
2.5 Globally-riddled basins of the synchronized chaotic attractor 23
2.6 Characterization of the riddled basin 24
2.7 Change of the bifurcation for the weak-coupling case when the asymmetry is introduced 27
2.8 Phase diagram for the weak-coupling case 29
2.9 Basin riddling via an appearance of an asynchronous periodic attractor . . . 30
2.10 Destruction of an asynchronous chaotic attractor via an appearance of an asynchronous periodic attractor 32
2.11 Appearance of a small asynchronous chaotic attractor through a (reverse) interior crisis 34
2.12 Change of the bifurcation for the strong-coupling case when the asymmetry is introduced 35
2.13 Phase diagram before the blowout bifurcation for the strong-coupling case . 38
2.14 Bubbling transition through the transcritical bifurcation 39
2.15 Riddling transition through the transcritical bifurcation 41
2.16 Types of the saddle-node bifurcation associated with the transcritical bifurcation 42
2.17 Synchronized chaotic attractor surrounded by a large absorbing area 43

2.18 Riddling transition through the transcritical bifurcation for the weakly asymmetric-coupling case 44
2.19 Phase diagram after the transcritical bifurcation for the strong-coupling case 45
2.20 Large asynchronous chaotic attractor, born via a supercritical blowout bifurcation 46
2.21 Effect of the parameter mismatch on the weak synchronization 52
2.22 Characterization of the parameter sensitivity 53
2.23 Parameter sensitivity function for the weakly stable synchronized chaotic attractor 54
2.24 Parameter sensitivity exponents 55
2.25 Positive local (M-time) Lyapunov exponents for the weak synchronization . 56
2.26 Characterization of attractor bubbling and chaotic transient 59
2.27 Effect of the noise on the weak synchronization 61
2.28 Characterization of the noise sensitivity on the weak synchronization 63
2.29 Noise sensitivity function and exponents for the weak synchronization 65
2.30 Distribution of bounded random numbers 66
2.31 Characterization of the attractor bubbling and chaotic transient 69
2.32 Effect of parameter mismatch in coupled Hénon maps 73
2.33 Characterization of the parameter sensitivity in coupled Hénon maps 76
2.34 Effect of parameter mismatch and characterization of the parameter sensitivity in coupled pendula 81
2.35 Blowout bifurcation of the synchronized chaotic attractor 87
2.36 Appearance of asynchronous hyperchaotic and chaotic attractors via a blowout bifurcation of the synchronized chaotic attractor 90
2.37 Intermittent burstings for the asynchronous chaotic attractors 91
2.38 Competition between bursting and laminar components 92
2.39 Decomposition of the weighted laminar and bursting Lyapunov exponents . . 93
2.40 Consequence of blowout bifurcations in coupled Hénon maps 97
2.41 Consequence of blowout bifurcations in coupled parametrically forced pendula 100
2.42 Complete synchronization in three coupled 1D maps 103
2.43 Occurrence of the partial synchronization and completely desynchronization 104

2.44 Transversely stable and unstable two-cluster states 106
2.45 Decomposition of the transverse Lyapunov exponents into the laminar and bursting components 109
2.46 Occurrence of the partial synchronization in three three coupled Hénon Maps 113
2.47 Occurrence of the partial synchronization in three coupled pendula 116

3.1 Phase diagram and intermittent route to strange nonchaotic attractors . . . 121
3.2 Birth and evolution of ring-shaped unstable set 123
3.3 Mechanism for the intermittent route to strange nonchaotic attractors 125
3.4 State diagram and intermittent route to strange nonchaotic attractors in quasiperiodically forced Hénon map 128
3.5 Mechanism for the intermittent route to strange nonchaotic attractors 130
3.6 Plot of parameters at which the transitions to intermittent strange nonchaotic attractor occur in the rational approximation 132
3.7 State diagram and intermittent route to strange nonchaotic attractors in the quasiperiodically forced ring map 133
3.8 Mechanism for the intermittent route to strange nonchaotic attractors 136
3.9 State diagram and intermittent route to strange nonchaotic attractors in the quasiperiodically forced Toda oscillator 138
3.10 Mechanism for the intermittent route to strange nonchaotic attractors 140
3.11 State diagram near the second-order tongue 143
3.12 Standard band-merging transition, basin boundary metamorphosis, and birth of the ring-shaped unstable set 145
3.13 Band-merging route to strange nonchaotic attractors and its mechanism . . . 148
3.14 Characterization of the single-band intermittent strange nonchaotic attractor 150
3.15 Band-merging transition of the two-band strange nonchaotic attractor 153
3.16 State diagram and band-merging route to strange nonchaotic attractors in the quasiperiodically forced Hénon map 157
3.17 Mechanism for the band-merging route to strange nonchaotic attractors . . . 160
3.18 State diagram and band-merging route to strange nonchaotic attractors in the quasiperiodically forced Toda oscillator 162

3.19 State diagram near the main tongue 165
3.20 Standard boundary crisis, basin boundary metamorphosis, and birth of the ring-shaped unstable sets 167
3.21 Boundary crisis of the smooth torus and its mechanism 170
3.22 Boundary crisis of the strange nonchaotic attractor and its mechansim . . . 172
3.23 State diagram in the quasiperiodically forced Hénon map 175
3.24 Boundary crisis of the smooth torus and its mechanism 177
3.25 Plot of parameters at which the boundary crises occur in the rational approximation 178

Chapter 1

Introduction

In this thesis, we consider the coupled chaotic systems and the quasiperiodically forced systems. They exhibit rich dynamical behaviors, among which we are interested in the chaos synchronization and the birth of strange nonchaotic attractors.

Recently, the phenomenon of synchronization in coupled chaotic systems has become a field of intensive study. A generic feature of a chaotic motion is the sensitivity to initial conditions [1]. This feature, called the "butterfly effect," would seem to defy synchronization among dynamical variables in coupled chaotic systems. However, when the coupling is sufficiently strong, coupled systems may exhibit synchronized chaotic motion on an invariant subspace of the whole phase space [see Fig. 1.1(a)] [2]. This chaos synchronization has a variety of applications, particularly in connection with secure communication [3, 4]. Figure 1.1(b) shows a schematic diagram for the transmission of a secret message. A secret signal, encoded with a chaotic signal (chaotic masking), can be decoded at the receiver using the chaos synchronization [3].

In the field of chaos synchronization, a fundamental and important problem concerns stability of the synchronized chaotic attractor with respect to a perturbation transverse to the invariant synchronization subspace [5, 6]. If its transverse Lyapunov exponent $\sigma_\perp$ is negative, the synchronous chaotic state on the invariant subspace becomes an attractor in the whole phase space. The loss of transverse stability of such a synchronized chaotic attractor is intimately associated with transverse bifurcations of periodic saddles embedded in the synchronized chaotic attractor [7, 8, 9, 10, 11, 12, 13, 14]. When all periodic saddles

are transversely stable, the synchronized chaotic attractor is "strongly" stable without any bursting from the synchronization subspace. As the coupling parameter passes through a threshold value, a periodic saddle (embedded in the synchronized chaotic attractor) first loses its transverse stability through a local bifurcation. After this first transverse bifurcation, trajectories may be locally repelled from the invariant subspace when they visit the neighborhood of the transversely unstable periodic repeller. Thus, loss of strong synchronization begins with such a first transverse bifurcation, and then we have "weak" synchronization [see Fig. 1.1(c)].

In the regime of weak synchronization, intermittent bursting [15, 16] or basin riddling [17] occurs, depending on the global dynamics. If the global dynamics of the system is bounded and there are no attractors off the invariant subspace, locally repelled trajectories exhibit transient intermittent bursting. On the other hand, if the global dynamics is unbounded or there exists an attractor off the invariant subspace, repelled trajectories may go to another attractor (or infinity), and hence the basin of attraction becomes riddled with a dense set of "holes," belonging to the basin of another attractor (or infinity). In a real situation, a small mismatch between the subsystems and noise that destroy the invariant synchronization subspace are unavoidable. Hence, the effect of the parameter mismatch and noise must be taken into consideration for the study on the loss of chaos synchronization. For the case of weak synchronization, a typical trajectory may have segments exhibiting positive local (finite-time) transverse Lyapunov exponents because of local repulsion of transversely unstable periodic repellers embedded in the synchronized chaotic attractor. Hence, any small mismatch or noise results in a permanent intermittent bursting and a chaotic transient with a finite lifetime for the bursting and riddling cases, respectively. These attractor bubbling and chaotic transient demonstrate the sensitivity of the weakly stable synchronized chaotic attractor with respect to the variation of the mismatching parameter and noise.

In Section 2.1, we study the loss of chaos synchronization in the unidirectionally coupled system without symmetry, consisting of two identical one-dimensional (1D) maps [11]. A transition from strong to weak synchronization is found to occur through a transcritical bifurcation between a periodic saddle embedded in the synchronized chaotic attractor and a repeller on the basin boundary. This bifurcation mechanism is also confirmed in general asymmetric systems [10, 12], and it is different from that in coupled chaotic systems with

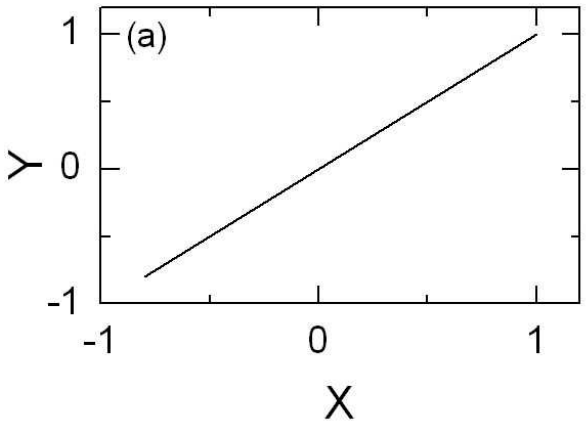

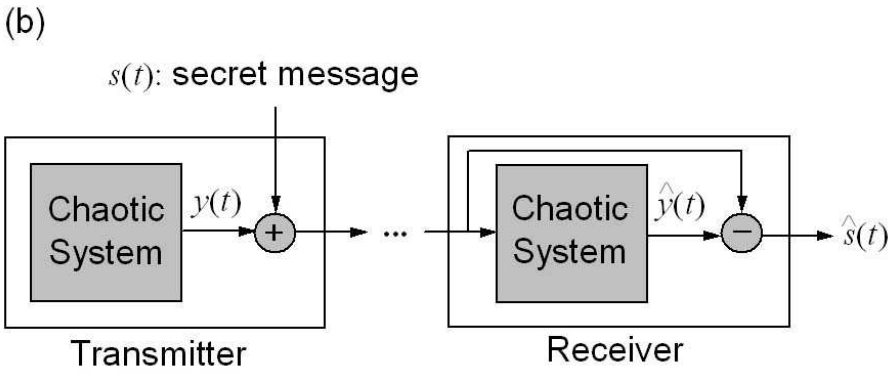

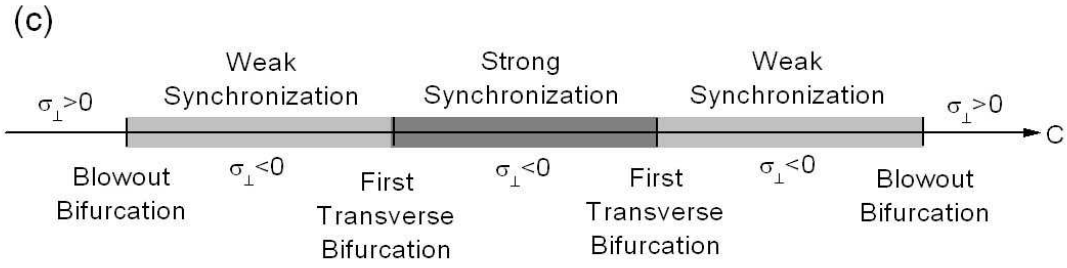

Figure 1.1: (a) Synchronous chaotic attractor in coupled systems. (b) a schematic diagram for the transmission of a secret message by using the chaos synchronization. A secret signal $s(t)$, encoded with a chaotic signal $y(t)$ (chaotic masking), can be decoded at the receiver using the chaos synchronization. (c) Loss of transverse stability of the synchronized chaotic attractor. The loss of strong synchronization begins with the first transverse bifurcation, and then we have "weak" synchronization. With further change of the coupling parameter, the transverse Lyapunov exponent of the synchronized chaotic attractor becomes positive via the blowout bifurcation, and then the synchronized chaotic attractor becomes transversely unstable.

symmetry [7, 9]. As a result of this first transverse bifurcation, the basin of attraction becomes globally riddled with a dense set of holes, leading to divergent orbits. This riddled basin is also characterized in terms of the divergence and uncertainty exponents [18], and thus typical power-law scaling is found. Furthermore, we investigate the effect of asymmetry of coupling on the bifurcation mechanism for the loss of chaos synchronization in coupled chaotic systems [13]. For the weak asymmetry, its effects are similar to those for the symmetric-coupling case. However, with increasing the degree of the asymmetry, the effects change qualitatively, and eventually become similar to those for the extreme case of unidirectional asymmetric coupling.

In Section 2.2, we investigate the effect of the parameter mismatch and noise on weak synchronization in two coupled identical 1D maps with an invariant diagonal [19]. In the regime of weak synchronization, transversely unstable periodic orbits are embedded in the synchronized chaotic attractor. Hence, when a typical trajectory visits the neighborhoods of such unstable periodic orbits, it experiences local transverse repulsion from the diagonal. As a result, the typical trajectory may have segments exhibiting positive local (finite time) transverse Lyapunov exponents, even if the averaged transverse Lyapunov exponent is negative. Because of the existence of these positive local transverse Lyapunov exponents, the weakly stable synchronized chaotic attractor becomes sensitive with respect to the variation of the mismatching parameter and the noise intensity. This is in contrast to the case of the strong synchronization that has no such sensitivity.

We first introduce a new quantifier, called the parameter sensitivity exponent, that measures the "degree" of the parameter sensitivity [19]. Such a parameter sensitivity exponent becomes a quantitative characteristic of the weakly stable synchronized chaotic attractor. As the coupling parameter is varied away from the point of the first transverse bifurcation, successive transverse bifurcations of periodic saddles occur. Hence the value of the parameter sensitivity exponent increases because local transverse repulsion of the periodic repellers embedded in the synchronized chaotic attractor becomes more and more strong. In terms of these parameter sensitivity exponents, the effect of the parameter mismatching on the intermittent bursting and basin riddling is characterized. For the case of bursting, any small mismatching results in a continual sequence of intermittent bursts, called the attractor bubbling, where the long period of nearly synchronous state (laminar phase) is randomly

interrupted by the short-time burst (burst phase). On the other hand, for the case of riddling the synchronized chaotic attractor on the diagonal is transformed into a chaotic transient. In both cases, the quantity of interest is the average time that a typical trajectory spends near the diagonal (i.e., the average interburst interval and the average lifetime of the chaotic transient) [16, 20]. As the parameter sensitivity exponent increases, local transverse repulsion of the periodic repellers embedded in the synchronized chaotic attractor becomes strong, and hence the average time spending near the diagonal becomes short. It is thus found that the scaling exponent for the average time is given by the reciprocal of the parameter sensitivity exponent.

We also investigate the effect of bounded noise on weak synchronization in two coupled identical 1D maps with an invariant diagonal [21]. To quantitatively characterize the noise sensitivity of the weakly stable synchronized chaotic attractor, we introduce a new quantifier, called the noise sensitivity exponent, as in the parameter-mismatching case. Thus the noise sensitivity exponent that measures the degree of the noise sensitivity becomes a quantitative characteristic of the weakly stable synchronized chaotic attractor. As the coupling parameter is varied away from the point of the first transverse bifurcation, successive transverse bifurcations of periodic saddles embedded in the synchronized chaotic attractor occur. Hence the value of the noise sensitivity exponent increases because local transverse repulsion of the embedded periodic repellers becomes more and more strong. For this case, the values of the noise sensitivity exponent are found to become the same as those of the parameter sensitivity exponent, because their values are determined only by the (same) local transverse Lyapunov exponents of the weakly stable synchronized chaotic attractor. Furthermore, it is found that the scaling exponent for the average time spending near the diagonal and the noise sensitivity exponent have a reciprocal relation, as in the parameter-mismatching case. Hence the noise and parameter mismatch have essentially the same effect on the power-law scaling behavior of the average time.

To examine the universality for the effect of parameter mismatch and noise effect on weak chaotic synchronization, we study coupled high-dimensional invertible systems such as the coupled Hénon maps and coupled pendula [22]. By generalizing the method proposed in coupled 1D noninvertible maps [19, 21], we introduce the parameter and noise sensitivity exponents δ to measure the degree of the parameter and noise sensitivity of a weakly stable

synchronized chaotic attractor. In terms of the parameter and noise sensitivity exponents, we characterize the effect of the parameter mismatch and noise on the intermittent bursting and the basin riddling occurring in the regime of weak synchronization. It is thus found that the scaling exponent μ for the average characteristic time (i.e., the average interburst time and the average chaotic transient lifetime) for both the bubbling and riddling cases is given by the reciprocal of the parameter and noise sensitivity exponent, as in the simple system of coupled 1D maps. Hence, the reciprocal relation (i.e., $\mu = 1/\delta$) seems to be "universal," in the sense that it holds in typical coupled chaotic systems of different nature.

As the coupling parameter is further varied and passes a threshold value, the synchronized chaotic attractor becomes transversely unstable (i.e., its largest transverse Lyapunov exponent becomes positive), and then desynchronization occurs via a blowout bifurcation [23, 24, 25, 26]. Depending on the global dynamics, two kinds of blowout bifurcations may occur. For the case of a supercritical (nonhysteretic) blowout bifurcation, an asynchronous attractor is born, and exhibits intermittent bursting, called on-off intermittency [27, 28, 29, 30, 31, 32, 33, 34, 35]; long periods of nearly synchronous motion (off state) are occasionally interrupted by short-term asynchronous burstings (on state). On the other hand, for the case of a subcritical (hysteretic) blowout bifurcation, an abrupt disappearance of the synchronized state occurs, and typical trajectories starting near the invariant subspace are attracted to another distant asynchronous attractor (or infinity).

Here, we are interested in the type of asynchronous intermittent attractors born via supercritical blowout bifurcations. In particular, we are interested in whether the intermittent bursting attractor born at the blowout bifurcation is hyperchaotic (i.e., has more than one positive Lyapunov exponent) or not. Examples of both hyperchaotic attractors [24, 36, 37] and chaotic attractors (i.e., an attractor with only one positive Lyapunov exponent) [11, 13, 24] were given in previous works. However, the dynamical origin for the appearance of such asynchronous hyperchaotic and chaotic attractors remains unclear. In Section 2.3, we investigate the dynamical origin for the occurrence of asynchronous hyperchaos and chaos via blowout bifurcations in coupled chaotic systems [38]. As a representative model, we consider a system of two coupled 1D maps with a parameter α tuning the degree of asymmetry of coupling [13]. This model system can be used to represent the two-cluster dynamics in globally coupled 1D maps, in which each element is coupled to all others with

equal strength, and the asymmetry parameter α is related to a parameter describing the distribution of elements between the two clusters [10]. Depending on the value of α, an asynchronous hyperchaotic or chaotic attractor appears through a blowout bifurcation. This transition to asynchronous hyperchaos or chaos via a blowout bifurcation corresponds to a transition from a fully synchronized state to a hyperchaotic or chaotic two-cluster state in globally coupled 1D maps. We study the type of asynchronous intermittent attractors born via blowout bifurcations in two coupled 1D maps by varying the asymmetry parameter α. A typical trajectory on the newly-born asynchronous attractor, exhibiting on-off intermittency, may be decomposed into laminar (i.e., nearly synchronous) and bursting components. It is found that the type of the asynchronous intermittent attractor (corresponding to an intermittent two-cluster state for the case of global coupling) may be determined through competition between its laminar and bursting components. When the "strength" (i.e., its weighted second Lyapunov exponent) of the bursting component is larger (smaller) than that of the laminar component, an asynchronous hyperchaotic (chaotic) attractor (corresponding to a hyperchaotic (chaotic) two-cluster state for the globally-coupled case) appears. These results are of wider significance because the (uncoupled) 1D map is a paradigm model for period-doubling dynamics in a large class of systems. As examples, we consider two coupled Hénon maps [32] and two coupled parametrically forced pendula [39], which are high-dimensional invertible period-doubling systems, and obtain similar results.

However, for three or more coupled systems, in addition to the complete desynchronization, partial synchronization, where some of the subsystems synchronize while others do not, may also occur via a blowout bifurcation of the synchronized chaotic attractor [40, 41, 42, 43, 44, 45]. Particularly, the partial synchronization (or clustering) has been extensively investigated in globally coupled systems where each subsystem is coupled to all the other subsystems with equal strength [46]. Here, we are interested in whether the asynchronous attractor born via a supercritical blowout bifurcation of the fully synchronized attractor is partially synchronized or completely desynchronized. Examples of both partially synchronized attractors [40, 42, 43, 44] and completely desynchronized attractors [41, 45] were reported. These previous results show that occurrence of partial synchronization depends on the type of the base map constituting the coupled system and the type of coupling between the base maps. However, the underlying mechanism for the occurrence of

partial synchronization remains unclear. In Section 2.4, we study the dynamical mechanism for the occurrence of partial synchronization in three coupled chaotic systems [47]. As a simple model where partial synchronization may occur, we consider three coupled 1D maps with a parameter p ($0 \leq p \leq 1/3$) tuning the degree of asymmetry in the coupling from the unidirectional coupling ($p = 0$) to the symmetric coupling ($p = 1/3$). This model can be used to represent the three-cluster dynamics in an ensemble of N globally coupled 1D maps and the parameter p describes the distribution of the elements between the three clusters [10]. For both extreme cases of the unidirectional [40] and symmetric [45] couplings, partial synchronization and complete desynchronization occur, respectively. We investigate the dynamical mechanism for the occurrence of partial synchronization by increasing the parameter p from 0 to 1/3. An asynchronous two-cluster state appears on an invariant plane via a supercritical blowout bifurcation of the fully synchronized attractor on the diagonal. A typical trajectory in the newly-born two-cluster state exhibits on-off intermittency. When the asymmetry parameter p is less than a threshold value p^* (i.e., $0 \leq p < p^*$), the two-cluster state on the invariant plane is transversely stable, and hence partial synchronization occurs. However, for $p > p^*$ a completely desynchronized attractor, occupying a three-dimensional (3D) finite volume, appears because the two-cluster state is transversely unstable. By generalizing the method proposed in the two-coupled case [38], we find that such transverse stability of the intermittent two-cluster state may be determined via competition between its laminar and bursting components. When the "transverse strength" of the laminar component is larger (smaller) than that of the bursting component, the two-cluster state becomes transversely stable (unstable), and hence a partially synchronized (completely desynchronized) attractor appears through the supercritical blowout bifurcation. These results are also confirmed for the case of three coupled multidimensional invertible period-doubling systems such as the coupled Hénon maps and coupled pendula. Hence, the mechanism for the occurrence of partial synchronization seems to be of wide significance because it holds in typical three-coupled period-doubling systems.

In Chapter 3, we study dynamical behaviors of quasiperiodically forced systems driven at two incommensurate frequencies. To probe dynamical properties of a system, one often applies an external stimulus to the system and observes its response. The dynamical responses of periodically forced systems have been well studied, and a transition from regular to chaotic

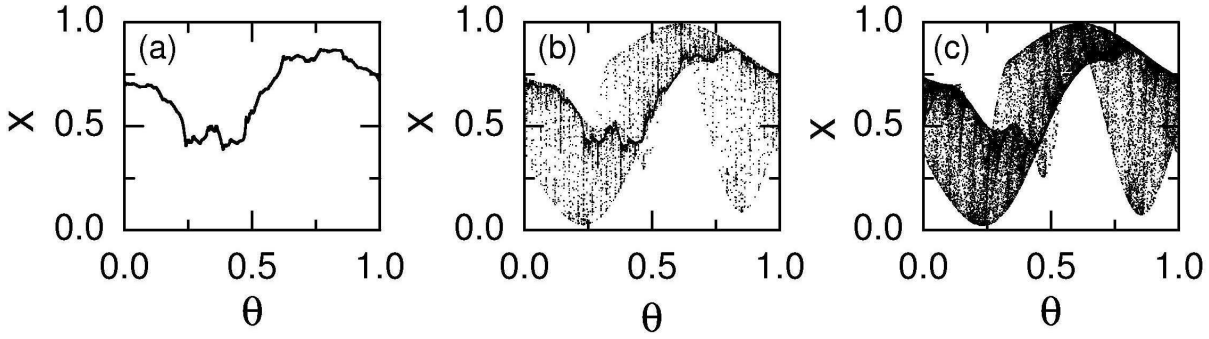

Figure 1.2: (a) Smooth torus, (b) strange nonchaotic attractor, and (c) chaotic attractor in the quasiperiodically forced logistic map of Eq. (3.1)

states has thus been found. Recently, much attention has been paid to the quasiperiodically forced systems because a new type of strange nonchaotic attractors which exhibit some properties of regular as well as chaotic attractors appear typically as intermediate states between the regular and chaotic states (see Fig. 1.2) [48]. These strange nonchaotic attractors were first described by Grebogi et al. [49] and have been extensively investigated both theoretically [50, 51, 52, 53, 54, 55, 56, 57, 58, 59, 60, 61, 62, 63, 64, 65, 66, 67, 68, 69, 70, 71] and experimentally [72]. Like regular attractors, their dynamics is nonchaotic in the sense that they do not have a positive Lyapunov exponent; like typical chaotic attractors, they exhibit fractal phase space structure. Furthermore, strange nonchaotic attractors are related to Anderson localization in the Schrödinger equation with a spatially quasiperiodic potential [73], and they may have a practical application in secure communication [74]. Therefore, dynamical transitions in quasiperiodically forced systems have become a topic of considerable current interest. However, the mechanisms of their occurrence as a system parameter is varied are much less clear than those of unforced or periodically forced systems.

In Section 3.1, we are interested in the dynamical transition to strange nonchaotic attractors accompanied by intermittent behavior. As a parameter passes a threshold value, a smooth torus abruptly transforms into an intermittent strange nonchaotic attractor. Near the transition point, the intermittent dynamics on the strange nonchaotic attractor was characterized in terms of the average interburst time and the Lyapunov exponent [60]. This route to an intermittent strange nonchaotic attractor is quite general and has been observed in a number of quasiperiodically forced period-doubling maps and flows [61, 62]. However,

the mechanism for this intermittent route to strange nonchaotic attractors remains unclear because an unstable orbit inducing such a transition was not located. We investigate the underlying mechanism for the intermittent transition in the quasiperiodically forced logistic map which we regard as a representative model for quasiperiodically forced period-doubling systems [66]. Using rational approximations to the quasiperiodic forcing, we observe a new type of invariant unstable set, which will be referred to as a "ring-shaped" unstable set in accordance with its geometry. When a smooth torus (corresponding to an ordinary quasiperiodic attractor) collides with this ring-shaped unstable set, a transition to an intermittent strange nonchaotic attractor is found to occur through a "phase-dependent saddle-node" bifurcation. To examine the universality for the intermittent route to strange nonchaotic attractors, we investigate the quasiperiodically forced Hénon map, ring map, and Toda oscillator which are high-dimensional invertible systems [67]. In these invertible systems, dynamical transition to an intermittent strange nonchaotic attractor occurs via a phase-dependent saddle-node bifurcation, when a smooth torus collides with a "ring-shaped" unstable set. We note that this bifurcation mechanism for the appearance of intermittent strange nonchaotic attractors is the same as that found in a simple system of the quasiperiodically forced noninvertible logistic map. Hence, the intermittent route to strange nonchaotic attractors seems to be "universal," in the sense that it occurs through the same mechanism in typical quasiperiodically forced systems of different nature.

Dynamical transitions of attractors which occur with variation of the system parameters have been a topic of considerable interest [75]. Particularly, chaotic transitions attracted much attention. In a large class of dissipative dynamical systems, a chaotic attractor appears via a period-doubling cascade when a nonlinearity parameter a passes a threshold value [76]. Beyond the critical value of a, successive band-merging transitions of the chaotic attractor occur through collision with unstable periodic orbits [77]. These band-merging transitions in period-doubling systems are well studied. In Section 3.2, we are interested in the band-merging transitions in quasiperiodically forced systems driven at two incommensurate frequencies [70, 71]. There are some previous works related to the band-merging transitions. In the quasiperiodically forced logistic map, a transition from a period-doubled torus with two bands to a single-band strange nonchaotic attractor has been found to occur through a collision with the unstable parent torus [30]. In some case, the unstable parent

torus becomes inaccessible from the interior of the basin of an attractor, and then it cannot induce any band-merging transition. Even for this case, band-mergings of smooth torus and strange nonchaotic attractors were observed in other quasiperiodically forced systems [55, 62]. However, the mechanism for such band-merging transitions remains unclear because unstable orbits involved in the transitions were not located.

In Section 3.2, we consider the quasiperiodically forced logistic map which is a representative model for quasiperiodically forced period-doubling systems, and investigate the mechanism for the band-merging transitions by varying the nonlinearity parameter a and the quasiperiodic forcing amplitude ε. For small ε, a standard band-merging transition of a chaotic attractor occurs through a collision with the smooth unstable torus. However, when ε passes a threshold value, a basin boundary metamorphosis occurs [78], and then the smooth unstable torus loses its accessibility from the interior of the basin of the attractor. For this case, the type of the band-merging transition changes. Using the rational approximations to the quasiperiodic forcing, it is found that a new type of band-merging transition occurs for a nonchaotic attractor (smooth torus or strange nonchaotic attractor) as well as a chaotic attractor via a collision with an invariant "ring-shaped" unstable set which has no counterpart in the unforced case. Particularly, for the case of a smooth doubled torus with two bands, the new band-merging transition results in the birth of a single-band strange nonchaotic attractor. This is a new mechanism for the appearance of strange nonchaotic attractors. As ε is further increased and passes another higher threshold value, the basin boundary metamorphosis no longer occurs, and then the smooth unstable torus regains its accessibility from the interior of the basin of the attractor. For this case, a standard band-merging transition of an attractor (smooth torus, strange nonchaotic attractor, or chaotic attractor) takes place again through a collision with the smooth unstable torus. The new type of band-merging route to an intermittent strange nonchaotic attractor is also observed in the quasiperiodically forced Hénon map and the quasiperiodically forced Toda oscillator. In addition to inducing the transition to strange nonchaotic attractors, such a band-merging transition is a direct cause for the truncation of the torus-doubling sequence.

Sudden qualitative changes in the attractor are of special interest. Such discontinuous abrupt changes, called the crises, were first extensively studied by Grebogi et al. [79] and two kinds of crises were discovered for the case of chaotic attractors. A sudden disappearance

of a chaotic attractor occurs when it collides with an unstable periodic orbit on its basin boundary, and is called the boundary crisis. On the other hand, an abrupt increase in the size of a chaotic attractor takes place when the unstable periodic orbit with which the chaotic attractor collides lies in the interior of the basin, and is called the interior crisis. Transient or intermittent dynamics associated with the boundary or interior crisis has been well characterized [80], and these crises have often been observed experimentally in periodically forced systems [81].

In Section 3.3, we study the boundary crisis in quasiperiodically forced systems driven at two incommensurate frequencies. In a recent work, Osinga and Feudel investigated the boundary crisis in the quasiperiodically forced Hénon map, and observed a new type of boundary crisis that occurs when the smooth unstable torus is inaccessible from the interior of the basin of the attractor due to the basin boundary metamorphosis. However, the unstable orbit inducing such a boundary crisis was not located, and thus the mechanism for the new boundary crisis remains unclear. Here, we investigate the underlying mechanism for the boundary crisis in the quasiperiodically forced logistic map [68]. For small quasiperiodic forcing ε, a sudden destruction of a chaotic attractor occurs through a "standard" boundary crisis when it collides with the smooth unstable torus on the basin boundary. However, as ε passes a threshold value, a basin boundary metamorphosis occurs, and then the smooth unstable torus loses its accessibility from the interior of the basin of the attractor. For this case, the type of the boundary crisis changes. Using the rational approximations to the quasiperiodic forcing, it is found that a nonchaotic attractor (smooth torus or strange nonchaotic attractor) as well as a chaotic attractor disappears suddenly via a new type of boundary crisis when it collides with an invariant "ring-shaped" unstable set on the basin boundary. Such a ring-shaped unstable set was first discovered in the study of the intermittent route to strange nonchaotic attractors [66]. The mechanism for this new kind of boundary crisis is also confirmed in the quasiperiodically forced Hénon map.

Finally, in Chapter 4 we summarize and discuss our results. Some directions for future researches associated with our works are also suggested.

Chapter 2

Synchronization in Coupled Chaotic Systems

In this chapter, we study the synchronization in two coupled chaotic systems. As a representative model, we consider two coupled 1D maps and investigate the loss of chaos synchronization by varying a coupling parameter. When all periodic saddles embedded in the synchronized chaotic attractor are transversely stable, we have strong synchronization without any burstings from the diagonal. In Section 2.1, a transition from strong to weak synchronization is found to occur when a periodic saddle first becomes transversely unstable via a transcritical bifurcation in two asymmetrically coupled 1D maps [11, 12]. Consequence of this first transcritical bifurcation is discussed. We note that this bifurcation mechanism is in contrast to that for the symmetrically coupling case. Furthermore, we investigate the effect of asymmetry of coupling on the loss of chaos synchronization by varying the asymmetry parameter from the symmetric to the unidirectional couplings [13]. A weakly stable synchronized chaotic attractor is very sensitive with respect to the parameter mismatch and noise [20]. In Section 2.2, we introduce new quantifiers, called the parameter sensitivity exponent [19] and noise sensitivity exponent [21], to measure such sensitivity, and investigate the effect of the parameter mismatch and noise on the intermittent bursting and basin riddling occurring in the regime of weak synchronization. As the coupling parameter is further varied from the first transverse bifurcation point, the synchronized chaotic attractor becomes more and more weakly stable, and eventually when passing another threshold value,

the synchronized chaotic attractor becomes transversely unstable through a blowout bifurcation [23, 24, 25, 26]. In Section 2.3, we investigate the dynamical origin for the appearance of asynchronous intermittent hyperchaotic and chaotic attractors through a supercritical blowout bifurcation [38]. When the bursting (laminar) component of the asynchronous intermittent attractor is dominant, asynchronous hyperchaos (chaos) occurs. Similar method is also developed for the investigation of the dynamical mechanism for the occurrence of partial synchronization in three coupled chaotic systems in Section 2.4 [47].

2.1 Bifurcation Mechanism for the Loss of Chaos Synchronization

We investigate the loss of chaos synchronization in the coupled chaotic systems without symmetry from the point of view of bifurcations of unstable periodic orbits embedded in the synchronized chaotic attractor. A new mechanism for a direct transition to global riddling through a transcritical contact bifurcation between a periodic saddle embedded in the synchronized chaotic attractor and a repeller on the boundary of its basin of attraction is thus found [11, 12]. Note that this bifurcation mechanism is in contrast with that in the coupled chaotic systems with symmetry. After such a riddling transition, the basin becomes globally riddled with a dense set of repelling tongues leading to divergent orbits. This riddled basin is also characterized by the divergence and uncertainty exponents, and thus typical power-law scaling is found. We also investigate the effect of asymmetry of coupling on the bifurcation mechanism for the loss of synchronous chaos in coupled systems [13]. It is found that, only when the symmetry-breaking pitchfork bifurcations take part in the process of the synchronization loss for the case of symmetric coupling, the asymmetry changes the bifurcation scenarios of the desynchronization. The bifurcation effects for small (large) asymmetry are similar to those in the symmetric (unidirectional) coupling case.

2.1.1 Transcritical Transition to Basin Riddling

Let us consider the unidirectionally coupled system T without symmetry, consisting of two identical 1D maps,

$$T : \begin{cases} x_{t+1} = 1 - ax_t^2, \\ y_{t+1} = 1 - ay_t^2 + c(x_t^2 - y_t^2), \end{cases} \tag{2.1}$$

where x_t and y_t are state variables of the first and second 1D maps at a discrete time t, a is the control parameter of the uncoupled 1D map, and c is a coupling parameter. Note that the unidirectionally coupled map T has an invariant synchronization line $y = x$, although it has no symmetry. This is in contrast to the previously-studied case with a symmetry [7, 8, 9]. Furthermore, this coupled map T is non-invertible, because its Jacobian determinant $\det(DT)$ (DT: Jacobian matrix of T) becomes zero along the critical curves, $L_0 = \{(x, y) \in R^2 : x = 0 \text{ or } y = 0\}$. The critical curves of rank k, L_k ($k = 1, 2, \ldots$), are then given by the images of rank k of L_0 [i.e., $L_k = T^k(L_0)$]. Segments of these critical curves can be used to define a bounded trapping region in the phase plane, called an absorbing area $\mathcal{A}$ with the properties that (i) trajectories that enter $\mathcal{A}$ cannot leave it again, and (ii) there exists a neighborhood $U \supset \mathcal{A}$, whose points enter $\mathcal{A}$ in a finite number of iterations [82]. Furthermore, boundaries of an absorbing area can be also obtained by the union of segments of critical curves and portions of unstable manifolds of unstable periodic orbits. For this case, $\mathcal{A}$ is called a mixed absorbing area.

With increasing the control parameter a, the coupled map T exhibits an infinite sequence of period-doubling bifurcations of synchronous attractors with period 2^n ($n = 0, 1, 2, \ldots$), ending at the accumulation point a_∞ ($= 1.401\,155\cdots$), in some region of c. When crossing a critical line in the $a - c$ plane, a transition from periodic to chaotic synchronization occurs. Figure 2.1 shows the stability diagram for the synchronized chaotic attractor on the main diagonal ($y = x$), which appears when crossing the critical line, denoted by a heavy solid horizontal line joining two points $c = 0$ and $c = -2a_\infty$ on the $a = a_\infty$ line. With further increase of a from a_∞, a sequence of band-merging bifurcations of the synchronized chaotic attractor take place. For $a = a_n$, the 2^{n+1} bands of the synchronized chaotic attractor merge into 2^n bands; $a = a_0$ ($= 1.543\,689\ldots$), $a = a_1$ ($= 1.430\,357\cdots$), and $a = a_2$ ($= 1.407\,405\cdots$) lines are shown the figure. The set of a values yielding synchronous chaotic attractors in the range $(a_\infty, 2]$ forms a fat fractal with a positive measure, riddled with a

dense set of windows of synchronous periodic attractors [83].

For the chaotic values of a, the synchronized chaotic attractor is at least weakly stable inside the region bounded by solid circles in Fig. 2.1, because its transverse Lyapunov exponent

$$\sigma_\perp = \lim_{N\to\infty} \frac{1}{N} \sum_{t=1}^{N} \ln |(1+\frac{c}{a})(-2ax_t)| \tag{2.2}$$

is negative. In the periodic windows of a, the solid circles go to the outside (e.g., see the region of the period-3 window near $a \simeq 1.75$). We note that the synchronized chaotic attractor becomes asymptotically (or strongly) stable in the hatched region with vertical lines, because there all periodic saddles embedded in the synchronized chaotic attractor are transversely stable. However, when crossing a boundary of the hatched region, this strongly stable synchronized chaotic attractor becomes weakly stable through a riddling bifurcation, in which the first periodic saddle loses its transverse stability. The solid and dashed boundary lines denote the transverse period-doubling and transcritical bifurcations, which occur when the transverse Floquet (stability) multiplier of the first periodic saddle with period q ($q = 1, 2, \ldots$),

$$\lambda_\perp = \prod_{t=1}^{q} (1+\frac{c}{a})(-2ax_t), \tag{2.3}$$

passes through -1 and $+1$, respectively. These period-doubling and transcritical bifurcation curves of the periodic saddle with period q are also labelled by D_q and T_q, respectively. Some of riddling bifurcation curves are explicitly shown for $a \geq a_2$. For $a \geq a_0$, the saddle fixed point with $q = 1$, embedded in the synchronized chaotic attractor with a single band, exhibits a riddling bifirucation. However, as a is decreased from a_0, the synchronized chaotic attractor becomes a two-band attractor, and then the saddle fixed point lies outside the synchronized chaotic attractor. Thus, in the range of $a_0 > a \geq a_1$, riddling bifurcations occur when the periodic saddle with $q = 2$ becomes transversely unstable. In such a way, with further decrease of a, periodic saddles with higher q exhibit riddling bifurcations.

From now on, we discuss the effect of such riddling bifurcations on the synchronized chaotic attractor. We first note that all but one riddling bifurcation (T_1) are supercritical period-doubling bifurcations (D_q). As shown in the coupled chaotic systems with symmetry [8, 9, 84], absorbing areas surround the synchronized chaotic attractor on the diagonal $y = x$ after such supercritical riddling bifurcations. Consequently, the synchronized chaotic

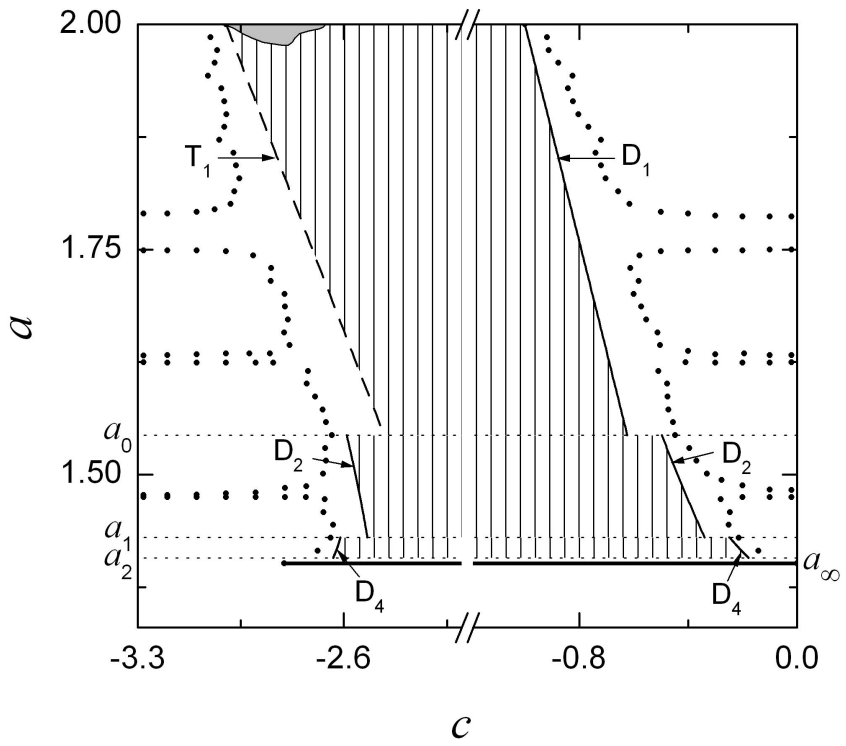

Figure 2.1: Stability diagram for the synchronized chaotic attractor on the diagonal $y = x$ in the $a - c$ plane. The synchronized chaotic attractor appears when crossing the critical line, denoted by a heavy solid horizontal line on the $a = a_\infty$ ($= 1.401\,155\ldots$) line. As a is increased from a_∞, a sequence of band-merging bifurcations occur; some of band-merging points are a_0 ($= 1.543\,689\ldots$), a_1 ($= 1.430\,357\cdots$), and a_2 ($= 1.407\,405\cdots$). The solid circles denote the points, where the transverse Lyapunov exponents of the synchronized chaotic attractor become zero. T_q and D_q are the riddling bifurcation curves through the transcritical and period-doubling bifurcations of the periodic saddles with period q, respectively. Note that the synchronized chaotic attractor is strongly stable in the hatched region with vertical lines. In the small gray region near the top of T_1, the basin is also globally riddled due to a boundary crisis between the minimal invariant absorbing area of the synchronized chaotic attractor and the basin boundary. For other details, see the text.

attractor becomes a weakly stable attractor with a locally-riddled basin. As an example consider the case of $a = 1.82$. A riddling bifurcation occurs when crossing the curve D_1 at $c = c_{r,1}$ $(= -0.850\,625\ldots)$. For this case, the saddle fixed point embedded in the synchronized chaotic attractor loses its transverse stability through a supercritical period-doubling bifurcation. After that, the synchronized chaotic attractor is surrounded by an absorbing area, acting as a bounded trapping vessel, as shown in Fig. 2.2(a) for $c = -0.82$. Hence the locally repelled trajectories exhibit transient intermittent bursting from the synchronization line $y = x$, i.e. the basin becomes only locally riddled. As c is further increased, periodic saddles embedded in the synchronized chaotic attractor become transversely unstable through successive transverse bifurcations. Eventually, the weakly-stable synchronized chaotic attractor becomes transversely unstable when its transverse Lyapunov exponent becomes positive for $c = c_{b,1}$ $(\simeq -0.677)$, and then it transforms to a chaotic saddle. Since an absorbing area exists, this blow-out bifurcation becomes supercritical. Hence, an asynchronous chaotic attractor, bounded to the absorbing area, is developed gradually from the synchronization line $y = x$, as shown in Fig. 2.2(b) for $c = -0.66$. Near the blow-out bifurcation point, such an asynchronous chaotic attractor exhibits a typical intermittent bursting, called the on-off intermittency [27, 28, 29, 30, 31, 32, 33, 34, 35], i.e. the long period of nearly synchronous state (off state) is occasionally interrupted by the short-time bursts (on state). As known well, the average bursting amplitude $\bar{d}$ from the synchronization line is found to increase linearly from zero with respect to Δc $(= c - c_{b,1})$, i.e. $\bar{d} \sim \Delta c$.

However, when crossing the curve T_1, the basin becomes globally riddled with a dense set of tongues, leading to divergent trajectories, through a transcritical contact bifurcation between the saddle fixed point embedded in the synchronized chaotic attractor and the repeller at the basin boundary. Note that this new bifurcation mechanism is in contrast with that in the coupled chaotic systems with symmetry [7, 9]. For several values of a, we have investigated this riddling transition with variation of the coupling parameter c, and found the same bifurcation mechanism. As an example, consider the case of $a = 1.82$. Figure 2.3 shows the change in the structure of the basin with respect to c. For $c = -2.67$, the synchronized chaotic attractor is strongly stable, because all periodic saddles embedded in the synchronized chaotic attractor are stable. The basin for this case is denoted by the gray region in Fig. 2.3(a). The segments of the unstable manifolds (whose directions are denoted

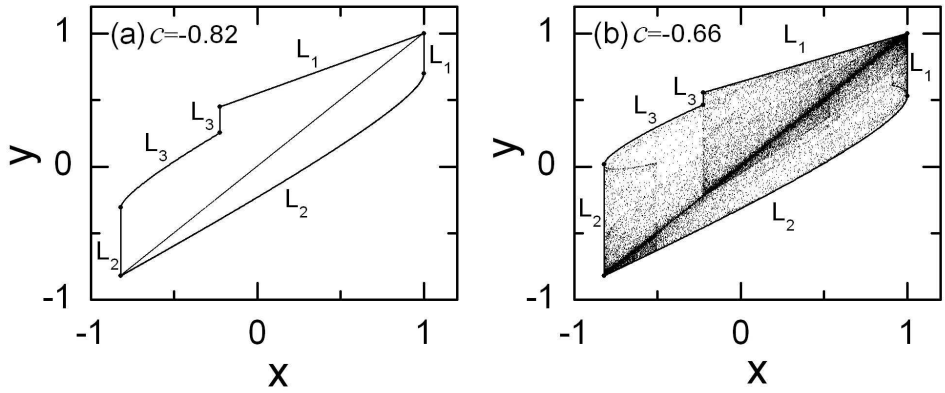

Figure 2.2: Global effects of the supercritical riddling and blow-out bifurcations for $a = 1.82$. (a) After the supercritical riddling bifurcation, an absorbing area, whose boundary is formed by the segments of the critical curves, L_1, L_2, and L_3, is surrounding the synchronized chaotic attractor on the diagonal $y = x$ for $c = -0.82$. (b) After the supercritical blow-out bifurcation, an asynchronous chaotic attractor, bounded to the absorbing area, is exhibiting intermittent bursting for $c = -0.66$.

by the arrows) of the repeller, denoted by the down-triangle ($\bigtriangledown$), at the cusp of the basin boundary connect to segments of the critical curves L_1 and L_2 (the dots indicate where these segments connect), and hence define a mixed absorbing area, surrounding the synchronized chaotic attractor, in which the saddle, denoted by the up-triangle ($\bigtriangleup$), is embedded. As c is decreased, the repeller approaches the saddle, and also the absorbing area shrinks, as shown in Fig. 2.3(b) for $c = -2.72$. Eventually, at the riddling bifurcation point $c = c_{r,2}$ ($= -2.789\,372\ldots$), the repeller and saddle collide, and hence the absorbing area disappears [see Fig. 2.3(c)]. Since the synchronized chaotic attractor is touching its basin boundary at the saddle point, such a riddling bifurcation induces a contact bifurcation between the synchronized chaotic attractor and its basin boundary. Note also that an infinitely narrow "tongue," belonging to the basin of an attractor at the infinity, opens at the saddle point, as shown in the inset of Fig. 2.3(c). In fact, the whole basin becomes globally riddled with a dense set of repelling tongues, emanating from the saddle point and its preimages. When passing the point $c_{r,2}$, the repeller moves down off the basin boundary, and exchanges stability with the saddle [i.e., the repeller (saddle) transforms to a saddle (repeller)]. However, the

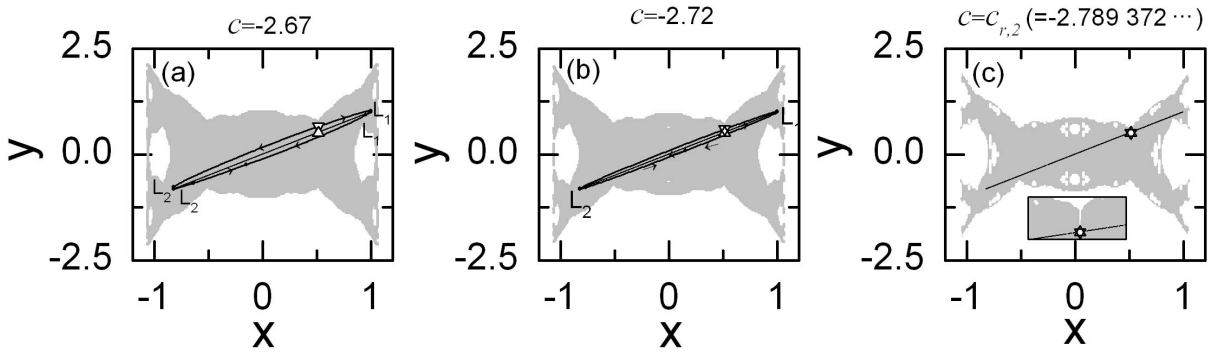

Figure 2.3: Change in the structure of the basin (gray region) of the synchronized chaotic attractor on the diagonal $y = x$ for $a = 1.82$. (a) Union of segments of the unstable manifolds of the repeller ($\bigtriangledown$) at the basin boundary and segments of the critical curves L_1 and L_2 defines a mixed absorbing area of the synchronized chaotic attractor for $c = -2.67$. (b) As c decreases, the repeller approaches the saddle point ($\bigtriangleup$) embedded in the synchronized chaotic attractor, and hence the absorbing area shrinks, as shown for $c = -2.72$. (c) Through a transcritical contact bifurcation between the repeller ($\bigtriangledown$) and the saddle point ($\bigtriangleup$) for $c = c_{r,2}$, the absorbing area disappears, and then the basin becomes globally riddled with a dense of tongues, leading to divergent trajectories. For other details, see the text.

synchronized chaotic attractor continues to contact its basin boundary at a new repelling fixed point ($\bigtriangleup$). This is just the transcritical contact bifurcation, occurring in asymmetric dynamical systems with invariant subspaces, when a Floquet multiplier passes 1 [85].

Near the riddling transition point $c = c_{r,2}$, the repelling tongues are too narrow to be observable. For this case, small changes in the dynamical system, destroying its invariant synchronization line $y = x$, leads to superpersistent chaotic transient behavior [86], as in the case of the coupled chaotic systems with symmetry [7]. To show this, we introduce a small parameter mismatching by taking the control parameter b of the second 1D map as $b = a - \epsilon$, where a is the control parameter of the first 1D map and ϵ is a small invariance-breaking parameter. When $\epsilon > 0$, $y = x$ is no longer an invariant line, and the synchronized chaotic attractor on the diagonal $y = x$ converts to an extremely long chaotic transient, eventually attracted to the infinity. For $c = -2.8$, we decrease ϵ from 0.1 and compute the average transient time. For each value of ϵ, we choose 1000 initial points at random with uniform probability in the range of $x \in (1 - a, 1)$ on the diagonal $y = x$. A trajectory may

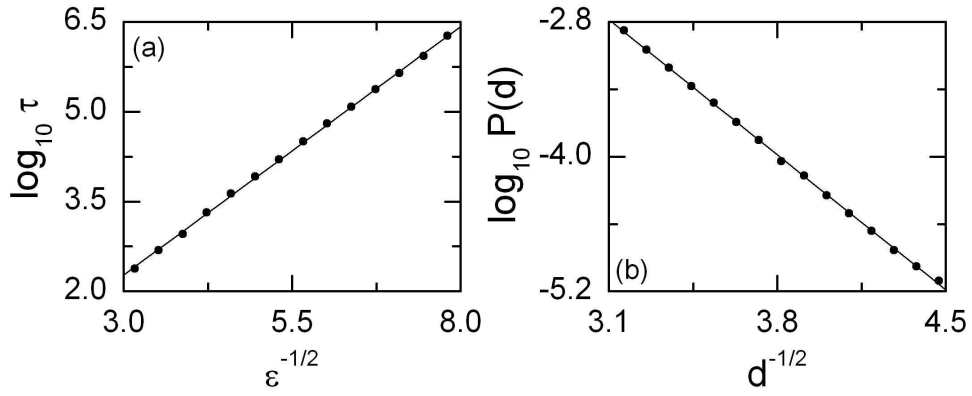

Figure 2.4: (a) Plot of $\log_{10}\tau$ (τ: average life-time of a chaotic transient) versus $\epsilon^{-1/2}$ (ϵ: mismatching parameter) for $a = 1.82$ and $c = -2.8$. (b) Plot of $\log_{10} P(d)$ ($P(d)$: divergence probability) versus $d^{-1/2}$ (d: distance from the diagonal $y = x$) for $a = 1.82$ and $c = -2.8$.

be regarded as having escaped once the magnitude of its y values becomes larger than 10, because an orbit point with $|y| > 10$ lies sufficiently outside the basin of the synchronized chaotic attractor. It is thus found that the average lifetime τ of the chaotic transient scales with ϵ as

$$\tau \sim e^{\mu\epsilon^{-\gamma}}, \tag{2.4}$$

where μ is a positive constant to be fitted, and the exponent γ is $1/2$ in contrast to the symmetric-coupling case with $\gamma = 2/3$ [7]. Figure 2.4(a) shows the plot of $\log_{10}\tau$ versus $\epsilon^{-1/2}$ for $0.1 \geq \epsilon \geq 0.015$. Note that this plot is well fitted with a straight line, which implies that Eq. (2.4) is well obeyed. As ϵ decreases toward zero, the average transient time increases faster than any power of ϵ^{-1}. Hence the chaotic transient near $c = c_{r,2}$ is very long-lived.

Alternatively, instead of computing the average life-time of the chaotic transient, we also estimate the "divergence" probability $P(d)$ of being attracted to the infinity with the distance d from the synchronization line $y = x$ for $\epsilon = 0$. When $c = -2.8$, with decreasing d from 0.1 to 0.05, we compute the divergence probability $P(d)$. For each value of d, we choose an initial condition at random with uniform probability in the range of $x \in (1 - a, 1)$ on the line $y = x + d$, and determine whether it is attracted to the synchronized chaotic attractor at $y = x$ or to the infinity. We repeat this process until 3000 divergent initial conditions are obtained, and thus estimate $P(d)$. Figure 2.4(b) shows the plot of $\log_{10} P(d)$ versus $d^{-1/2}$.

It is thus found that the divergence probability $P(d)$ scales with d as

$$P(d) \sim e^{-\nu d^{-1/2}}, \tag{2.5}$$

where ν is a positive constant to be fitted. Note that as d decreases toward zero, $P(d)$ decreases more rapidly than any power of d. Hence the measure of the set of repelling tongues is extremely small near the riddling bifurcation point $c = c_{r,2}$.

2.1.2 Characterization of the Riddled Basin

In the parameter region away from the riddling transition point $c_{r,2}$ for $a = 1.82$, we characterize the measure of the basin riddling and the arbitrarily fine scaled riddling of the basin of the synchronized chaotic attractor by the divergence and uncertainty exponents, respectively [11, 12]. As c decreases toward the blow-out bifurcation point $c_{b,2}$ ($\simeq -2.963$), the repelling tongues, leading to divergent trajectories, continuously expands, as shown in Figs. 2.5(a), 2.5(b), and 2.5(c), and hence the measure of the riddled basin of the synchronized chaotic attractor decreases to zero. At last, when passing the blow-out bifurcation point $c_{b,2}$, a subcritical blow-out bifurcation, leading to the abrupt collapse of the synchronized state, occurs. For this subcritical case, there is no absorbing area, and hence typical trajectories starting near the synchronization line $y = x$ diverge to the infinity, in contrast to the supercritical case where an asynchronous chaotic attractor is gradually developed from the synchronization line.

We first characterize the measure of the basin riddling (i.e., the measure of the set of repelling tongues, leading to divergent trajectories) by the divergence probability $P(d)$ of being attracted to the infinity [17] with the distance d from the synchronization line $y = x$. Near the riddling-bifurcation point ($c \simeq c_{r,2}$), $P(d)$ exhibits the exponential scaling of Eq. (2.5), because the measure of the set of repelling tongues is extremely small. However, a transition from the exponential to the algebraic scaling occurs when passing a crossover region ($-2.84 \lesssim c \lesssim -2.81$). Thus, for $c \lesssim -2.84$, the divergence probability $P(d)$ scales with d as

$$P(d) \sim d^{\eta}, \tag{2.6}$$

where η is referred to as the divergence exponent. As the value of η becomes smaller, it becomes easier for trajectories starting near the synchronization line to go to the infinity.

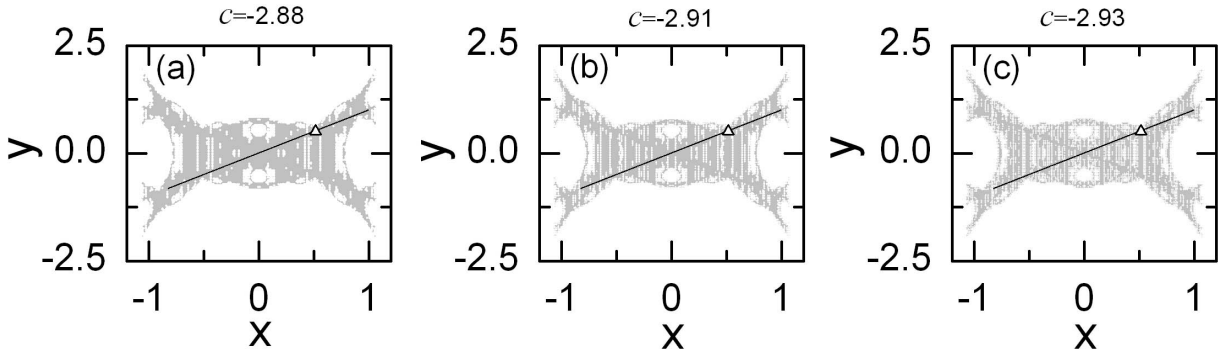

Figure 2.5: Globally-riddled basins (gray region) of the synchronized chaotic attractor on the diagonal $y = x$ for (a) $c = -2.88$, (b) $c = -2.91$, and (c) $c = -2.94$. As c decreases toward the blow-out bifurcation point $c_{b,2}$ ($\simeq -2.963$), the measure of the set of repelling tongues (shown white) increases, and hence the measure of the riddled basin decreases to zero.

For a given value of c, we take many randomly chosen initial conditions on the line $y = x + d$ and determine which basin they lie in. Then, $P(d)$ is estimated as the fraction of the points that are attracted to the infinity. When plotting $\log_{10} P(d)$ versus $\log_{10} d$, the slope of the fitted straight line gives the value of the divergence exponent η. Figure 2.6(a) shows the plot of η versus c for $-2.96 \leq c \leq -2.85$. With decreasing c toward the blow-out bifurcation point $c_{b,2}$, the value of η becomes smaller, and hence the measure of the basin riddling increases.

The results of Eq. (2.6) gives just the measure of the basin riddling, but it says nothing about the arbitrarily fine scaled riddling of the basin of the synchronized chaotic attractor. The riddled basin of the synchronized chaotic attractor is a fat fractal. The fine scaled riddling of the fat fractal is also characterized by the uncertainty exponent α [17] with decreasing c from -2.85 to -2.96. For a given c, consider a square with the sides of length 0.3, centered at a point $(0.35, 0.35)$. We first choose a point z at random with uniform probability inside the square. Also choose a second point z' at random within a small square with the sides of length 2ϵ, centered at the first point z. Then determine the final states of the trajectories starting with the two initial conditions z and z'. If the final states are different, the initial point z is said to be uncertain. We repeat this process for a large number of randomly chosen initial conditions until 4000 uncertain initial conditions are obtained, and

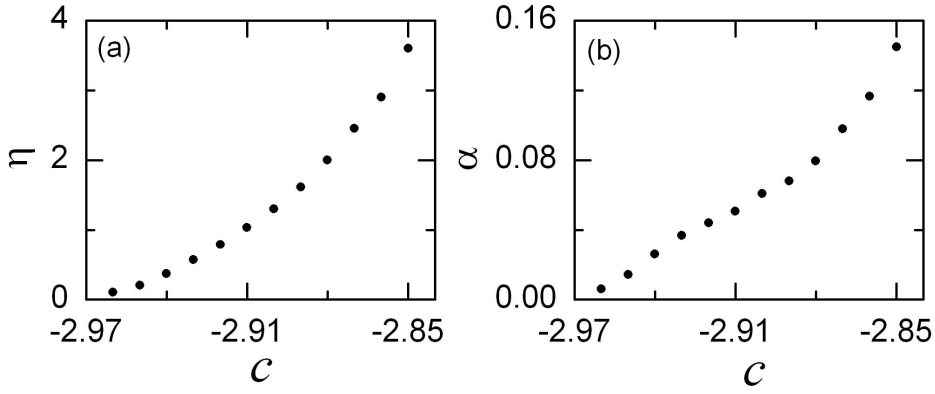

Figure 2.6: (a) Plot of the divergence exponent η versus c for $a = 1.82$. (b) Plot of the uncertainty exponent α versus c for $a = 1.82$.

estimate the probability $P(\epsilon)$ that the two initial conditions z and z' yield different final states. With decreasing ϵ, $P(\epsilon)$ exhibits a power-law scaling,

$$P(\epsilon) \sim \epsilon^{\alpha}, \tag{2.7}$$

where α is referred to as the uncertainty exponent. Note that, if $\alpha < 1$, then a substantial improvement in the accuracy of the initial conditions yields only a small decrease in the uncertainty of the final state. Figure 2.6(b) shows the plot of α versus c for $-2.96 \leq c \leq -2.85$. As c decreases toward the blow-out bifurcation point $c_{b,2}$, the value of α becomes smaller, and hence the uncertainty in determining the final state increases.

2.1.3 Effect of Asymmetry on the Loss of Chaos Synchronization

We investigate the effect of asymmetry of coupling on the bifurcation mechanism for the loss of synchronous chaos in coupled systems [13]. It is found that, only when the symmetry-breaking pitchfork bifurcations take part in the process of the synchronization loss for the case of symmetric coupling, the asymmetry changes the bifurcation scenarios of the desynchronization. For the case of weak coupling, pitchfork bifurcations of asynchronous periodic saddles are replaced by saddle-node bifurcations, while for the case of strong coupling, pitchfork bifurcations of synchronous periodic saddles transform to transcritical bifurcations. The effects of the saddle-node and transcritical bifurcations for the weak asymmetry are similar to those of the pitchfork bifurcations for the symmetric-coupling case. However, with

increasing the "degree" of the asymmetry, their effects change qualitatively, and eventually become similar to those for the extreme case of unidirectional asymmetric coupling.

2.1.3.1 Bifurcation scenarios for the case of weak coupling

First, with decreasing the coupling parameter we investigate the effect of the asymmetry of coupling on the bifurcation scenarios of the loss of chaos synchronization. For this weak-coupling case, it is found that due to the asymmetry, subcritical pitchfork bifurcations of asynchronous periodic saddles are replaced by the saddle-node bifurcations, while other bifurcations such as period-doubling bifurcations are preserved. When the asymmetry parameter α is small, the bifurcation effect is similar to that for the symmetric-coupling case ($\alpha = 0$). However, as α is increased, diverse bifurcation effects, that are different from those for $\alpha = 0$, occur.

Let us consider two asymmetrically coupled identical 1D maps T,

$$T : \begin{cases} x_{t+1} = f(x_t) + (1-\alpha)\, c\, [f(y_t) - f(x_t)], \\ y_{t+1} = f(y_t) + c\, [f(x_t) - f(y_t)], \end{cases} \tag{2.8}$$

where x_t and y_t are state variables of the subsystems at a discrete time t, local dynamics in each subsystem is governed by the 1D map $f(x) = 1 - ax^2$, a is the control parameter of the 1D map, c is a coupling parameter, and α ($0 \leq \alpha \leq 1$) is a parameter tuning the degree of asymmetry. The cases of $\alpha = 0$ and 1 correspond to the symmetric and unidirectional couplings, respectively. Note that this asymmetrically coupled map T has an invariant synchronization line $y = x$, irrespectively of the symmetry. If an orbit lies on this synchronization line, then it is called a synchronous orbit; otherwise it is called an asynchronous orbit.

We also note that the coupled map T is non-invertible, because its Jacobian determinant $\det(DT)$ (DT is the Jacobian matrix of T) becomes zero along the critical curves, $L_0 = \{(x, y) \in R^2 : x = 0 \text{ or } y = 0\}$. A finite number of segments of images L_k ($k = 1, 2, \ldots$) of the critical curves of L_0 can be used to define the boundary of an absorbing area $\mathcal{A}$ with the properties that (i) $\mathcal{A}$ is trapping (i.e., trajectories that enter $\mathcal{A}$ cannot leave it again) and (ii) superattracting (i.e., every point sufficiently close to the boundary of $\mathcal{A}$ will jump into $\mathcal{A}$ after a finite number of iterations) [82]. Furthermore, boundaries of an absorbing area

can be also obtained by the union of segments of critical curves and portions of unstable manifolds of unstable periodic orbits. For this case, $\mathcal{A}$ is called a mixed absorbing area.

With increasing the control parameter a, the coupled map T exhibits an infinite sequence of period-doubling bifurcations of synchronous attractors with period 2^n ($n = 0, 1, 2, \ldots$), ending at the accumulation point a_∞ ($= 1.401\,155\cdots$), in some region of c. This period-doubling cascade leads to creation of the synchronized chaotic attractor on the synchronization line. With further increase of a from a_∞, a sequence of band-merging bifurcations of the synchronized chaotic attractor take place. The set of a values yielding synchronized chaotic attractors in the range $(a_\infty, 2]$ forms a fat fractal with a positive Lebesgue measure, riddled with a dense set of windows of synchronous periodic attractors [83]. Hereafter, without loss of generality we fix the value of a as $a = 1.6$, where a single-band synchronized chaotic attractor exists on the synchronization line. Its transverse stability is determined by a transverse Lyapunov exponent,

$$\sigma_\perp = \ln|1 - (2-\alpha)c| + \lim_{N\to\infty} \frac{1}{N} \sum_{t=1}^{N} \ln|2ax_t|. \tag{2.9}$$

For the symmetric-coupling case of $\alpha = 0$, the following process of desynchronization was found [8]. As the coupling parameter c is decreased through $c = 0.209\ldots$, the saddle fixed point embedded in the synchronized chaotic attractor first becomes transversely unstable through a supercritical period-doubling bifurcation when its transverse Floquet (stability) multiplier,

$$\lambda_\perp = [1 - (2-\alpha)c] f'(x^*) \tag{2.10}$$

passes through -1, where x^* [$= (-1 + \sqrt{1+4a})/2a$] is the fixed point of the 1D map $f(x)$. After this first transverse bifurcation, the synchronous saddle fixed point is transformed into a repeller, and an asynchronous period-2 saddle appears in its vicinity. For this case, along with segments of the critical curves L_1 and L_2, portions of the unstable manifolds of the asynchronous period-2 saddle form a boundary of a mixed absorbing area, surrounding the synchronized chaotic attractor. Hence locally repelled trajectories near the synchronized chaotic attractor cannot leave the mixed absorbing area, and they exhibit transient intermittent bursting from the synchronization line. Thus, this first transverse (period-doubling) bifurcation induces a bubbling transition. However, as c is further decreased, the asynchronous period-2 saddle becomes stabilized for $c = 0.157\ldots$ through a (reverse) subcritical pitchfork

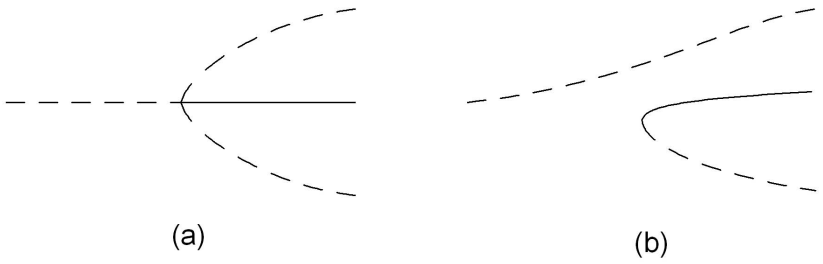

Figure 2.7: Schematic bifurcation diagrams for (a) $\alpha = 0$ and (b) $\alpha > 0$ in the weak-coupling case. Here the solid and dashed lines represent the periodic attractor and saddle, respectively. When the asymmetry is introduced (i.e., $\alpha \neq 0$), the (reverse) subcritical pitchfork bifurcation of an asynchronous periodic saddle for $\alpha = 0$ is transformed into a smooth shift of the asynchronous periodic saddle (without any bifurcation) and a saddle-node bifurcation, creating a new pair of asynchronous saddle and stable node (attractor). For other details, see the text.

bifurcation when its maximal Floquet (stability) multiplier decreases through $+1$ [see the schematic bifurcation diagram in Fig. 2.7(a)]. Then the basin of the synchronized chaotic attractor becomes riddled with a dense set of repelling tongues leading to the asynchronous period-2 attractor. Note that this kind of stabilization of an asynchronous periodic saddle is the only mechanism of the riddling transition for the case of $\alpha = 0$. With further decrease of the coupling parameter c, the synchronized chaotic attractor loses its transverse stability for $c \simeq 0.155$ through a blow-out bifurcation. After this subcritical blow-out bifurcation, the synchronized chaotic attractor transforms to a chaotic saddle with a positive transverse Lyapunov exponent, and the system is asymptotically attracted to the asynchronous period-2 attractor.

From now on, with increasing the asymmetry parameter from $\alpha = 0$, we investigate the bifurcation scenarios of the loss of chaos synchronization. It is thus found that the asymmetry affects the bifurcation mechanism only for the case of the pitchfork bifurcation of an asynchronous periodic saddle, while other bifurcations such as period-doubling bifurcations are preserved. For the symmetric coupling case ($\alpha = 0$), an asynchronous periodic saddle (denoted by the horizontal dashed line) is transformed into an attractor (denoted by the solid line) by emitting a pair of asynchronous saddles (denoted by the dashed lines) with the

same period through a (reverse) subcritical pitchfork bifurcation, as shown in Fig. 2.7(a). However, as α is increased from $\alpha = 0$, the upper dashed branch for the case of $\alpha = 0$ becomes split from the middle solid and lower dashed branches. As a result, the asynchronous periodic saddle varies smoothly along the split upper branch without any bifurcation, and a pair of asynchronous saddle and stable node (attractor) appears along the former middle and lower branches via a saddle-node bifurcation, as shown in Fig. 2.7(b). In such a way, for small α the subcritical pitchfork bifurcation of an asynchronous periodic saddle is replaced with a saddle-node bifurcation, giving rise to the birth of a pair of new asynchronous saddle and stable node. However, as α is further increased, the type of the saddle-node bifurcation may be changed into another one, leading to the birth of a pair of new asynchronous saddle and unstable node (repeller), and then its effect becomes qualitatively different from that for $\alpha = 0$, as will be seen below.

Figure 2.8 shows the phase diagram in the $\alpha - c$ plane. When passing the supercritical period-doubling bifurcation line D_1, the synchronous saddle fixed point first becomes transversely unstable, and an asynchronous period-2 saddle is born. After this first transverse bifurcation, the synchronized chaotic attractor is surrounded by a mixed absorbing area, acting as a bounded trapping vessel, and hence locally repelled trajectories near the synchronized chaotic attractor exhibit transient intermittent bursting from the synchronization line. Thus, a bubbling transition occurs through the first transverse (period-doubling) bifurcation. Note that this period-doubling bifurcation mechanism for the bubbling transition and its effect are the same as those for $\alpha = 0$, independently of the value of α. With further decrease of c, the synchronized chaotic attractor becomes transversely unstable through a blow-out bifurcation at the line B. However, the type of this blow-out bifurcation depends on the value of α. As mentioned above, with increasing α from 0, the subcritical pitchfork bifurction of the asynchronous period-2 saddle for $\alpha = 0$ is replaced by the saddle-node bifurcation, which occurs on the heavy solid line S_2. As shown in the inset of Fig. 2.8, for $0 < \alpha < \alpha_1$ ($\simeq 0.0078$), a pair of asynchronous saddle and stable node with period 2 appears through the saddle-node bifurcation before the blow-out bifurcation. Consequently, the basin (shown in gray) of the synchronized chaotic attractor becomes riddled with a dense set of tongues, belonging to the basin (shown in dark gray) of the newly-born asynchronous period-2 attractor (denoted by the solid circle), which is shown in Fig. 2.9 for $\alpha = 0.005$ and $c = 0.1555$.

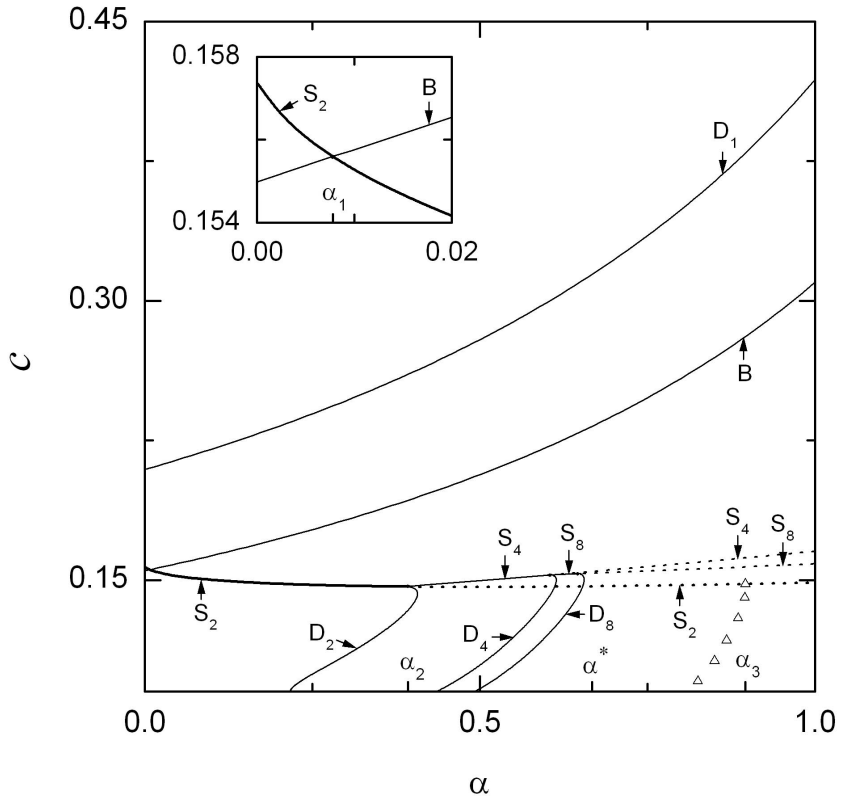

Figure 2.8: Phase diagram in the $\alpha - c$ plane for the case of weak coupling. A bubbling transition occurs on the line D_1 through the supercritical period-doubling bifurcation of the saddle fixed point embedded in the synchronized chaotic attractor. With further decrease of c, the synchronized chaotic attractor becomes transversely unstable through a blow-out bifurcation on the line B. However, dynamical behaviors after the blow-out bifurcation vary depending on the value of α, particularly because of the diverse effect of the saddle-node bifurcation on the curve S_q ($q = 2^n$, $n = 1, 2, \ldots$). The type of the saddle-node bifurcation on S_q changes at the point where the period-doubling bifurcation line D_q of an asynchronous period-q orbit touches the S_q line. Thus, a pair of asynchronous saddle and stable (unstable) node with period q appears when crossing the solid (dotted) part of S_q. Note also that an interior crisis occurs when the line, denoted by the triangles, is crossed. For other details, see the text.

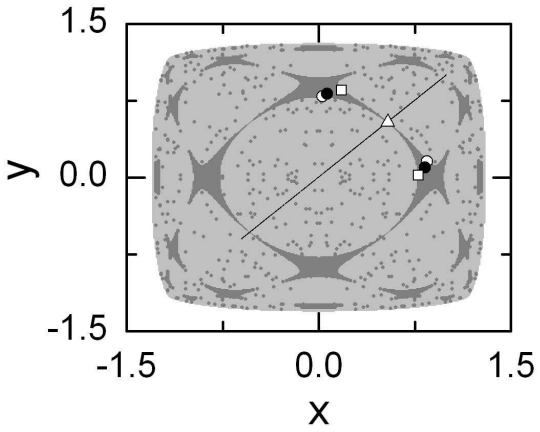

Figure 2.9: Riddled basin of the synchronized chaotic attractor for $\alpha = 0.005$ and $c = 0.1555$ after appearance of a new asynchronous period-2 attractor via a saddle-node bifurcation. Here the square denotes an asynchronous period-2 saddle, born from the synchronous fixed point (denoted by the triangle), through the first transverse period-doubling bifurcation. A pair of asynchronous saddle (denoted by the open circle) and attractor (denoted by the solid circle) with period 2 appears through a saddle-node bifurcation. As a result, the basin of the synchronized chaotic attractor (shown in gray) becomes riddled with a dense set of tongues, belonging to the basin (shown in dark gray) of the asynchronous period-2 attractor.

Note that the stable manifolds of the asynchronous period-2 saddles (denoted by the open circle and square) bound the main tongue, emanating from the synchronous repelling fixed point (denoted by the triangle). Here an asynchronous period-2 saddle (square) is born from the synchronous saddle fixed point (triangle) through the first transverse (period-doubling) bifurcation, while another asynchronous period-2 saddle (open circle) appears along with the asynchronous period-2 attractor (solid circle) via the saddle-node bifurcation. All the other tongues are preimages of this main tongue. Thus, the effect of the saddle-node bifurcation becomes the same as that of the subcritical pitchfork bifurcation for $\alpha = 0$ (i.e., a riddling transition occurs through the appearance of an asynchronous periodic attractor). For this case, when crossing the line B, the synchronized chaotic attractor loses its transverse stability via a subcritical blow-out bifurcation, and then the system is asymptotically attracted to the asynchronous period-2 attractor.

For $\alpha > \alpha_1$, the saddle-node bifurcation on S_2 occurs after the blow-out bifurcation (see

the inset of Fig. 2.8). Hence, when passing the line B, an asynchronous chaotic attractor, bounded to the absorbing area, appears through a supercritical blow-out bifurcation and exhibits a typical intermittent bursting, called the on-off intermittency. However, the subsequent fate of the asynchronous chaotic attractor depends on the value of α. Figure 2.10(a) shows the asynchronous chaotic attractor for $\alpha = 0.2$ and $c = 0.15$, born via the supercritical blow-out bifurcation. However, when passing the S_2 line, the asynchronous chaotic attractor becomes broken up suddenly, because a pair of asynchronous saddle and stable node (attractor) with period 2 appears inside the asynchronous chaotic attractor via the saddle-node bifurcation. After this break up, the asymptotic state changes from the asynchronous chaotic state to an asynchronous period-2 state (denoted by the solid circle), as shown in Fig. 2.10(b) for $\alpha = 0.2$ and $c = 0.14$, where an open circle denotes an asynchronous period-2 saddle born via the saddle-node bifurcation. Note that this destruction effect of the saddle-node bifurcation is in contrast with the riddling effect for $\alpha < \alpha_1$. This kind of destruction through the appearance of an asynchrnous period-2 attractor occurs only when passing the heavy solid part of the S_2 curve for $\alpha_1 < \alpha < \alpha_2$ ($\simeq 0.3924$) (see Fig. 2.8). Note that for $\alpha = \alpha_2$, a period-doubling bifurcation line D_2 of an asynchronous period-2 orbit touches the saddle-node bifurcation line S_2, and then the type of the saddle-node bifurcation changes from the unstable-stable pair bifurcation to the unstable-unstable pair bifurcation. That is, when passing the heavy dotted part of the S_2 curve for $\alpha > \alpha_2$, a pair of asynchronous saddle and unstable node (repeller) with period 2 appears. We also note that a saddle-node bifurcation line S_4, giving rise to the birth of a pair of asynchronous saddle and stable node with period 4, emanates from the contact point of the S_2 line with the D_2 line. In such a way, with increasing α higher-order saddle-node and period-doubling bifurcations of period-q ($q = 2^n,\ n = 2, 3, 4, \ldots$) orbit occur on the S_q and D_q curves, respectively. Thus, the destruction of the asynchronous chaotic attractor continues to take place through the appearance of an asynchronous period-q attractor when passing the solid part of the S_q curve until $\alpha = \alpha^*$ ($\simeq 0.6673$) (see Fig. 2.8). For $\alpha > \alpha^*$, the type of all saddle-node bifurcations on the S_q curves becomes the unstable-unstable pair bifurcations, giving rise to the birth of asynchronous saddle-repeller pairs, and hence destruction phenomena no longer occur.

For $\alpha > \alpha^*$, a large asynchronous chaotic attractor, born via the blow-out bifurcation, is transformed into a small chaotic attractor through a reverse interior crisis, mediated by

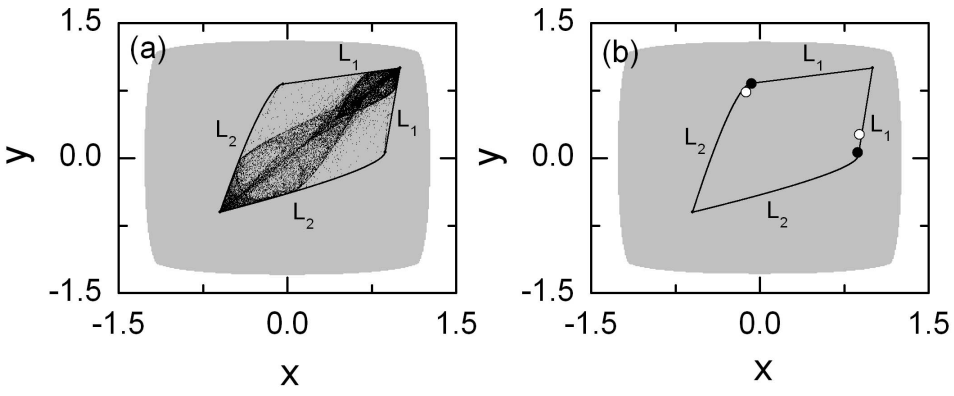

Figure 2.10: Destruction of an asynchronous chaotic attractor through appearance of an asynchronous period-2 attractor inside the asynchronous chaotic attractor via a saddle-node bifurcation for $\alpha = 0.2$. (a) The asynchronous chaotic attractor bounded by segments of the critical curves L_1 and L_2 for $c = 0.15$, born via a supercritical blow-out bifurcation. (b) Asynchronous period-2 attractor (denoted by the solid circle) and its counterpart saddle (denoted by the open circle) for $c = 0.14$ after the destruction of the asynchronous chaotic attractor.

the saddle-node bifurcation. Figure 2.11(a) shows the large asynchronous chaotic attractor, bounded by the segments of the critical curves L_1 and L_2 for $\alpha = 0.85$ and $c = 0.18$. When passing the dotted S_2 curve for $c \simeq 0.1476$, along with a pair of asynchronous saddle and repeller with period 2, born through the saddle-node bifurcation, a small two-piece asynchronous chaotic attractor appears, as shown in Fig. 2.11(b) for $c = 0.14$. Note that the asynchronous period-2 saddle (denoted by the solid circle) is embedded in the small asynchronous chaotic attractor, and the asynchronous period-2 repeller (denoted by the open circle) lies on the dotted line. In fact, all higher-order asynchronous period-q saddles and repellers, born via the saddle-node bifurcations on S_q, also lie on the asynchronous chaotic attractor and the dotted line, respectively. On the other hand, the asynchronous period-2 orbit (denoted by the square), born via the first transverse period-doubling bifurcation of the synchronous fixed point (denoted by the triangle), and its descendant orbits lie on the dashed line. Note that these two lines are bounding a region, where asynchronous unstable periodic orbits (denoted by dots) lie, inside the absorbing area. As we increase the coupling parameter c from 0.14 in a reverse way, the asynchronous period-2 saddle (solid

circle) on the asynchronous chaotic attractor approaches the asynchronous period-2 repeller (open circle) on the dotted boundary line, and they coalesce at their saddle-node bifurcation point ($c \simeq 0.1476$) on S_2. After that, a sudden increase in the size of the asynchronous chaotic attractor occurs through the interior crisis mediated by the saddle-node bifurcation. A similar expansion of the asynchronous chaotic attractor also takes place through another interior crisis when decreasing the coupling parameter c from 0.14. With decrease of c, the asynchronous chaotic attractor becomes larger in a horizontal direction, and it collides with the dashed boundary line when passing the crisis line, denoted by the triangles in Fig. 2.8. After that, the small asynchronous chaotic attractor transforms to a large asynchronous chaotic attractor, covering the whole absorbing area. Note that this interior-crisis curve touches the S_2 curve for $\alpha = \alpha_3$ ($\simeq 0.8965$) (see Fig. 2.8). Hence, for $\alpha > \alpha_3$, no interior crises occur when passing the S_2 curve. Consequently, the large asynchronous chaotic attractor, born via the blow-out bifurcation, is preserved without any qualitative change when passing the S_2 curve, as in the unidirectionally-coupled case ($\alpha = 1$) [11].

2.1.3.2 Bifurcation scenarios for the case of strong coupling

From now on, we investigate the effect of the asymmetry of coupling on the bifurcation scenarios of desynchronization with increasing the coupling parameter. For this strong-coupling case, it is found that the asymmetry changes the supercritical pitchfork bifurcation of a synchronous periodic saddle into a transcritical bifurcation. However, the effect of the transcritical bifurcation varies depending on whether or not it induces a contact between the synchronized chaotic attractor and its basin boundary. If such a contact does not occur, a bubbling transition occurs, while when a contact is induced, a riddling transition takes place. For small α, the transcritical bifurcation does not induce any contact, and hence its effect becomes similar to that in the symmetrically-coupled case ($\alpha = 0$). However, as α is further increased, the type of the transcritical bifurcation is changed into another one inducing a contact, and then the effect of the transcritical bifurcation becomes qualitatively different from that for $\alpha = 0$.

For the case of the symmetric coupling ($\alpha = 0$), the following desynchronization process was found [8]. The synchronous saddle fixed point embedded in the synchronized chaotic attractor first becomes transversely unstable via a supercritical pitchfork bifurcation when

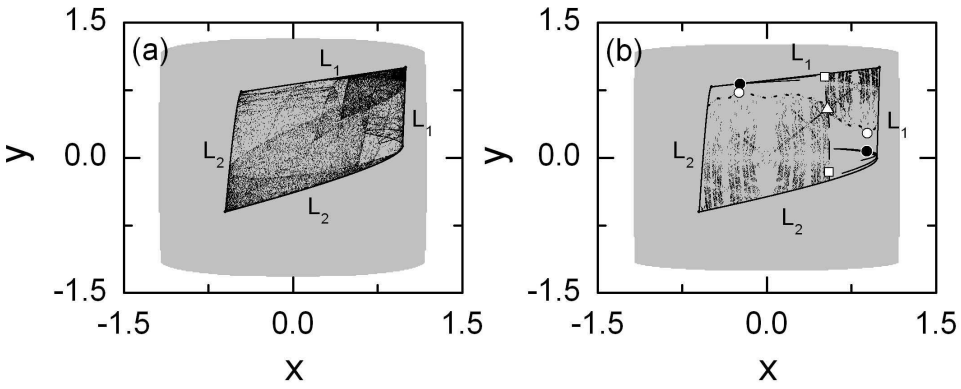

Figure 2.11: Appearance of a small asynchronous chaotic attractor through a (reverse) interior crisis for $\alpha = 0.85$. (a) Large asynchronous chaotic attractor bounded by the segments of the critical curves L_1 and L_2 for $c = 0.18$, born via a supercritical blow-out bifurcation. (b) Small asynchronous chaotic attractor for $c = 0.14$ born through a (reverse) interior crisis, mediated by a saddle-node bifurcation on S_2. Note that the dotted and dashed lines bound the region, where unstable asynchronous periodic orbits lie, inside the absorbing area bounded by segments of the critical curves L_1 and L_2. Here unstable asynchronous orbit points are plotted up to period 16. The asynchronous period-2 saddle (denoted by the solid circle) is embedded in the asynchronous chaotic attractor and the asynchronous period-2 repeller (denoted by the open circle) lies on the dotted line. As c is further decreased, this asynchronous small chaotic attractor is transformed into a large one through another interior crisis occurring when crossing the dashed line, where the asynchronous period-2 orbit (denoted by the square), born through the first transverse period-doubling bifurcation of the synchronous fixed point (represented by the triangle) lies. For other details, see the text.

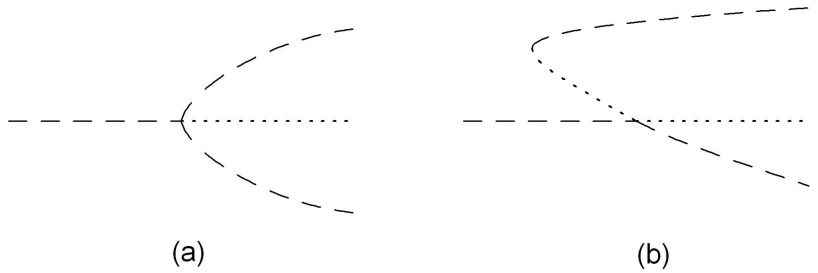

Figure 2.12: Schematic bifurcation diagrams for (a) $\alpha = 0$ and (b) $\alpha > 0$ in the strong-coupling case. Here the dashed and dotted lines represent the periodic saddle and repeller, respectively. When the asymmetry is introduced (i.e., $\alpha \neq 0$), the supercritical pitchfork bifurcation of a synchronous periodic saddle for $\alpha = 0$ is transformed into a transcritical bifurcation of the synchronous periodic saddle and a saddle-node bifurcation, creating a new pair of asynchronous saddle and unstable node (repeller). For other details, see the text.

its minimal Floquet multiplier increases through $+1$ for $c = 0.790\ldots$. As a result of this first transverse bifurcation, the synchronous saddle fixed point is transformed into a repelling fixed point, and a conjugate pair of asynchronous period-1 saddle appears in its neighborhood [see the schematic bifurcation diagram in Fig. 2.12(a)]. For this case, the synchronized chaotic attractor is surrounded by a mixed absorbing area, bounded by union of segments of the unstable manifolds of the asynchronous period-1 saddle and portions of the critical curves L_1 and L_2. Hence, locally repelled trajectories near the synchronized chaotic attractor cannot leave the mixed absorbing area, and they exhibit transient intermittent bursting. Thus, the first transverse (pitchfork) bifurcation induces a bubbling transition. With further increase of c, the asynchronous period-1 saddles are stabilized through subcritical period-doubling bifurcations for $c = 0.842\ldots$. Consequently, the basin of the synchronized chaotic attractor becomes riddled with a dense set of tongues, belonging to the basins of the stabilized asynchronous period-1 attractors. This riddling transition is similar to the weak-coupling case for $\alpha = 0$, although the underlying bifurcation mechanisms for the stabilization are different. As c is further increased, the synchronized chaotic attractor becomes transversely unstable through a subcritical blow-out bifurcation for $c \simeq 0.845$, and then the system is asymptotically attracted to one of the asynchronous period-1 attractors.

We now investigate the bifurcation scenarios of the synchronization loss with increasing

the asymmetry parameter from $\alpha = 0$. It is thus found that the bifurcation mechanism for the case of the pitchfork bifurcation of a synchronous periodic saddle is affected by the asymmetry, while other bifurcations such as period-doubling bifurcations are conserved. For the symmetric coupling case ($\alpha = 0$), a synchronous periodic saddle (denoted by the horizontal dashed line) is transformed into a repeller (denoted by the dotted line) by emitting a conjugate pair of asynchronous saddles (denoted by the dashed lines) with the same period through a supercritical pitchfork bifurcation, as shown in Fig. 2.12(a). However, with increasing the asymmetry parameter from $\alpha = 0$, the upper branch for the case of $\alpha = 0$ is smoothly shifted backward from the bifurcation point, and then two new branches, corresponding to the asynchronous periodic saddle (dashed line) and repeller (dotted line), appear through a saddle-node bifurcation, as shown in Fig. 2.12(b). Note that with increasing the coupling parameter, the asynchronous periodic repeller (dotted line) approaches the synchronous periodic saddle (horizontal dashed line), and eventually they coalesce at a bifurcation point. After that, they exchange only their stability [i.e., the saddle (repeller) transforms to a repeller (saddle)]. Through this transcritical bifurcation, occurring in asymmetric dynamical systems with some constraint [85], the synchronous periodic saddle loses its transverse stability, when its minimal Floquet multiplier increases through +1. However, the effect of this transcritical bifurcation depends on whether or not it induces a contact between the synchronized chaotic attractor and its basin boundary, as will be seen below.

Figure 2.13 shows the phase diagram before the blow-out bifurcation in the $\alpha - c$ plane. As mentioned above, for $\alpha > 0$ the synchronous saddle fixed point first becomes transversely unstable through a transcritical bifurcation, occurring on the line T_1, where the synchronous saddle fixed point exchanges stability with an asynchronous repelling fixed point, born through a saddle-node bifurcation occurring on the line S_1. Note that these transcritical and saddle-node bifurcation lines T_1 and S_1 emanate from the pitchfork bifurcation point for $\alpha = 0$. The type of the transcritical bifurcation of the synchronous saddle fixed point depends on whether or not its "counterpart" (asynchronous repelling fixed point) lies on a basin boundary. Note that the asynchronous period-1 repeller is lying on a basin boundary in the regions hatched with vertical and horizontal lines. Only when the synchronous period-1 saddle collides with an asynchronous period-1 repeller on a basin boundary, the transcritical bifurcation may induce a contact between the synchronized chaotic attractor

and its basin boundary, and then an absorbing area, surrounding the synchronized chaotic attractor, disappears. Consequently, when crossing the heavy dotted part of the T_1 curve, a direct transition to riddling occurs, while when its heavy solid part is passed, a bubbling transition takes place because an absorbing area, surrounding the synchronized chaotic attractor, is preserved. Thus, the T_1 curve is divided into four parts (two heavy solid parts and two heavy dotted parts). The values of α at their boundary points are α_4 ($\simeq 0.3846$), α_5 ($\simeq 0.6187$), and α_6 ($\simeq 0.6667$).

For $0 < \alpha < \alpha_4$, when crossing the S_1 curve, a pair of asynchronous period-1 saddle (denoted by the solid down-triangle) and unstable node (repeller, denoted by the open down-triangle) appears, as shown in Fig. 2.14(a) for $\alpha = 0.3$ and $c = 0.923$. Together with segments of the critical curves L_1 and L_2, portions of the unstable manifolds of the asynchronous saddle fixed point (solid down-triangle) form a boundary of a mixed absorbing area, surrounding the synchronized chaotic attractor. Note that the asynchronous period-1 repeller (open down-triangle) lies strictly inside the absorbing area (i.e., it does not lie on any basin boundary). As c is increased, the asynchronous period-1 repeller (open down-triangle) approaches the synchronous period-1 saddle (denoted by the open up-triangle), embedded in the synchronized chaotic attractor. Eventually, they coalesce and a transcritical bifurcation occurs for $c = 0.930\ldots$. When passing the transcritical bifurcation point, the asynchronous period-1 repeller (open down-triangle) moves down off the synchronization line, and exchanges stability with the synchronous period-1 saddle (open up-triangle), as shown in Fig. 2.14(b) for $c = 0.943$. Since the mixed absorbing area is still surrounding the synchronized chaotic attractor, locally repelled trajectories near the synchronized chaotic attractor exhibit transient intermittent bursting from the synchronization line. Thus the effect of the transcritical bifurcation becomes similar to that of the supercritical pitchfork bifurcation for $\alpha = 0$ (i.e., a bubbling transition occurs). With further increase of c, the asynchronous saddle fixed point becomes stabilized through a subcritical period-doubling bifurcation when crossing the D_1 line for $c = 0.945\ldots$. Consequently, the basin (shown in gray) of the synchronized chaotic attractor becomes riddled with a dense set of tongues, belonging to the basin (shown in dark gray) of the stabilized asynchronous period-1 attractor (solid down-triangle), which is shown in Fig. 2.14(c) for $c = 0.992$. Note that this stabilization mechanism is the same as that for $\alpha = 0$.

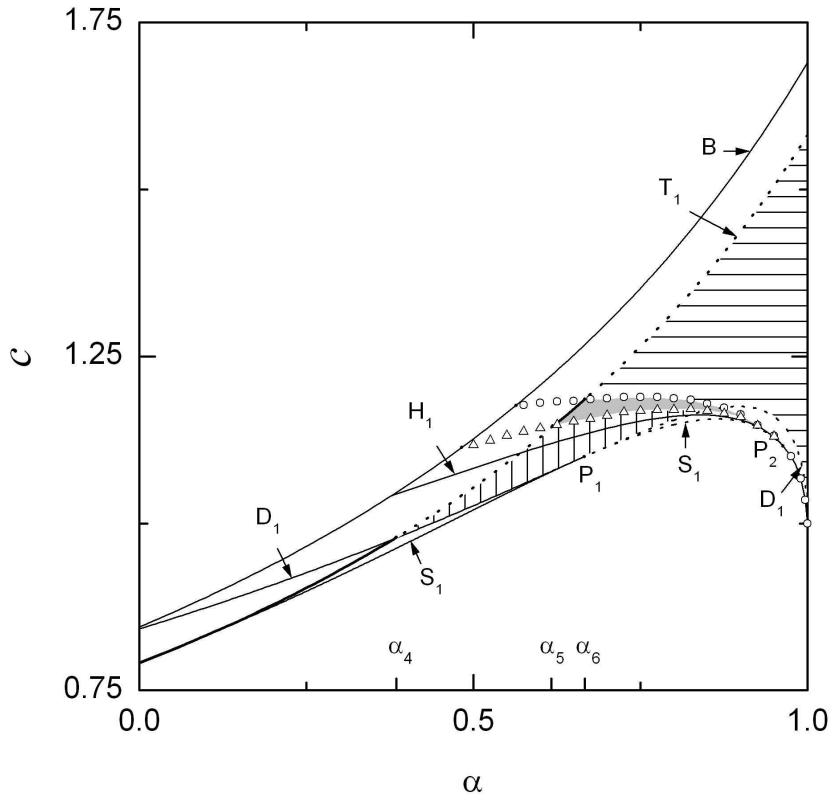

Figure 2.13: Phase diagram before the blow-out bifurcation in the $\alpha - c$ plane for the strong-coupling case. The synchronous saddle fixed point first becomes transversely unstable through a transcritical bifurcation on the line T_1. The effect of the transcritical bifurcation varies depending on whether or not it induces a contact between the synchronized chaotic attractor and its basin boundary. An asynchronous period-1 repeller, which is a counterpart of the synchronous period-1 saddle for the transcritical bifurcation, lies on a basin boundary of the synchronized chaotic attractor in the regions hatched with vertical and horizontal lines. Hence, when crossing the dotted part of T_1, a riddling transition through the transcritical contact bifurcation occurs, while when its solid part is crossed, a bubbling transition takes place, because an absorbing area surrounding the synchronized chaotic attractor is preserved. Thus, the T_1 curve is divided into four parts (two heavy solid parts and two heavy dotted parts). Other diverse dynamical phenomena also occur on the saddle-node bifurcation curve S_1, period-doubling bifurcation curve D_1, Hopf bifurcation curve H_1, boundary-crisis curves (denoted by the open triangles and circles), and blow-out bifurcation curve B. For further details, see the text.

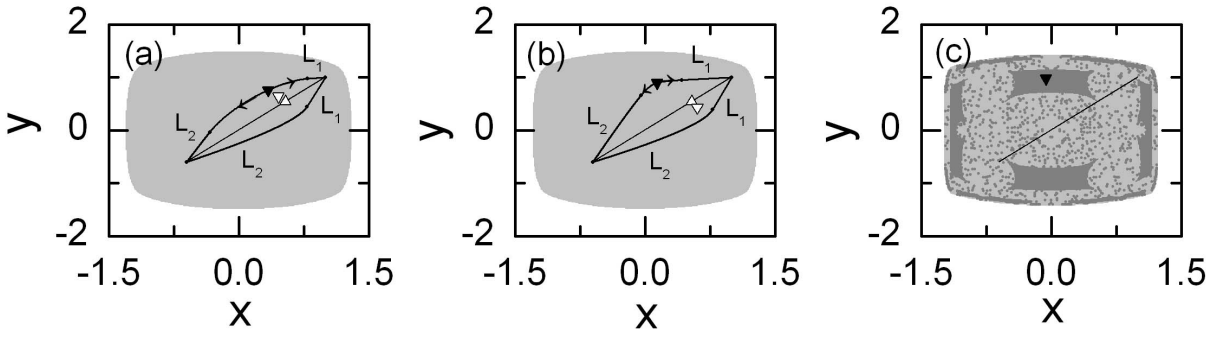

Figure 2.14: Bubbling transition through the transcritical bifurcation that does not induce any contact between the synchronized chaotic attractor and its basin boundary for $\alpha = 0.3$. Here the asynchronous period-1 saddle and repeller, born through the saddle-node bifurcation on S_1, are denoted by the solid and open down-triangles, respectively, and the synchronous period-1 saddle is represented by the open up-triangle. The situations before and just after the transcritical bifurcation of the synchronous period-1 saddle are depicted in (a) for $c = 0.923$ and in (b) for $c = 0.943$, respectively. (c) Basin (shown in gray) of the synchronized chaotic attractor for $c = 0.992$, riddled with a dense set of tongues, belonging to the basin (shown in dark gray) of the stabilized asynchronous period-1 attractor (solid down-triangle), through a subcritical period-doubling bifurcation.

When α increases through α_4, the D_1 curve crosses the T_1 curve (see Fig. 2.13). Consequently, for $\alpha > \alpha_4$ the stabilization of the asynchronous period-1 saddle (solid down-triangle) through a subcritical period-doubling bifurcation occurs before the first transverse (transcritical) bifurcation on the T_1 curve. As a result of this stabilization, the asynchronous period-1 repeller (open down-triangle) lies on the basin (shown in dark gray) boundary of the stabilized asynchronous period-1 attractor (solid down-triangle), as shown in Fig. 2.15(a) for $\alpha = 0.48$ and $c = 1.03$. For this case, a mixed absorbing area, formed by union of segments of the unstable manifolds of the asynchronous period-1 repeller and portions of the critical curves L_1 and L_2, is surrounding the synchronized chaotic attractor. As c is increased, the asynchronous period-1 repeller (open down-triangle) approaches the synchronous period-1 saddle (open up-triangle), embedded in the synchronized chaotic attractor, and hence the absorbing area shrinks. Eventually, for $c = 1.040\ldots$ a transcritical contact bifurcation between the synchronous period-1 saddle and the asynchronous period-1 repeller on the basin bound-

ary occurs, and then the absorbing area disappear, as shown in Fig. 2.15(b). Note that this transcritical bifurcation induces a contact between the synchronized chaotic attractor and its basin boundary. When passing the transcritical bifurcation point, the asynchronous period-1 repeller (open down-triangle) moves down off the basin boundary, and exchanges stability with the synchronous period-1 saddle (open up-triangle). However, the synchronized chaotic attractor continues to contact its basin boundary at a new synchronous repelling fixed point (open up-triangle). As a result of this transcritical bifurcation, the basin of the synchronized chaotic attractor becomes riddled with a dense set of tongues, belonging to the basin of the asynchronous period-1 attractor (solid down-triangle). Thus, this transcritical bifurcation induces a riddling transition. However, near the riddling transition point, the tongues are too narrow to be seen. With further increase of c, the asynchronous period-1 attractor (solid down-triangle) is transformed into a quasiperiodic attractor through a Hopf bifurcation when crossing the H_1 curve, and then an asynchronous chaotic attractor is developed from the quasiperiodic attractor. During this process, the repelling tongues become large to be seen, as shown in Fig. 2.15(c) for $c = 1.1$. Note that this kind of a direct transition to riddling takes place when passing the heavy dotted part of the T_1 curve for $\alpha_4 < \alpha < \alpha_5$, in contrast to the case of $\alpha < \alpha_4$ where only a bubbling transition occurs through the transcritical bifurcation on T_1.

As α is increased from α_5, the D_1 curve touches the S_1 curve at the point P_1 [$\simeq (0.6660, 1.0999)$], and then the type of the saddle-node bifurcation changes (see Fig. 2.13). On the solid part of S_1 (below P_1), the saddle-node bifurcation gives rise to the birth of a pair of asynchronous period-1 saddle and unstable node (repeller), while on the dotted part of S_1 (above P_1), it leads to the birth of a pair of asynchronous period-1 saddle and stable node (attractor) [see the schematic bifurcation diagram in Fig. 2.16(a)]. Note also that a supercritical period-doubling bifurcation (dotted) line D_1 emanates from P_1, in contrast with the subcritical solid part of D_1 below P_1. At the right end point P_2 [$\simeq (0.9635, 1.1161)$] of the dotted part of S_1, where the curve H_1 touches the curve S_1, the type of the saddle-node bifurcation changes again, i.e., on the solid part of S_1 above P_2, a pair of asynchronous period-1 saddle and unstable node (repeller) is born [see also the schematic bifurcation diagram in Fig. 2.16(b)]. As shown in Figs. 2.16(a) and (b), for $\alpha > 0.666$ (above P_1) the asynchronous period-1 saddle, born through a saddle-node bifurcation, is transformed into

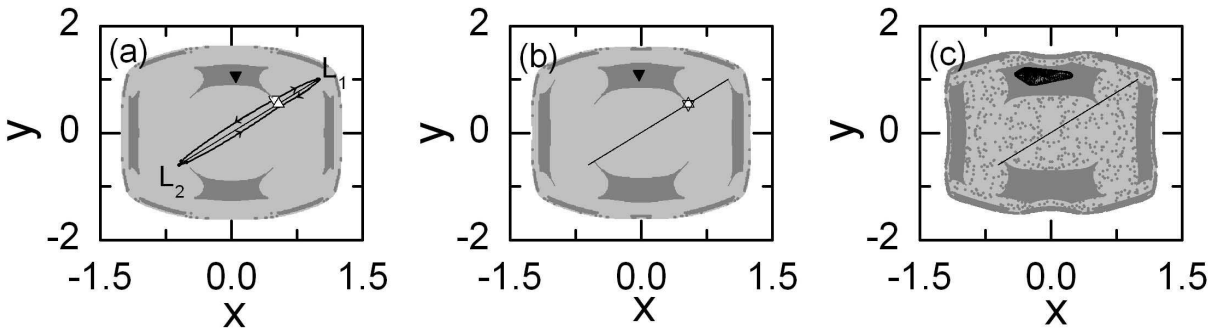

Figure 2.15: Riddling transition through the transcritical contact bifurcation for $\alpha = 0.48$. Before the transcritical bifurcation, the asynchronous period-1 saddle (denoted by the solid down-triangle) becomes stabilized through a subcritical period-doubling bifurcation, and hence the asynchronous period-1 repeller (denoted by the open down-triangle), which is the counterpart of the synchronous period-1 saddle (represented by the open up-triangle) lies on the basin boundary. The situations before and just at the transcritical bifurcation of the synchronous period-1 saddle are depicted in (a) for $c = 1.03$ and in (b) for $c = 1.040\ldots$, respectively. (c) Basin (shown in gray) of the synchronized chaotic attractor for $c = 1.1$, riddled with a dense set of tongues, belonging to the basin (shown in dark gray) of the asynchronous chaotic attractor, developed from the asynchronous period-1 attractor (solid down-triangle).

a repeller via a supercritical period-doubling bifurcation, which then becomes a counterpart of the synchronous period-1 saddle for the transcritical bifurcation. This is in contrast to the case of $\alpha < 0.666$ (below P_1), where the asynchronous period-1 repeller, born through a saddle-node bifurcation, is involved in the transcritical bifurcation as a counterpart of the synchronous period-1 saddle.

The asynchronous period-1 repellers, associated with the transcritical bifurcations, lie on the basin boundary of an asynchronous period-1 attractor (or an attractor developed from it) in the region hatched with vertical lines in Fig. 2.13. Here the asynchronous period-1 attractor appears through stabilization of the asynchronous period-1 saddle born through the saddle-node bifurcation for $\alpha < 0.666$, while for $\alpha > 0.666$ it is just the attractor born through the saddle-node bifurcation on the dotted part of S_1. For this case, the synchronized chaotic attractor is surrounded by a small mixed absorbing area [e.g, see Fig. 2.15(a)].

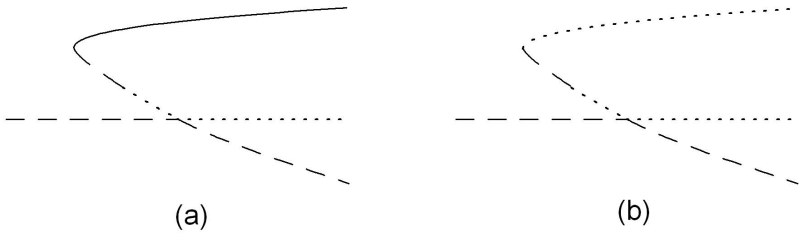

Figure 2.16: Types of the saddle-node bifurcation, associated with the transcritical bifurcation, for large α (> 0.666). Solid, dashed, and dotted lines denote the attractor, saddle, and repeller, respectively. The saddle-node bifurcation gives rise to the birth of a pair of asynchronous saddle and (a) stable or (b) unstable node. For both cases, the asynchronous saddle is transformed into a repeller, acting as the counterpart of the synchronous saddle for the transcritical bifurcation, through a period-doubling bifurcation.

For $\alpha > \alpha_5$, the asynchronous chaotic attractor developed from the asynchronous period-1 attractor disappears with its basin through a boundary crisis when crossing the line denoted by the open triangles in Fig. 2.13. Note that this boundary-crisis curve ends at the point P_2. Thus, when entering the shaded region through the boundary-crisis curve, the whole basin becomes occupied only by the synchronized chaotic attractor, surrounded by a large absorbing area, which is shown in Fig. 2.17 for $\alpha = 0.68$ and $c = 1.17$. Note that the asynchronous period-1 repeller (open down-triangle: counterpart of the synchronous period-1 saddle (open up-triangle) for the transcritical bifurcation) lies strictly inside the absorbing area (i.e., it no longer lies on any basin boundary). Hence, when passing the solid part of T_1 for $\alpha_5 < \alpha < \alpha_6$ (left boundary of the shaded region), the transcritical bifurcation does not induce any contact between the synchronized chaotic attractor and its basin boundary. After this transcritical bifurcation, locally repelled trajectories near the synchronized chaotic attractor exhibit transient intermittent bursting from the synchronization line (i.e., a bubbling transition occurs), because the large absorbing area, surrounding the synchronized chaotic attractor, is preserved.

However, when crossing the upper boundary of the the shaded region, denoted by the open circles in Fig. 2.13, the large absorbing area disappears suddenly through a contact with the basin boundary of the synchronized chaotic attractor. As a result of this crisis of the

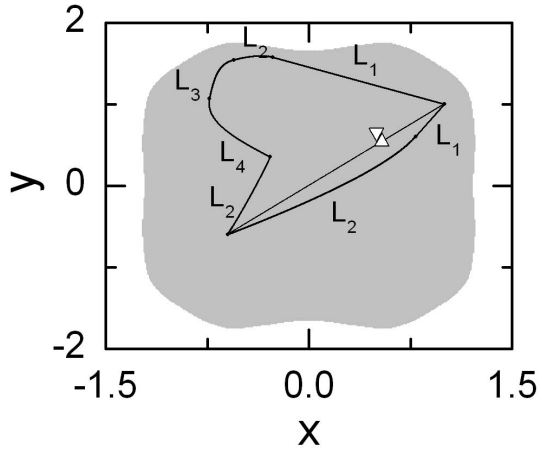

Figure 2.17: Synchronized chaotic attractor surrounded by a large absorbing area for $\alpha = 0.68$ and $c = 1.17$. Note that the asynchronous period-1 repeller (denoted by the open down-triangle), which acts as the counterpart of the synchronous period-1 saddle (denoted by the open up-triangle) for the transcritical bifurcation, lies strictly inside the absorbing area.

absorbing area, the basin (shown in white) of the attractor at infinity penetrates the basin (shown in gray) of the synchronized chaotic attractor, as shown in Fig. 2.18(a) for $\alpha = 0.8$ and $c = 1.27$. Note that the asynchronous period-1 repeller (open down-triangle: counterpart of the synchronous period-1 saddle (open up-triangle) for the transcritical bifurcation) lies on the basin boundary of the synchronized chaotic attractor, surrounded by a small mixed absorbing area. This kind of situation occurs in the whole region hatched with horizontal lines in Fig. 2.13. With increasing the coupling parameter c, the asynchronous period-1 repeller (open down-triangle) approaches the synchronous period-1 saddle (open up-triangle), the mixed absorbing area shrinks, and eventually a transcritical contact bifurcation occurs when crossing the upper dotted part of T_1 for $c = 1.317\ldots$, as shown in Fig. 2.18(b). As a result of this transcritical bifurcation, the basin of the synchronized chaotic attractor becomes riddled with a dense set of repelling tongues, leading to the divergent trajectories, because the mixed absorbing area, surrounding the synchronized chaotic attractor, disappears, which is shown in Fig. 2.18(c) for $c = 1.4$. Note that this mechanism for the riddling transition through the transcritical contact bifurcation on the upper dotted part of T_1 is similar to that in the unidirectionally-coupled case ($\alpha = 1$) [11].

From now on, we study the dynamical behaviors after the bubbling and riddling tran-

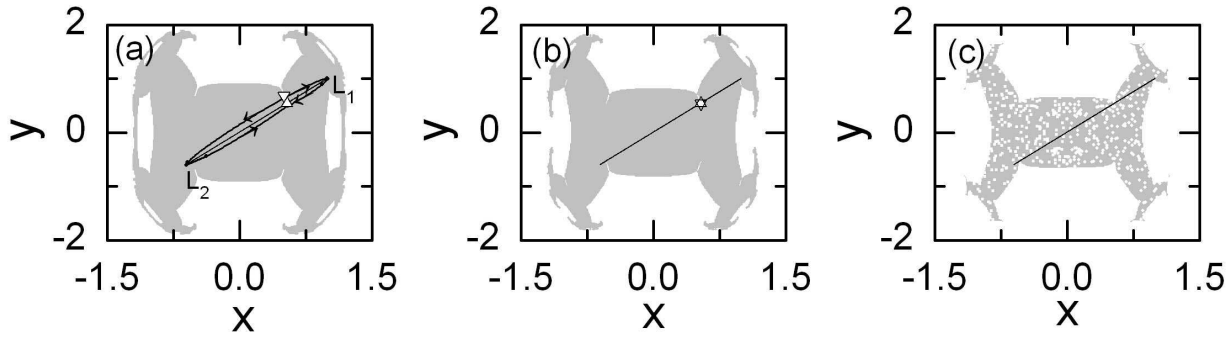

Figure 2.18: Riddling transition through the transcritical contact bifurcation for $\alpha = 0.8$. (a) Synchronized chaotic attractor surrounded by a mixed absorbing area for $c = 1.27$. Note that the asynchronous period-1 repeller (denoted by the open down-triangle), which is the counterpart of the synchronous period-1 saddle (represented by the open up-triangle), lies on the basin boundary. (b) At the transcritical bifurcation point ($c = 1.317\ldots$), the saddle (open up-triangle) and the repeller (open down-triangle) coalesce, and thus the absorbing area disappears. (c) Basin (shown in gray) of the synchronized chaotic attractor for $c = 1.4$, riddled with a dense set of tongues, belonging to the basin (shown in white) of the attractor at infinity.

sitions. Figure 2.19 shows the phase diagram after the transcritical bifurcation in the α-c plane. As explained above, a direct transition to riddling occurs through a transcritical contact bifurcation when crossing the dotted part of T_1, because the absorbing area, surrounding the synchronized chaotic attractor, disappears. On the other hand, when the solid part of T_1 is crossed, a bubbling transition takes place, because an absorbing area is surrounding the synchronized chaotic attractor. However, with further increase of c, a riddling transition also occurs through stabilization of an asynchronous period-1 saddle, born by the saddle-node bifurcation on S_1, via a subcritical period-doubling bifurcation on the lower branch of D_1. Thus, the basin of the synchronized chaotic attractor becomes riddled in the region hatched with horizontal lines, while an absorbing area is surrounding the synchronized chaotic attractor in the region hatched with vertical lines. Eventually, when crossing the blow-out bifurcation curve B, the synchronized chaotic attractor becomes transversely unstable, and then it is transformed into a chaotic saddle (i.e., a complete loss of chaos synchronization occurs). However, the type of the blow-out bifurcation also depends on the existence of an

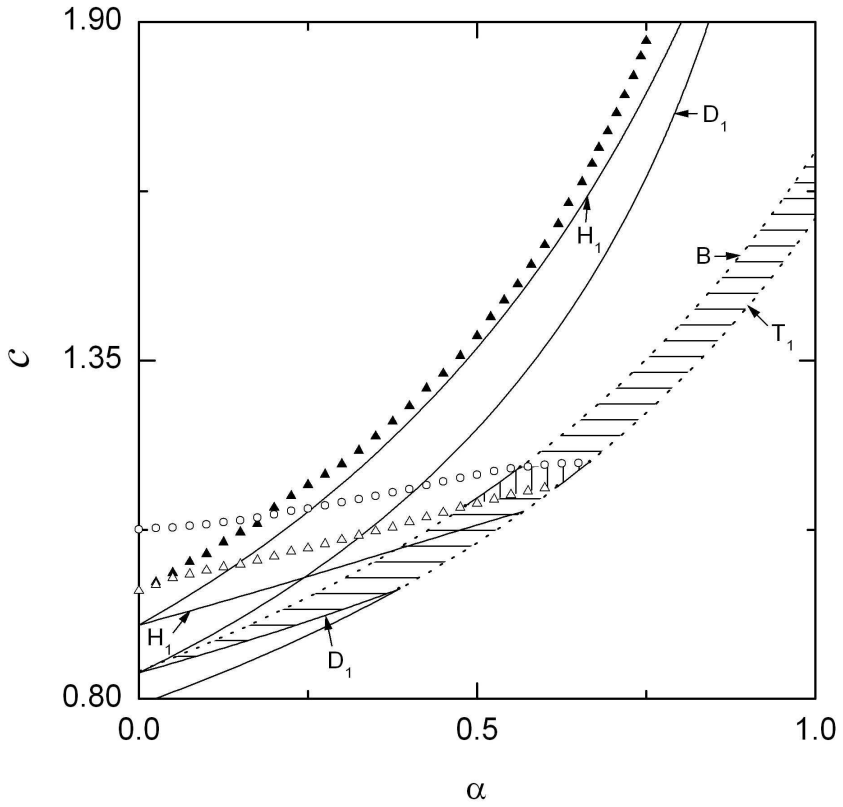

Figure 2.19: Phase diagram after the transcritical bifurcation in the $\alpha - c$ plane for the case of strong coupling. As a result of the transcritical bifurcation at the line T_1, a riddling transition occurs in the horizontally-hatched region, while a bubbling transition takes place in the vertically-hatched region. Hence, when crossing the dotted and solid parts of the curve B, subcritical and supercritical blow-out bifurcations occur, respectively. Note also that the period-doubling bifurcation curves D_1, the Hopf bifurcation curves H_1, and the boundary-crisis curves (denoted by the open and solid triangles) come in pairs from the period-doubling bifurcation, Hopf bifurcation, and the crisis points for $\alpha = 0$, respectively. For further details, see the text.

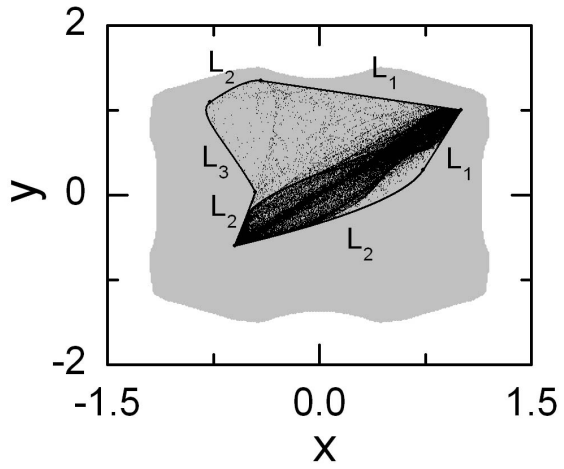

Figure 2.20: Large asynchronous chaotic attractor, born via a supercritical blow-out bifurcation for $\alpha = 0.5$ and $c = 1.14$, which covers the whole absorbing area, bounded by the segments of the critical curves, L_1, L_2 and L_3.

absorbing area. When crossing the lower and upper dotted parts of B, the state of the system is asymptotically attracted to an asynchronous period-1 attractor (or an asynchronous attractor developed from it) and the attractor at infinity, respectively, through a subcritical blow-out bifurcation, because there is no absorbing area. Note also that the blow-out bifurcations near $\alpha = 0$ and 1 are similar to those in the cases of symmetric coupling ($\alpha = 0$) [8] and unidirectional coupling ($\alpha = 1$) [11], respectively. However, when crossing the solid part of B, an asynchronous chaotic attractor spreads to the whole absorbing area through a supercritical blow-out bifurcation, as shown in Fig. 2.20 for $\alpha = 0.5$ and $c = 1.14$. This asynchronous chaotic attractor makes a contact with its basin boundary on the curve, denoted by the open circles in Fig. 2.19, and then it disappears with its basin through a boundary crisis.

Finally, we discuss the bifurcation behaviors after the blow-out bifurcation. As shown in Fig. 2.19, as α is increased from 0, the period-doubling bifurcation curves D_1, the Hopf bifurcation curves H_1, and the boundary-crisis curves (denoted by the open and solid triangles) come in pairs from the period-doubling bifurcation, Hopf bifurcation, and the crisis points for $\alpha = 0$, respectively. For the case of subcritical period-doubling bifurcations on D_1, the lower branch of D_1 is associated with stabilization of the asynchronous period-1 saddle

[corresponding to the upper dashed curve in Fig. 2.12(b)], born through the saddle-node bifurcation. On the other hand, when crossing the upper branch of D_1 another period-1 saddle [corresponding to the lower dashed curve in Fig. 2.12(b)], which is transformed from the asynchronous period-1 repeller through the transcritical bifurcation in Fig. 2.12(b), also becomes stabilized. These asynchronous period-1 attractors, stabilized at the upper and lower branches of D_1, become unstable when passing the upper and lower branches of H_1, respectively, and then generally quasiperiodic attractors appear. With further increase of c, asynchronous chaotic attractors, developed from the asynchronous quasiperiodic attractors, born at the upper and lower branches of H_1, disappear through boundary crises at the upper (solid triangle) and lower (open triangle) crisis curves, respectively. As an example, consider the case of $\alpha = 0.75$. When crossing the curve B for $c \simeq 1.352$, an abrupt collapse of the synchronous state occurs through a subcritical blow-out bifurcation, and then typical trajectories, starting near the synchronization line, are divergent to infinity. However, as the upper branch of D_1 is passed for $c = 1.647\ldots$, a stabilized asynchronous period-1 attractor appears with its basin. With further increase of c, this asynchronous period-1 attractor is transformed into an asynchronous quasiperiodic attractor when the upper branch of H_1 is crossed at $c = 1.784\ldots$. Finally, the asynchronous chaotic attractor, developed from the asynchronous quasiperiodic attractor, disappears suddenly with its basin through a boundary crisis, occurring for $c \simeq 1.869$ at the curve (denoted by the solid triangles).

2.2 Effect of Parameter Mismatching and Noise on Weak Synchronization

We investigate the effect of the parameter mismatch on the weak synchronization in coupled one-dimensional maps [19]. Loss of strong synchronization begins with a first transverse bifurcation of a periodic saddle embedded in the synchronized chaotic attractor, and then the synchronized chaotic attractor becomes weakly stable. Because of local transverse repulsion of the periodic repellers embedded in the weakly stable synchronized chaotic attractor, a typical trajectory may have segments of arbitrary length that have positive local transverse Lyapunov exponents. Consequently, the weakly stable synchronized chaotic attractor

becomes sensitive with respect to the variation of the mismatching parameter [20]. To quantitatively characterize such parameter sensitivity, we introduce a new quantifier, called the parameter sensitivity exponent. As the local transverse repulsion of the periodic repellers strengthens, the value of the parameter sensitivity exponent increases. In terms of parameter sensitivity exponents, we characterize the parameter mismatching effect on the intermittent bursting and basin riddling occurring in the regime of weak synchronization. It is thus found that the scaling exponent for the average time spent near the diagonal is given by the reciprocal of the parameter sensitivity exponent. Similar to the case of parameter mismatching, we introduce a quantity, called the noise sensitivity exponent, to measure the degree of noise sensitivity and characterize the effect of noise on weak synchronization [21]. It is thus found that the noise and parameter mismatch have the same effect on the scaling behavior of the average characteristic time. We extend the method of characterizing the parameter and noise sensitivity of the synchronized chaotic attractor in terms of the parameter and noise sensitivity exponent to the coupled systems consisting of the high-dimensional invertible systems such as the Hénon map and oscillators [22].

2.2.1 Characterization of the Parameter Sensitivity

We investigate the parameter-mismatching effect on the weak synchronization in two coupled 1D maps [12]:

$$T : \begin{cases} x_{n+1} = F(x_n, y_n) = f(x_n, a) + (1-\alpha)cg(x_n, y_n), \\ y_{n+1} = G(x_n, y_n) = f(y_n, b) + c\, g(y_n, x_n), \end{cases} \tag{2.11}$$

where x_n and y_n are state variables of the subsystems at a discrete time n, local dynamics in each subsystem with a control parameter p ($p = a, b$) is governed by the 1D map $f(x, p) = 1 - p\,x^2$, c is a coupling parameter between the two subsystems, and $g(x, y)$ is a coupling function of the form,

$$g(x, y) = y^2 - x^2. \tag{2.12}$$

For $\alpha = 0$, the coupling becomes symmetric, while for nonzero α ($0 < \alpha \leq 1$) it becomes asymmetric. The extreme case of asymmetric coupling with $\alpha = 1$ corresponds to the unidirectional coupling. In such a way, α tunes the degree of asymmetry in the coupling.

For the case of identical 1D maps (i.e., $a = b$), there exists an invariant synchronization line, $y = x$, in the $x-y$ phase space. However, in presence of a mismatching between the two 1D maps, the diagonal is no longer invariant. To take into consideration such a mismatching effect, we introduce a small mismatching parameter ε in the coupled 1D maps of Eq. (2.11) such that

$$b = a - \varepsilon, \tag{2.13}$$

and consider an orbit $\{(x_n, y_n)\}$ starting from an initial point on the diagonal (i.e., $x_0 = y_0$). As the strength of the local transverse repulsion from the diagonal increases, the synchronized chaotic attractor becomes more and more sensitive with respect to the variation of ε. Such parameter sensitivity of the synchronized chaotic attractor for $\varepsilon = 0$ may be characterized by calculating the derivative of the transverse variable u_n $(= x_n - y_n)$, denoting the deviation from synchronization, with respect to ε,

$$\begin{aligned}
\left.\frac{\partial u_{n+1}}{\partial \varepsilon}\right|_{\varepsilon=0} &= \left.\frac{\partial x_{n+1}}{\partial \varepsilon}\right|_{\varepsilon=0} - \left.\frac{\partial y_{n+1}}{\partial \varepsilon}\right|_{\varepsilon=0} \\
&= \left[\left.\frac{\partial F(x_n, y_n)}{\partial x_n}\right|_{\varepsilon=0} - \left.\frac{\partial G(x_n, y_n)}{\partial x_n}\right|_{\varepsilon=0}\right] \left.\frac{\partial x_n}{\partial \varepsilon}\right|_{\varepsilon=0} \\
&+ \left[\left.\frac{\partial F(x_n, y_n)}{\partial y_n}\right|_{\varepsilon=0} - \left.\frac{\partial G(x_n, y_n)}{\partial y_n}\right|_{\varepsilon=0}\right] \left.\frac{\partial y_n}{\partial \varepsilon}\right|_{\varepsilon=0} - \left.\frac{\partial G(x_n, y_n, \varepsilon)}{\partial \varepsilon}\right|_{\varepsilon=0}.
\end{aligned} \tag{2.14}$$

Using Eq. (2.11), we may obtain a recurrence relation

$$\left.\frac{\partial u_{n+1}}{\partial \varepsilon}\right|_{\varepsilon=0} = [f_x(x_n^*, a) - (2-\alpha)c\, h(x_n^*)] \left.\frac{\partial u_n}{\partial \varepsilon}\right|_{\varepsilon=0} + f_a(x_n^*, a), \tag{2.15}$$

where f_x and f_a are the derivatives of f with respect to x and a, $\{(x_n^*, y_n^*)\}$ is the synchronous orbit with $x_n^* = y_n^*$ for $\varepsilon = 0$, and $h(x)$ is a reduced coupling function defined by [87]

$$h(x) \equiv \left.\frac{\partial g(x, y)}{\partial y}\right|_{y=x}. \tag{2.16}$$

Hence, starting from an initial orbit point (x_0^*, y_0^*) on the diagonal, we may obtain derivatives at all points of the orbit:

$$\left.\frac{\partial u_N}{\partial \varepsilon}\right|_{\varepsilon=0} = \sum_{k=1}^{N} R_{N-k}(x_k^*) f_a(x_{k-1}^*, a) + R_N(x_0^*) \left.\frac{\partial u_0}{\partial \varepsilon}\right|_{\varepsilon=0}, \tag{2.17}$$

where

$$R_M(x_m^*) = \prod_{i=0}^{M-1} \left[f_x(x_{m+i}^*, a) - (2-\alpha)c\, h(x_{m+i}^*)\right]. \tag{2.18}$$

One can easily show that the factor $R_M(x_m^*)$ is associated with a local (M-time) transverse Lyapunov exponent $\sigma_M^T(x_m^*)$ of the synchronized chaotic attractor that is averaged over M synchronous orbit points starting from x_m^* as follows:

$$\sigma_M^T(x_m^*) = \frac{1}{M} \ln |R_M(x_m^*)|. \tag{2.19}$$

Thus $R_M(x_m^*)$ becomes a local (stability) multiplier that determines local sensitivity of the motion during a finite time M. As $M \to \infty$, σ_M^T approaches the usual transverse Lyapunov exponent σ_T that denotes the average exponential rate of divergence of an infinitesimal perturbation transverse to the synchronized chaotic attractor. Since $\frac{\partial u_0}{\partial \varepsilon}\big|_{\varepsilon=0} = 0$, Eq. (2.17) reduces to

$$\left.\frac{\partial u_N}{\partial \varepsilon}\right|_{\varepsilon=0} = S_N(x_0^*) \equiv \sum_{k=1}^{N} R_{N-k}(x_k^*) f_a(x_{k-1}^*, a). \tag{2.20}$$

In the case of weak synchronization, there are transversely unstable periodic repellers embedded in the synchronized chaotic attractor. When a typical trajectory visits neighborhoods of such repellers and their preimages, it has segments experiencing local repulsion from the diagonal. Thus the distribution of local transverse Lyapunov exponents σ_M^T for a large ensemble of trajectories and large M may have a positive tail. For the segments of a trajectory exhibiting a positive local Lyapunov exponent ($\sigma_M^T > 0$), the local multipliers R_M $[= \pm \exp(\sigma_M^T M)]$ can be arbitrarily large, and hence the partial sum S_N may be arbitrarily large. This implies unbounded growth of the derivatives $\frac{\partial u_N}{\partial \varepsilon}\big|_{\varepsilon=0}$ as N tends to infinity, and consequently the weakly stable synchronized chaotic attractor may have a parameter sensitivity.

As an example, we consider the synchronized chaotic attractor that exists in the interval of $c_{b,l}[\simeq -2.963] < c < c_{b,r}[\simeq -0.677]$ for $a = 1.82$ in the unidirectionally coupled case of $\alpha = 1$. When the coupling parameter c passes through $c_{b,l}$ or $c_{b,r}$, the synchronized chaotic attractor becomes transversely unstable through a blow-out bifurcation, and then a complete desynchronization occurs. In the regime of synchronization, a strongly stable synchronized chaotic attractor exists for $c_{t,l}[\simeq -2.789] < c < c_{t,r}[\simeq -0.850]$. For this case of strong synchronization, there is no parameter sensitivity, because all periodic saddles embedded in the synchronized chaotic attractor are transversely stable. Hence, in presence of a small parameter mismatching ε the strongly-stable synchronized chaotic attractor becomes slightly perturbed, as shown in Figs. 2.21(a) and 2.21(b). However, when the coupling parameter

c passes $c_{t,r}$ and $c_{t,l}$, bubbling and riddling transitions occur through the first transverse bifurcations of periodic saddles, respectively. For this case, the weakly stable synchronized chaotic attractor has a parameter sensitivity, because of local transverse repulsion of the periodic repellers embedded in the synchronized chaotic attractor. Thus, however small the parameter mismatching ε, a persistent intermittent bursting, called the attractor bubbling, occurs in the regime of bubbling ($c_{t,r} < c < c_{b,r}$), as shown in Figs. 2.21(c) and 2.21(d). On the other hand, in the regime of riddling ($c_{b,l} < c < c_{t,l}$), the weakly synchronized chaotic attractor with a riddled basin for $\varepsilon = 0$ is transformed into a chaotic transient with a finite lifetime in presence of a parameter mismatch [see Fig. 2.21(e)]. As c is varied away from $c_{t,l}$ or $c_{t,r}$, transversely unstable periodic repellers appear successively in the synchronized chaotic attractor through transverse bifurcations. Then the degree of the parameter sensitivity of the synchronized chaotic attractor increases, because of the increase in the strength of local transverse repulsion of the periodic repellers. To quantitatively characterize the parameter sensitivity of the synchronized chaotic attractor, we iterate Eqs. (2.11) and (2.15) starting from an initial orbit point (x_0^*, y_0^*) on the diagonal and $\frac{\partial u_0}{\partial \varepsilon}\big|_{\varepsilon=0} = 0$, and then we obtain the partial sum $S_N(x_0^*)$ of Eq. (2.20). The quantity S_N becomes very intermittent, as shown in Fig. 2.22(a). However, looking only at the maximum

$$\gamma_N(x_0^*) = \max_{0 \le n \le N} |S_N(x_0^*)|, \tag{2.21}$$

one can easily see the boundedness of S_N. Figure 2.22(b) shows the functions γ_N for both cases of strong and weak synchronization. For the case of strong synchronization with $c = -1.5$, γ_N grows up to the largest possible value of the derivative $|\partial u/\partial \varepsilon|$ along the synchronized chaotic attractor and remains constant for all subsequent iterations. Thus, γ_N saturates for large N and hence the strongly stable synchronized chaotic attractor has no parameter sensitivity. On the other hand, for the case of weak synchronization with $c = -0.7$, γ_N grows unboundedly and exhibits no saturation. Consequently, the weakly stable synchronized chaotic attractor has a parameter sensitivity.

The growth rate of the function $\gamma_N(x_0^*)$ with time N represents a degree of the parameter sensitivity, and can be used as a quantitative characteristic of the weakly stable synchronized chaotic attractor. However, $\gamma_N(x_0^*)$ depends on a particular trajectory. To obtain a representative quantity, we consider an ensemble of randomly chosen initial points (x_0^*, y_0^*)

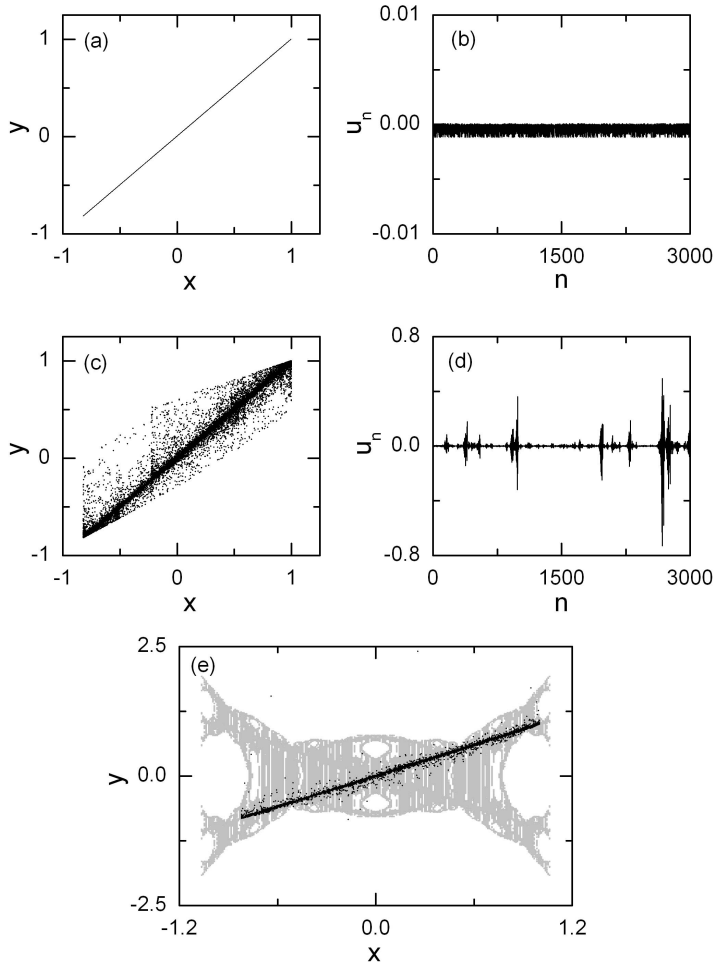

Figure 2.21: Effect of the parameter mismatch with $\varepsilon = 0.001$ on the chaos synchronization for $a = 1.82$ in the unidirectionally coupled case of $\alpha = 1$. (a) A slightly perturbed synchronized chaotic attractor and (b) the evolution of the transverse variable u_n $(x_n - y_n)$ versus the discrete time n for the case of strong synchronization with $c = -1.5$. (c) A bubbling attractor and (d) the evolution of u_n versus n for the bubbling case of $c = -0.7$. For the riddling case of $c = -2.91$ the synchronized chaotic attractor with a basin (gray region) riddled with a dense set of tongues leading to divergent orbits (white region) for $\varepsilon = 0$ is transformed into a chaotic transient (black dots) for $\varepsilon = 0.001$ as shown in (e).

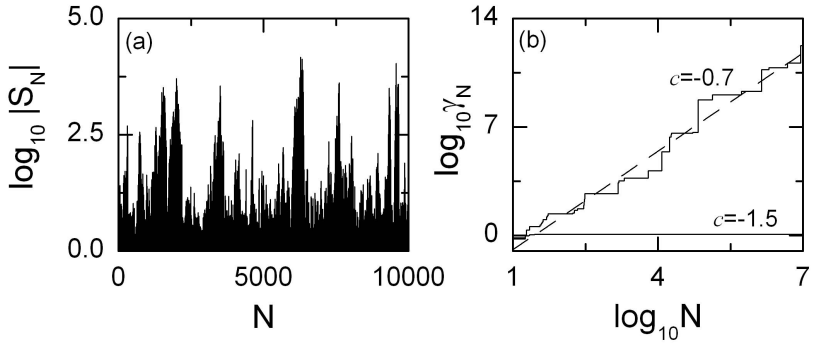

Figure 2.22: (a) Intermittent behavior of the partial sum $|S_N|$ for $\alpha = 1$, $a = 1.82$, and $c = -0.7$. (b) Two functions γ_N looking only at the maximum for $c = -1.5$ (strong synchronization) and $c = -0.7$ (weak synchronization). These results are obtained for the trajectory starting from the initial orbit point $(x_0^*, y_0^*) = (0.5, 0.5)$ in the case of $\alpha = 1$ and $a = 1.82$

on the diagonal, and take the minimum value of γ_N with respect to the initial orbit points,

$$\Gamma_N = \min_{x_0^*} \gamma_N(x_0^*). \tag{2.22}$$

Figure 2.23 shows a parameter sensitivity function Γ_N for $c = -0.7$. Note that Γ_N grows unboundedly with some power,

$$\Gamma_N \simeq N^\delta. \tag{2.23}$$

Here the value $\delta \simeq 2.58$ is a quantitative characteristic of the parameter sensitivity of the synchronized chaotic attractor, and we call it the parameter sensitivity exponent. In each regime of bubbling or riddling, we vary the coupling parameter from the bubbling or riddling transition point to the blow-out bifurcation point and obtain the parameter sensitivity exponents. For obtaining a satisfactory statistics, we consider 100 ensembles for each c, each of which contains 100 randomly chosen initial orbit points and choose the average value of the 100 parameter sensitivity exponents obtained in the 100 ensembles. Figure 2.24(a) shows the plot of such parameter sensitivity exponents versus c. Note that the parameter sensitivity exponent δ monotonically increases as c is varied away from the bubbling or riddling transition point, and tends to infinity as c approaches the blow-out bifurcation point. This increase in the parameter sensitivity of the synchronized chaotic attractor is caused by the increase in the strength of local transverse repulsion of the periodic repellers embedded in the synchronized chaotic attractor. After the blow-out bifurcation,

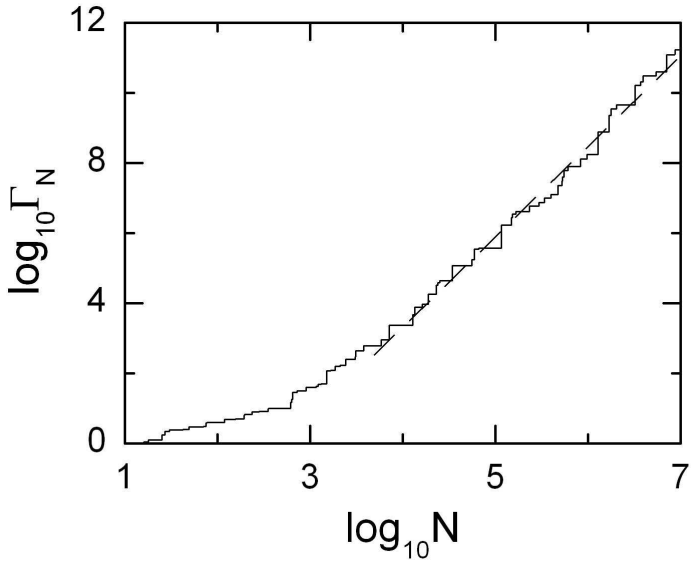

Figure 2.23: Parameter sensitivity function Γ_N for $\alpha = 1$, $a = 1.82$, and $c = -0.7$ that takes the minimum value of γ_N in the ensemble containing 100 randomly chosen initial orbit points on the diagonal.

the weakly stable synchronized chaotic attractor is transformed into a transversely unstable chaotic saddle exhibiting an exponential parameter sensitivity as shown in Fig. 2.24(b). Thus a complete desynchronization occurs.

We also discuss the distribution of positive local (M-time) transverse Lyapunov exponents, causing the parameter sensitivity of the weakly stable synchronized chaotic attractor. As an example, we consider the case of $a = 1.82$ and $c = -0.7$ and obtain the probability distribution $P_M(\sigma)$ of local (M-time) transverse Lyapunov exponents, where $P_M(\sigma)\, d\sigma$ is the probability that σ_M^T has a value between σ and $\sigma + d\sigma$, by taking a long trajectory dividing it into segments of length M and calculating σ_M^T in each segment. Figure 2.25(a) shows the distributions $P_M(\sigma)$ for $M = 100$, 500, and 900. In the limit $M \to \infty$, $P_M(\sigma)$ approaches the delta distribution $\delta(\sigma - \sigma_T)$, where σ_T is the usual averaged transverse Lyapunov exponent. However, for finite M there is a variance $\langle(\sigma_M^T - \langle\sigma_M^T\rangle)^2\rangle$ $[\equiv \int_{-\infty}^{\infty} P_M(\sigma)(\sigma - \langle\sigma_M^T\rangle)^2 d\sigma]$ from the average value $\langle\sigma_M^T\rangle$ $[\equiv \int_{-\infty}^{\infty} P_M(\sigma)\sigma d\sigma]$. As shown in Fig. 2.25(b) this variance approaches zero inversely with M as follows:

$$\langle(\sigma_M^T - \langle\sigma_M^T\rangle)^2\rangle = \frac{2D}{M}. \tag{2.24}$$

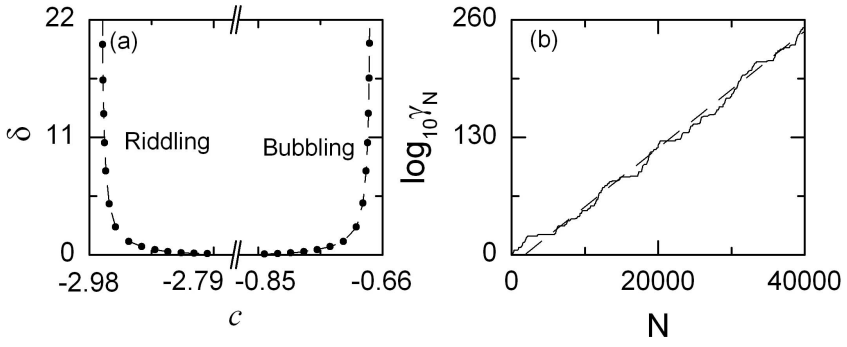

Figure 2.24: (a) The plot of the parameter sensitivity exponents δ versus c in the regime of weak synchronization for $\alpha = 1$ and $a = 1.82$. (b) The exponential parameter sensitivity for the a trajectory starting from the initial point $(0.5, 0.5)$ for $\alpha = 1$, $a = 1.82$, and $c = -0.66$.

Here the value of D ($\simeq 0.054$) is the same, independently of the values of c for $a = 1.82$ in the regime of weak synchronization. One remarkable feature of the distribution is the slow decay of the positive tail of the distribution. In order to quantify this, we define the fraction of positive local Lyapunov exponents as

$$F_M^+ = \int_0^\infty P_M(\sigma) d\sigma. \tag{2.25}$$

These fractions F_M^+'s are plotted for $c = -0.7$, -0.695, and -0.69 in Fig. 2.25(c). Note that for each value of c, the fraction F_M^+ exhibits a power-law decay,

$$F_M^+ \sim M^{-\eta}. \tag{2.26}$$

Here the values of the exponent η decreases as c increases. Consequently, for any case of weak synchronization a trajectory has segments of arbitrarily long M that have positive local Lyapunov exponents, and then the partial sum S_N in Eq. (2.20) may be arbitrarily large. Thus the weakly stable synchronized chaotic attractor may have a parameter sensitivity. As shown in Fig. 2.25(c), as c increases the value of F_M^+ becomes larger. Hence, the degree of the parameter sensitivity of the weakly stable synchronized chaotic attractor increases.

So far, we have characterized the parameter mismatching effect in terms of the parameter sensitivity exponents in the unidirectionally coupled case with the asymmetry parameter $\alpha = 1$. Through Eq. (2.15), one can easily see that the parameter sensitivity exponent for a given (a, c) in the case of $\alpha = 1$ is the same as that for the value of $[a, c/(2-\alpha)]$ in other

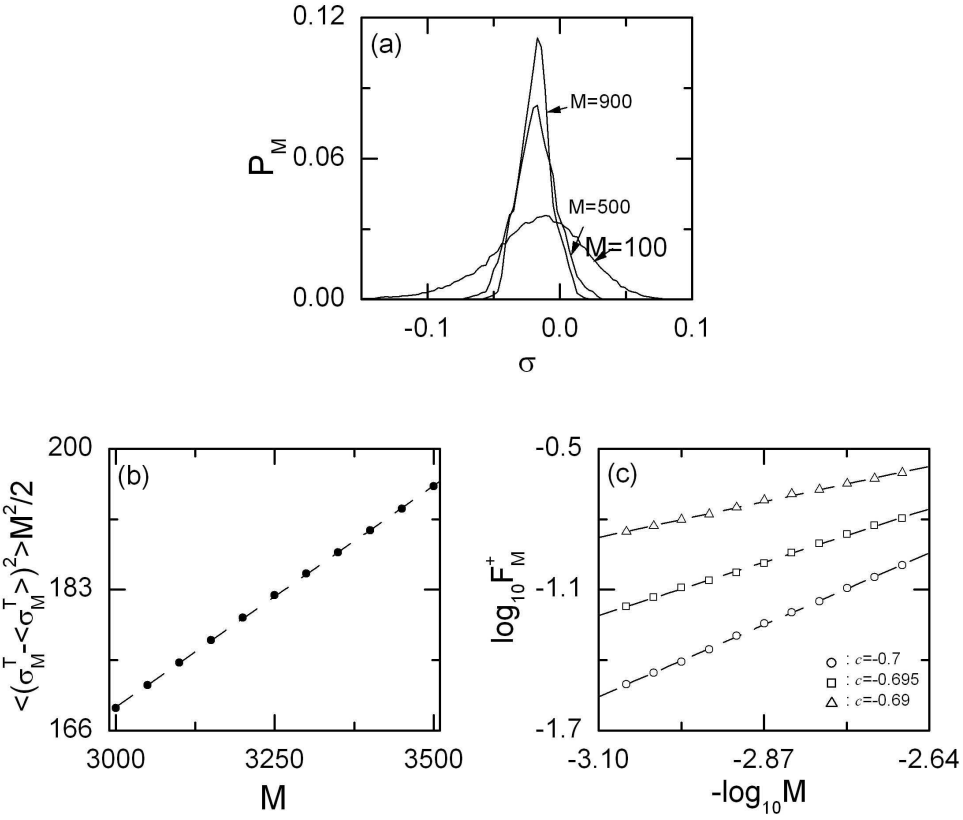

Figure 2.25: (a) Three probability distributions P_M of the local M-time Lyapunov exponents for $M = 100$, 500, and 900 when $\alpha = 1$, $a = 1.82$, and $c = -0.7$. (b) The plot of $\langle(\sigma_M^T - \langle\sigma_M^T\rangle)^2\rangle M^2/2$ versus M when $\alpha = 1$, $a = 1.82$, and $c = -0.7$. Note that the variance decreases inversely with M. (c) Plots of $\log_{10} F_M^+$ (F_M^+: fraction of the positive local transverse Lyapunov exponent) versus $-\log_{10} M$. Note that the three plots for $c = -0.7$ (circles), -0.695 (squares), and -0.69 (triangles) are well fitted with the straight lines with the slopes $\eta = 1.33$, 0.99, and 0.66, respectively. Hence F_M^+ decays with some power η.

coupled 1D maps with $0 \leq \alpha < 1$ in Eq. (2.11). Thus, the results of the parameter sensitivity exponents given in Fig. 2.24(a) may be converted into those for the case of general α only by a scale change in the coupling parameter such that $c \to c/(2-\alpha)$. For this case, the bubbling regime for the case of $\alpha = 1$ is always transformed into a bubbling regime for any other value of α, because the bubbling transition occurs through the first transverse supercritical period-doubling bifurcation, independently of the value of α. However, the riddling regime for the case of $\alpha = 1$ is transformed into a bubbling or riddling regime depending on the value of α. For example, for the symmetrically coupled case of $\alpha = 0$, the riddling regime for $\alpha = 1$ is transformed into a bubbling regime, because a bubbling transition occurs through a first trasnverse supercritical pitchfork bifurcation. For all other asymmetric cases with nonzero α, the transtion to the weak synchronization occurs through the first trasnverse transcritical bifurcation. Depending on whether or not such a transcritical bifurcation induce a contact between the saddle fixed point embedded in the synchronized chaotic attractor and the repelling fixed point on the basin boundary, a riddling or bubbling transtion occurs. Thus, a bubbling transition occurs through a transcritical noncontact bifurcation for small α, while a riddling transition takes place through a transcritical contact bifurcation for the values close to $\alpha = 1$. For more details, refer to Ref. [12].

2.2.2 Characterization of the Bubbling Attractor and the Chaotic Transient

We characterize the parameter-mismatching effect on the bubbling and riddling in terms of the parameter sensitivity exponents for $a = 1.82$ in the unidirectionally coupled case of $\alpha = 1$. The quantity of interest in both cases is the average time τ that a typical trajectory spends near the diagonal. As c is varied from the bubbling or riddling transition point, such average time becomes short because the strength of local transverse repulsion of the periodic repellers embedded in the synchronized chaotic attractor increases. For the case of bubbling, the bubbling attractor is in the laminar phase when the magnitude of the deviation from the diagonal is less than a threshold value u_b^* (i.e., $|u_n| < u_b^*$). Otherwise, it is in the bursting phase. Here u_b^* is very small compared to the maximum bursting amplitude and it is the maximum deviation from the diagonal that may be acceptable in the context of

synchronization. For each c, we follow the trajectory starting from the initial condition (0,0) until 50,000 laminar phases are obtained, and then we get the average laminar length τ (i.e., the average interburst interval) that scales with ε as [13]

$$\tau \sim \varepsilon^{-\mu}, \tag{2.27}$$

where μ will be referred to the laminar phase exponent (LPE). The plot of the LPE μ versus c is shown in Fig. 2.26(a). As c increases, the value of μ decreases, because the average laminar length shortens. Note that this LPE μ is associated with the parameter sensitivity exponent δ as follows. For a given ε, consider a trajectory starting from a randomly chaosen initial orbit point on the diagonal. Then, From Eq. (2.23) the "average" time τ at which the magnitude of the deviation from the diagonal becomes the threshold value u_b^* can be obtained:

$$\tau \sim \varepsilon^{-1/\delta}. \tag{2.28}$$

Thus, the two exponents have a reciprocal relation,

$$\mu = 1/\delta. \tag{2.29}$$

The reciprocal values of δ are also plotted in Fig. 2.26(a), and they agree well with the values of μ. This reciprocal relation is valid also in the riddling regime. For each c we consider an ensemble of trajectories starting from 1,000 randomly chosen initial points on the diagonal, and obtain the average lifetime of the chaotic transients. A trajectory may be regarded as having escaped once the magnitude of deviation u_n from the diagonal becomes larger than a threshold value u_c^* such that an orbit point with $|u| > u_c^*$ lies sufficiently outside the basin of the synchronized chaotic attractor. Thus, the average lifetime τ_c is found to scale with ε as [13]

$$\tau_c \sim \varepsilon^{-\nu}, \tag{2.30}$$

where ν will be referred to the chaotic transient exponent (CTE). The plot of the CTE ν versus c is given in Fig. 2.26(b). Like the bubbling case, the parameter sensitivity exponent and CTE also have a reciprocal relation (i.e., $\nu = 1/\delta$), as shown in Fig. 2.26(b).

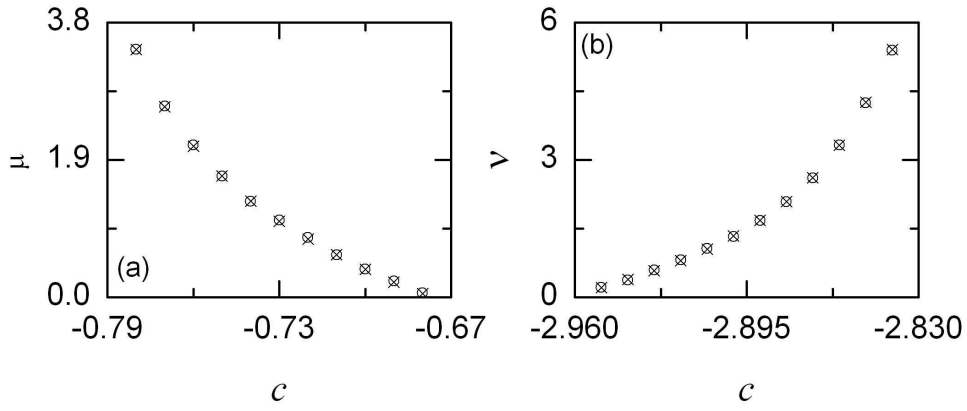

Figure 2.26: (a) The plot of the laminar phase exponents (LPEs) μ (open circles) versus c for $\alpha = 1$ and $a = 1.82$. They agree well with the reciprocals of the parameter sensitivity exponents (crosses). (b) The plot of the chaotic transient exponent (CTEs) (open circles) versus c for $\alpha = 1$ and $a = 1.82$. They agree well with the reciprocals of the parameter sensitivity exponents (crosses).

2.2.3 Characterization of the Noise Sensitivity

We study the effect of additive and parametric noise on the weakly stable synchronized chaotic attractor. For the case of weak synchronization, the synchronized chaotic attractor becomes sensitive with respect to the variation of noise strength. First, we investigate the effect of additive noise on weak synchronization in two coupled identical 1D maps [12]:

$$T : \begin{cases} x_{n+1} = F(x_n, y_n) = f(x_n, a) + (1-\alpha)cg(x_n, y_n) + \sigma\xi_n^{(1)}, \\ y_{n+1} = G(x_n, y_n) = f(y_n, a) + c\, g(y_n, x_n) + \sigma\xi_n^{(2)}, \end{cases} \tag{2.31}$$

where x_n and y_n are state variables of the subsystems at a discrete time n, local dynamics in each subsystem with a control parameter a is governed by the 1D map $f(x, a) = 1 - a\,x^2$, c is a coupling parameter between the two subsystems, and $g(x, y)$ is a coupling function of the form,

$$g(x, y) = y^2 - x^2. \tag{2.32}$$

For $\alpha = 0$, the coupling becomes symmetric, while for nonzero α ($0 < \alpha \leq 1$) it becomes asymmetric. The extreme case of asymmetric coupling with $\alpha = 1$ corresponds to the unidirectional coupling. In such a way, α tunes the degree of asymmetry in the coupling. In an ideal case without noise (i.e., $\sigma = 0$), there exists an invariant synchronization line,

$y = x$, in the $x - y$ phase space. However, in a real situation noise is unavoidable, and hence the diagonal is no longer invariant. To take into consideration such noise effect, random numbers are added to Eq. (2.31). For this case $\xi_n^{(i)}$ $(i = 1, 2)$ are statistically independent random numbers chosen at each discrete time n from the uniform distribution with a zero mean $< \xi_n^{(i)} >= 0$ and a unit variance $< {\xi_n^{(i)}}^2 >= 1$. Hence $\xi_n^{(i)}$ are just bounded random values uniformly distributed in the interval $[-\sqrt{3}, \sqrt{3}]$, and σ controls the "strength" of such a random noise.

As an example, we choose the unidirectionally coupled case of $\alpha = 1$ [11]. For this case, the drive 1D map acts on the response 1D map, while the response 1D map does not influence the drive one. Here we fix the value of a as $a = 1.82$, and investigate the noise effect by varying the coupling parameter c. For this case a synchronized chaotic attractor exists in the interval of $c_{b,l}[\simeq -2.963] < c < c_{b,r}[\simeq -0.677]$. As the coupling parameter c passes $c_{b,l}$ or $c_{b,r}$, the synchronized chaotic attractor loses its transverse stability through a blow-out bifurcation, and then a complete desynchronization occurs. In the regime of synchronization, a strongly stable synchronized chaotic attractor exists for $c_{t,l}[\simeq -2.789] < c < c_{t,r}[\simeq -0.850]$. For this case of strong synchronization, the synchronized chaotic attractor exhibits no noise sensitivity, because all periodic saddles embedded in the synchronized chaotic attractor are transversely stable. However, as the coupling parameter c passes $c_{t,r}$ and $c_{t,l}$, bubbling and riddling transitions occur through the first transverse bifurcations of periodic saddles, respectively, [11] and then we have weak synchronization. For this case, the weakly stable synchronized chaotic attractor exhibits a noise sensitivity, because of local transverse repulsion of the periodic repellers embedded in the synchronized chaotic attractor. Hence, however small the noise strength σ, a persistent intermittent bursting, called the attractor bubbling, occurs in the regime of bubbling $(c_{t,r} < c < c_{b,r})$. Figures 2.27(a) and 2.27(b) show such attractor bubbling for $\sigma = 0.0005$. On the other hand, in the regime of riddling $(c_{b,l} < c < c_{t,l})$, the weakly stable synchronized chaotic attractor with a riddled basin for $\sigma = 0$ is transformed into a chaotic transient (denoted by black dots) with a finite lifetime in presence of noise, as shown in Fig. 2.27(c). As c is changed away from $c_{t,l}$ or $c_{t,r}$, transversely unstable periodic repellers appear successively in the synchronized chaotic attractor via transverse bifurcations. Then the degree of the noise sensitivity of the synchronized chaotic attractor increases, because of the increase in the strength of local transverse repul-

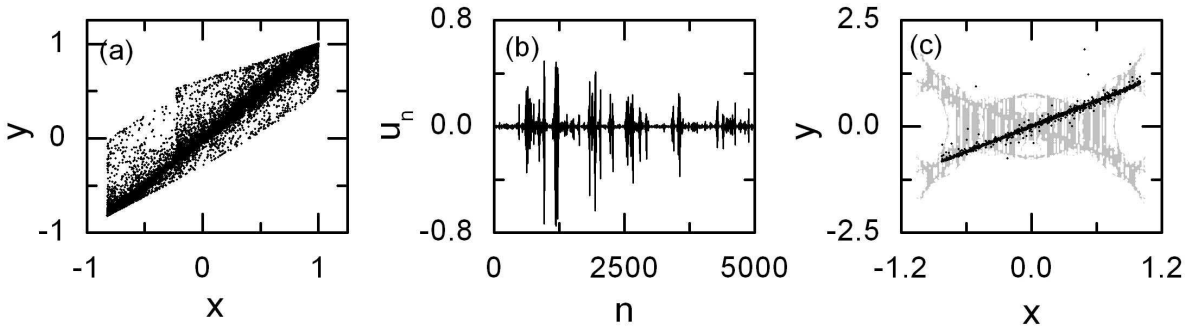

Figure 2.27: Effect of the additive noise with $\sigma = 0.0005$ on weak synchronization for $a = 1.82$ in the unidirectionally coupled case of $\alpha = 1$. (a) A bubbling attractor and (b) the evolution of the transverse variable u_n $(= x_n - y_n)$ representing the deviation from the diagonal versus n for the bubbling case of $c = -0.7$. For the riddling case of $c = -2.91$ the synchronized chaotic attractor with a basin (gray region) riddled with a dense set of repelling "holes" leading to divergent orbits (white region) for $\sigma = 0$ is transformed into a chaotic transient (black dots) for $\sigma = 0.0005$ as shown in (c). The sequence of $\{u_n\}$ in (b) and the chaotic transient in (c) are obtained from the trajectories starting from the same initial point $(x_0^*, y_0^*) = (0.5, 0.5)$.

sion of the periodic repellers embedded in the synchronized chaotic attractor.

To quantitatively characterize the noise sensitivity of the synchronized chaotic attractor, we consider an orbit $\{(x_n, y_n)\}$ starting from an initial point on the diagonal (i.e., $x_0 = y_0$). As the strength of the local transverse repulsion from the diagonal increases, the synchronized chaotic attractor becomes more and more sensitive with respect to the variation of σ. Such noise sensitivity of the synchronized chaotic attractor for $\sigma = 0$ may be characterized by calculating the derivative of the transverse variable u_n $(= x_n - y_n)$, denoting the deviation from the diagonal, with respect to σ,

$$\begin{aligned}
\left.\frac{\partial u_{n+1}}{\partial \sigma}\right|_{\sigma=0} &= \left.\frac{\partial x_{n+1}}{\partial \sigma}\right|_{\sigma=0} - \left.\frac{\partial y_{n+1}}{\partial \sigma}\right|_{\sigma=0} \\
&= \left[\left.\frac{\partial F(x_n, y_n)}{\partial x_n}\right|_{\sigma=0} - \left.\frac{\partial G(x_n, y_n)}{\partial x_n}\right|_{\sigma=0}\right] \left.\frac{\partial x_n}{\partial \sigma}\right|_{\sigma=0} \\
&\quad + \left[\left.\frac{\partial F(x_n, y_n)}{\partial y_n}\right|_{\sigma=0} - \left.\frac{\partial G(x_n, y_n)}{\partial y_n}\right|_{\sigma=0}\right] \left.\frac{\partial y_n}{\partial \sigma}\right|_{\sigma=0} \\
&\quad + [\xi_n^{(1)} - \xi_n^{(2)}]. \qquad (2.33)
\end{aligned}$$

Using Eq. (2.31), we obtain the following recurrence relation

$$\left.\frac{\partial u_{n+1}}{\partial \sigma}\right|_{\sigma=0} = [f_x(x_n^*, a) - (2-\alpha)c\,h(x_n^*)]\left.\frac{\partial u_n}{\partial \sigma}\right|_{\sigma=0} + [\xi_n^{(1)} - \xi_n^{(2)}], \tag{2.34}$$

where f_x is the derivative of f with respect to x, $\{(x_n^*, y_n^*)\}$ is the synchronous orbit with $x_n^* = y_n^*$ for $\sigma = 0$, and $h(x)$ is a reduced coupling function defined by $h(x) \equiv \left.\frac{\partial g(x,y)}{\partial y}\right|_{y=x}$ [87]. Iterating the formula (2.34) along a synchronous trajectory starting from an initial point (x_0^*, y_0^*) on the diagonal, we may obtain derivatives at all subsequent points of the trajectory:

$$\left.\frac{\partial u_N}{\partial \sigma}\right|_{\sigma=0} = \sum_{k=1}^{N} R_{N-k}(x_k^*)[\xi_{k-1}^{(1)} - \xi_{k-1}^{(2)}] + R_N(x_0^*)\left.\frac{\partial u_0}{\partial \sigma}\right|_{\sigma=0}, \tag{2.35}$$

where

$$R_M(x_m^*) = \prod_{i=0}^{M-1}\left[f_x(x_{m+i}^*, a) - (2-\alpha)c\,h(x_{m+i}^*)\right] \tag{2.36}$$

and $R_0 = 1$. Note that the factor $R_M(x_m^*)$ is associated with a local (M-time) transverse Lyapunov exponent $\sigma_M^T(x_m^*)$ of the synchronized chaotic attractor that is averaged over M synchronous orbit points starting from x_m^* as follows:

$$\sigma_M^T(x_m^*) = \frac{1}{M}\ln|R_M(x_m^*)|. \tag{2.37}$$

Thus $R_M(x_m^*)$ becomes a local (transverse stability) multiplier that determines local sensitivity of the transverse motion during a finite time M. As $M \to \infty$, σ_M^T approaches the usual transverse Lyapunov exponent σ_T that denotes the average exponential rate of divergence of an infinitesimal perturbation transverse to the synchronized chaotic attractor. If we introduce a new random variable $\eta_n = \xi_n^{(1)} - \xi_n^{(2)}$, Eq. (2.35) reduces to

$$\left.\frac{\partial u_N}{\partial \sigma}\right|_{\sigma=0} = S_N^{(n)}(x_0^*) \equiv \sum_{k=1}^{N} R_{N-k}(x_k^*)\eta_{k-1}, \tag{2.38}$$

because $\left.\frac{\partial u_0}{\partial \sigma}\right|_{\sigma=0} = 0$. Here η_n are bounded random numbers distributed in the interval $[-2\sqrt{3}, 2\sqrt{3}]$, and their distribution density function will be given below.

For the case of weak synchronization, transversely unstable periodic repellers are embedded in the synchronized chaotic attractor. When a typical trajectory visits neighborhoods of such repellers and their preimages, it has segments experiencing local repulsion from the diagonal. Consequently, the distribution of local transverse Lyapunov exponents σ_M^T for a large ensemble of trajectories and large M may have a positive tail [see Fig. 5 in Ref. [19]].

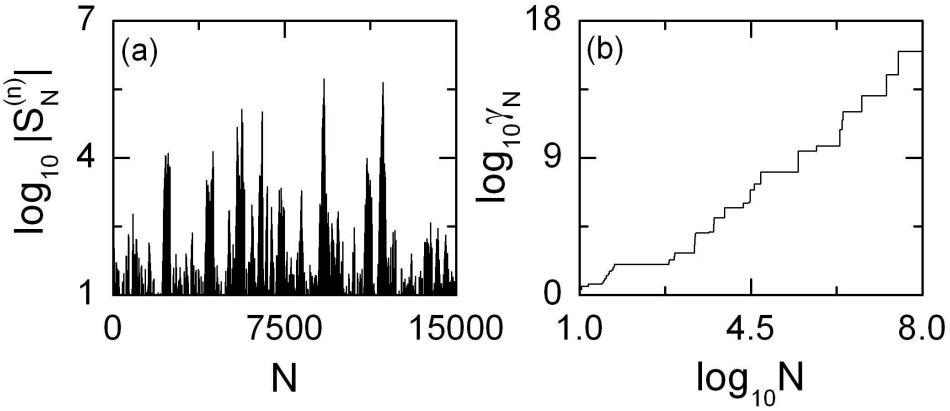

Figure 2.28: (a) Intermittent behavior of the partial sum $|S_N^{(n)}|$ for $\alpha = 1$, $a = 1.82$, and $c = -0.7$. (b) The function γ_N looking only at the maximum of $|S_N^{(n)}|$. Note that γ_N grows unboundedly with N. The results in (a) and (b) are obtained from the trajectory starting from the initial orbit point $(x_0^*, y_0^*) = (0.5, 0.5)$.

For the segments of a trajectory exhibiting a positive local transverse Lyapunov exponent ($\sigma_M^T > 0$), the local multipliers R_M [$= \pm \exp(\sigma_M^T M)$] can be arbitrarily large, and hence the partial sum $S_N^{(n)}$ may be arbitrarily large. This implies unbounded growth of the derivatives $\frac{\partial u_N}{\partial \sigma}\big|_{\sigma=0}$ as N tends to infinity. Consequently, the weakly stable synchronized chaotic attractor may exhibit a noise sensitivity. As an example, we consider the case of weak synchronization for $c = -0.7$. If we iterate Eqs. (2.31) and (2.34) starting from an initial orbit point (x_0^*, y_0^*) on the diagonal and $\frac{\partial u_0}{\partial \sigma}\big|_{\sigma=0} = 0$, then we obtain the partial sum $S_N^{(n)}(x_0^*)$ of Eq. (2.38). The results of such calculation for a trajectory starting from $(x_0^*, y_0^*) = (0.5, 0.5)$ are presented in Fig. 2.28(a). The quantity $S_N^{(n)}$ seems very intermittent. However, looking only at the maximum

$$\gamma_N(x_0^*) = \max_{0 \le k \le N} |S_k^{(n)}(x_0^*)|, \tag{2.39}$$

one can easily see the boundedness of $S_N^{(n)}$. Figure 2.28(b) shows such function γ_N. Note that γ_N grows unboundedly and exhibits no saturation. Consequently, the weakly stable synchronized chaotic attractor exhibits a noise sensitivity. This is in contrast to the case of strong synchronization for which the synchronized chaotic attractor has no noise sensitivity because the function γ_N saturates with N.

The growth rate of the function $\gamma_N(x_0^*)$ with time N represents a degree of the noise sen-

sitivity, and can be used as a quantitative characteristic of the weakly stable synchronized chaotic attractor. However, $\gamma_N(x_0^*)$ depends on a particular trajectory. To obtain a representative quantity, we consider an ensemble of initial points randomly chosen with uniform probability in the range of $x \in (1-a, 1)$ on the diagonal, and take the minimum value of γ_N with respect to the initial orbit points,

$$\Gamma_N = \min_{x_0^*} \gamma_N(x_0^*). \tag{2.40}$$

Figure 2.29(a) shows a noise sensitivity function Γ_N for $c = -0.7$. Note that Γ_N grows unboundedly with some power δ,

$$\Gamma_N \simeq N^\delta. \tag{2.41}$$

Here the value $\delta \simeq 2.58$ is a quantitative characteristic of the noise sensitivity of the synchronized chaotic attractor, and we call it the noise sensitivity exponent. In each regime of bubbling or riddling, we obtain the noise sensitivity exponents by changing the coupling parameter c from the bubbling or riddling transition point to the blow-out bifurcation point. For obtaining a satisfactory statistics, we also consider 100 ensembles for each c, each of which contains 100 initial orbit points randomly chosen with uniform probability in the range of $x \in (1-a, 1)$ on the diagonal and choose the average value of the 100 noise sensitivity exponents obtained in the 100 ensembles. Figure 2.29(b) shows the plot of such noise sensitivity exponents (denoted by circles) versus c. Note that the noise sensitivity exponent δ monotonically increases as c is varied away from the bubbling or riddling transition point, and tends to infinity as c approaches the blow-out bifurcation point. This increase in the noise sensitivity of the synchronized chaotic attractor is caused by the increase in the strength of local transverse repulsion of periodic repellers embedded in the synchronized chaotic attractor. After the blow-out bifurcation, the weakly stable synchronized chaotic attractor is transformed into a transversely unstable chaotic saddle exhibiting an exponential noise sensitivity. Thus a complete desynchronization occurs.

We now compare the formula (2.38) for the partial sum $S_N^{(n)}$ with the following analogous formula for $S_N^{(p)}$ that has been obtained in the parameter-mismatching case [19]:

$$\left.\frac{\partial u_N}{\partial \epsilon}\right|_{\epsilon=0} = S_N^{(p)}(x_0^*) \equiv \sum_{k=1}^{N} R_{N-k}(x_k^*) f_a(x_{k-1}^*, a), \tag{2.42}$$

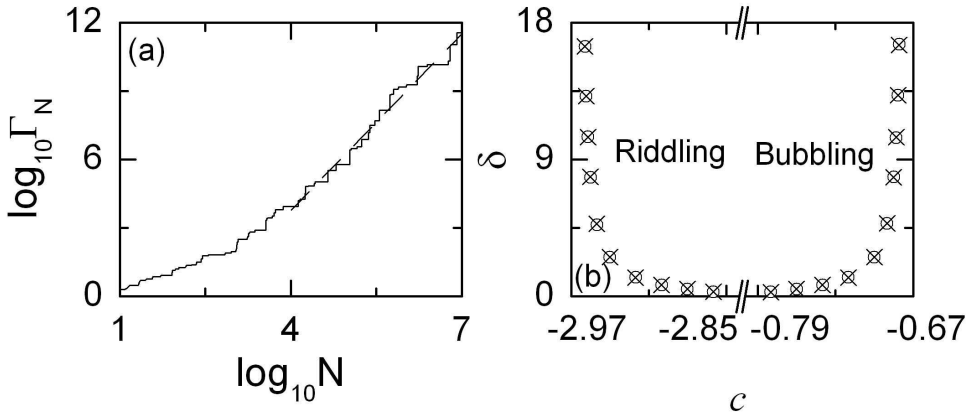

Figure 2.29: (a) Noise sensitivity function Γ_N for $\alpha = 1$, $a = 1.82$, and $c = -0.7$ that takes the minimum value of γ_N in the ensemble containing 100 randomly chosen initial orbit points on the diagonal. It is well fitted with a dashed line with slope $\delta \simeq 2.58$. (b) Plot of the noise sensitivity exponents δ (denoted by the open circles) versus c for the bubbling and riddling cases for $\alpha = 1$ and $a = 1.82$. Note that the values of the noise sensitivity exponents are the same as those of the parameter sensitivity exponent (denoted by the crosses) within the numerical accuracy.

where ϵ is a mismatching parameter, f_a is the derivative of $f(x, a)$ with respect to a, and R_{N-k} are local multipliers of Eq. (2.36). As in the case of noise, the weakly stable synchronized chaotic attractor exhibits a parameter sensitivity because of the unbounded growth of the partial sum $S_N^{(p)}$ with N. For each case of the noise and parameter mismatch, $S_N^{(n,p)}$ represents the sum of the (same) local multipliers R_{N-k}, multiplied by some coefficients. For the case of noise, the coefficients η_{k-1} are random numbers chosen from the bounded distribution density function, $P(\eta) = -\frac{1}{12}|\eta| + \frac{\sqrt{3}}{6}$, in the interval $[-2\sqrt{3}, 2\sqrt{3}]$ [see Fig. 2.30(a)], which can be easily obtained using the uniform distribution density functions in the interval $[-\sqrt{3}, \sqrt{3}]$ for the random variables ξ_1 and ξ_2. Since the random numbers η_n are bounded, the boundedness of the partial sum $S_N^{(n)}$ is determined just by the local multipliers R_M. For the case of parameter mismatch, the coefficients are the derivative values $f_a(x^*_{k-1}, a)$ $(= -x^{*2}_{k-1})$. Since the synchronous trajectory $\{x^*_n\}$ on the diagonal is chaotic, the coefficients f_a may be regarded as "weakly correlated" random numbers. Using a histogram method, we obtain the distribution density function for f_a, which is shown in Fig. 2.30(b). Since the values of f_a are bounded in the interval $[-1, 0]$, the boundedness of the partial sum $S_N^{(p)}$ is also determined

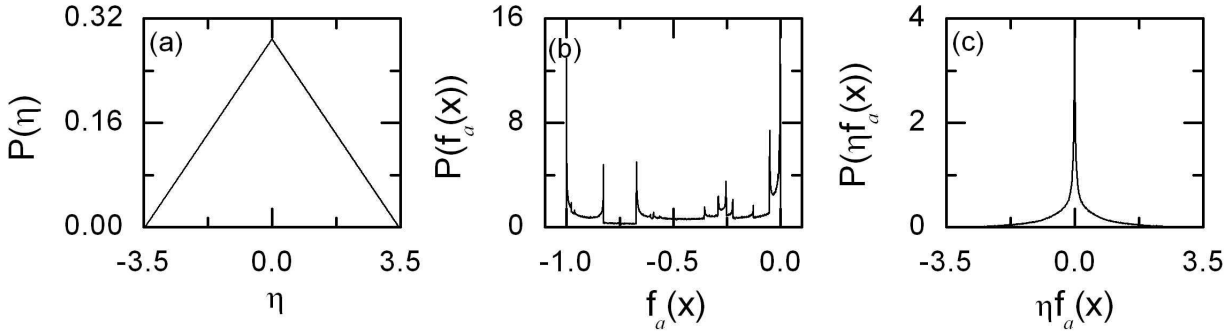

Figure 2.30: (a) Distribution density function $P(\eta)$ $(= -\frac{1}{12}|\eta| + \frac{\sqrt{3}}{6})$ for the random variable η $(= \xi^{(1)} - \xi^{(2)})$. (b) and (c) Distribution density functions for the variables $f_a(x)$ $(= -x^2)$ and $\eta f_a(x)$ in the case of $\alpha = 1$ and $a = 1.82$. For these cases, the distribution density functions are obtained using a histogram method as follows. We divide each interval ($[-1, 0]$ for the case (b) and $[-2\sqrt{3}, 2\sqrt{3}]$ for the case of (c)) into 1000 bins, and get the distribution density from the data of 10^6 orbit points.

only by the (same) local multipliers R_M, as in the case of noise. This implies that the noise sensitivity function Γ_N grows unboundedly with the same power as in the case of parameter mismatch. Hence the values of the noise sensitivity exponent (denoted by circles) become the same as those of the parameter sensitivity exponent (denoted by crosses), as shown in Fig. 2.29(b). Note that this is a general result valid for any case of bounded noise.

In addition to the case of additive noise, we also consider the case when the nonlinearity parameters of the 1D maps have small random variations due to external noise. These parametric fluctuations can be simulated by modulating the values of the nonlinearity parameters by uniform random numbers in a small interval. Thus we investigate the effect of such parametric noise on weak synchronization in the following two coupled 1D maps:

$$T : \begin{cases} x_{n+1} = f(x_n, a + \sigma\xi_n^{(1)}) + (1-\alpha)cg(x_n, y_n), \\ y_{n+1} = f(y_n, a + \sigma\xi_n^{(2)}) + c\, g(y_n, x_n). \end{cases} \tag{2.43}$$

Here $\xi^{(1)}$ and $\xi^{(2)}$ are bounded random numbers chosen from the uniform distribution with a zero mean and a unit variance, and σ represents the amplitude of noise. Following the same procedure as in the case of additive noise, one can easily obtain the following recurrence relation for the derivative of the transverse variable u_n $(= x_n - y_n)$ with respect to the noise

strength σ,

$$\left.\frac{\partial u_{n+1}}{\partial \sigma}\right|_{\sigma=0} = [f_x(x_n^*, a) - (2-\alpha)c\,h(x_n^*)] \left.\frac{\partial u_n}{\partial \sigma}\right|_{\sigma=0} + f_a(x_n^*, a)[\xi_n^{(1)} - \xi_n^{(2)}]. \tag{2.44}$$

Iterating the above formula along the synchronous trajectory starting from an initial point (x_0^*, y_0^*) on the diagonal, we obtain the derivatives at all points of the trajectory:

$$\left.\frac{\partial u_N}{\partial \sigma}\right|_{\sigma=0} = S_N^{(n)}(x_0^*) \equiv \sum_{k=1}^{N} R_{N-k}(x_k^*)\eta_{k-1} f_a(x_{k-1}^*, a), \tag{2.45}$$

where $\eta_n = \xi_n^{(1)} - \xi_n^{(2)}$ and R_{N-k} are local multipliers of Eq. (2.36). Comparing this formula with Eq. (2.38), one can see that the only difference between them is the coefficients of the (same) local multipliers R_{N-k}. For the case of parametric noise, the coefficients $\eta_{k-1} f_a(x_{k-1}^*, a)$ are also weakly-correlated random numbers, because the synchronous trajectory $\{x_n^*\}$ on the diagonal is chaotic. The distribution density function for ηf_a is presented in Fig. 2.30(c). Since the values of ηf_a are bounded in the interval $[-2\sqrt{3}, 2\sqrt{3}]$, the coefficients have no effect on the unbounded growth of $S_N^{(n)}$, as in the case of additive noise. Consequently, the values of the noise sensitivity exponent for both cases of additive and parametric noise become the same, which has also been numerically confirmed in the unidirectionally coupled case of $\alpha = 1$. In this sense, the effect of parametric noise on weak synchronization becomes the same as that of additive noise.

So far, we have investigated the noise effect in the unidirectionally coupled case with the asymmetry parameter $\alpha = 1$. Through Eq. (2.34), one can easily see that the noise sensitivity exponent for a given (a, c) in the case of $\alpha = 1$ is the same as that for the value of $[a, c/(2-\alpha)]$ in other coupled 1D maps with $0 \le \alpha < 1$ in Eq. (2.31). Thus, the results of the noise sensitivity exponents given in Fig. 2.29(b) may be converted into those for the case of general α only by a scale change in the coupling parameter such that $c \to c/(2-\alpha)$. For this case, the bubbling regime for the case of $\alpha = 1$ is always transformed into a bubbling regime for any other value of α. However, the riddling regime for the case of $\alpha = 1$ is transformed into a bubbling or riddling regime depending on the value of α. For more details on the effect of asymmetry, refer to Ref. [12].

From now on, in terms of the noise sensitivity exponents we characterize the noise effect on the power-law scaling behavior of the average time spent near the diagonal for the bubbling and riddling cases. The scaling exponent for such average characteristic time is found to be

given by the reciprocal of the noise sensitivity exponent, as in the parameter-mismatching case. Consequently, both the noise and parameter mismatch have essentially the same effect on the scaling behavior of the average characteristic time.

As an example, we consider the effect of additive noise on both the bubbling and riddling occurring in the regime of weak synchronization for $a = 1.82$ in the unidirectionally coupled case of $\alpha = 1$. In presence of noise, the weakly stable synchronized chaotic attractor is transformed into a bubbling attractor or a chaotic transient, depending on the global dynamics. For this case the quantity of interest is the average time τ spent near the diagonal. For the case of the bubbling attractor, τ is the average interburst time, while for the case of the chaotic transient, τ is its average lifetime. As c is varied from the bubbling or riddling transition point, τ becomes short because the strength of local transverse repulsion of periodic repellers embedded in the synchronized chaotic attractor increases.

For the case of bubbling, the bubbling attractor is in the laminar phase when the magnitude of the deviation from the diagonal is less than a threshold value u_b^* (i.e., $|u_n| < u_b^*$). Otherwise, it is in the bursting phase. Here u_b^* is very small compared to the maximum bursting amplitude. For each c, we follow the trajectory starting from the initial condition (0,0) until 50 000 laminar phases are obtained, and then we get the average laminar length τ (i.e., the average interburst time) that scales with σ as [13]

$$\tau \sim \sigma^{-\mu}. \tag{2.46}$$

The plot of the scaling exponent μ (denoted by circles) versus c is shown in Fig. 2.31. As c increases toward the blow-out bifurcation point, the value of μ decreases, because the average laminar length shortens.

For each c in the regime of riddling, we consider an ensemble of trajectories starting from 1000 initial points randomly chosen with uniform probability in the range of $x \in (1-a, 1)$ on the diagonal, and obtain the average lifetime of the chaotic transients. A trajectory may be regarded as having escaped once the magnitude of deviation u_n from the diagonal becomes larger than a threshold value u_c^* such that an orbit point with $|u| > u_c^*$ lies sufficiently outside the basin of the synchronized chaotic attractor. Thus, the average lifetime τ is found to scale with σ as [13]

$$\tau \sim \sigma^{-\mu}. \tag{2.47}$$

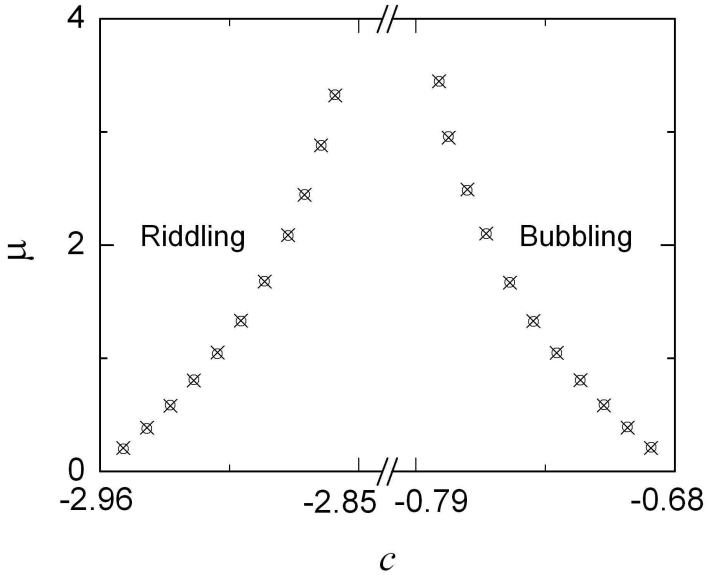

Figure 2.31: (a) Plot of the scaling exponents μ (open circles) for the average characteristic time (i.e., average interburst time for the bubbling case and average chaotic transient lifetime for the riddling case) versus c in the case of additive noise when $\alpha = 1$ and $a = 1.82$. They agree well with the reciprocals of the noise sensitivity exponents (crosses).

The plot of the scaling exponent μ (denoted by circles) versus c is given in Fig. 2.31. As c decreases toward the blow-out bifurcation point, the average lifetime shortens, and hence the value of μ decreases.

We note that the scaling exponent μ is associated with the noise sensitivity exponent δ as follows. For a given σ, consider a trajectory starting from a randomly chosen initial orbit point on the diagonal. Then, From Eq. (2.41) the average characteristic time τ at which the magnitude of the deviation from the diagonal becomes the threshold value $u^*_{b,c}$ can be obtained:

$$\tau \sim \sigma^{-1/\delta}. \tag{2.48}$$

Hence the scaling exponent μ for τ is given by the reciprocal of the noise sensitivity exponent δ,

$$\mu = 1/\delta. \tag{2.49}$$

The reciprocal values of δ (denoted by crosses) are also plotted in Fig. 2.31, and they agree well with the values of μ (denoted by circles). This reciprocal relation has also been confirmed

for the case of parametric noise. Furthermore, the same reciprocal relation between the scaling exponent for τ and the parameter sensitivity exponent exists also in the parameter-mismatching case [19]. Thus the scaling exponents for τ in both cases of noise and parameter mismatch also become the same [13], because the values of the noise sensitivity exponent and the parameter sensitivity exponent are the same. Hence the noise and parameter mismatch have the same effect on the power-law scaling behavior of the average characteristic time τ.

2.2.4 Universality for the Parameter-Mismatching and Noise Effect

By generalizing the method proposed in coupled 1D noninvertible maps, we introduce the parameter sensitivity exponent in the coupled Hénon maps and coupled pendula, and quantitatively characterize the parameter sensitivity of the weakly stable synchronous chaotic attractor. In terms of the parameter sensitivity exponents, the effect of parameter mismatch on the bubbling and riddling is characterized. Thus, the scaling exponent μ for the average interburst time and the average chaotic transient lifetime is found to be given by the reciprocal of the parameter sensitivity exponent (i.e., $\mu = 1/\delta$), as in the coupled 1D maps.

As a first example, we consider two coupled invertible Hénon maps, often used as a representative model for the Poincaré maps of coupled chaotic oscillators [13]:

$$T : \begin{cases} \mathbf{x}_{n+1} = \mathbf{F}(\mathbf{x}_n, \mathbf{y}_n) = \mathbf{f}(\mathbf{x}_n, a) + (1-\alpha)\, c\, \mathbf{g}(\mathbf{x}_n, \mathbf{y}_n), \\ \mathbf{y}_{n+1} = \mathbf{G}(\mathbf{x}_n, \mathbf{y}_n) = \mathbf{f}(\mathbf{y}_n, b) + c\, \mathbf{g}(\mathbf{y}_n, \mathbf{x}_n), \end{cases} \tag{2.50}$$

where $\mathbf{x}_n = (x_n^{(1)}, x_n^{(2)})$ and $\mathbf{y}_n = (y_n^{(1)}, y_n^{(2)})$ are state variables of the two subsystems at a discrete time n, the uncoupled dynamics ($c = 0$) is governed by the Hénon map with a nonlinearity parameter p ($p = a, b$) and a damping parameter β ($|\beta| < 1$),

$$\mathbf{f}(\mathbf{x}, p) = (f(x^{(1)}, p) - x^{(2)}, \beta\, x^{(1)});\ \ f(x, p) = 1 - p\, x^2, \tag{2.51}$$

c is a coupling parameter between the two subsystems, and $\mathbf{g}(\mathbf{x}, \mathbf{y})$ is a coupling function of the form,

$$\mathbf{g}(\mathbf{x}, \mathbf{y}) = (g(x^{(1)}, y^{(1)}), 0);\ \ g(x, y) = y^2 - x^2. \tag{2.52}$$

For $\alpha = 0$, the coupling is symmetric, while for nonzero α ($0 < \alpha \leq 1$) it becomes asymmetric. The extreme case of asymmetric coupling with $\alpha = 1$ corresponds to the unidirectional

coupling. In such a way, α tunes the degree of asymmetry in the coupling. This asymmetric coupling naturally arises in the dynamics of two clusters for the case of global coupling, in which each element is coupled to all the other elements with equal strength [13]. For the ideal case of identical Hénon maps (i.e., $a = b$), there exists an invariant synchronization plane, $x^{(1)} = y^{(1)}$ and $x^{(2)} = y^{(2)}$, in the $x^{(1)} - x^{(2)} - y^{(1)} - y^{(2)}$ phase space. However, in a real situation a small mismatch between the two subsystems and a small noise are unavoidable, and hence the synchronization plane is no longer invariant. Here, we restrict our attention only to the mismatching case in the absence of noise. To take into consideration such a mismatching effect, we introduce a small mismatching parameter ε in the coupled Hénon maps of Eq. (2.50) such that

$$b = a - \varepsilon. \tag{2.53}$$

Recently, some results on the attractor bubbling in the unidirectionally coupled case of $\alpha = 1$ have been reported in [88]. Here, as an example, we choose a mutually coupled case of $\alpha = 0.75$, and investigate both the bubbling and riddling for a fixed value of $\beta = 0.1$. For $a = 1.8$, we investigate the parameter-mismatching effect by varying the coupling parameter c. For this case a synchronous chaotic attractor exists in the interval of $c_{b,l} < c < c_{b,r}$, where $c_{b,l} = -2.3979$ and $c_{b,r} = -0.4821$. As the coupling parameter c passes $c_{b,l}$ or $c_{b,r}$, the synchronous chaotic attractor loses its transverse stability through a blowout bifurcation [13], and then a complete desynchronization occurs. In the regime of synchronization, a strongly stable synchronous chaotic attractor exists for $c_{t,l} < c < c_{t,r}$, where $c_{t,l} = -2.32$ and $c_{t,r} = -0.56$. For this case of strong synchronization, the synchronous chaotic attractor exhibits no parameter sensitivity, because all periodic saddles embedded in the synchronous chaotic attractor are transversely stable. However, as the coupling parameter c passes $c_{t,r}$ and $c_{t,l}$, bubbling and riddling transitions occur through the first transverse bifurcations of periodic saddles, respectively [9, 11], and then we have weak synchronization. For this case, the weakly stable synchronous chaotic attractor has a parameter sensitivity, because of local transverse repulsion of the periodic repellers embedded in the synchronous chaotic attractor. Hence, however small the parameter mismatching ε, a persistent intermittent bursting, called the attractor bubbling, occurs in the regime of bubbling ($c_{t,r} < c < c_{b,r}$). Figures 2.32(a) and 2.32(b) show such attractor bubbling for $c = -0.49$ and $\varepsilon = 0.002$. On the other hand, in the regime of riddling ($c_{b,l} < c < c_{t,l}$), the weakly stable synchronous chaotic attractor

with a riddled basin for $\varepsilon = 0$ is transformed into a chaotic transient (denoted by black dots) with a finite lifetime in the presence of parameter mismatch, as shown in Figs. 2.32(c) and 2.32(d) for $c = -2.39$. As c is changed away from $c_{t,l}$ or $c_{t,r}$, transversely unstable periodic repellers appear successively in the synchronous chaotic attractor via transverse bifurcations. Then, the degree of the parameter sensitivity of the synchronous chaotic attractor increases, because of the increase in the strength of local transverse repulsion of the periodic repellers embedded in the synchronous chaotic attractor.

We generalize the method proposed in the coupled 1D maps [12] to the case of the coupled Hénon maps and quantitatively characterize the parameter sensitivity of the synchronous chaotic attractor as follows. As the strength of the local transverse repulsion from the synchronization plane increases, the synchronous chaotic attractor becomes more and more sensitive with respect to the variation of ε. Such parameter sensitivity of the synchronous chaotic attractor for $\varepsilon = 0$ may be characterized by calculating the derivative of the transverse variable $\mathbf{u}_n = \mathbf{x}_n - \mathbf{y}_n$, denoting the deviation from the synchronization plane, with respect to ε (i.e. $\left.\frac{\partial \mathbf{u}_{n+1}}{\partial \varepsilon}\right|_{\varepsilon=0} = \left.\frac{\partial \mathbf{x}_{n+1}}{\partial \varepsilon}\right|_{\varepsilon=0} - \left.\frac{\partial \mathbf{y}_{n+1}}{\partial \varepsilon}\right|_{\varepsilon=0}$). Using Eq. (2.50), we may obtain the following recurrence relation

$$\left.\frac{\partial \mathbf{u}_{n+1}}{\partial \varepsilon}\right|_{\varepsilon=0} = r(\mathbf{x}_n^*) \left.\frac{\partial \mathbf{u}_n}{\partial \varepsilon}\right|_{\varepsilon=0} + \mathbf{f}_a(\mathbf{x}_n^*, a), \tag{2.54}$$

where $\left.\frac{\partial \mathbf{u}_n}{\partial \varepsilon}\right|_{\varepsilon=0} = \left(\left.\frac{\partial u_n^{(1)}}{\partial \varepsilon}\right|_{\varepsilon=0}, \left.\frac{\partial u_n^{(2)}}{\partial \varepsilon}\right|_{\varepsilon=0} \right)$, the 2×2 matrix $r(\mathbf{x}_n^*)$ is given by

$$r(\mathbf{x}_n^*) \equiv \begin{pmatrix} f_{x^{(1)}}(x_n^{(1)*}, a) - (2-\alpha) c\, h(x_n^{(1)*}) & -1 \\ \beta & 0 \end{pmatrix}, \tag{2.55}$$

and

$$\mathbf{f}_a(\mathbf{x}_n^*, a) = \begin{pmatrix} f_a(x_n^{(1)*}, a) \\ 0 \end{pmatrix}. \tag{2.56}$$

Here, f_x and f_a are the derivatives of $f(x, a)$ with respect to x and a, $\{(\mathbf{x}_n^*, \mathbf{y}_n^*)\}$ is a synchronous orbit with $\mathbf{x}_n^* = \mathbf{y}_n^*$ for $\varepsilon = 0$, and $h(x)$ is a reduced coupling function defined by [87]

$$h(x) \equiv \left.\frac{\partial g(x, y)}{\partial y}\right|_{y=x}. \tag{2.57}$$

Hence, starting from an initial orbit point $(\mathbf{x}_0^*, \mathbf{y}_0^*)$ on the synchronization plane, we may

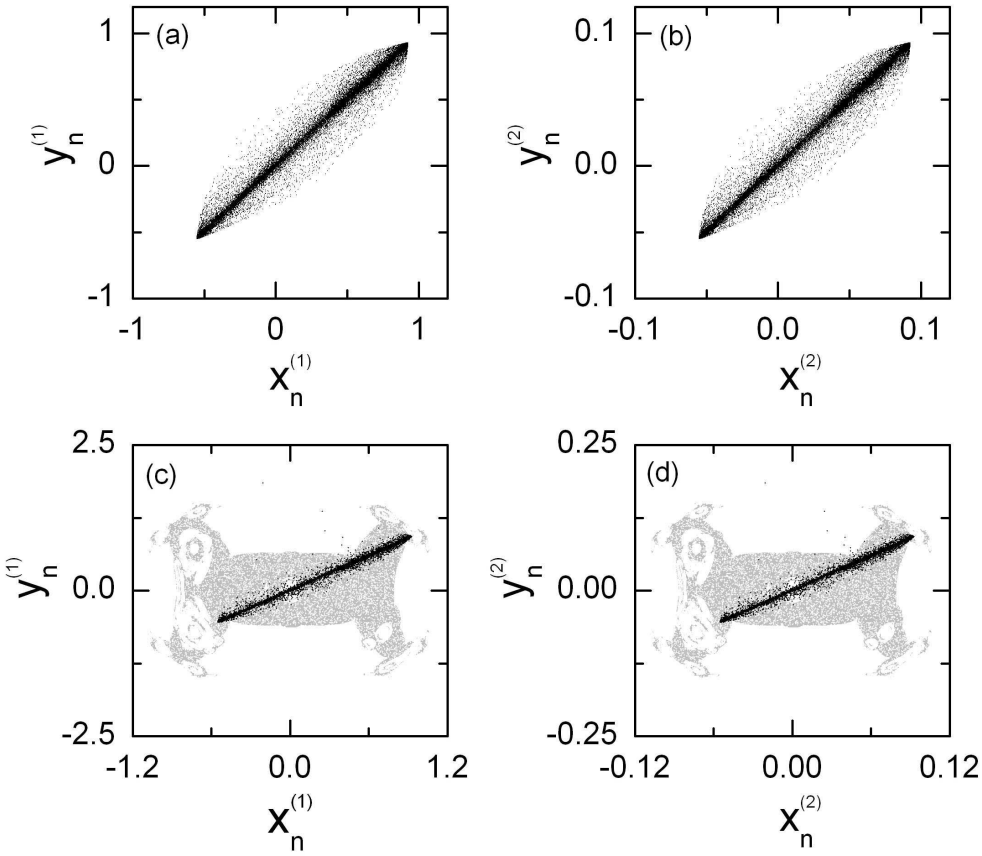

Figure 2.32: Effect of parameter mismatch with $\varepsilon = 0.002$ on weak synchronization for $a = 1.8$ in mutually coupled Hénon maps with $\alpha = 0.75$. For $c = -0.49$, projections of a bubbling attractor onto the (a) $x^{(1)} - y^{(1)}$ and (b) $x^{(2)} - y^{(2)}$ planes are given. In both (a) and (b), the initial orbit point is $(x^{(1)}, x^{(2)}, y^{(1)}, y^{(2)}) = (0.7, 0.07, 0.7, 0.07)$, the 5×10^3 points are computed before plotting, and the next 4×10^4 points are plotted. For the riddling case of $c = -2.39$, the synchronous chaotic attractor with a basin (gray region) riddled with a dense set of "holes" leading to divergent trajectories (white region) for $\varepsilon = 0$ is transformed into a chaotic transient (black dots). In (c) [(d)], a 2D slice with $x^{(2)} = y^{(2)} = 0.05$ [$x^{(1)} = y^{(1)} = 0.5$] through the 4D riddled basin of the weakly stable synchronous chaotic attractor is shown. Projections of a chaotic transient starting from an initial orbit point $(x^{(1)}, x^{(2)}, y^{(1)}, y^{(2)}) = (0.7, 0.07, 0.7, 0.07)$ onto the (c) $x^{(1)} - y^{(1)}$ and (d) $x^{(2)} - y^{(2)}$ planes are given.

obtain derivatives at all points of the orbit:

$$\left.\frac{\partial \mathbf{u}_N}{\partial \varepsilon}\right|_{\varepsilon=0} = \sum_{k=1}^{N} R_{N-k}(\mathbf{x}_k^*)\mathbf{f}_a(\mathbf{x}_{k-1}^*, a) + R_N(\mathbf{x}_0^*) \left.\frac{\partial \mathbf{u}_0}{\partial \varepsilon}\right|_{\varepsilon=0}, \tag{2.58}$$

where

$$R_M(\mathbf{x}_m^*) = \prod_{i=0}^{M-1} r(\mathbf{x}_{m+i}^*), \tag{2.59}$$

which is a product of the "transverse Jacobian matrices" $r(\mathbf{x}^*)$ determining the stability against a perturbation transverse to the synchronization plane and $R_0 = I$ (identity matrix). Note that the eigenvalues, $\lambda_M^{T,1}(\mathbf{x}_m^*)$ and $\lambda_M^{T,2}(\mathbf{x}_m^*)$ ($|\lambda_M^{T,1}(\mathbf{x}_m^*)| \geq |\lambda_M^{T,2}(\mathbf{x}_m^*)|$), of $R_M(\mathbf{x}_m^*)$ are associated with local (M-time) transverse Lyapunov exponents $\sigma_M^{T,1}$ and $\sigma_M^{T,2}$ ($\sigma_M^{T,1} \geq \sigma_M^{T,2}$) of the synchronous chaotic attractor that are averaged over M synchronous orbit points starting from $\mathbf{x}_m^*$ as follows:

$$\sigma_M^{T,i}(\mathbf{x}_m^*) = \frac{1}{M} \ln |\lambda_M^{T,i}(\mathbf{x}_m^*)|, (i = 1, 2). \tag{2.60}$$

Thus, $\lambda_M^{T,1}$ and $\lambda_M^{T,2}$ become local (transverse stability) multipliers that determine local sensitivity of the motion during a finite time M. As $M \to \infty$, $\sigma_M^{T,1}$ approaches the largest transverse Lyapunov exponent $\sigma_T^{(1)}$ that denotes the average exponential rate of divergence of an infinitesimal perturbation transverse to the synchronous chaotic attractor. Because the initial point (x_0^*, y_0^*) starts on the synchronization plane (i.e., $x_0^* = y_0^*$), the value of the initial transverse variable $\mathbf{u}_0 = \mathbf{x}_0^* - \mathbf{y}_0^*$ is always zero, independently of ε (i.e., $\left.\frac{\partial \mathbf{u}_0}{\partial \varepsilon}\right|_{\varepsilon=0} = 0$). Hence, Eq. (2.58) reduces to

$$\left.\frac{\partial \mathbf{u}_N}{\partial \varepsilon}\right|_{\varepsilon=0} = \mathbf{S}_N(\mathbf{x}_0^*) \equiv \sum_{k=1}^{N} R_{N-k}(\mathbf{x}_k^*)\mathbf{f}_a(\mathbf{x}_{k-1}^*, a). \tag{2.61}$$

Since the values of $\mathbf{f}_a$ are bounded, the boundedness of the partial sum $\mathbf{S}_N$ is determined just by the largest eigenvalues $\lambda_M^{T,1}$ of R_M.

For the case of weak synchronization, there are transversely unstable periodic repellers embedded in the synchronous chaotic attractor. When a typical trajectory visits neighborhoods of such repellers, it has segments experiencing local repulsion from the synchronization plane. Thus, the distribution of largest local transverse Lyapunov exponents $\sigma_M^{T,1}$ for a large ensemble of trajectories and for large M may have a positive tail [12]. For the segments of a trajectory exhibiting a positive largest local transverse Lyapunov exponent ($\sigma_M^{T,1} > 0$), the

largest local transverse multipliers $\lambda_M^{T,1}$ $[= \pm \exp(\sigma_M^{T,1} M)]$ can be arbitrarily large, and hence the partial sums $S_N^{(i)}$ $(i = 1, 2)$ may be arbitrarily large. This implies unbounded growth of the derivatives $\frac{\partial u_N^{(i)}}{\partial \varepsilon}|_{\varepsilon=0}$ $(i = 1, 2)$ as N tends to infinity, and consequently the weakly stable synchronous chaotic attractor may have a parameter sensitivity.

As an example, we consider the case of weak synchronization in the mutually coupled case of $\alpha = 0.75$ for $c = -0.49$. If we iterate Eq. (2.54) with $\frac{\partial \mathbf{u}_0}{\partial \varepsilon}\big|_{\varepsilon=0} = 0$ along a synchronous trajectory starting from an initial orbit point $(\mathbf{x}_0^*, \mathbf{y}_0^*)$ on the synchronization plane, then we obtain the partial sum $\mathbf{S}_N(\mathbf{x}_0^*)$ of Eq. (2.61). The partial sum $S_N^{(i)}$ $\left[= \left.\frac{\partial u_N^{(i)}}{\partial \varepsilon}\right|_{\varepsilon=0}\right]$ $(i = 1, 2)$ becomes very intermittent. However, by looking only at the maximum

$$\gamma_N^{(i)}(x_0^*) = \max_{0 \le n \le N} |S_n^{(i)}(\mathbf{x}_0^*)| \ \ (i = 1, 2), \tag{2.62}$$

one can easily see the boundedness of $S_N^{(i)}$. For this case, $\gamma_N^{(1)}$ and $\gamma_N^{(2)}$ grow unboundedly, and hence the weakly stable synchronous chaotic attractor has a parameter sensitivity. The growth rate of the function $\gamma_N^{(i)}(\mathbf{x}_0^*)$ with time N represents a degree of the parameter sensitivity, and can be used as a quantitative characteristic of the weakly stable synchronous chaotic attractor. However, $\gamma_N^{(i)}(\mathbf{x}_0^*)$ depends on a particular trajectory. To obtain a "representative" quantity that is independent of a particular trajectory, we consider an ensemble of randomly chosen initial points $(\mathbf{x}_0^*, \mathbf{y}_0^*)$ on the synchronization plane, and take the minimum value of $\gamma_N^{(i)}$ with respect to the initial orbit points,

$$\Gamma_N^{(i)} = \min_{\mathbf{x}_0^*} \gamma_N^{(i)}(\mathbf{x}_0^*) \ \ (i = 1, 2). \tag{2.63}$$

While other representative quantities may be defined (e.g., the average of γ_N over an ensemble of trajectories), the numerical convergence for the case of minimum value is better than that for other cases, and hence we choose the minimum value as a representative one, as in the case of the phase sensitivity exponent in the quasiperiodically forced systems [47]. Figure 2.33(a) shows parameter sensitivity functions $\Gamma_N^{(1)}$ and $\Gamma_N^{(2)}$, which are obtained in an ensemble containing 100 random initial orbit points. The unbounded growth of both $\Gamma_N^{(1)}$ and $\Gamma_N^{(2)}$ is determined by the same largest local transverse multiplier $\lambda_M^{T,1}$ [i.e., the largest eigenvalue of R_M in Eq. (2.59)]. Hence, they grow unboundedly with the same power δ,

$$\Gamma_N^{(i)} \sim N^{\delta} \text{ for } i = 1, 2. \tag{2.64}$$

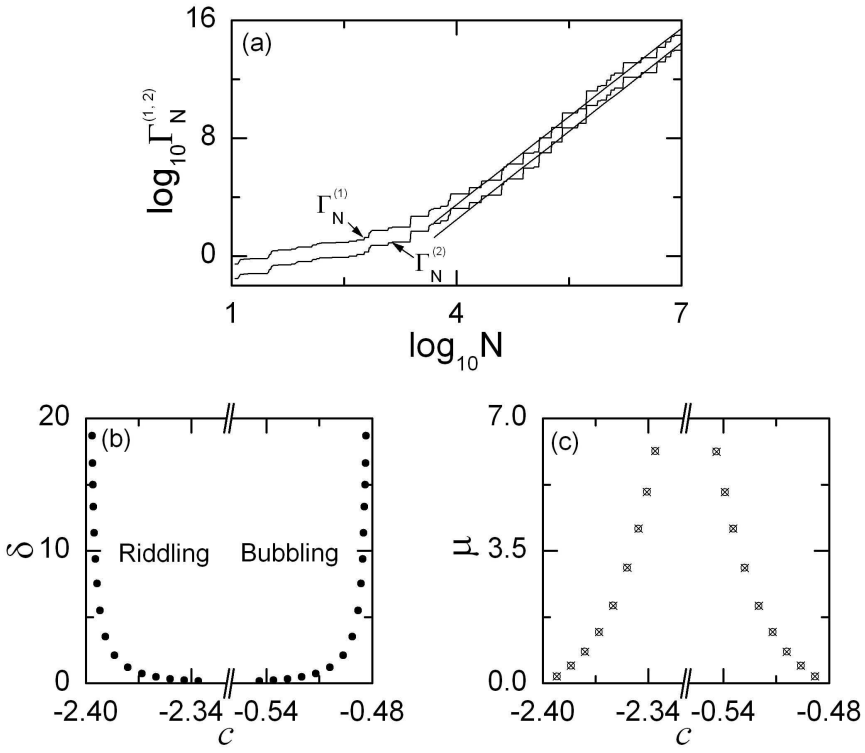

Figure 2.33: Parameter sensitivity for $a = 1.8$ in mutually coupled Hénon maps with $\alpha = 0.75$. Parameter sensitivity functions $\Gamma_N^{(1)}$ and $\Gamma_N^{(2)}$, exhibiting asymptotic power-law behaviors are shown in (a) for $c = -0.49$. They are well fitted with straight lines with the slope $\delta \simeq 4.6$. (b) Plot of the parameter sensitivity exponents δ (solid circles) versus c. (c) Plot of the scaling exponents μ (open circles) for the average characteristic time versus c. They agree well the reciprocal of the parameter sensitivity exponents (crosses).

Here, the value of $\delta \simeq 4.6$ is a quantitative characteristic of the parameter sensitivity of the synchronous chaotic attractor for $c = -0.49$, and we call it the parameter sensitivity exponent.

In each regime of bubbling or riddling, we obtain the parameter sensitivity exponents by changing the coupling parameter c from the bubbling or riddling transition point to the blowout bifurcation point. However, the value of the parameter sensitivity exponent obtained in an ensemble containing 100 random initial points fluctuates a little, depending on the chosen ensemble. Hence, it is necessary to consider many ensembles for obtaining a better statistics. From our extensive numerical simulations, we find that it is enough

to consider about 100 ensembles for each c, each of which contains 100 randomly chosen initial orbit points. Thus, we choose the average value of the 100 parameter sensitivity exponents obtained in the 100 ensembles. Figure 2.33(b) shows the plot of such averaged parameter sensitivity exponents (denoted by solid circles) versus c. Note that the parameter sensitivity exponent δ monotonically increases as c is varied away from the bubbling or riddling transition point, and tends to infinity as c approaches the blowout bifurcation point. This increase in the parameter sensitivity of the synchronous chaotic attractor is caused by the increase in the strength of local transverse repulsion of periodic repellers embedded in the synchronous chaotic attractor. After the blowout bifurcation, the weakly stable synchronous chaotic attractor becomes transversely unstable, and hence a complete desynchronization occurs.

In terms of the parameter sensitivity exponents, we characterize the parameter-mismatching effect on the bubbling and riddling of a weakly stable synchronous chaotic attractor. In the presence of parameter match, the weakly stable synchronous chaotic attractor is transformed into a bubbling attractor or a chaotic transient, depending on the global dynamics. For this case the quantity of interest is the average time τ spent near the synchronization plane. For the case of the bubbling attractor, τ is the average interburst time, while for the case of the chaotic transient, τ is its average lifetime. As c is varied from the bubbling or riddling transition point, τ becomes short because the strength of local transverse repulsion of periodic repellers embedded in the synchronous chaotic attractor increases.

For the case of bubbling, a typical trajectory on the bubbling attractor exhibits a persistent intermittent bursting, in which long episodes of nearly synchronous evolution are occasionally interrupted by short-term bursts. To characterize the intermittent bursting, we use a small quantity d_b^* for the threshold value of the magnitude of the deviation from the synchronization plane, d_n $[\equiv (|u_n^{(1)}| + |u_n^{(2)}|)/2]$, such that for $d_n < d_b^*$ the bubbling attractor is in the laminar phase, where a typical trajectory exhibits nearly synchronous motion, and for $d_n \geq d_b^*$ it is in the bursting phase. Here d_b^* is very small compared to the maximum bursting amplitude and it is the maximum deviation from the synchronization plane that may be acceptable in the context of synchronization. For each c, we follow a trajectory starting from a random initial orbit point until 50,000 laminar phases are obtained, and then we get the average laminar length τ (i.e., the average interburst interval) that scales

with ε as [14]

$$\tau \sim \varepsilon^{-\mu}. \tag{2.65}$$

The plot of μ (denoted by open circles) versus c is shown in Fig. 2.33(c). As c increases, the value of μ decreases, because the average laminar length shortens.

For each c in the regime of riddling, we consider an ensemble of trajectories starting from 1000 randomly chosen initial points on the synchronization plane, and obtain the average lifetime of the chaotic transients. A trajectory may be regarded as having escaped once the magnitude of deviation d_n from the synchronization plane becomes larger than a threshold value d_c^* such that an orbit point with $d > d_c^*$ lies sufficiently outside the basin of the synchronous chaotic attractor. Thus, the average lifetime τ is found to exhibit a power-law scaling behavior as in Eq. (2.65). The plot of the scaling μ (denoted by open circles) versus c is given in Fig. 2.33(c). As c decreases toward the blowout bifurcation point, the average lifetime shortens, and hence the value of μ decreases.

For both the bubbling and riddling cases, a reciprocal relation between the the scaling exponent μ and the parameter sensitivity exponent δ is derived and numerically confirmed. For a given ε, consider a trajectory starting from a randomly chosen initial orbit point on the synchronization plane. Then, from Eqs. (2.20)-(2.64) the "average" deviation of the trajectory from the synchronization plane after N iterations can be obtained for sufficiently small ε:

$$d_N = \frac{1}{2}(|u_N^{(1)}| + |u_N^{(2)}|) \sim (\Gamma_N^{(1)} + \Gamma_N^{(2)})\,\varepsilon \sim N^{\delta}\varepsilon. \tag{2.66}$$

Then, the "average" characterization time τ at which the magnitude of the deviation d_τ becomes the threshold value $d_{b,c}^*$ (i.e., $d_\tau = d_{b,c}^*$) is given by

$$\tau \sim \varepsilon^{-1/\delta}. \tag{2.67}$$

Hence, the scaling exponent μ for τ becomes just the reciprocal of the parameter sensitivity exponent δ,

$$\mu = 1/\delta, \tag{2.68}$$

as in the case of the coupled 1D maps [12]. To confirm the reciprocal relation, the reciprocal values of numerically obtained δ (denoted by crosses) are plotted in Fig. 2.33(c), and we note that they agree well with the values of μ (denoted by open circles).

As a second example, we consider an invertible system of two coupled parametrically forced pendula [13]:

$$\begin{aligned} \dot{\mathbf{x}} &= \mathbf{F}(\mathbf{x},\mathbf{y}) = \mathbf{f}(\mathbf{x},a) + (1-\alpha)\, c\, \mathbf{g}(\mathbf{x},\mathbf{y}), \\ \dot{\mathbf{y}} &= \mathbf{G}(\mathbf{x},\mathbf{y}) = \mathbf{f}(\mathbf{y},b) + c\, \mathbf{g}(\mathbf{y},\mathbf{x}), \end{aligned} \tag{2.69}$$

where the overdot denotes the differentiation with respect to the time, $\mathbf{x} = (x^{(1)}, x^{(2)})$ and $\mathbf{y} = (y^{(1)}, y^{(2)})$ are state variables of the two subsystems, c is a coupling parameter between the subsystems, α $(0 \le \alpha \le 1)$ is a parameter tuning the degree of the asymmetry of coupling, and $\mathbf{g}(\mathbf{x},\mathbf{y})$ is a coupling function of the form,

$$\mathbf{g}(\mathbf{x},\mathbf{y}) = (g(x^{(1)}, y^{(1)}), g(x^{(2)}, y^{(2)})); \;\; g(x,y) = y - x. \tag{2.70}$$

Here, the uncoupled dynamics ($c = 0$) is governed by a parametrically forced pendulum,

$$\begin{aligned} \mathbf{f}(\mathbf{x},p) &= (x^{(2)}, f(x^{(1)}, x^{(2)}, p)); \\ f(x^{(1)}, x^{(2)}, p) &= -2\pi\beta\Omega\, x^{(2)} - 2\pi(\Omega^2 - p\cos 2\pi t)\sin 2\pi x^{(1)}, \end{aligned} \tag{2.71}$$

where $x^{(1)}$ is a normalized angle with range $x^{(1)} \in [0,1)$, $x^{(2)}$ is a normalized angular velocity, β is a normalized damping parameter, Ω is a normalized natural frequency of the unforced pendulum, p $(p = a, b)$ is a normalized driving amplitude of the vertical oscillation of the suspension point. As in two coupled Hénon maps, these two coupled pendula may also be used as a model for investigating the two-cluster dynamics in many globally coupled pendula.

The phase space of the coupled parametrically forced pendula is five dimensional with coordinates $x^{(1)}$, $x^{(2)}$, $y^{(1)}$, $y^{(2)}$, and t. Since the system is periodic in t, it is convenient to regard time as a circular coordinate in the phase space. We also consider the surface of section, the $x^{(1)}$- $x^{(2)}$-$y^{(1)}$-$y^{(2)}$ hypersurface at integer times (i.e., $t = m$, m: integer). Then, using the 4th-order Runge-Kutta method with a time step $h = 0.05$, we integrate Eq. (2.69) and follow a trajectory. This phase-space trajectory intersects the surface of section in a sequence of points. This sequence of points corresponds to a mapping on the 4D hypersurface. The map can be computed by stroboscopically sampling the orbit points $\mathbf{z}_m \equiv (x^{(1)}(m), x^{(2)}(m), y^{(1)}(m), y^{(2)}(m))$ at the discrete time m. We call the transformation $\mathbf{z}_m \to \mathbf{z}_{m+1}$ the Poincaré map, and write $\mathbf{z}_{m+1} = P(\mathbf{z}_m)$. This 4D Poincaré map P has a constant Jacobian determinant of $e^{-4\pi\beta\Omega-(4-2\alpha)c}$.

As an example, we consider the 4D Poincaré map P for the unidirectionally coupled case of $\alpha = 1$ and fix the values of β and Ω at $\beta = 1.0$ and $\Omega = 0.5$. For the ideal

case without parameter mismatch (i.e., $a = b$), there exists an invariant synchronization plane, $x^{(1)} = y^{(1)}$ and $x^{(2)} = y^{(2)}$, in the $x^{(1)}$-$x^{(2)}$-$y^{(1)}$-$y^{(2)}$ phase space. However, in a real situation the parameter mismatch between the two subsystems is unavoidable, and hence the synchronization plane is no longer invariant. To take into consideration such a mismatching effect, we introduce a small mismatching parameter ε such that $b = a - \varepsilon$.

For $a = 0.85$, we investigate the parameter-mismatching effect by varying the coupling parameter c. For this case an synchronous chaotic attractor exists for $c > c_b \simeq 0.648$. As the coupling parameter c passes c_b, the synchronous chaotic attractor loses its transverse stability through a blowout bifurcation, and then a complete desynchronization occurs. In the regime of synchronization, a strongly stable synchronous chaotic attractor without parameter sensitivity exists for $c > c_t = 0.858\,688$, because all periodic saddles embedded in the synchronous chaotic attractor are transversely stable. However, as the coupling parameter c passes c_t, a bubbling transition occurs through the first transverse bifurcation of a periodic saddle, and then we have weak synchronization. Hence, only the attractor bubbling occurs in the regime of weak synchronization ($c_b < c < c_t$), as shown in Figs. 2.34(a) and 2.34(b) for $c = 0.67$ and $\varepsilon = 0.0001$. For this case, the weakly stable synchronous chaotic attractor exhibits a parameter sensitivity, because of local transverse repulsion of the periodic repellers embedded in the synchronous chaotic attractor.

Such parameter sensitivity of the weakly stable synchronous chaotic attractor for $\varepsilon = 0$ may be characterized by calculating the derivative of the transverse variable $\mathbf{u} = \mathbf{x} - \mathbf{y}$, denoting the deviation from the synchronization plane, with respect to ε (i.e. $\frac{\partial \mathbf{u}}{\partial \varepsilon}\big|_{\varepsilon=0} = \frac{\partial \mathbf{x}}{\partial \varepsilon}\big|_{\varepsilon=0} - \frac{\partial \mathbf{y}}{\partial \varepsilon}\big|_{\varepsilon=0}$). Using Eq. (2.69), we may obtain the following governing equation for $\frac{\partial \mathbf{u}}{\partial \varepsilon}\big|_{\varepsilon=0}$

$$\left.\frac{\partial \dot{\mathbf{u}}}{\partial \varepsilon}\right|_{\varepsilon=0} = r(\mathbf{x}^*)\left.\frac{\partial \mathbf{u}}{\partial \varepsilon}\right|_{\varepsilon=0} + \mathbf{f}_a(\mathbf{x}^*, a), \tag{2.72}$$

where $\frac{\partial \mathbf{u}}{\partial \varepsilon}\big|_{\varepsilon=0} = \left(\frac{\partial u^{(1)}}{\partial \varepsilon}\Big|_{\varepsilon=0}, \frac{\partial u^{(2)}}{\partial \varepsilon}\Big|_{\varepsilon=0}\right)$, the 2×2 matrix $r(\mathbf{x}^*)$ is given by

$$r(\mathbf{x}^*) \equiv \begin{pmatrix} -(2-\alpha)\, c\, h(x^{(1)*}) & 1 \\ f_{x^{(1)}}(x^{(1)}, x^{(2)}, a) & f_{x^{(2)}}(x^{(1)}, x^{(2)}, a) - (2-\alpha)\, c\, h(x^{(2)*}) \end{pmatrix}, \tag{2.73}$$

and

$$\mathbf{f}_a(\mathbf{x}^*, a) = \begin{pmatrix} 0 \\ f_a(x^{(1)}, x^{(2)}, a) \end{pmatrix}. \tag{2.74}$$

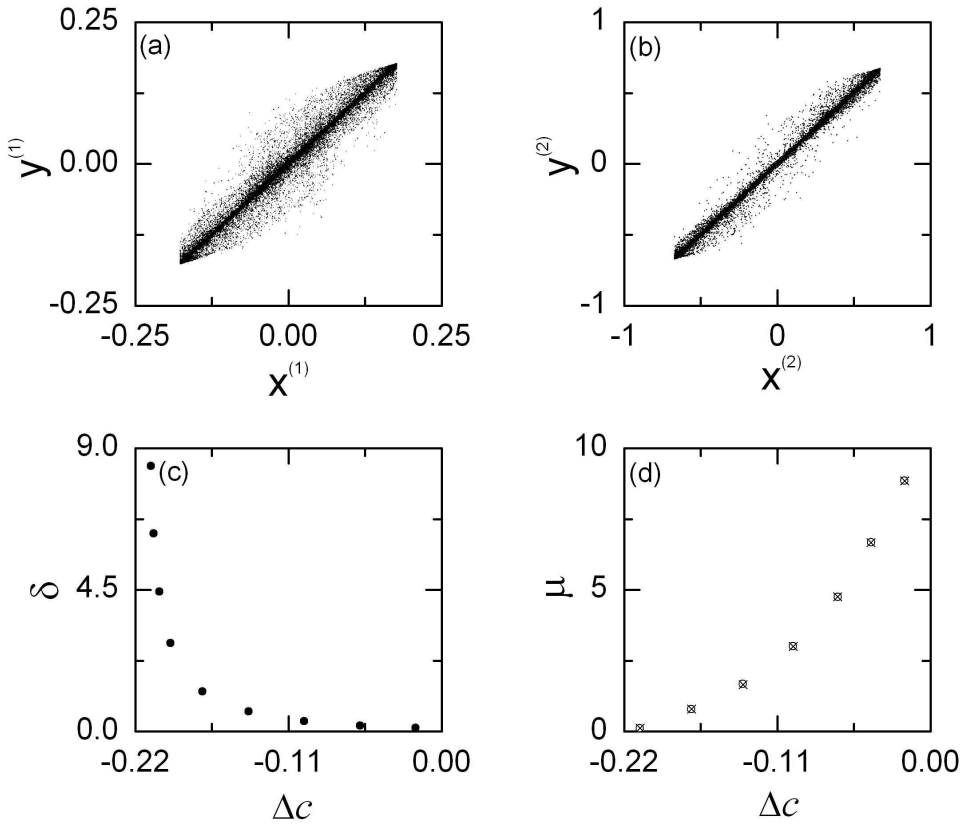

Figure 2.34: Effect of parameter mismatch on weak synchronization for $a = 0.85$ in the 4D Poincaré map of unidirectionally coupled pendula. For $c = 0.67$ and $\varepsilon = 0.0001$, projections of a bubbling attractor onto the (a) $x^{(1)} - y^{(1)}$ and (b) $x^{(2)} - y^{(2)}$ planes are given. In both (a) and (b), the initial orbit point is $(x^{(1)}, x^{(2)}, y^{(1)}, y^{(2)}) = (0.1, 0.3, 0.1, 0.3)$, the 5×10^3 points are computed before plotting, and the next 5×10^4 points are plotted. (c) Plot of the parameter sensitivity exponents δ (solid circles) versus $\Delta c = c - c_t$ for $a = 0.85$. (d) Plot of the scaling exponents μ (open circles) for the average interburst interval versus Δc for $a = 0.85$. They agree well the reciprocal of the parameter sensitivity exponents (crosses).

Here, $f_{x^{(1)}}$, $f_{x^{(2)}}$ and f_a are the derivatives of $f(x^{(1)}, x^{(2)}, a)$ with respect to $x^{(1)}$, $x^{(2)}$ and a, $\{(\mathbf{x}_n^*, \mathbf{y}_n^*)\}$ is a synchronous orbit with $\mathbf{x}_n^* = \mathbf{y}_n^*$ for $\varepsilon = 0$, and $h(x) \equiv \left.\frac{\partial g(x,y)}{\partial y}\right|_{y=x}$ is a reduced coupling function. Integrating the formula (2.72) along a synchronous trajectory starting from an initial orbit point $(\mathbf{x}_0^*, \mathbf{y}_0^*)$ on the synchronization plane and an initial value $\left.\frac{\partial \mathbf{u}}{\partial \varepsilon}\right|_{\varepsilon=0} = \mathbf{0}$ for $t = 0$, we may obtain derivatives $\mathbf{S}_n(\mathbf{x}^*) \equiv \left.\frac{\partial \mathbf{u}}{\partial \varepsilon}\right|_{\varepsilon=0}$ at all subsequent discrete time $t = n$. Then, following the same procedure as in the coupled Hénon maps, one can obtain the parameter sensitivity exponent δ of Eq. (2.64) which measures the degree of parameter sensitivity of the synchronous chaotic attractor.

In the regime of bubbling, we obtain the parameter sensitivity exponents by changing the coupling parameter c from the bubbling transition point c_t to the blowout bifurcation point c_b. As in the case of coupled Hénon maps, for obtaining a satisfactory statistics, we consider 100 ensembles for each c, each of which contains 20 randomly chosen initial orbit points on the synchronization plane and choose the average value of the 100 parameter sensitivity exponents obtained in the 100 ensembles. Figure 2.34(c) shows the plot of such parameter sensitivity exponents (denoted by solid circles) versus $\Delta c \equiv c - c_t$. Note that the parameter sensitivity exponent δ monotonically increases as c is varied away from the bubbling transition point, and tends to infinity as c approaches the blowout bifurcation point. This increase in the parameter sensitivity of the synchronous chaotic attractor is caused by the increase in the strength of local transverse repulsion of periodic repellers embedded in the synchronous chaotic attractor.

In terms of the parameter sensitivity exponents, we characterize the parameter-mismatching effect on the bubbling of a weakly stable synchronous chaotic attractor. For each c, we follow a trajectory starting from a random initial orbit point until 50,000 laminar phases are obtained, and then we find that the average laminar length τ exhibits a power-law scaling behavior as in Eq. (2.65). The plot of the scaling exponent μ (denoted by open circles) versus $\Delta c \equiv c - c_t$ is shown in Fig. 2.34(d). As c decreases from c_t, the value of μ decreases, because the average laminar length shortens. As in the case of coupled Hénon maps, the scaling exponent μ is given by the reciprocal of the parameter sensitivity exponent δ [see Eq. (2.68)]. To examine the reciprocal relation, the reciprocal values of numerically obtained δ (denoted by crosses) are plotted in Fig. 2.34(d). Note that they agree well with the values of μ (denoted by open circles), as in the preceding example of coupled Hénon maps.

So far, in both systems of mutually coupled Hénon maps with $\alpha = 0.75$ and unidirectionally coupled pendula with $\alpha = 1$, we have characterized the parameter-mismatching effect. Through Eq. (2.55) [Eq. (2.73)], one can easily see that the parameter sensitivity exponent for a given (a, c) in the case of $\alpha = 0.75$ ($\alpha = 1$) is the same as that for the value of $[a, 1.25c/(2-\alpha)]$ ($[a, c/(2-\alpha)]$) for any other case of α. Thus, the results of the parameter sensitivity exponents given in Fig. 2.33(b) [Fig. 2.34(c)] may be converted into those for the case of general α only by a scale change in the coupling parameter such that $c \to 1.25c/(2-\alpha)$ [$c \to c/(2-\alpha)$].

Finally, we confirm that the method of characterizing the noise sensitivity of the weakly stable synchronized chaotic attractor in terms of the noise sensitivity exponent may be generalized to the coupled systems consisting of the high-dimensional maps such as the Hénon map or the oscillators [22].

2.3 Dynamical Consequence of Blowout Bifurcations

We investigate the dynamical origin for the occurrence of asynchronous hyperchaos and chaos via blowout bifurcations in coupled chaotic systems [38]. An asynchronous hyperchaotic or chaotic attractor with a positive or negative second Lyapunov exponent appears through a blowout bifurcation. It is found that the sign of the second Lyapunov exponent of the newly-born asynchronous attractor, exhibiting on-off intermittency, is determined through competition between its laminar and bursting components. When the "strength" (i.e., a weighted second Lyapunov exponent) of the bursting component is larger (smaller) than that of the laminar component, an asynchronous hyperchaotic (chaotic) attractor appears.

2.3.1 Consequence of Blowout Bifurcations in Two Coupled 1D Maps

We investigate the dynamical origin for the appearance of asynchronous hyperchaotic and chaotic attractors via blowout bifurcations in a representative model system of two coupled 1D maps with a parameter α tuning the asymmetry of coupling. The asymmetric coupling naturally appears in the dynamics of two clusters for the case of global coupling [10], in which

each element is coupled to all the other elements with equal strength. Examples of globally coupled systems are laser arrays [89], Josephson junction arrays [90], cardiac pacemaker cells [91], flashing fireflies [92], and chirping crickets [93]. As a basic model, we consider N globally coupled 1D maps [46],

$$x_i(t+1) = f(x_i(t)) + \frac{\varepsilon}{N}\sum_{j=1}^{N}[f(x_j(t)) - f(x_i(t))], \tag{2.75}$$

where $x_i(t)$ is a state variable of the ith element at a discrete time t, the uncoupled dynamics ($\varepsilon = 0$) is governed by the 1D map $f(x) = 1 - ax^2$ with a control parameter a, and ε is a coupling parameter. For certain values of ε, full synchronization in which all elements exhibit the same temporal behaviors [i.e., $x_1(t) = \cdots = x_N(t)$] occurs. For other values of ε, the population of elements splits into groups with different dynamics. For example, in the case of two clusters, we have

$$x_{i_1}(t) = x_{i_2}(t) = \cdots = x_{i_{N_1}}(t) \equiv x_t, \quad x_{i_{N_1+1}}(t) = x_{i_{N_1+2}}(t) = \cdots = x_{i_N}(t) \equiv y_t, \tag{2.76}$$

where N_1 and N_2 ($= N - N_1$) represent the number of elements in the first and second clusters, exhibiting the x- and y-dynamics, respectively. This two-cluster state is a usual clustering to occur when the full synchronization breaks down. Under the condition (2.76), the system of globally coupled 1D maps is reduced to a system of two coupled 1D maps with a parameter p describing the distribution of elements between the two clusters [10],

$$x_{t+1} = f(x_t) + p\,\varepsilon\,[f(y_t) - f(x_t)], \quad y_{t+1} = f(y_t) + (1-p)\,\varepsilon\,[f(x_t) - f(y_t)], \tag{2.77}$$

where $p = N_2/N$ ($0 \le p \le 1$) denotes the fraction of the total population of elements in the second cluster. Note that an uneven distribution of elements between the two clusters causes an asymmetry in the coupling. Since the two coupled maps (2.77) are invariant under the interchange of x and y ($x \leftrightarrow y$) and a change of p ($p \to 1-p$), it is sufficient to consider only the case of $0 \le p \le 1/2$. Furthermore, through a transformation of parameters

$$p \to \frac{1-\alpha}{2-\alpha} \ \text{ and } \ \varepsilon \to (2-\alpha)\,c, \tag{2.78}$$

we obtain two coupled 1D maps T, which were used in our previous work [11],

$$T : \begin{cases} x_{t+1} = f(x_t) + (1-\alpha)\,c\,[f(y_t) - f(x_t)], \\ y_{t+1} = f(y_t) + c\,[f(x_t) - f(y_t)]. \end{cases} \tag{2.79}$$

Here, c is a coupling parameter and α ($0 \leq \alpha \leq 1$) is a parameter tuning the degree of asymmetry of coupling from symmetric coupling ($\alpha = 0$) to unidirectional coupling ($\alpha = 1$). Consequently, Eq. (2.79) may be used as a model map for studying a transition from full synchronization to two-cluster dynamics in globally coupled systems.

The coupled map T has an invariant synchronization line $x = y$. If an orbit lies on this invariant diagonal, then it is called a synchronous orbit because the state variables x_t and y_t become the same for all t; otherwise it is called an asynchronous orbit. For the accuracy of numerical calculations [1], we introduce new coordinates, u and v,

$$u = \frac{x+y}{2}, \quad v = \frac{x-y}{2}. \tag{2.80}$$

Under the coordinate change, the invariant diagonal $x = y$ is transformed into a new invariant line $v = 0$. In these new coordinates, the coupled map T of Eq. (2.79) becomes

$$T : \begin{cases} u_{t+1} = 1 - a(u_t^2 + v_t^2) - 2a\,\alpha\,c\,u_t v_t, \\ v_{t+1} = -2a[1 - (2-\alpha)\,c\,]u_t v_t. \end{cases} \tag{2.81}$$

From now on, we investigate the dynamical origin for the occurrence of asynchronous hyperchaos and chaos via blowout bifurcations in the new map T by varying the asymmetry parameter α.

We also note that the coupled map T is noninvertible, because its Jacobian determinant $\det(DT)$ (DT is the Jacobian matrix of T) becomes zero along the critical curves, $C_0 = \{(u, v) \in R^2 : u = v \text{ or } u = -v\}$. Critical curves of rank k, C_k ($k = 1, 2, \ldots$), are then given by the images of C_0 [i.e., $C_k = T^k(C_0)$]. Segments of these critical curves can be used to bound a compact region of the phase space that acts as a trapping bounded vessel, called an absorbing area $\mathcal{A}$, inside which trajectories bursting away from the invariant line

[1] When the magnitude of a transverse variable d of an asynchronous trajectory, representing the deviation from the invariant synchronization line, is less than a threshold value $\tilde{d}$, the computed trajectory falls into an exactly synchronous state due to a finite precision. In the system of coordinates x and y, the order of magnitude of the threshold value $\tilde{d}$ for d ($= |x - y|$) is about 10^{-15} except the region near the origin, because the double-precision values of x and y have about 15 decimal places of precision. On the other hand, in the system of u and v, the order of magnitude of the threshold value $\tilde{d}$ for $d (= |v|)$ is about 2.2×10^{-308}, which is a threshold value for the numerical underflow in the double-precision calculation. Hence, in the system of u and v, we can follow a trajectory until its length becomes sufficiently long for the calculation of Lyapunov exponents of an asynchronous attractor.

$v = 0$ are confined [82, 84]. Furthermore, boundaries of such an absorbing area can also be obtained by the union of segments of critical curves and portions of unstable manifolds of unstable periodic orbits. For this case, $\mathcal{A}$ is called a mixed absorbing area. We note that the consequence of the blowout bifurcation of the synchronized chaotic attractor depends on the existence of an absorbing area, controlling the global dynamics. In the presence of an absorbing area, an asynchronous attractor within this absorbing area is born through a supercritical blowout bifurcation. However, in the absence of an absorbing area, an abrupt change from the synchronized state occurs via a subcritical blowout bifurcation, because almost all points near the invariant line $v = 0$ eventually move away and never return.

With increase of the control parameter a, the coupled map T exhibits an infinite sequence of period-doubling bifurcations of synchronous attractors with period 2^n ($n = 0, 1, 2, \ldots$), ending at the accumulation point a_∞ ($= 1.401\,155\cdots$), in some region of c. This period-doubling cascade leads to creation of the synchronized chaotic attractor on the invariant line $v = 0$. With further increase of a past a_∞, a sequence of band-merging bifurcations of the synchronized chaotic attractor takes place. Hereafter, we fix the value of a as $a = 1.97$, where a single-band synchronized chaotic attractor exists on the invariant $v = 0$ line, as shown in Fig. 2.35(a). The longitudinal stability of trajectories on the synchronized chaotic attractor against perturbation along the $v = 0$ line is determined by its longitudinal Lyapunov exponent

$$\sigma_{||} = \lim_{N\to\infty} \frac{1}{N} \sum_{t=1}^{N} \ln |2au_t|, \tag{2.82}$$

which is just the Lyapunov exponent in the uncoupled 1D map. For $a = 1.97$, we have $\sigma_{||} = 0.6157$. On the other hand, the transverse stability of the synchronized chaotic attractor against perturbation across the $v = 0$ line is determined by its transverse Lyapunov exponent, which for the map T is given by

$$\sigma_\perp = \sigma_{||} + \ln |1 - 2s|, \tag{2.83}$$

where s [$\equiv (1 - \alpha/2)c$] is a scaled coupling parameter. A plot of $\sigma_\perp$ versus s is shown in Fig. 2.35(b). If s is relatively large such that $\sigma_{||} < -\ln(1 - 2s)$, then the synchronized chaotic attractor becomes transversely stable (i.e., its transverse Lyapunov exponent $\sigma_\perp$ is negative). Intuitively, this result seems to make sense since strongly coupled systems tend

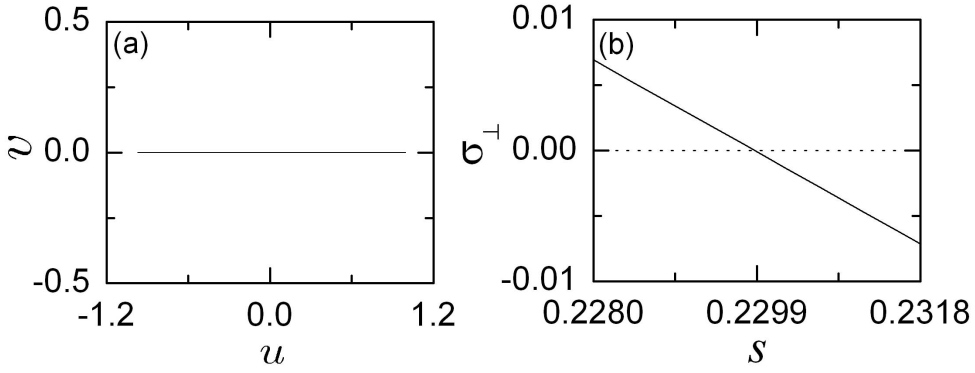

Figure 2.35: (a) One-band synchronized chaotic attractor on the invariant line $v = 0$ for $a = 1.97$ and $s[\equiv (1 - \alpha/2)c] = 0.23$. (b) Plot of the transverse Lyapunov exponent $\sigma_\perp$ of the synchronized chaotic attractor versus the scaled coupling parameter s. As s decreases through a threshold value s^* ($\simeq 0.2299$), $\sigma_\perp$ becomes positive.

to synchronize. However, as s is decreased and passes a threshold value s^*,

$$s^* = \frac{1}{2}(1 - e^{-\sigma_{||}}), \tag{2.84}$$

the transverse Lyapunov exponent $\sigma_\perp$ of the synchronized chaotic attractor becomes positive. For $a = 1.97$, we have $s^* \simeq 0.2299$. Consequently, when passing s^*, the synchronized chaotic attractor becomes transversely unstable, and then an asynchronous attractor, filling an absorbing area, is born through a supercritical blowout bifurcation.

To determine the type of a newly-born asynchronous attractor, its Lyapunov exponents are numerically calculated as follows. We choose a random initial orbit point with uniform probability in the range of $u \in (1 - a, 1)$ on a line $v = \varepsilon$ ($\varepsilon = 10^{-6}$) near the invariant line $v = 0$ and follow the trajectory until its length L becomes 10^8 [2]. Then we obtain the Lyapunov exponents through the Gram-Schmidt reorthonormalization (GSR) procedure

[2]Due to the finite numerical precision, the computer compiler regards very small (nonzero) numbers as zeros when their magnitudes are less than a threshold value r^* for numerical underflow [$r^* \simeq 2.2 \times 10^{-308}$ for IEEE (Institute of Electrical and Electronics Engineers) double precision]. Once the magnitude of the transverse variable v becomes less than r^*, the computed trajectory falls into an exactly synchronous state ($v = 0$), and further bursting from the $v = 0$ line cannot occur. As s approaches s^* from below, the probability of occurrence of such a synchronous state increases. For this case, we choose another random initial orbit points and repeat the procedure for calcualting the Lyapunov exponents until a trajectory segment of length L ($= 10^8$) is obtained.

[94]. For a trajectory segment, we consider the evolution of a set of two orthonormal tangent vectors $\{\mathbf{z}_t^{(1)}, \mathbf{z}_t^{(2)}\}$ along the trajectory $\{\mathbf{w}_t\,[\equiv (u_t, v_t)]\}$ $(t = 0, 1, 2, \ldots)$. By an application of the linearized map $DT(\mathbf{w}_t)$ (i.e., Jacobian matrix of T at the orbit point $\mathbf{w}_t$) on $\{\mathbf{z}_t^{(1)}, \mathbf{z}_t^{(2)}\}$, we obtain a set of two evolved tangent vectors, $\{DT(\mathbf{w}_t)\mathbf{z}_t^{(1)}, DT(\mathbf{w}_t)\mathbf{z}_t^{(2)}\}$. At each time step, we replace the evolved tangent vectors with a new set of reorthonormalized tangent vectors $\{\mathbf{z}_{t+1}^{(1)}, \mathbf{z}_{t+1}^{(2)}\}$ using the GSR method:

$$\mathbf{z}_{t+1}^{(1)} = \frac{DT(\mathbf{w}_t)\mathbf{z}_t^{(1)}}{d_{t+1}^{(1)}}, \quad \mathbf{z}_{t+1}^{(2)} = \frac{\mathbf{q}_{t+1}^{(2)}}{d_{t+1}^{(2)}}, \tag{2.85}$$

$$d_{t+1}^{(1)} = ||DT(\mathbf{w}_t)\mathbf{z}_t^{(1)}|| = \sqrt{< DT(\mathbf{w}_t)\mathbf{z}_t^{(1)}, DT(\mathbf{w}_t)\mathbf{z}_t^{(1)} >}, \tag{2.86}$$

$$d_{t+1}^{(2)} = ||\mathbf{q}_{t+1}^{(2)}|| = \sqrt{< \mathbf{q}_{t+1}^{(2)}, \mathbf{q}_{t+1}^{(2)} >}, \tag{2.87}$$

$$\mathbf{q}_{t+1}^{(2)} = DT(\mathbf{w}_t)\mathbf{z}_t^{(2)} - <DT(\mathbf{w}_t)\mathbf{z}_t^{(2)}, \mathbf{z}_{t+1}^{(1)}> \mathbf{z}_{t+1}^{(1)}, \tag{2.88}$$

where $<\,,\,>$ denotes the inner product of two vectors and $d_{t+1}^{(1)}$ ($d_{t+1}^{(2)}$) represents the length of the evolved first vector (the component of the evolved second vector orthogonal to the evolved first vector, i.e., $\mathbf{q}_{t+1}^{(2)}$). Note that the GSR never affects the direction of the first vector $\mathbf{z}_{t+1}^{(1)}$ and the second vector $\mathbf{z}_{t+1}^{(2)}$ is orthogonal to $\mathbf{z}_{t+1}^{(1)}$. Through this GSR procedure, we numerically calculate the first and second Lyapunov exponents σ_1 and σ_2 of a trajectory segment with length L,

$$\sigma_1 = \frac{1}{L}\sum_{t=0}^{L-1} r_t^{(1)}, \quad r_t^{(1)} = \ln d_{t+1}^{(1)}, \tag{2.89}$$

$$\sigma_2 = \frac{1}{L}\sum_{t=0}^{L-1} r_t^{(2)}, \quad r_t^{(2)} = \ln d_{t+1}^{(2)}, \tag{2.90}$$

where $r_t^{(1)}$ ($r_t^{(2)}$) denotes the rate of exponential growth of the length of the first vector (the component of the evolved second vector orthogonal to the evolved first vector) at the time t. In this way, we obtain an approximation for the first and second Lyapunov exponents of the asynchronous attractor born through the blowout bifurcation.

Figures 2.36(a) and 2.36(b) show σ_1 and σ_2 of the asynchronous attractors born through blowout bifurcations for $\alpha = 0$ (up triangles), 0.852 (crosses), and 1 (down triangles). For the case of unidirectional coupling ($\alpha = 1$), σ_1 is just the longitudinal Lyapunov exponent $\sigma_{||}$ of the synchronized chaotic attractor. On the other hand, as α is decreased toward zero, the value of σ_1 becomes smaller [see Fig. 2.36(a)]. However, σ_1 is always positive for all α.

For this case, the type of the asynchronous attractor with $\sigma_1 > 0$ is determined through the sign of σ_2. For the symmetric coupling case ($\alpha = 0$), the asynchronous attractor is hyperchaotic with $\sigma_2 > 0$. On the other hand, as α is increased from zero, the value of σ_2 decreases, eventually it becomes zero for a threshold value α^* ($\simeq 0.852$), and then it becomes negative [see Fig. 2.36(b)]. Hence, an asynchronous chaotic attractor with $\sigma_2 < 0$ appears for $\alpha > \alpha^*$. As examples for $\Delta s (= s - s^*) = -0.0016$, see Figs. 2.36(c) and 2.36(d) that show the asynchronous hyperchaotic ($\sigma_1 = 0.6087$ and $\sigma_2 = 0.0024$) and chaotic ($\sigma_1 = 0.6157$ and $\sigma_2 = -0.0028$) attractors when $\alpha = 0$ and 1, respectively.

As shown in Fig. 2.37, the time series of the variable d ($= |v|$) of typical trajectories on the newly-born asynchronous attractors exhibits on-off intermittency, in which long episodes of nearly synchronous evolution are occasionally interrupted by short-term bursts. To characterize the on-off intermittent time series, we use a small quantity d^* for the threshold value of d such that for $d < d^*$ the signal is considered to be in the laminar (off) state and for $d \geq d^*$ it is considered to be in the bursting (on) state. So far, statistical properties of such on-off intermittent attractors have been well characterized through investigation of the distribution of the laminar lengths and the scaling of the average laminar length and the average bursting amplitude [29, 30, 31, 32, 33, 34, 35].

However, although examples were given in previous works (e.g., see Refs. [24, 36, 37, 11]), the dynamical origin for the appearance of asynchronous hyperchaotic and chaotic intermittent attractors through blowout bifurcations remains unclear. Hence, we investigate the type of asynchronous intermittent attractors by varying the asymmetry parameter α. As explained above, a typical trajectory, exhibiting on-off intermittency, may be decomposed into its laminar and bursting components. Then the second Lyapunov exponent σ_2 of an asynchronous attractor [see Eq. (2.90) for the second Lyapunov exponent of a trajectory segment] can be given by the sum of the two weighted second Lyapunov exponents of the laminar and bursting components, Λ_2^l and Λ_2^b:

$$\sigma_2 = \Lambda_2^l + \Lambda_2^b \tag{2.91}$$

$$= \Lambda_2^b - |\Lambda_2^l|, \tag{2.92}$$

where the laminar component always has a negative weighted second Lyapunov exponent ($\Lambda_2^l < 0$). Here, the weighted second Lyapunov exponent Λ_2^i for each component ($i = l, b$) is

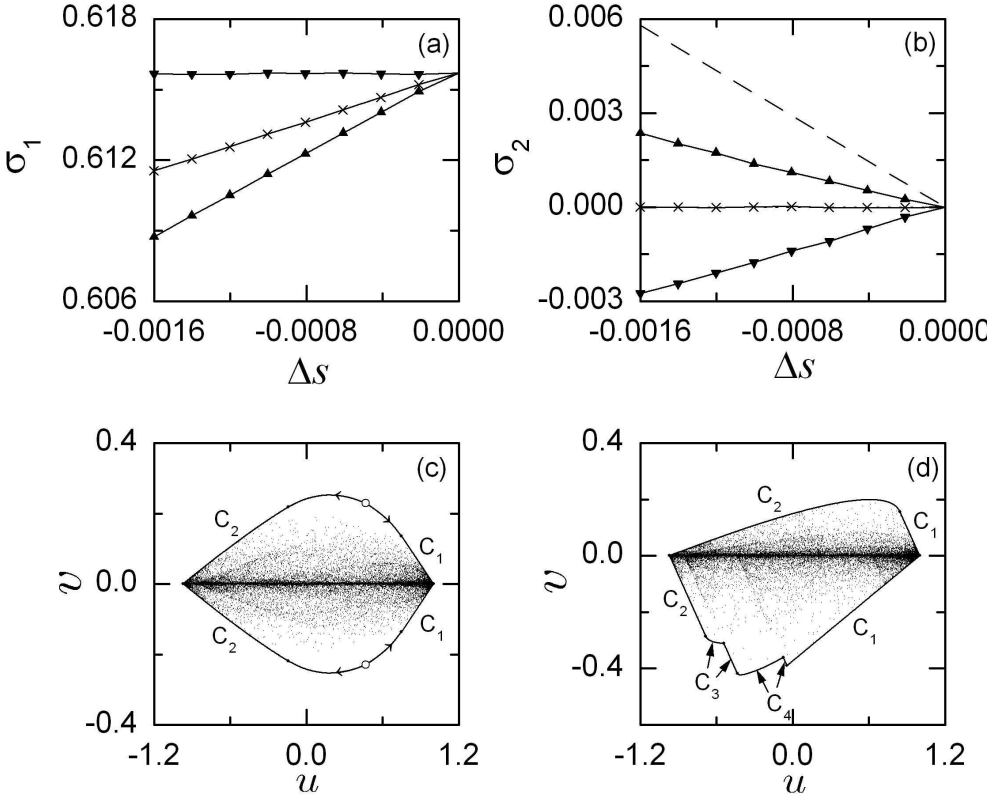

Figure 2.36: Plots of the (a) first (σ_1) and (b) second (σ_2) Lyapunov exponents of the newly-born asynchronous attractors born through supercritical blowout bifurcations versus the deviation Δs ($= s - s^*$) from the blowout bifurcation point s^* ($\simeq 0.2299$) for $a = 1.97$ with $\alpha = 0$ (up triangles), 0.852 (crosses), and 1 (down triangles). The length of a trajectory segment for the calculation of σ_1 and σ_2 is $L = 10^8$, and straight line segments between neighboring data symbols are plotted only to guide the eye. For reference, the transverse Lyapunov exponent of the synchronized chaotic attractor, $\sigma_\perp$, is represented by a dashed line in (b). For $\Delta s = -0.0016$, examples of (c) hyperchaotic ($\sigma_1 = 0.6087$ and $\sigma_2 = 0.0024$) and (d) chaotic ($\sigma_1 = 0.6157$ and $\sigma_2 = -0.0028$) attractors are given when $\alpha = 0$ and 1, respectively. In both (c) and (d), the initial orbit point is $(u_0, v_0) = (0.5, 0.01)$, 5×10^3 points are computed before plotting, and the next 4×10^4 points are plotted. In (c) segments of unstable manifolds (whose direction are denoted by arrows) of an asynchronous period-2 saddle (denoted by open circles) connect to segments of the critical curves C_k ($k = 1, 2$) (dots denote where these segments connect), and hence define a mixed absorbing area which a hyperchaotic attractor fills. In (d), a chaotic attractor fills an absorbing area bounded by segments of the critical curves C_k ($k = 1, 2, 3, 4$).

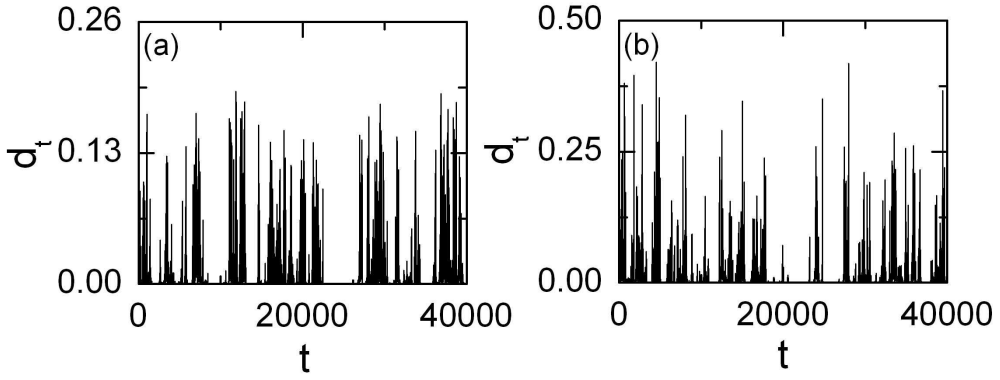

Figure 2.37: Time series of the variable $d(=|v|)$, representing the deviation from the invariant $v = 0$ line, for $a = 1.97$ and $\Delta s = -0.0016$ with (a) $\alpha = 0$ and (b) $\alpha = 1$. In both cases, the initial orbit point is $(u_0, v_0) = (0.5, 0.01)$.

given by the product of the fraction μ_i of time spent in the i state and its second Lyapunov exponent σ_2^i, i.e.,

$$\Lambda_2^i = \mu_i \sigma_2^i; \;\; \mu_i = \frac{L^i}{L}, \;\; \sigma_2^i = \frac{1}{L^i} {\sum_{t \in \, i \, \text{state}}}' r_t^{(2)} \;\; (i = l, b), \tag{2.93}$$

where L^i is the time spent in the i state for a trajectory segment of length L and the primed summation is performed in each i state. As can be seen in Eq. (2.92), the sign of σ_2 is determined through competition of the laminar and bursting components. Hence, when the strength (i.e., the weighted second Lyapunov exponent Λ_2^b) of the bursting component is larger (smaller) than that (i.e., $|\Lambda_2^l|$) of the laminar component, an asynchronous hyperchaotic (chaotic) attractor appears. We also note that the weighted Lyapunov exponents Λ_2^l and Λ_2^b depend on the threshold value d^*, although σ_2 is independent of d^*. With decreasing d^*, Λ_2^l decreases to zero because the time μ_l spent in the laminar state goes to zero; thus Λ_2^b $[= |\Lambda_2^l| + \sigma_2]$ converges to σ_2. Here, we again emphasize that σ_2, determining the type of asynchronous attractors, depends only on the difference between Λ_2^b and $|\Lambda_2^l|$, which is independent of d^* [see Eq. (2.92)]. Hence, although $\Lambda_2^{l(b)}$ depends on d^*, the conclusion as to the type of asynchronous attractors is independent of d^*. Hereafter, we fix the value of the threshold value of d at $d^* = 10^{-5}$.

Figures 2.38(a) and 2.38(b) show the strength of the bursting and laminar components, Λ_2^b and $|\Lambda_2^l|$, respectively. As mentioned above, the type of newly-born asynchronous attractor is determined through competition between the laminar and the bursting components as

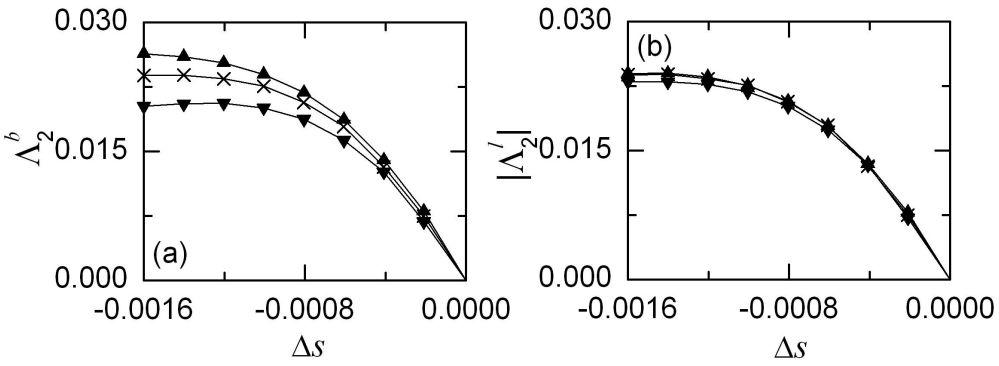

Figure 2.38: Plots of strength of the (a) bursting and (b) laminar components (i.e., (a) Λ_2^b and (b) $|\Lambda_2^l|$) versus Δs $(= s - s^*)$ for $a = 1.97$ with $\alpha = 0$ (up triangles), 0.852 (crosses), and 1 (down triangles). The threshold value of the variable $d(= |v|)$ is $d^* = 10^{-5}$, and straight line segments between neighboring data symbols are plotted just to guide the eye. Note that as α is increased from zero, Λ_2^b decreases, while $|\Lambda_2^l|$ is nearly independent of α.

follows. We first note that for $\alpha = 0$ (up triangles), the bursting component is dominant, because $\Lambda_2^b > |\Lambda_2^l|$. However, as α is increased from zero, Λ_2^b decreases, while $|\Lambda_2^l|$ is nearly independent of α. Eventually, for a threshold value α^* [$\simeq 0.852$ (crosses)], the strength of the bursting and laminar components becomes balanced (i.e., $\Lambda_2^b = |\Lambda_2^l|$), and then the laminar component becomes dominant for $\alpha > \alpha^*$ [e.g., $\alpha = 1$ (down triangles)], because $\Lambda_2^b < |\Lambda_2^l|$. Consequently, for $\alpha < \alpha^*$, there is a hyperchaotic attractor with $\sigma_2 > 0$, while for $\alpha > \alpha^*$, there is a chaotic attractor with $\sigma_2 < 0$.

The fraction $\mu_{l(b)}$ of the laminar (bursting) time [i.e., the time spent in the laminar (bursting) state] and the second Lyapunov exponent $\sigma_2^{l(b)}$ of the laminar (bursting) component are also given in Fig. 2.39. For the case of the laminar component, both μ_l and σ_2^l are nearly independent of α, and hence its weighted second Lyapunov exponent Λ_2^l $(= \mu_l \sigma_2^l)$ becomes nearly the same, independently of α. On the other hand, the second Lyapunov exponent σ_2^b of the bursting component decreases with increasing α from zero [$\alpha = 0$ (up triangles), 0.852 (crosses), and 1 (down triangles)], while its fraction μ_b [$= 1 - \mu_l$] of the bursting time is nearly independent of α. Consequently, the strength of the bursting component [i.e., $\Lambda_2^b (= \mu_b \sigma_2^b)$] becomes smaller as α is increased from zero. Thus, for a threshold value α^* ($\simeq 0.852$), the strength of the laminar and bursting components becomes balanced (i.e., $\Lambda_2^b = |\Lambda_2^l|$), and then a transition from asynchronous hyperchaos to chaos occurs.

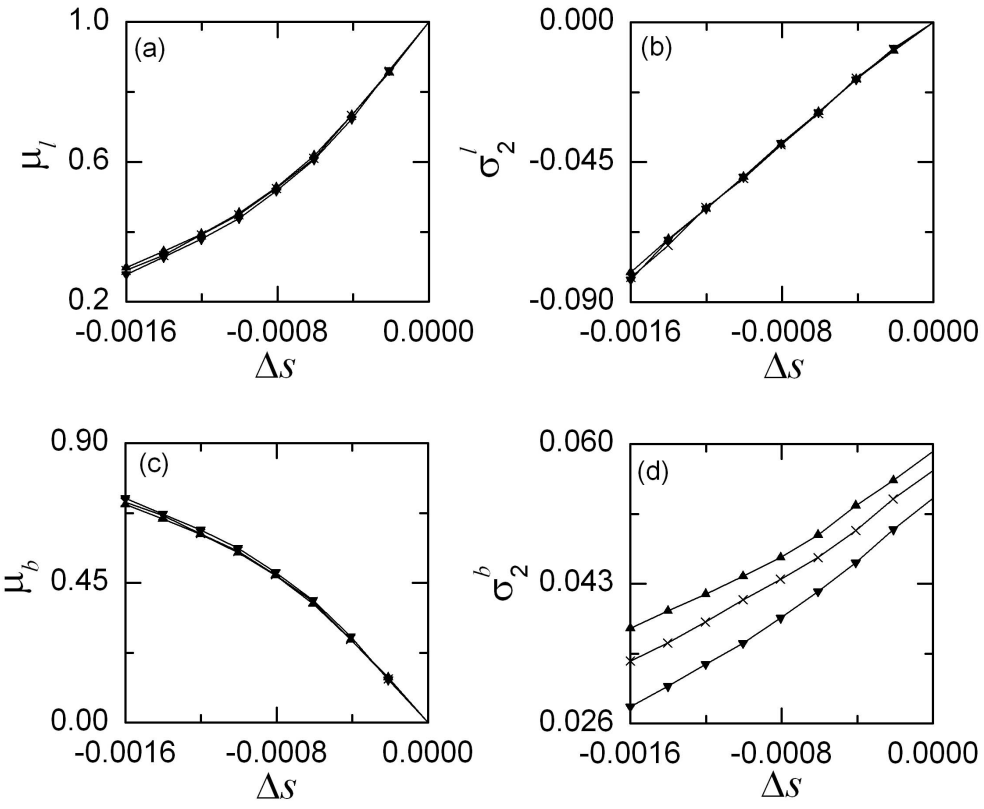

Figure 2.39: Plots of (a) [(c)] the fraction $\mu_{l(b)}$ of the laminar (bursting) time and (b) [(d)] the second Lyapunov exponent $\sigma_2^{l(b)}$ of the laminar (bursting) component versus Δs $(= s - s^*)$ for $a = 1.97$ with $\alpha = 0$ (up triangles), 0.852 (crosses), and 1 (down triangles). The threshold value of the variable $d(= |v|)$ is $d^* = 10^{-5}$, and straight line segments between neighboring data symbols are plotted only to guide the eye. Note that as α is increased from zero, σ_2^b decreases, while $\mu_{l(b)}$ and σ_2^l are nearly independent of α.

We believe that the transition we have found from a hyperchaotic to a chaotic asynchronous attractor can be understood as follows. After the blowout bifurcation, the asynchronous attractor includes an infinite number of asynchronous unstable periodic orbits that are off the invariant line $v = 0$. Some of these unstable periodic orbits have two positive Lyapunov exponents and some others have only one positive Lyapunov exponent. It is conjectured that as α increases from zero, the strength of the group of asynchronous unstable periodic orbits with negative second Lyapunov exponents might increase, which may result in the observed decrease in σ_2^b.

Finally, we discuss implication of the above results for the case of global coupling. The transition from synchronous chaos to asynchronous hyperchaos or chaos via a blowout bifurcation corresponds to a transition from a fully synchronized state to a two-cluster state in globally coupled 1D maps. Depending on the value of the parameter p (describing the distribution of elements between the two clusters), the intermittent two-cluster state is hyperchaotic or chaotic. The type of this intermittent two-cluster state may be determined through a competition between its laminar and bursting components. If the bursting (laminar) component becomes dominant, then a hyperchaotic (chaotic) two-cluster state appears.

2.3.2 Consequence of Blowout Bifurcations in High-Dimensional Invertible Systems

Since the (noninvertible) 1D map is a paradigm model for period-doubling dynamics in a large class of systems, the results obtained in the preceding section are of wider significance. As examples, we consider coupled Hénon maps [32] and coupled parametrically forced pendula [12] which are high-dimensional invertible systems exhibiting period doublings and find similar results.

First, we consider two coupled Hénon maps, often used as a representative model for the Poincaré map of coupled oscillators:

$$x_{t+1}^{(1)} = f(x_t^{(1)}) - y_t^{(1)} + (1-\alpha)\, c\, [f(x_t^{(2)}) - f(x_t^{(1)})], \tag{2.94}$$

$$y_{t+1}^{(1)} = b x_t^{(1)}, \tag{2.95}$$

$$x_{t+1}^{(2)} = f(x_t^{(2)}) - y_t^{(2)} + c\, [f(x_t^{(1)}) - f(x_t^{(2)})], \tag{2.96}$$

$$y_{t+1}^{(2)} = bx_t^{(2)}, \tag{2.97}$$

where $(x_t^{(i)}, y_t^{(i)})$ $(i = 1, 2)$ is a state vector of the ith subsystem at a discrete time t, $f(x) = 1 - ax^2$, c is a coupling parameter, α $(0 \leq \alpha \leq 1)$ is a parameter tuning the degree of asymmetry of coupling, and the Jacobian determinant of this system is b^2 $(|b| < 1)$. As in the case of two coupled 1D maps, the two coupled Hénon maps may also be used as a model system for studying the two-cluster dynamics in many globally coupled Hénon maps.

As in the coupled 1D maps, we introduce new coordinates for the accuracy of numerical calculations,

$$u^{(1)} = \frac{x^{(1)} + x^{(2)}}{2}, \quad u^{(2)} = \frac{y^{(1)} + y^{(2)}}{2}, \quad v^{(1)} = \frac{x^{(1)} - x^{(2)}}{2}, \quad v^{(2)} = \frac{y^{(1)} - y^{(2)}}{2}. \tag{2.98}$$

Then, the coupled Hénon maps of Eq. (2.97) become

$$u_{t+1}^{(1)} = 1 - a({u_t^{(1)}}^2 + {v_t^{(1)}}^2) - 2a\,\alpha\,c\,u_t^{(1)}v_t^{(1)} - u_t^{(2)}, \tag{2.99}$$

$$u_{t+1}^{(2)} = bu_t^{(1)}, \tag{2.100}$$

$$v_{t+1}^{(1)} = -2a[1 - (2 - \alpha)\,c\,]u_t^{(1)}v_t^{(1)} - v_t^{(2)}, \tag{2.101}$$

$$v_{t+1}^{(2)} = bv_t^{(1)}. \tag{2.102}$$

In this new map, we investigate the type of asynchronous intermittent attractors born via blowout bifurcations by varying the asymmetry parameter α when $b = 0.1$ and $a = 1.83$. Synchronous orbits lie on an invariant plane where $v^{(1)} = v^{(2)} = 0$. When the scaled coupling parameter s $[= (1 - \alpha/2)c]$ passes a threshold value s^* $(\simeq 0.1787)$, the synchronized chaotic attractor on the invariant plane becomes transversely unstable, because its largest transverse Lyapunov exponent becomes positive. Then, a new asynchronous attractor appears through a supercritical blowout bifurcation. To calculate the Lyapunov exponents of the newly-born asynchronous attractor, we choose a random value for $u_0^{(1)}$ with uniform probability in the range of $u_0^{(1)} \in (-0.5, 0.5)$ and follow a trajectory starting from an initial orbit point $(u_0^{(1)}, bu_0^{(1)}, \varepsilon, b\varepsilon)$ $(\varepsilon = 10^{-5})$ until its length L becomes 10^8. As shown in Fig. 2.40(a), the second Lyapunov exponent σ_2 of the asynchronous attractor depends on the asymmetry parameter α [$\alpha = 0$ (up triangles), 0.905 (crosses), and 1 (down triangles)]. There exists a threshold value α^* $(\simeq 0.905)$ such that for $\alpha < \alpha^*$ the asynchronous attractor is hyperchaotic with $\sigma_2 > 0$, while for $\alpha > \alpha^*$ it is chaotic with $\sigma_2 < 0$. Figures 2.40(b) and 2.40(c)

show examples of the asynchronous hyperchaotic and chaotic attractors for $\Delta s(= s - s^*) = -0.0016$ with $\alpha = 0$ and 1, respectively. As in the coupled 1D maps, we use a threshold value d^* $(= 10^{-4})$ for the variable d $[\equiv \frac{1}{2}(|v^{(1)}| + |v^{(2)}|)]$, representing the deviation from the invariant plane. When $d < d^*$, the system is said to be in the laminar (off) state, while for $d \geq d^*$ it is said to be in the bursting (on) state. We find that the type of an asynchronous intermittent attractor is determined through the competition between its laminar and bursting components [see Eq. (2.92)]. Figures 2.40(d) and 2.40(e) show the strength of the bursting and laminar components (i.e., Λ_2^b and $|\Lambda_2^l|$), respectively. Note that as α increases from zero [$\alpha = 0$ (up triangles), 0.905 (crosses), and 1 (down triangles)], Λ_2^b decreases, while $|\Lambda_2^l|$ is nearly independent of α. For $\alpha < \alpha^*$ ($\simeq 0.905$), the bursting component is dominant because $\Lambda_2^b > |\Lambda_2^l|$, and hence a hyperchaotic attractor with $\sigma_2 > 0$ appears. On the other hand, for $\alpha > \alpha^*$, a chaotic attractor with $\sigma_2 < 0$ appears because the laminar component becomes dominant (i.e., $\Lambda_2^b < |\Lambda_2^l|$).

As a second example, we consider a system of two coupled parametrically forced pendula:

$$\dot{x}_1 = y_1 + (1-\alpha)\, c\,(x_2 - x_1), \tag{2.103}$$

$$\dot{y}_1 = f(x_1, y_1, t) + (1-\alpha)\, c\,(y_2 - y_1), \tag{2.104}$$

$$\dot{x}_2 = y_2 + c\,(x_1 - x_2), \tag{2.105}$$

$$\dot{y}_2 = f(x_2, y_2, t) + c\,(y_1 - y_2), \tag{2.106}$$

where (x_i, y_i) $(i = 1, 2)$ is a state vector of the ith subsystem, $f(x, y, t) = -2\pi\beta\Omega y - 2\pi(\Omega^2 - A\cos 2\pi t)\sin 2\pi x$, x is a normalized angle with range $x \in [0, 1)$, y is a normalized angular velocity, the overdot denotes a derivative with respect to time t, β is a normalized damping parameter, Ω is a normalized natural frequency of the unforced pendulum, A is a normalized driving amplitude of the vertical oscillation of the suspension point, c is a coupling parameter, and α is a parameter tuning the degree of the asymmetry of coupling. As in two coupled 1D maps, these two coupled parametrically forced pendula may also be used as a model for investigating the two-cluster dynamics in many globally coupled pendula.

As in the coupled Hénon maps, we introduce new coordinates,

$$u_1 = \frac{x_1 + x_2}{2}, \quad u_2 = \frac{y_1 + y_2}{2}, \quad v_1 = \frac{x_1 - x_2}{2}, \quad v_2 = \frac{y_1 - y_2}{2}. \tag{2.107}$$

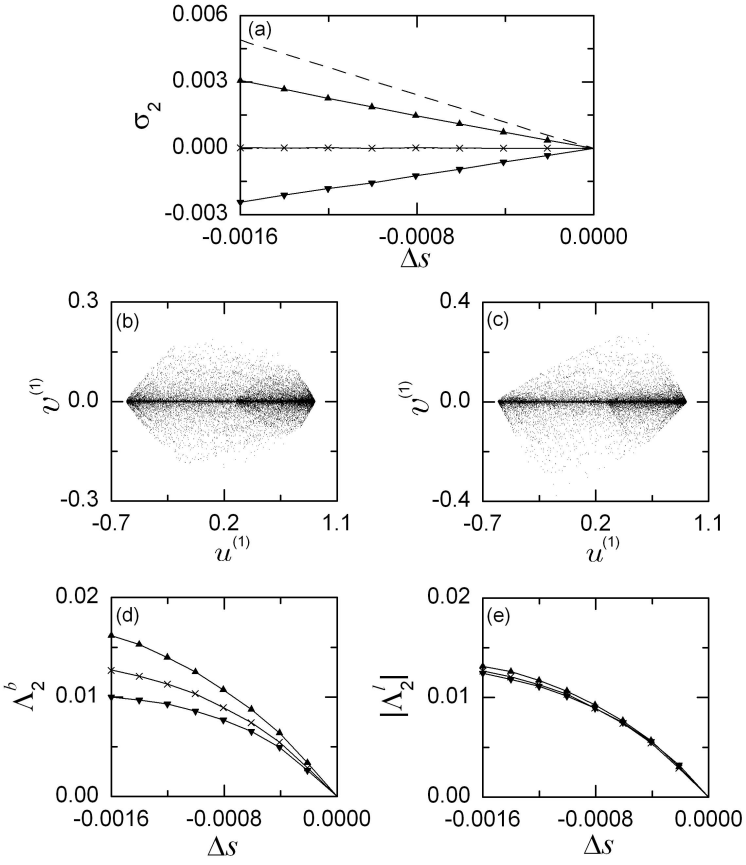

Figure 2.40: Consequence of blowout bifurcations in two coupled Hénon maps for $b = 0.1$ and $a = 1.83$. When the scaled coupling parameter s passes a threshold value s^* ($= 0.1787$), an intermittent asynchronous attractor is born via a blowout bifurcation. The length of a trajectory segment for the calculation of the Lyapunov exponents of the asynchronous attractor is $L = 10^8$ and the threshold value of the variable d [$= \frac{1}{2}(|v_1| + |v_2|)$], representing the deviation from the invariant plane, is $d^* = 10^{-4}$. (a) Plot of σ_2 versus Δs ($= s - s^*$) for $\alpha = 0$ (up triangles), 0.905 (crosses), and 1 (down triangles). The dashed line represents the largest transverse Lyapunov exponent of the synchronized chaotic attractor. Note that σ_2 depends on α. Projections of (b) hyperchaotic ($\sigma_1 = 0.4340$ and $\sigma_2 = 0.0031$) and (c) chaotic ($\sigma_1 = 0.4406$ and $\sigma_2 = -0.0024$) attractors onto the $u^{(1)} - v^{(1)}$ plane are given for $\Delta s = -0.0016$ with $\alpha = 0$ and 1, respectively. In both (b) and (c) the initial orbit point is $(u_0^{(1)}, u_0^{(2)}, v_0^{(1)}, v_0^{(2)}) = (0.5, 0.05, 0.01, 0.001)$, the 5×10^3 points are computed before plotting, and the next 5×10^4 points are plotted. Plots of Λ_2^b and $|\Lambda_2^l|$ versus Δs are also given in (d) and (e), respectively. The symbols are the same as those in (a). For $\alpha < \alpha^* (\simeq 0.905)$, $\Lambda_2^b > |\Lambda_2^l|$, while for $\alpha > \alpha^*$, $\Lambda_2^b < |\Lambda_2^l|$. In (a), (d), and (e), straight line segments between neighboring data symbols are plotted only to guide the eye.

Then, the equations of motion of Eq. (2.106) become

$$\dot{u}_1 = u_2 + \alpha\, c\, v_1, \tag{2.108}$$

$$\dot{u}_2 = -2\pi\beta\Omega u_2 - 2\pi(\Omega^2 - A\cos 2\pi t)\sin 2\pi u_1 \cos 2\pi v_1 + \alpha\, c\, v_2, \tag{2.109}$$

$$\dot{v}_1 = v_2 - (2-\alpha)\, c\, v_1, \tag{2.110}$$

$$\dot{v}_2 = -2\pi\beta\Omega v_2 - 2\pi(\Omega^2 - A\cos 2\pi t)\cos 2\pi u_1 \sin 2\pi v_1 - (2-\alpha)\, c\, v_2. \tag{2.111}$$

The phase space of the coupled parametrically forced pendula is five dimensional with coordinates u_1, u_2, v_1, v_2, and t. Since the system is periodic in t, it is convenient to regard time as a circular coordinate in the phase space. We also consider the surface of section, the u_1-u_2-v_1-v_2 hypersurface at integer times (i.e., $t = m$, m: integer). Then, using the 4th-order Runge-Kutta method with a time step $h = 0.02$, we integrate Eq. (2.111) and follow a trajectory. This phase-space trajectory intersects the surface of section in a sequence of points. This sequence of points corresponds to a mapping on the 4D hypersurface. The map can be computed by stroboscopically sampling the orbit points $\mathbf{w}_m$ $[\equiv (u_1(m), u_2(m), v_1(m), v_2(m))]$ at the discrete time m. We call the transformation $\mathbf{w}_m \to \mathbf{w}_{m+1}$ the Poincaré map, and write $\mathbf{w}_{m+1} = P(\mathbf{w}_m)$. This 4D Poincaré map P has a constant Jacobian determinant of $e^{-4\pi\beta\Omega - 4s}$, where s $[= (1-\alpha/2)c]$ is the scaled coupling parameter, and synchronous orbits lie on the invariant plane where $v_1 = v_2 = 0$.

As an example, we consider the 4D Poincaré map P for the case of $\beta = 1.0$, $\Omega = 0.5$, and $A = 0.85$. When the scaled coupling parameter s passes a threshold value s^* ($\simeq 0.324$), a new asynchronous attractor appears through a supercritical blowout bifurcation, as the synchronized chaotic attractor on the invariant plane becomes transversely unstable (i.e., its largest transverse Lyapunov exponent becomes positive). To calculate the Lyapunov exponents of the newly-born asynchronous attractor, we choose a random value for $u_1(0)$ $[u_2(0)]$ with uniform probability in the range of $u_1(0) \in (-0.15, 0.15)$ $[u_2(0) \in (-0.5, 0.5)]$ and follow a trajectory starting from an initial orbit point $(u_1(0), u_2(0), \varepsilon, \varepsilon)$ ($\varepsilon = 10^{-5}$) until its length L becomes 10^7. As shown in Fig. 2.41(a), the second Lyapunov exponent σ_2 of the asynchronous attractor depends on the asymmetry parameter α [$\alpha = 0$ (up triangles), 0.84 (crosses), and 1 (down triangles)]. For $\alpha < \alpha^*$ ($\simeq 0.84$), the asynchronous attractor is hyperchaotic with $\sigma_2 > 0$, while for $\alpha > \alpha^*$, it is chaotic with $\sigma_2 < 0$. Examples of asynchronous hyperchaotic and chaotic attractors for $\Delta s = -0.006$ with $\alpha = 0$ and 1

are given in Figs. 2.41(b) and 2.41(c), respectively. As in the coupled Hénon maps, the asynchronous attractor exhibits on-off intermittency, and hence its type may be determined through the competition between its laminar and bursting components [see Eq. (2.92)]. Figures 2.41(d) and 2.41(e) show the strength of the bursting and laminar components, Λ_2^b and $|\Lambda_2^l|$, respectively. We note that as α is increased from zero [$\alpha = 0$ (up triangles), 0.84 (crosses), and 1 (down triangles)], the strength of the bursting component (i.e., Λ_2^b) decreases, while the strength of the laminar component (i.e., $|\Lambda_2^l|$) is nearly independent of α. For $\alpha < \alpha^*$ ($\simeq 0.84$), $\Lambda_2^b > |\Lambda_2^l|$, and hence a hyperchaotic attractor with $\sigma_2 > 0$ appears. On the other hand, for $\alpha > \alpha^*$, a chaotic attractor with $\sigma_2 < 0$ appears because $\Lambda_2^b < |\Lambda_2^l|$.

2.4 Partial Synchronization in Three Coupled Chaotic Systems

We investigate the dynamical mechanism for the occurrence of partial synchronization in three coupled chaotic systems [47]. A completely synchronized attractor on the diagonal becomes transversely unstable via a blowout bifurcation, and then a two-cluster state, exhibiting on-off intermittency, appears on an invariant plane. If the newly-born two-cluster state is transversely stable, then partial synchronization occurs on the invariant plane; otherwise, complete desynchronization takes place. It is found that the transverse stability of the intermittent two-cluster state may be determined through the competition between its laminar and bursting components. When the laminar (bursting) component is dominant, partial synchronization (complete desynchronization) occurs through the blowout bifurcation.

2.4.1 Partial Synchronization in Three Coupled 1D Maps

We investigate the dynamical mechanism for the occurrence of partial synchronization in three coupled 1D maps with a parameter tuning the asymmetry in the coupling.

$$x_{t+1}^{(i)} = f(x_t^{(i)}) + \varepsilon\,[\sum_{j=1}^{3} p_j f(x_t^{(j)}) - f(x_t^{(i)})], \quad i = 1, 2, 3, \tag{2.112}$$

where $x_t^{(i)}$ is a state variable of the ith element at a discrete time t, the uncoupled dynamics ($\varepsilon = 0$) is governed by the 1D map $f(x) = 1 - ax^2$ with a control parameter a, ε is a coupling

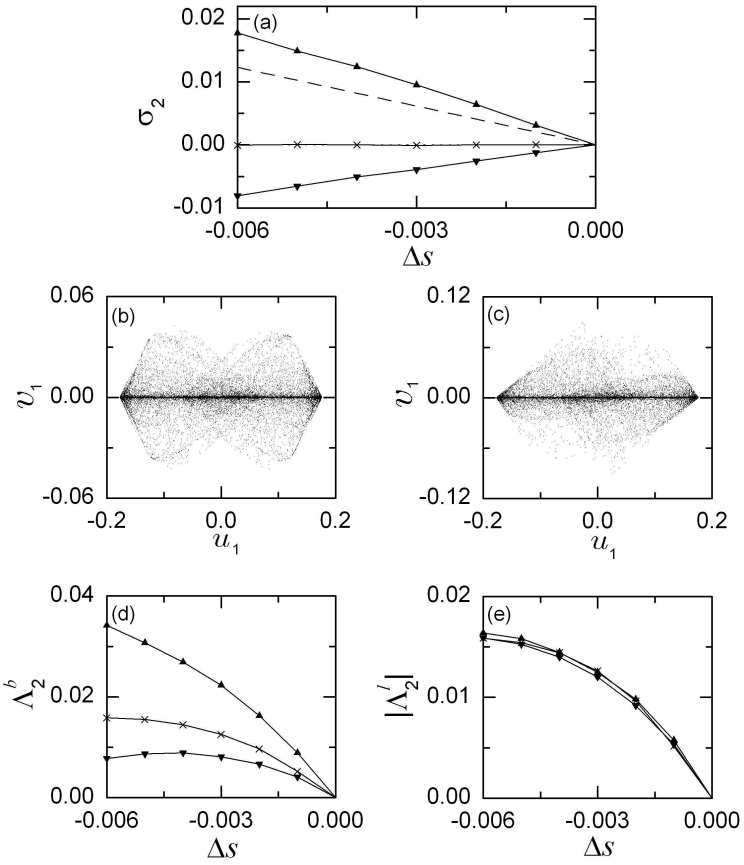

Figure 2.41: Consequence of blowout bifurcations in two coupled parametrically forced pendula for $\beta = 1.0$, $\Omega = 0.5$, and $A = 0.85$. When the scaled coupling parameter s passes a threshold value s^* ($\simeq 0.324$), an intermittent asynchronous attractor is born via a blowout bifurcation. The length of a trajectory segment for the calculation of the Lyapunov exponents of an asynchronous attractor in the 4D Poincaré map P is $L = 10^7$ and the threshold value of the variable d [$\equiv \frac{1}{2}(|v_1| + |v_2|)$], representing the deviation from the invariant plane, is $d^* = 10^{-4}$. (a) Plot of σ_2 versus Δs ($= s - s^*$) for $\alpha = 0$ (up triangles), 0.84 (crosses), and 1 (down triangles). The dashed line represents the largest transverse Lyapunov exponent of the synchronized chaotic attractor. Note that σ_2 depends on α. Projections of (b) hyperchaotic ($\sigma_1 = 0.628$ and $\sigma_2 = 0.017$) and (c) chaotic ($\sigma_1 = 0.648$ and $\sigma_2 = -0.008$) attractors onto the $u_1 - v_1$ plane are given for $\Delta s = -0.006$ with $\alpha = 0$ and 1, respectively. In both (b) and (c), the initial orbit point is $(u_1, u_2, v_1, v_2) = (0.1, 0.1, 0.01, 0.01)$, the 5×10^3 points are computed before plotting, and the next 3×10^4 points are plotted. Plots of Λ_2^b and $|\Lambda_2^l|$ versus Δs are also given in (d) and (e), respectively. The symbols are the same as those in (a). For $\alpha < \alpha^* (\simeq 0.84)$, $\Lambda_2^b > |\Lambda_2^l|$, while for $\alpha > \alpha^*$, $\Lambda_2^b < |\Lambda_2^l|$. In (a), (d), and (e), straight line segments between neighboring data symbols are plotted only to guide the eye.

parameter, and p_j denotes the coupling weight for the jth element ($\sum_{j=1}^{3} p_j = 1$). Here, the asymmetric coupling naturally appears when studying the three-cluster dynamics in an ensemble of N globally coupled 1D maps [46, 10, 42], where each 1D map is coupled to all the other ones with equal strength,

$$x_{t+1}^{(i)} = f(x_t^{(i)}) + \varepsilon[\frac{1}{N}\sum_{j=1}^{N} f(x_t^{(j)}) - f(x_t^{(i)})]. \tag{2.113}$$

For the case of three clusters with N_j elements in each jth cluster ($j = 1, 2, 3$), Eq. (2.113) is reduced to the three-coupled system of Eq. (2.112), where p_j ($= N_j/N$) represents the fraction of the total population of elements in the jth cluster. Two extreme cases of the unidirectional and symmetric couplings were previously considered. The unidirectionally coupled map with $p_2 = p_3 = 0$ (i.e., $p_1 = 1$), where the first drive subsystem with the state variable $x^{(1)}$ acts on the second and third response subsystems with the state variables $x^{(2)}$ and $x^{(3)}$, was studied in [40], and partial synchronization was observed to occur on an invariant plane via a supercritical blowout bifurcation of the fully synchronized attractor on the diagonal. On the other hand, a completely desynchronized 3D attractor appears through the supercritical blowout bifurcation for the case of symmetric coupling with $p_1 = p_2 = p_3 = 1/3$ [45]. To connect these two extreme cases, we consider a path with $p_2 = p_3 \equiv p$ ($0 \le p \le 1/3$) in the $p_2 - p_3$ plane, and then the parameter p tunes the degree of asymmetry in the coupling of Eq. (2.112) from the unidirectional coupling ($p = 0$) to the symmetric coupling ($p = 1/3$).

From now on, we investigate the dynamical origin for the occurrence of partial synchronization by varying the asymmetry parameter p in the three coupled 1D maps of Eq. (2.112) for $a = 1.95$. We first consider complete synchronization occurring in the case of strong coupling. Such complete synchronization is independent of p. Figures 2.42(a) and 2.42(b) show a fully synchronized attractor on the invariant diagonal for $\varepsilon = 0.5$. The longitudinal stability of a synchronized trajectory $\{x_t^* (= x_t^{(1)} = x_t^{(2)} = x_t^{(3)})\}$ on the attractor against the perturbation along the diagonal is determined by its longitudinal Lyapunov exponent

$$\sigma_{||} = \lim_{M\to\infty} \frac{1}{M}\sum_{t=0}^{M-1} \ln|f'(x_t^*)|, \tag{2.114}$$

where the prime represents the differentiation of f with respect to x. This longitudinal Lyapunov exponent is just the Lyapunov exponent of the 1D map f. For $a = 1.95$, we have

$\sigma_{||} = 0.5795$, and hence the attractor is a chaotic one. On the other hand, the transverse stability of the fully synchronized attractor against perturbation across the diagonal (i.e., asynchronous perturbation) is determined by its transverse Lyapunov exponent with a two-fold multiplicity,

$$\sigma_\perp = \sigma_{||} + \ln|1-\varepsilon|. \tag{2.115}$$

A plot of $\sigma_\perp$ versus ε is shown in Fig. 2.42(c). If ε is relatively large such that $\sigma_{||} < -\ln|1-\varepsilon|$, then the transverse Lyapunov exponent $\sigma_\perp$ is negative, and hence the fully synchronized attractor becomes transversely stable. However, as ε decreases and passes a threshold value ε^* $(= 0.4398)$, the fully synchronized attractor becomes transversely unstable, because the transverse Lyapunov exponent $\sigma_\perp$ becomes positive. Then, an asynchronous attractor, containing the diagonal, is born via a supercritical blowout bifurcation, but its type depends on the value of p.

In the unidirectionally coupled case with $p = 0$, a partially synchronized attractor appears via a supercritical blowout bifurcation on the invariant Π_{23} $(= \{(x^{(1)}, x^{(2)}, x^{(3)})|x^{(2)} = x^{(3)}\})$ plane, as shown in Figs. 2.43(a) and 2.43(b) for $\varepsilon = 0.42$. The partially synchronized attractor is a chaotic one with two longitudinal Lyapunov exponents $\sigma_{||,1}(= 0.5795)$ and $\sigma_{||,2}(= -0.014)]$, and it is transversely stable against the perturbation across the Π_{23} plane, because its transverse Lyapunov exponent $\sigma_\perp(= -0.014)$ is negative. On the other hand, for the symmetrically coupled case with $p = 1/3$, a completely desynchronized attractor, occupying a finite 3D volume, appears through a supercritical blowout bifurcation, as shown in Figs. 2.43(c) and 2.43(d) for $\varepsilon = 0.42$, and it is a hyperchaotic attractor with three positive Lyapunov exponents ($\sigma_1 = 0.539$, $\sigma_2 = 0.021$, and $\sigma_3 = 0.01$). Such complete desynchronization occurs because the two-cluster state on the Π_{23} plane, born via the supercritical blowout bifurcation, becomes transversely unstable, as will be shown below.

When the fully synchronized attractor on the diagonal becomes transversely unstable, a two-cluster state appears on the invariant Π_{23} plane through a supercritical blowout bifurcation. This two-cluster state satisfies $x_t^{(1)} \equiv X_t$ and $x_t^{(2)} = x_t^{(3)} \equiv Y_t$, and its dynamics is governed by a reduced 2D map,

$$X_{t+1} = f(X_t) + 2p\,\varepsilon[f(Y_t) - f(X_t)], \tag{2.116}$$

$$Y_{t+1} = f(Y_t) + (1-2p)\,\varepsilon[f(X_t) - f(Y_t)]. \tag{2.117}$$

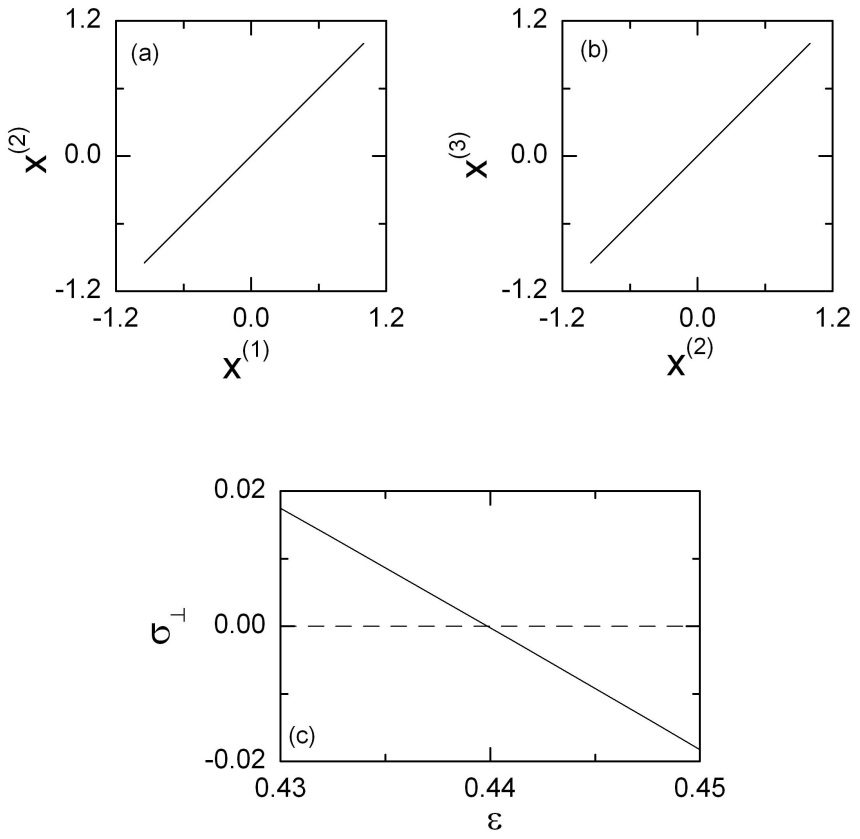

Figure 2.42: Projections of a fully synchronized attractor onto the (a) $x^{(1)} - x^{(2)}$ and (b) $x^{(2)} - x^{(3)}$ planes for $a = 1.95$ and $\varepsilon = 0.5$. (c) Plot of $\sigma_\perp$ (transverse Lyapunov exponent of the fully synchronized attractor) versus ε for $a = 1.95$. The data of $\sigma_\perp$ are represented by a solid line.

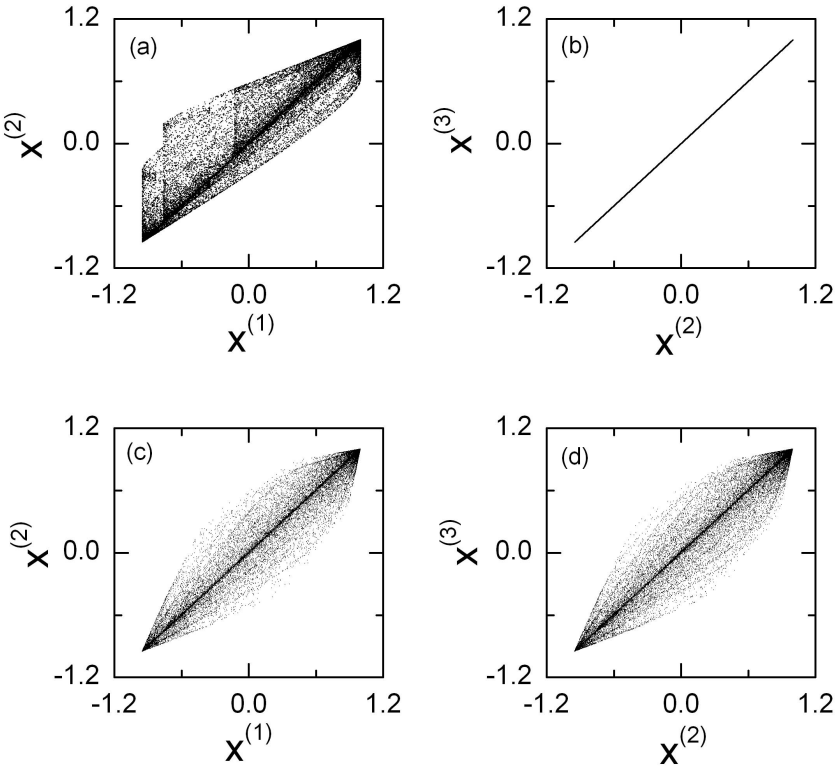

Figure 2.43: Projections of the partially synchronized attractor onto the (a) $x^{(1)} - x^{(2)}$ and (b) $x^{(2)} - x^{(3)}$ planes for $a = 1.95$ and $\varepsilon = 0.42$ in the unidirectionally coupled case with $p = 0$. Projections of the completely desynchronized attractor onto the (a) $x^{(1)} - x^{(2)}$ and (b) $x^{(2)} - x^{(3)}$ planes for $a = 1.95$ and $\varepsilon = 0.42$ in the symmetrically coupled case with $p = 1/3$.

For the accuracy of numerical calculations, we introduce new coordinates, U and V,

$$U = \frac{X + Y}{2}, \quad V = \frac{X - Y}{2}. \tag{2.118}$$

Then, the invariant diagonal is transformed into a new invariant line $V = 0$. In these new coordinates, the 2D reduced map of Eq. (2.117) becomes

$$U_t = 1 - a(U_t^2 + V_t^2) - 2\,a\,\varepsilon(1 - 4p)\,U_t V_t, \tag{2.119}$$

$$V_t = 2a(\varepsilon - 1)U_t V_t. \tag{2.120}$$

Figures 2.44(a) and 2.44(b) show the two-cluster states, born via supercritical blowout bifurcations, in the $U - V$ plane for the unidirectionally ($p = 0$) and symmetrically ($p = 1/3$) coupled cases, respectively. These two-cluster states are chaotic attractors in the reduced 2D map (i.e., they are chaotic attractors in the restricted Π_{23} plane). However, their transverse

stability against perturbation across the invariant Π_{23} plane depends on the value of p. Only when the two-cluster state is transversely stable, it becomes an attractor in the whole 3D space. To determine the transverse stability of a two-cluster state, we numerically follow a typical trajectory in the two-cluster state until its length L becomes 10^8, and then the transverse Lyapunov exponent for the trajectory segment with length L is given by

$$\sigma_\perp = \frac{1}{L} \sum_{t=0}^{L-1} \ln |(1-\varepsilon)\, f'(U_t - V_t)|. \tag{2.121}$$

A plot of $\sigma_\perp$ versus $\Delta\varepsilon$ ($= \varepsilon - \varepsilon^*$) is given in Fig. 2.44(c) [$p = 0$ (up triangles), 0.146 (crosses), and 1/3 (down triangles)], where ε^* ($= 0.4398$) is the blowout bifurcation point of the fully synchronized attractor. For the case of unidirectional coupling ($p = 0$), the two-cluster state is transversely stable, because its transverse Lyapunov exponent $\sigma_\perp$ is negative, and hence partial synchronization occurs on the Π_{23} plane via a supercritical blowout bifurcation (i.e., a partially synchronized attractor appears on the Π_{23} plane.). On the other hand, as p is increased from 0, the value of $\sigma_\perp$ increases, eventually it becomes zero for a threshold value $p^* (\simeq 0.146)$, and then it becomes positive. Hence, for $p^* < p \leq 1/3$, complete desynchronization takes place through a supercritical blowout bifurcation (i.e., a completely desynchronized 3D attractor appears), because the two-cluster on the Π_{23} plane becomes transversely unstable. Examples in Figs. 2.44(a) and 2.44(b) for $\Delta\varepsilon = -0.003$ show the transversely stable ($\sigma_\perp = -0.0027$) and unstable ($\sigma_\perp = 0.002$) two-cluster states for $p = 0$ and 1/3, respectively.

We now investigate the mechanism for the transition from partial synchronization to complete desynchronization by varying the asymmetry parameter p. A typical trajectory in the two-cluster state, born via a supercritical blowout bifurcation, exhibits on-off intermittency near the main diagonal. We use a small quantity d^* for the threshold value of the magnitude of the transverse variable d ($= |V|$) such that for $d < d^*$ the trajectory is considered to be in the laminar (off) state, where it exhibits a nearly synchronous motion, while for $d > d^*$ it is considered in the bursting (on) state. Thus, a typical trajectory may be decomposed into the laminar and bursting components. Then, dynamical properties of the two-cluster state may be understood through competition of the laminar and bursting components [38]. Here, we are concerned about the transverse stability of an intermittent two-cluster state. Its transverse Lyapunov exponent $\sigma_\perp$ [see Eq. (2.121) for the transverse

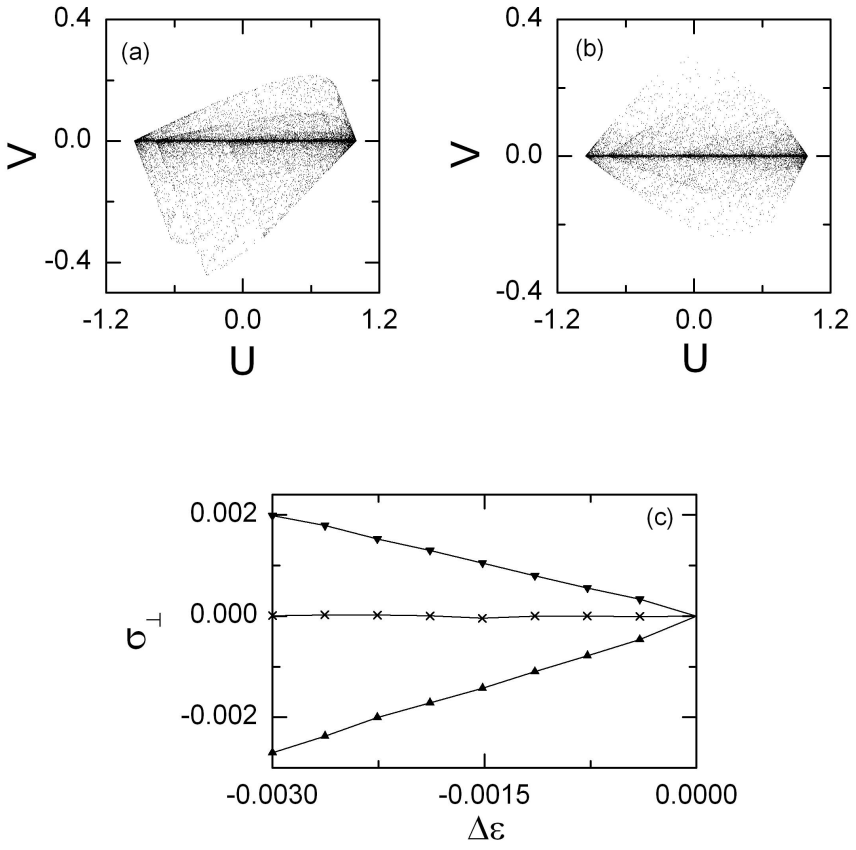

Figure 2.44: (a) Transversely stable ($\sigma_\perp = -0.0027$) two-cluster state for $p = 0$ and (b) transversely unstable ($\sigma_\perp = 0.002$) two-cluster for $p = 1/3$ in the $U - V$ plane when $a = 1.95$ and $\Delta\varepsilon$ $[= \varepsilon - \varepsilon^*(= 0.4398)] = -0.003$. (c) Plot of $\sigma_\perp$ (transverse Lyapunov exponent of the two-cluster state) versus $\Delta\varepsilon$ for $a = 1.95$ [$p = 0$ (up triangles), 0.146 (crosses), 1.3 (down triangles)]. Straight lines between the data symbols are plotted only to guide the eye.

Lyapunov exponent of a trajectory segment] can be given by the sum of the two weighted transverse Lyapunov exponents of the laminar and bursting components, $\Sigma_\perp^l$ and $\Sigma_\perp^b$:

$$\sigma_\perp = \Sigma_\perp^l + \Sigma_\perp^b \tag{2.122}$$

$$= \Sigma_\perp^b - |\Sigma_\perp^l|, \tag{2.123}$$

where the laminar component always has a negative weighted transverse Lyapunov exponent ($\Sigma_\perp^l < 0$). For each component ($i = l, b$), the weighted transverse Lyapunov exponent $\Sigma_\perp^i$ is given by the product of the fraction, μ_i, of time spent in the i state and its transverse

Lyapunov exponent $\sigma_\perp^i$, i.e.,

$$\Sigma_\perp^i = \mu_i \sigma_\perp^i; \;\; \mu_i = \frac{L_i}{L}, \;\; \sigma_\perp^i = \frac{1}{L_i} \sum_{t \in i \, \text{state}}{}' \ln |(1-\varepsilon) f'(U_t - V_t)| \;\; (i = l, b), \tag{2.124}$$

where L_i is the time spent in the i state for a trajectory segment of length L and the primed summation is performed in each i state. Then, the sign of $\sigma_\perp$ may be determined through competition between the laminar and bursting components [see Eq. (2.123)]. When the "transverse strength" of the laminar component [i.e., the magnitude of the weighted transverse Lyapunov exponent ($|\Sigma_\perp^l|$)] is larger (smaller) than that of the bursting component (i.e., $\Sigma_\perp^b$), partial synchronization (complete desynchronization) occurs, because the two-cluster becomes transversely stable (unstable).

Figures 2.45(a)-2.45(f) show the fraction $\mu_{l(b)}$ of the laminar (bursting) time (i.e., the time spent in the laminar (bursting) state), the transverse Lyapunov exponent $\sigma_\perp^{l(b)}$ of the laminar (bursting) component, and the weighted transverse Lyapunov exponent $\Sigma_\perp^{l(b)}$ of the laminar (bursting) component when the threshold value for the laminar state is $d^* = 10^{-4}$. For the case of the laminar component, both μ_l and $\sigma_\perp^l$ are nearly independent of p, and hence its weighted transverse Lyapunov exponent $\Sigma_\perp^l$ ($= \mu_l \sigma_\perp^l$) becomes nearly the same, irrespectively of p [see Figs. 2.45(a)-2.45(c)]. On the other hand, the transverse Lyapunov exponent $\sigma_\perp^b$ of the bursting component increases as p is increased from zero [see Fig. 2.45(e); $p = 0$ (up triangles), 0.146 (crosses), and 1/3 (down triangles)], although its fraction μ_b [$= 1 - \mu_l$] of the bursting time is nearly independent of p, as shown in Fig. 2.45(d). Hence, the transverse strength of the bursting component [i.e., $\Sigma_\perp^b (= \mu_b \sigma_\perp^b)$] becomes larger as p is increased from zero [see Fig. 2.45(f)]. For $p = 0$ (up triangles), the laminar component is dominant, because $|\Sigma_\perp^l| > \Sigma_\perp^b$. Hence, the two-cluster becomes transversely stable, and it becomes an attractor in the whole 3D phase space (i.e., partial synchronization occurs). However, as p is increased from zero, $\Sigma_\perp^b$ increases, while $|\Sigma_\perp^l|$ is nearly independent of p. Eventually, for a threshold value p^* [$\simeq 0.146$ (crosses)], the transverse strength of the bursting and laminar components becomes balanced (i.e., $\Sigma_\perp^b = |\Sigma_\perp^l|$), and then the bursting component becomes dominant for $p^* < p \leq 1/3$ [e.g., see the case of $p = 1/3$ (down triangles)], because $\Sigma_\perp^b > |\Sigma_\perp^l|$. Thus, when passing the threshold value p^*, a transition from partial synchronization to complete desynchronization occurs. Consequently, for $0 \leq p < p^*$, there exists a partially synchronized attractor with $\sigma_\perp < 0$ on the invariant Π_{23} plane (e.g., see Figs. 2.43(a) and

2.43(b) for $p = 0$), while for $p^* < p \leq 1/3$, a completely desynchronized 3D attractor appears (e.g., see Figs. 2.43(c) and 2.43(d) for $p = 1/3$) because the two-cluster on the Π_{23} plane is transversely unstable.

The above transition from a partially synchronized to a completely desynchronized attractor could be understood as follows. The newly-born intermittent two-cluster on the invariant Π_{23} plane includes an infinite number of asynchronous unstable periodic orbits that are off the invariant diagonal. Some of these unstable periodic orbits are transversely stable, while some others are transversely unstable. It is conjectured that as p is increased from zero, the strength of the group of asynchronous unstable periodic orbits with positive transverse Lyapunov exponents might increase, which may result in the observed increase in $\sigma_\perp^b$.

To sum up the main results of this section, we consider an intermittent two-cluster state born via a blowout bifurcation in the three-coupled 1D maps of Eq. (2.112) and show that the sign of its transverse Lyapunov exponent $\sigma_\perp$ of Eq. (2.121) can be determined through competition between the laminar and bursting components. However, we note that the transverse stability of a two-cluster state in the three-coupled 1D maps does not imply its transverse stability in an ensemble of N globally coupled 1D maps of Eq. (2.113). In fact, it was shown in [10] that two-cluster states born via blowout bifurcations in the N globally coupled 1D maps are transversely unstable for all the cases of distributions of elements between the two clusters. To make the point clear, we consider a two-cluster state ($x_t^{(1)} = \cdots = x_t^{(N_1)} \equiv X_t$, $x_t^{(N_1+1)} = \cdots = x_t^{(N)} \equiv Y_t$) with N_i elements in the ith cluster ($i = 1, 2$). Then, there exist two transverse Lyapunov exponents determining the transverse stability of the two-cluster state

$$\sigma_{\perp,1} = \lim_{L\to\infty} \frac{1}{L} \sum_{t=0}^{L-1} \ln |(1-\varepsilon)\, f'(X_t)|, \;\; \sigma_{\perp,2} = \lim_{L\to\infty} \frac{1}{L} \sum_{t=0}^{L-1} \ln |(1-\varepsilon)\, f'(Y_t)|. \tag{2.125}$$

Here, $\sigma_{\perp,1}$ and $\sigma_{\perp,2}$ with $N_1 - 1$ and $N_2 - 1$ multiplicities determine the stability against perturbations destroying the synchronization of the first and second clusters, respectively. As shown in Fig. 6 of Ref. [10], the first largest transverse Lyapunov exponent $\sigma_{\perp,1}$ is positive for all values of the distribution parameter $q\,(= \frac{N_2}{N})$, and hence all two-cluster states (born via blowout bifurcations) become transversely unstable. Following the similar procedure developed in the above three-coupled case [see Eq. (2.123)], the transverse instability of all

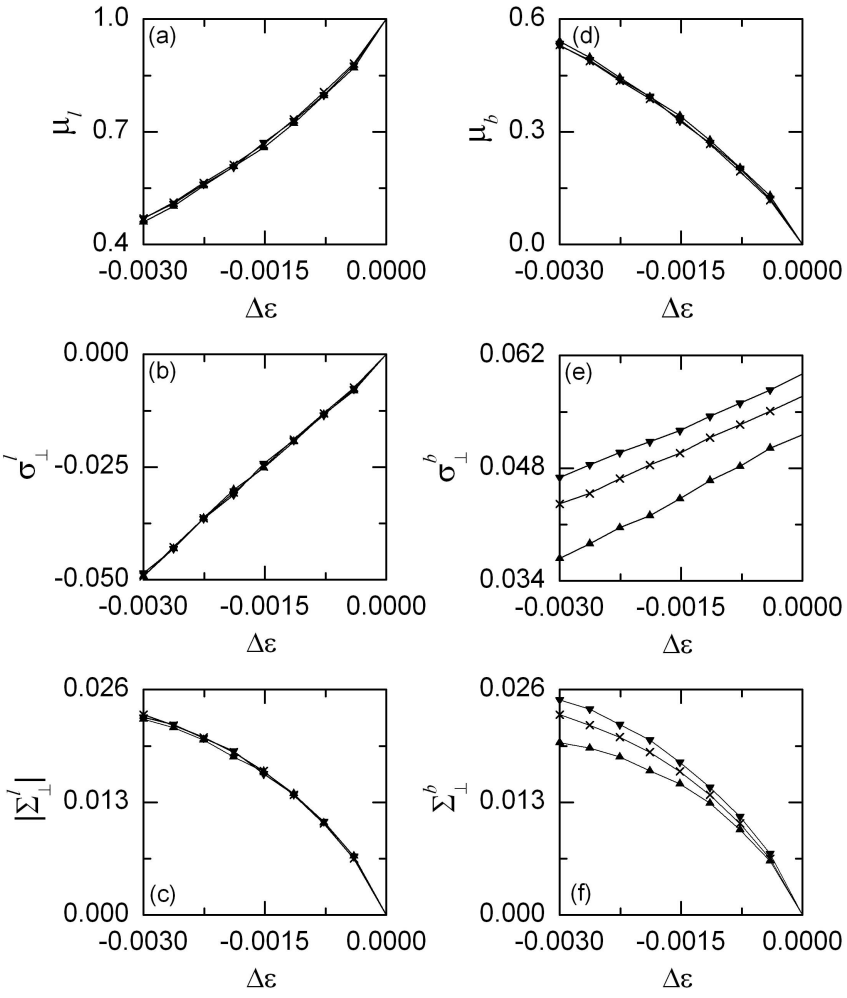

Figure 2.45: Plots of (a) [(d)] the fraction $\mu_{l(b)}$ of the laminar (bursting) time, (b) [(e)] the transverse Lyapunov exponent $\sigma_\perp^{l(b)}$ of the laminar (bursting) component, and (c) [(f)] the weighted transverse Lyapunov exponents $\Sigma_\perp^{l(b)}$ of the laminar (bursting) component versus $\Delta\varepsilon$ [$= \varepsilon - \varepsilon^*(= 0.4398)$] for $a = 1.95$ with $p = 0$ (up triangles), 0.146 (crosses), and 1/3 (down crosses). Straight lines between the data symbols are plotted only to guide the eye.

two-cluster states is also determined through competition between their laminar and bursting components. Since its bursting component is dominant for all q, any two-cluster state (born through a blowout bifurcation) becomes transversely unstable for the N globally-coupled case. This is in contrast to our three-coupled case, where only one transverse Lyapunov exponent $\sigma_\perp$ of Eq. (2.121) determines the transverse stability of the two-cluster state ($x_t^{(1)} = X_t$, $x_t^{(2)} = x_t^{(3)} = Y_t$) on the Π_{23} plane. We note that the transverse Lyapunov exponent $\sigma_\perp$, determining stability against perturbation breaking the synchrony of the second cluster ($x_t^{(2)} = x_t^{(3)}$), corresponds to the second transverse Lyapunov exponent $\sigma_{\perp,2}$ in Eq. (2.125) for the N globally-coupled case. (However, for the three-coupled case, there is no transverse Lyapunov exponent corresponding to $\sigma_{\perp,1}$ in Eq. (2.125), because there exists only one element $x_t^{(1)}$ in the first cluster.) Thus, in our three-coupled case partial synchronization (complete desynchronization) is found to occur via a blowout bifurcation when the laminar (bursting) component is dominant. Finally, we emphasize that our method to determine the transverse stability of an intermittent two-cluster state through its decomposition into the laminar and bursting components may be applied to a large class of coupled systems (including the three-coupled and globally-coupled cases we consider).

2.4.2 Partial Synchronization in Multi-Dimensional Invertible Systems

The results obtained in the preceding section are of wide significance, because the 1D map is a representative model for a large class of period-doubling systems. As examples, we study coupled multidimensional invertible systems, exhibiting period doublings, and find similar results.

First, we consider three coupled Hénon maps:

$$x_{t+1}^{(i)} = f(x_t^{(i)}) - y_t^{(i)} + \varepsilon\,[M_t - f(x_t^{(i)})],\ \ y_{t+1}^{(i)} = b x_t^{(i)}; \tag{2.126}$$

$$M_t \equiv (1-2\,p) f(x_t^{(1)}) + p f(x_t^{(2)}) + p f(x_t^{(3)}), \tag{2.127}$$

where $(x_t^{(i)}, y_t^{(i)})$ $(i = 1, 2, 3)$ is a state vector of the ith subsystem at a discrete time t, $f(x) = 1 - ax^2$, ε is a coupling parameter, p $(0 \le p \le 1/3)$ is a parameter tuning the degree of asymmetry in the coupling from the unidirectional $(p = 0)$ to symmetric coupling

($p = 1/3$), M_t can be regarded as a "weighted" mean field, and b ($|b| < 1$) is a damping parameter. As in the case of three coupled 1D maps, the three coupled Hénon maps may also be used as a model system for investigating the three-cluster dynamics in an ensemble of globally coupled Hénon maps.

Here, we fix the values of b and a at $b = 0.1$ and $a = 1.83$ and investigate the mechanism for the occurrence of partial synchronization by varying the asymmetry parameter p. For a sufficiently strong coupling, there exists a completely synchronized attractor $[x_t^{(1)} = x_t^{(2)} = x_t^{(3)},\ y_t^{(1)} = y_t^{(2)} = y_t^{(3)}]$, independently of p. When the coupling parameter ε decreases and passes a threshold value ε^* ($= 0.3574$), the completely synchronized attractor becomes transversely unstable, because its largest transverse Lyapunov exponent becomes positive. Then, a new asynchronous two-cluster state, exhibiting on-off intermittency, is born on an invariant subspace $\{(x^{(1)}, y^{(1)}, x^{(2)}, y^{(2)}, x^{(3)}, y^{(3)}) | x^{(2)} = x^{(3)},\ y^{(2)} = y^{(3)}\}$ via a supercritical blowout bifurcation. If this two-cluster is transversely stable against the perturbation across the invariant subspace, it becomes a partially synchronized attractor in the whole phase space; otherwise, a completely desynchronized attractor, occupying a finite 6D volume, appears. The dynamics of this two-cluster, satisfying $x_t^{(1)} \equiv X_t^{(1)}$, $y_t^{(1)} \equiv Y_t^{(1)}$, $x_t^{(2)} = x_t^{(3)} \equiv X_t^{(2)}$, and $y_t^{(2)} = y_t^{(3)} \equiv Y_t^{(2)}$, is governed by a reduced 4D map,

$$
\begin{aligned}
X_{t+1}^{(1)} &= f(X_t^{(1)}) - Y_t^{(1)} + 2p\,\varepsilon[f(X_t^{(2)}) - f(X_t^{(1)})], && (2.128)\\
Y_{t+1}^{(1)} &= bX_t^{(1)}, && (2.129)\\
X_{t+1}^{(2)} &= f(X_t^{(2)}) - Y_t^{(2)} + (1-2p)\,\varepsilon[f(X_t^{(1)}) - f(X_t^{(2)})], && (2.130)\\
Y_{t+1}^{(2)} &= bX_t^{(2)}. && (2.131)
\end{aligned}
$$

As in the coupled 1D maps, we introduce new coordinates for the accuracy of numerical calculations,

$$
\begin{aligned}
U^{(1)} &= \frac{X^{(1)} + X^{(2)}}{2},\ \ U^{(2)} = \frac{Y^{(1)} + Y^{(2)}}{2}, && (2.132)\\
V^{(1)} &= \frac{X^{(1)} - X^{(2)}}{2},\ \ V^{(2)} = \frac{Y^{(1)} - Y^{(2)}}{2}. && (2.133)
\end{aligned}
$$

Then, the coupled Hénon maps of Eq. (2.131) become

$$
\begin{aligned}
U_{t+1}^{(1)} &= 1 - a({U_t^{(1)}}^2 + {V_t^{(1)}}^2) + 2a\varepsilon(4p-1)U_t^{(1)}\,V_t^{(1)} - U_t^{(2)}, && (2.134)\\
U_{t+1}^{(2)} &= bU_t^{(1)}, && (2.135)
\end{aligned}
$$

$$V_{t+1}^{(1)} = 2a(\varepsilon - 1)U_t^{(1)} V_t^{(1)} - V_t^{(2)}, \tag{2.136}$$

$$V_{t+1}^{(2)} = bV_t^{(1)}. \tag{2.137}$$

In this new map, we numerically follow a typical trajectory in the intermittent two-cluster state until its length L becomes 10^8, and obtain its two transverse Lyapunov exponents, $\sigma_{\perp,1}$ and $\sigma_{\perp,2}$ ($\leq \sigma_{\perp,1}$), for the trajectory segment.

Figure 2.46(a) shows the largest transverse Lyapunov exponent $\sigma_{\perp,1}$ which depends on the the asymmetry parameter p [$p = 0$ (up triangles), 0.151 (crosses), and 1/3 (down triangles)]. Below a threshold value p^* ($\simeq 0.151$), the two-cluster is transversely stable (i.e., $\sigma_{\perp,1} < 0$), while above p^*, it is transversely unstable (i.e., $\sigma_{\perp,1} > 0$). Hence, for $0 \leq p < p^*$ partial synchronization occurs through a supercritical blowout bifurcation. On the other hand, complete desynchronization takes place for $p^* < p \leq 1/3$. As in the coupled 1D maps, such a transverse stability of the two-cluster state may be understood through a decomposition of the intermittent two-cluster into its laminar and bursting components. We use a threshold value d^* ($= 10^{-4}$) for the transverse variable d [$\equiv \frac{1}{2}(|V^{(1)}|+|V^{(2)}|)$], representing the deviation from the invariant synchronization plane. When $d < d^*$, the system is in the laminar (off) state, while for $d \geq d^*$ it is in the bursting (on) state. The sign of the largest transverse Lyapunov exponent $\sigma_{\perp,1}$ of the two-cluster state is determined through the competition between its laminar and bursting components [see Eq. (2.123)]. Figures 2.46(b)-2.46(c) show the strength of the laminar and bursting components (i.e., $|\Sigma_{\perp,1}^l|$ and $\Sigma_{\perp,1}^b$), respectively. We note that as p increases from zero [$p = 0$ (up triangles), 0.151 (crosses), and 1/3 (down triangles)], $\Sigma_{\perp,1}^b$ increases, while $|\Sigma_{\perp,1}^l|$ is nearly independent of p. For $0 \leq p < p^*$ ($\simeq$ 0.151), the laminar component is dominant because $|\Sigma_{\perp,1}^l| > \Sigma_{\perp,1}^b$, and hence a partially synchronized attractor is born through the supercritical blowout bifurcation. On the other hand, for $p^* < p \leq 1/3$, a completely desynchronized 6D attractor appears because the bursting component becomes dominant (i.e., $\Sigma_{\perp,1}^b > |\Sigma_{\perp,1}^l|$). As examples for $\varepsilon = 0.34$, see Figs. 2.46(d)-2.46(e) and 5(f)-5(g) that show the partially synchronized attractor and the completely desynchronized attractor for $p = 0$ and 1/3, respectively.

As a second example, we consider a system of three coupled parametrically forced pendula:

$$\dot{x}_i = y_i + \varepsilon\,[M_x - x_i], \quad \dot{y}_i = f(x_i, y_i, t) + \varepsilon\,[M_y - y_i]; \tag{2.138}$$

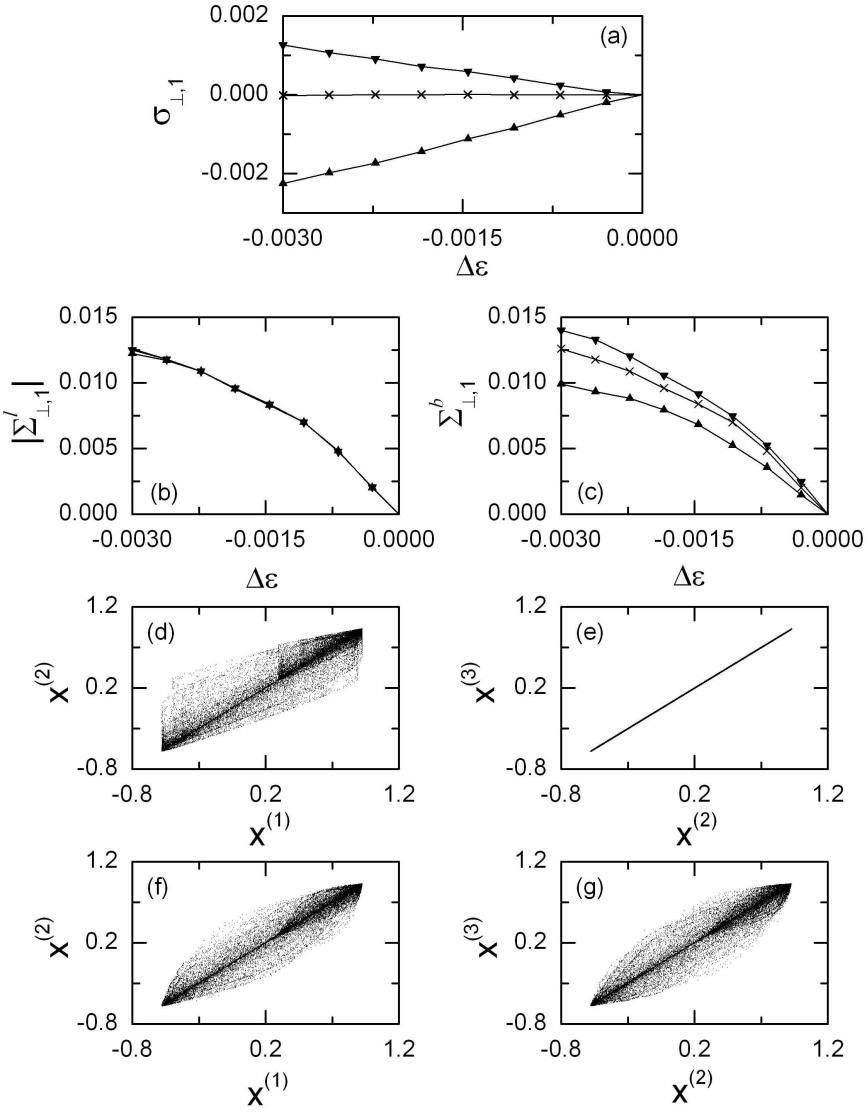

Figure 2.46: Consequence of the supercritical blowout bifurcation of the completely synchronized attractor in three coupled Hénon Maps for $b = 0.1$ and $a = 1.83$. (a) Plot of the largest transverse Lyapunov exponent $\sigma_{\perp,1}$ versus $\Delta\varepsilon$ $[\varepsilon - \varepsilon^*(= 0.3574)]$ for $p = 0$ (up triangles), 0.151 (crosses), and 1/3 (down triangles). (b) [(c)] Plot of the transverse strength of the laminar (bursting) component [i.e., $|\Sigma^l_{\perp,1}|$ $(\Sigma^b_{\perp,1})$] versus $\Delta\varepsilon$. The symbols are the same as those in (a), and the threshold value for the laminar state is $d^* = 10^{-4}$. Straight lines between the data symbols are plotted only to guide the eye. Projections of the partially synchronized attractor onto the (d) $x^{(1)} - x^{(2)}$ and (e) $x^{(2)} - x^{(3)}$ planes for $\varepsilon = 0.34$ in the unidirectionally coupled case with $p = 0$. Projections of the completely desynchronized attractor onto the (f) $x^{(1)} - x^{(2)}$ and (g) $x^{(2)} - x^{(3)}$ planes for $\varepsilon = 0.34$ in the symmetrically coupled case with $p = 1/3$.

$$M_x \equiv (1-2p)\,x_1 + p\,x_2 + p\,x_3, \quad M_y \equiv (1-2p)\,y_1 + p\,y_2 + p\,y_3, \tag{2.139}$$

where (x_i, y_i) $(i = 1, 2, 3)$ is a state vector of the ith pendulum, $f(x, y, t) = -2\pi\beta\Omega y - 2\pi(\Omega^2 - A\cos 2\pi t)\sin 2\pi x$, x is a normalized angle with range $x \in [0, 1)$, y is a normalized angular velocity, the overdot denotes a derivative with respect to time t, β is a normalized damping parameter, Ω is a normalized natural frequency of the unforced pendulum, A is a normalized driving amplitude of the vertical oscillation of the suspension point, ε is a coupling parameter. and p $(0 \le p \le 1/3)$ is a parameter tuning the degree of the asymmetry in the coupling. The two extreme cases of coupling correspond to the unidirectional $(p = 0)$ and symmetric $(p = 1/3)$ couplings, and (M_x, M_y) is a "weighted" mean field. As in the three coupled 1D maps, these three coupled pendula may also be used as a model for studying the three-cluster dynamics in an ensemble of globally coupled pendula.

We fix the values of β, Ω, and A at $\beta = 1.0$, $\Omega = 0.5$, and $A = 0.85$, and investigate the dependence of the occurrence of partial synchronization on the asymmetry parameter p. When the coupling parameter ε decreases and passes a threshold value ε^* $(= 0.648)$, the completely synchronized attractor becomes transversely unstable, independently of p. Then, an asynchronous two-cluster, exhibiting on-off intermittency, appears on an invariant subspace via a supercritical blowout bifurcation. If the two-cluster is transversely stable (unstable), partial synchronization (complete desynchronization) occurs. This two-cluster satisfies $x_1(t) \equiv X_1(t)$, $y_1(t) \equiv Y_1(t)$, $x_2(t) = x_3(t) \equiv X_2(t)$, and $y_2(t) = y_3(t) \equiv Y_2(t)$, and its dynamics is governed by a system of four coupled ordinary differential equations,

$$\dot{X}_1 = Y_1 + 2p\,\varepsilon[X_2 - X_1], \tag{2.140}$$

$$\dot{Y}_1 = f(X_1, Y_1, t) + 2p\,\varepsilon[Y_2 - Y_1], \tag{2.141}$$

$$\dot{X}_2 = Y_2 + (1-2p)\varepsilon[X_1 - X_2], \tag{2.142}$$

$$\dot{Y}_2 = f(X_2, Y_2, t) + (1-2p)\varepsilon[Y_1 - Y_2]. \tag{2.143}$$

As in the coupled Hénon maps, we introduce new coordinates for the accuracy of numerical calculations,

$$U_1 = \frac{X_1 + X_2}{2}, \quad U_2 = \frac{Y_1 + Y_2}{2}, \tag{2.144}$$

$$V_1 = \frac{X_1 - X_2}{2}, \quad V_2 = \frac{Y_1 - Y_2}{2}. \tag{2.145}$$

Then, the equations of motion of Eq. (2.143) become

$$\dot{U}_1 = U_2 + (1-4p)\varepsilon V_1, \tag{2.146}$$

$$\dot{U}_2 = -2\pi\beta\Omega U_2 - 2\pi(\Omega^2 - A\cos 2\pi t)\sin 2\pi U_1 \cos 2\pi V_1 + (1-4p)\varepsilon V_2, \tag{2.147}$$

$$\dot{V}_1 = V_2 - \varepsilon V_1, \tag{2.148}$$

$$\dot{V}_2 = -(2\pi\beta\Omega + \varepsilon)V_2 - 2\pi(\Omega^2 - A\cos 2\pi t)\cos 2\pi U_1 \sin 2\pi V_1 \tag{2.149}$$

By stroboscopically sampling the orbit points $[U_1(m), U_2(m), V_1(m), V_2(m)]$ at the discrete time m, we obtain the 4D Poincaré map P.

As in the coupled Hénon maps, we follow a trajectory in the intermittent two-cluster until its length L becomes 10^8, and obtain its transverse Lyapunov exponents. As shown in Fig. 2.47(a), the largest transverse Lyapunov exponent $\sigma_{\perp,1}$ depends on p [$p = 0$ (up triangles), 0.17 (crosses), and 1/3 (down triangles)]. For $p < p^*$ ($\simeq 0.17$), the two-cluster is transversely stable with $\sigma_{\perp,1} < 0$, while for $p > p^*$, it is transversely unstable with $\sigma_{\perp,1} > 0$. Like the cases of the coupled 1D and Hénon maps, this transverse stability of the intermittent two-cluster state (i.e., the sign of $\sigma_{\perp,1}$)) may be determined via competition between its laminar and bursting components. The weighted transverse Lyapunov exponents of the laminar and bursting components, $|\Sigma^l_{\perp,1}|$ and $\Sigma^b_{\perp,1}$, are shown in Figs. 2.47(b) and 2.47(c), respectively. As p is increased from zero [$p = 0$ (up triangles), 0.17 (crosses), and 1/3 (down triangles)], the strength of the bursting component (i.e., $\Sigma^b_{\perp,1}$) increases, while the strength of the laminar component (i.e., $|\Sigma^l_{\perp,1}|$) is nearly independent of p. For the threshold value p^* ($\simeq 0.17$), the strengths of laminar and bursting components become balanced. Thus, for $0 \le p < p^*$, the two-cluster is transversely stable because the laminar component is dominant, and hence a partially synchronized attractor is born via the supercritical blowout bifurcation [e.g., see Figs. 2.47(d)-2.47(e) for $p = 0$ and $\varepsilon = 0.63$]. On the other hand, since the bursting component is dominant for $p^* < p \le 1/3$, the two-cluster is transversely unstable, and hence a completely desynchronized attractor appears [e.g., see Figs. 2.47(f)-2.47(g) for $p = 1/3$ and $\varepsilon = 0.63$].

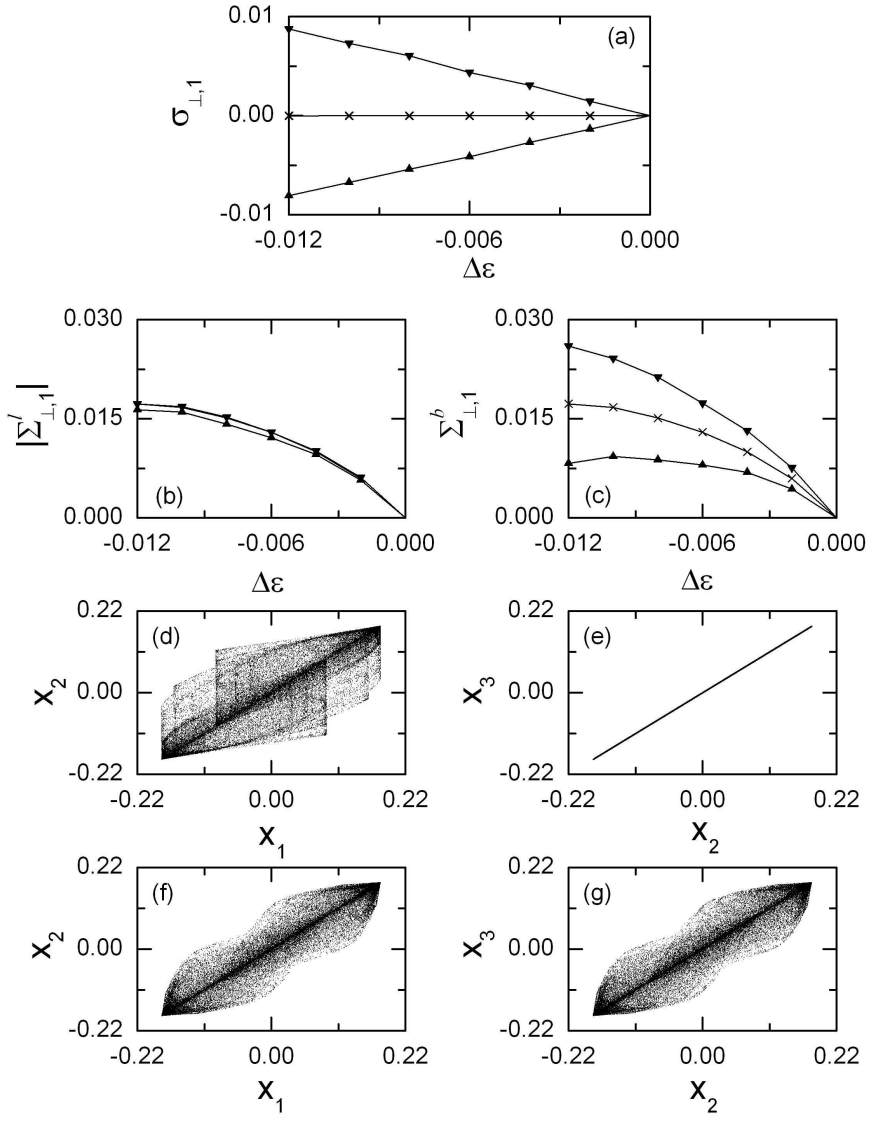

Figure 2.47: Consequence of the supercritical blowout bifurcation of the completely synchronized attractor in three coupled pendula for $\beta = 1.0$, $\Omega = 0.5$ and $A = 0.85$. (a) Plot of the largest transverse Lyapunov exponent $\sigma_{\perp,1}$ versus $\Delta\varepsilon$ $[\varepsilon - \varepsilon^*(= 0.648)]$ for $p = 0$ (up triangles), 0.151 (crosses), and 1/3 (down triangles). (b) [(c)] Plot of the transverse strength of the laminar (bursting) component [i.e., $|\Sigma^l_{\perp,1}|$ $(\Sigma^b_{\perp,1})$] versus $\Delta\varepsilon$. The symbols are the same as those in (a), and the threshold value for the laminar state is $d^* = 10^{-4}$. Straight lines between the data symbols are plotted only to guide the eye. Projections of the partially synchronized attractor onto the (d) $x_1 - x_2$ and (e) $x_2 - x_3$ planes for $\varepsilon = 0.63$ in the unidirectionally coupled case with $p = 0$. Projections of the completely desynchronized attractor onto the (f) $x_1 - x_2$ and (g) $x_2 - x_3$ planes for $\varepsilon = 0.63$ in the symmetrically coupled case with $p = 1/3$.

Chapter 3

Dynamical Transitions in Quasiperiodically Forced Systems

In this chapter, we study the dynamical transitions in quasiperiodically forced systems driven at two incommensurate frequencies. As a representative model we consider the quasiperiodically forced logistic 1D map and particularly investigate dynamical routes to strange nonchaotic attractors. When passing a threshold value, a smooth torus transforms into an intermittent strange nonchaotic attractor. Using the rational approximation to the quasiperiodic forcing, we study the dynamical mechanism for the intermittent route to strange nonchaotic attractors in Section 3.1 [66, 67]. Thus, such a transition to an intermittent strange nonchaotic attractor is found to occur through a phase-dependent saddle-node bifurcation when a smooth torus collides with a new type of ring-shaped unstable set which has no counterpart in the unforced case. In Section 3.2, a similar mechanism is also found for the case of band-merging route to strange nonchaotic attractors [68, 69]. This new type of band-merging transition is a direct cause for the truncation for the torus-doubling sequence. Finally, in Section 3.3 we discuss boundary crises occurring in quasiperiodically forced systems [70, 71]. A nonchaotic attractor (torus, strange nonchaotic attractor) as well as a chaotic attractor is found to suddenly disappear when it collides with a ring-shaped unstable set.

3.1 Intermittent Route to Strange Nonchaotic Attractors

We investigate the intermittent route to strange nonchaotic attractors in the quasiperiodically forced logistic map [66]. Using rational approximations to the quasiperiodic forcing we investigate the mechanism for the intermittent route to strange nonchaotic attractors. It is found that a smooth torus transforms into an intermittent strange nonchaotic attractor via a phase-dependent saddle-node bifurcation when it collides with a new type of "ring-shaped" unstable set. Such an intermittent transition to strange nonchaotic attractors is also found to occur in quasiperiodically forced systems of different nature such as the quasiperiodically forced Hénon map, ring map, and pendulum [67]. Consequently, the intermittent route to strange nonchaotic attractors seems to be universal.

3.1.1 Intermittent Transition to Strange Nonchaotic Attractors in the Quasiperiodically Forced Logistic Map

We investigate the mechanism for the intermittent route to strange nonchaotic attractors in the quasiperiodically forced logistic map M [30] :

$$M : \begin{cases} x_{n+1} = (a + \varepsilon \cos 2\pi\theta_n) x_n (1 - x_n), \\ \theta_{n+1} = \theta_n + \omega \pmod 1, \end{cases} \tag{3.1}$$

where $x \in [0, 1]$, $\theta \in S^1$, a is the nonlinearity parameter of the logistic map, and ω and ε represent the frequency and amplitude of the quasiperiodic forcing, respectively. We set the frequency to be the reciprocal of the golden mean, $\omega = (\sqrt{5} - 1)/2$. The intermittent transition is then investigated using rational approximations. For the inverse golden mean, its rational approximants are given by the ratios of the Fibonacci numbers, $\omega_k = F_{k-1}/F_k$, where the sequence of $\{F_k\}$ satisfies $F_{k+1} = F_k + F_{k-1}$ with $F_0 = 0$ and $F_1 = 1$. Instead of the quasiperiodically forced system, we study an infinite sequence of periodically forced systems with rational driving frequencies ω_k. We suppose that the properties of the original system M may be obtained by taking the quasiperiodic limit $k \to \infty$. Using this technique, a transition from a smooth torus to an intermittent strange nonchaotic attractor is found to occur through collision with a new type of ring-shaped unstable set.

The quasiperiodically forced logistic map M is non-invertible, because its Jacobian determinant becomes zero along the critical curve, $L_0 = \{x = 0.5,\ \theta \in [0, 1)\}$. Critical curves of rank k, L_k $(k = 1, 2, \ldots)$, are then given by the images of L_0, [i.e., $L_k = M^k(L_0)$]. Segments of these critical curves can be used to define a bounded trapping region of the phase space, called an "absorbing area," inside which, upon entering, trajectories are henceforth confined [82]. It is found that the newly-born intermittent strange nonchaotic attractor fills the absorbing area. Hence the critical curves determine the global structure of the strange nonchaotic attractor.

Figure 3.1(a) shows a phase diagram in the $a - \varepsilon$ plane. Each phase is characterized by the Lyapunov exponent σ_x in the x-direction as well as the phase sensitivity exponent δ. The exponent δ measures the sensitivity with respect to the phase of the quasiperiodic forcing and was introduced in [53] [1] to characterize the strangeness of an attractor of a quasiperiodically driven system. A smooth torus that has a negative Lyapunov exponent without phase sensitivity ($\delta = 0$) exists in the region denoted by T and shown in light gray. Upon crossing the solid line, the smooth torus becomes unstable and bifurcates to a smooth doubled torus in the region denoted by $2T$. Chaotic attractors with positive Lyapunov exponents exist in the region shown in black. Between these regular and chaotic regions, strange nonchaotic attractors that have negative Lyapunov exponents with high phase sensitivity ($\delta > 0$) exist in the regions shown in gray and dark gray. Consistent with their positive phase sensitivity exponent δ, these strange nonchaotic attractors are observed to have fractal structure [53]. Here we restrict our considerations only to the intermittent strange nonchaotic attractors that exist in the thin gray region [e.g., see a magnified part in Fig. 3.1(a)]. (In the dark-gray region, non-intermittent strange nonchaotic attractors, born through other mechanisms, such as gradual fractalization [58] and torus collision [30], exist.) This phase diagram is typical for quasiperiodically forced period-doubling systems [60, 61, 62, 63, 64, 70, 71, 68, 69], and its main interesting feature is the existence of the

[1] To characterize strangeness of an attractor in a quasiperiodically forced system, a phase sensitivity function Γ_N $[\equiv \min_{\{(x_0,\theta_0)\}}(\max_{0\le n\le N} \left|\frac{\partial x_n}{\partial \theta}\right|)]$ was introduced, where the minimum is taken with respect to randomly chosen initial orbit points (x_0, θ_0). For a strange nonchaotic attractor, Γ_N grows as a power, $\Gamma_N \sim N^\delta$. Here δ is called the phase sensitivity exponent to measure the sensitivity with respect to the phase θ.

"tongue" of quasiperiodic motion that penetrates into the chaotic region and separates it into upper and lower parts. We also note that this tongue lies near the terminal point (denoted by the cross) of the torus doubling bifurcation curve. When crossing the upper boundary of the tongue, a smooth torus transforms into an intermittent strange nonchaotic attractor that exists in the thin gray region. Hereafter this intermittent route to strange nonchaotic attractors will be referred to as the route a [see Fig. 3.1(a)].

As an example, we consider the case $a = 3.38$. Figure 3.1(b) shows a smooth torus with $\sigma_x = -0.059$ for $\varepsilon = 0.584\,7$ inside an absorbing area whose boundary is formed by segments of the critical curves L_k $(k = 1, \ldots, 5)$ (the dots indicate where these segments connect). We also note that the smooth unstable torus $x = 0$ and its first preimage $x = 1$ form the basin boundary of the smooth torus in the $\theta - x$ plane. However, as ε passes a threshold value ε^* $(= 0.584\,726\,781)$, a transition to an intermittent strange nonchaotic attractor occurs. As shown in Fig. 3.1(c) for $\varepsilon = 0.584\,75$, the newly-born intermittent strange nonchaotic attractor with $\sigma_x = -0.012$ and $\delta = 19.5$ appears to fill the absorbing area, and its typical trajectory spends most of its time near the former torus with sporadic large bursts away from it. This intermittent transition may be expected to have occurred through collision of the smooth attracting torus with an unstable orbit. However, the smooth unstable torus $x = 0$ cannot interact with the smooth stable torus, because it lies outside the absorbing area. Hence we search inside the absorbing area for an unstable orbit that might collide with the smooth stable torus.

Using rational approximations we find a new type of ring-shaped unstable set that causes the intermittent transition through collision with the smooth torus. When passing the dashed curve in Fig. 3.1(a), such a ring-shaped unstable set appears via a phase-dependent saddle-node bifurcation. This bifurcation has no counterpart in the unforced case. (The dashed line is numerically obtained for a sufficiently large level $k = 10$ of the rational approximations.) For each rational approximation of level k, a periodically forced logistic map with rational driving frequency ω_k has a periodic or chaotic attractor that depends on the initial phase θ_0 of the external forcing. Then the union of all attractors for different θ_0 gives the kth approximation to the attractor in the quasiperiodically forced system. As an example, consider the rational approximation of low level $k = 6$. As shown in Fig. 3.2(a) for $a = 3.246$ and $\varepsilon = 0.446$, the rational approximation to the smooth torus (denoted by a black line),

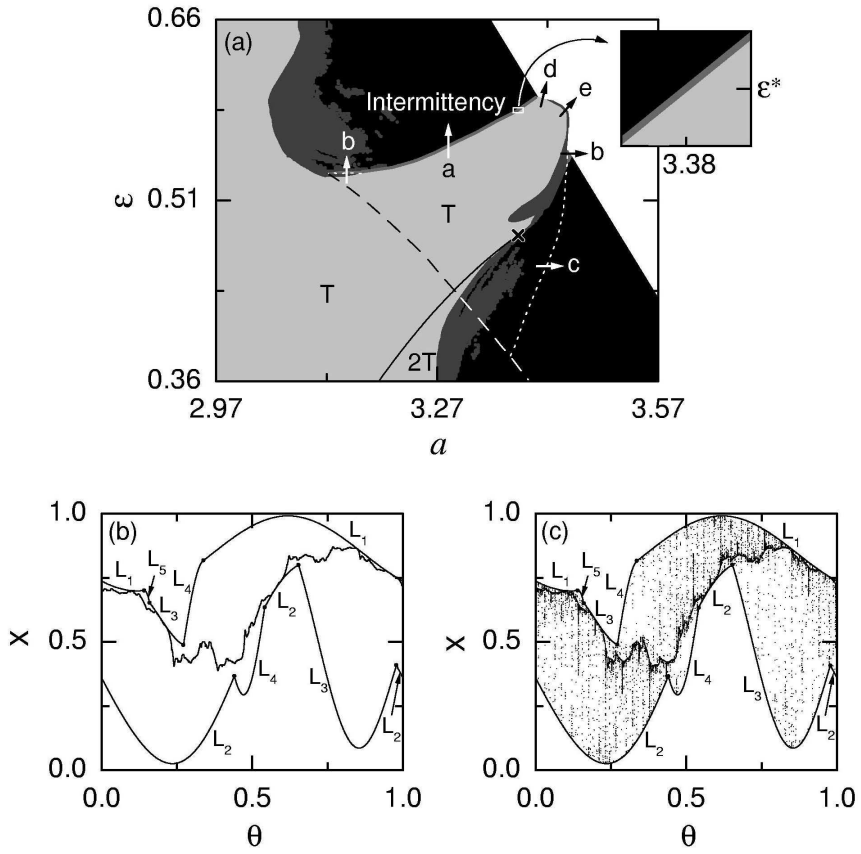

Figure 3.1: (a) Phase Diagram in the $a - \varepsilon$ plane. Regular, chaotic, strange nonchaotic attractor, and divergence regimes are shown in light gray, black, gray (or dark gray), and white, respectively. To show the region of existence (gray) of the intermittent strange nonchaotic attractor occurring between T (light gray) and the chaotic attractor region (black), a small box near $(a, \varepsilon) = [3.38, \varepsilon^*(= 0.584\,726\,781)]$ is magnified. Through interaction with the ring-shaped unstable set born when passing the dashed line, typical dynamical transitions such as the intermittency (route a) and the interior (routes b and c; the dotted line is an interior crisis line) and boundary (routes d and e) crises may occur. Here the torus and the doubled torus are denoted by T and $2T$ and the solid line represents a torus doubling bifurcation curve whose terminal point is marked with the cross. (b) Smooth torus inside an absorbing area with boundary formed by segments of the critical curves L_k $(k = 1, \ldots, 5)$ (the dots indicate where these segments connect) for $a = 3.38$ and $\varepsilon = 0.584\,7$. (c) Strange nonchaotic attractor filling the absorbing area for $a = 3.38$ and $\varepsilon = 0.584\,75$. For other details, see the text.

consisting of stable orbits with period F_6 (= 8), exists inside an absorbing area bounded by segments of the critical curves L_k ($k = 1, \ldots, 4$). Note also that a ring-shaped unstable set, born via a phase-dependent saddle-node bifurcation and composed of 8 small rings, lies inside the absorbing area. At first, each ring consists of the stable (shown in black) and unstable (shown in gray) orbits with forcing period F_6 (= 8) [see the inset in Fig. 3.2(a)]. However, as the parameters increase such rings evolve, as shown in Fig. 3.2(b) for $a = 3.26$ and $\varepsilon = 0.46$. For fixed values of a and ε, the phase θ may be regarded as a "bifurcation parameter." As θ changes, a chaotic attractor appears through an infinite sequence of period doubling bifurcations of stable periodic orbits in each ring, and then it disappears through collision with the unstable F_6-periodic orbit [see the inset in Fig. 3.2(b)]. Thus the attracting part (shown in black) of each ring consists of the union of the originally stable F_6-periodic attractor and the higher $2^n F_6$-periodic ($n = 1, 2, \ldots$) and chaotic attractors born through the period-doubling process. On the other hand, the unstable part (shown in gray) of each ring is composed of the union of the originally unstable F_6-periodic orbit [e.g., the lower gray line in the inset in Fig. 3.2(b)] born via a saddle-node bifurcation and the destabilized F_6-periodic orbit [e.g., the upper gray line in the inset in Fig. 3.2(b)] born through a period doubling bifurcation. (As will be seen below, only the originally unstable F_6-periodic orbit may interact with the stable F_6-periodic orbit in the rational approximation to the smooth torus through a saddle-node bifurcation.) With further increase in the parameters, both the size and shape of the rings change, and for sufficiently large parameters, each ring consists of a large unstable part (shown in gray) and a small attracting part (shown in black), as shown in Fig. 3.2(c) for $a = 3.326$ and $\varepsilon = 0.526$. For the same parameter values as in Fig. 3.2(c), we increase the level of the rational approximation to $k = 8$. Then the number of rings (= 336) increases significantly, and the unstable part [shown in gray and consisting of unstable orbits with period F_8 (= 21)] becomes dominant, because the attached attracting part (shown in black) becomes negligibly small [see Fig. 3.2(d)]. In this way, as the level k increases the ring-shaped unstable set consists of a larger number of rings with a smaller attracting part (i.e., as the level k is increased, the unstable part of each ring becomes more and more dominant). Hence, it is conjectured that, in the quasiperiodic limit, these ring-shaped unstable sets might form a complicated invariant unstable set composed of only unstable orbits.

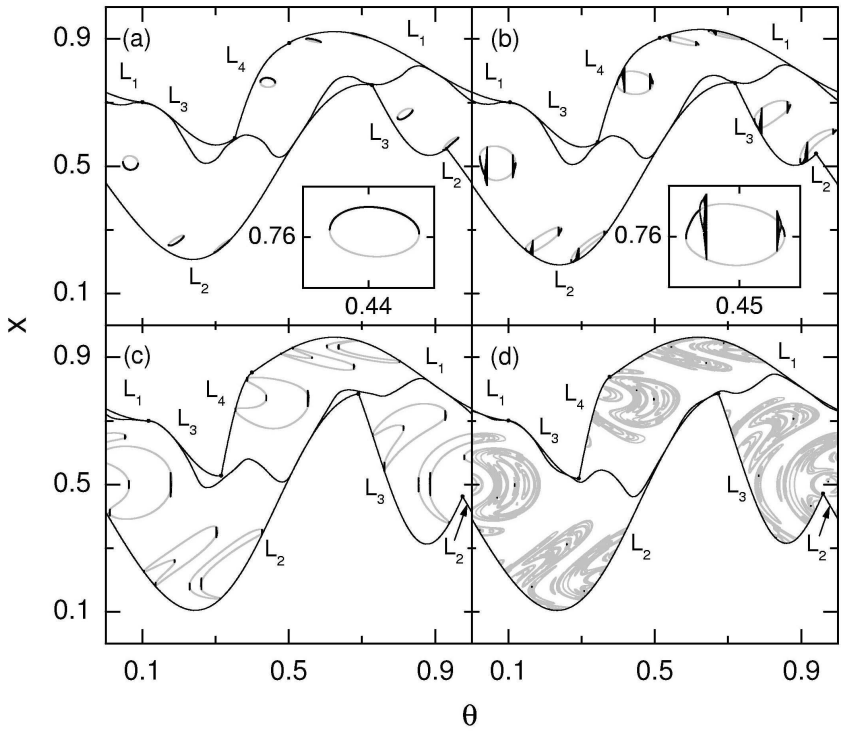

Figure 3.2: Smooth torus and ring-shaped unstable set in the rational approximation of level 6 for (a) $a = 3.246$ and $\varepsilon = 0.446$, (b) $a = 3.26$ and $\varepsilon = 0.46$, and (c) $a = 3.326$ and $\varepsilon = 0.526$. (d) Smooth torus and ring-shaped unstable set in the rational approximation of level 8 for $a = 3.326$ and $\varepsilon = 0.526$. Both the smooth torus (denoted by a black line) and the ring-shaped unstable set (composed of rings) exist inside the absorbing area with boundary formed by portions of the critical curves L_k ($k = 1, \ldots, 4$) (the dots indicate where these portions connect). For the rational approximation of level k, each ring is composed of the attracting part (shown in black) and the unstable part (shown in gray and consisting of unstable F_k-periodic orbits). As the level k increases, the unstable part becomes dominant, as the attracting part becomes negligibly small. For more details, see the text.

We now use rational approximations to explain the mechanism for the intermittent transition occurring in Figs. 3.1(b) and 3.1(c) for $a = 3.38$. Figures 3.3(a) and 3.3(b) show that, inside the absorbing area, the ring-shaped unstable set (shown in gray) lies very close to the smooth torus (shown in black) for $\varepsilon = 0.586$ in the rational approximation of level $k = 8$. As ε passes a threshold value ε_8 ($= 0.586\,366$), a phase-dependent saddle-node bifurcation occurs through collision of the smooth torus and the ring-shaped unstable set. As a result "gaps," where no orbits with period F_8 ($= 21$) exist, are formed. A magnified gap is shown in Fig. 3.3(c) for $\varepsilon = 0.586\,4$. Note that this gap is filled by intermittent chaotic attractors together with orbits with period higher than F_8 embedded in very small windows. As shown in Fig. 3.3(d), the rational approximation to the whole attractor consists of the union of the periodic component and the intermittent chaotic component, where the latter occupies the 21 gaps in θ and is vertically bounded by segments of the critical curves L_k ($k = 1, \ldots, 5$). However, the periodic component dominates: the average Lyapunov exponent ($\langle \sigma_x \rangle = -0.09$) is negative, where $\langle \cdots \rangle$ denotes the average over the whole θ. We note that Fig. 3.3(d) resembles Fig. 3.1(c), although the level $k = 8$ is low. Increasing the level to $k = 15$, we find that the threshold value ε_k at which the phase-dependent saddle-node bifurcation occurs converges to the quasiperiodic limit ε^* ($= 0.584\,726\,781$) in an algebraic manner, $|\Delta\varepsilon_k| \sim F_k^{-\alpha}$, where $\Delta\varepsilon_k = \varepsilon_k - \varepsilon^*$ and $\alpha \simeq 2.2$. In the quasiperiodic limit $k \to \infty$ the rational approximation to the attractor has a dense set of gaps that are filled by intermittent chaotic attractors and bounded by portions of the critical curves. Thus, an intermittent strange nonchaotic attractor, containing the ring-shaped unstable set and filling the absorbing area, appears, as shown in Fig. 3.1(c).

In addition to the transition to an intermittent strange nonchaotic attractor, we also find that as ε passes another threshold value ε_c ($= 0.584\,8$), the strange nonchaotic attractor transforms into a chaotic attractor with a positive Lyapunov exponent. Using the rational approximation, this transition to chaos may be explained. For each rational approximation to the attractor, its angle averaged Lyapunov exponent $\langle \sigma_x \rangle$ is given by the sum of the "weighted" Lyapunov exponents of its periodic and chaotic components, Λ_p and Λ_c, (i.e., $\langle \sigma_x \rangle = \Lambda_p + \Lambda_c$), where $\Lambda_{p(c)} \equiv M_{p(c)} \langle \sigma_x \rangle_{p(c)}$, and $M_{p(c)}$ and $\langle \sigma_{p(c)} \rangle$ are the Lebesgue measure in θ and average Lyapunov exponent of the periodic (chaotic) component, respectively. After passing a threshold value where the magnitude of Λ_p and Λ_c are balanced, the chaotic

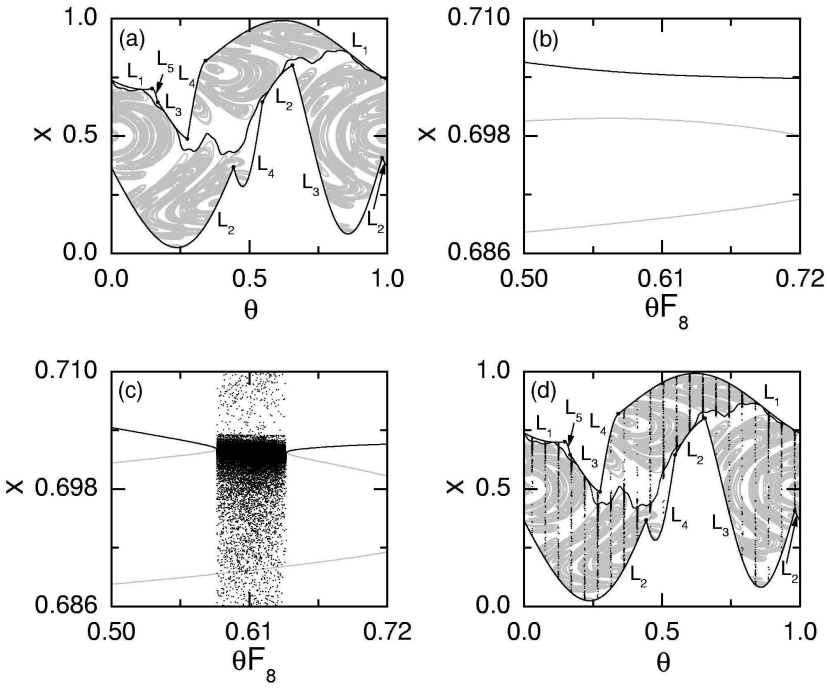

Figure 3.3: (a) Smooth torus and ring-shaped unstable set in the rational approximation of level 8 ($F_8 = 21$) for $a = 3.38$ and $\varepsilon = 0.586$. The ring-shaped unstable set (shown in gray) lies very close to the smooth torus (denoted by a black line) inside the absorbing area with boundary formed by segments of the critical curves L_k ($k = 1, \ldots, 5$) (the dots indicate where these segments connect). A magnified view near $(\theta F_8, x) = (0.61, 0.698)$ is given in (b). (c) and (d) 8th rational approximation to the intermittent strange nonchaotic attractor for $a = 3.38$ and $\varepsilon = 0.586\,4$. The rational approximation to the strange nonchaotic attractor is composed of the union of the periodic component and the intermittent chaotic component, where the latter occupies the 21 gaps in θ and is vertically bounded by portions of the critical curves L_k ($k = 1, \ldots, 5$) [a magnified gap near $\theta F_8 = 0.61$ is shown in (c)]. For more details, see the text.

component becomes dominant, and hence a chaotic attractor appears.

3.1.2 Universality for the Intermittent Route to Strange Nonchaotic Attractors

As a first example, we consider the quasiperiodically forced Hénon map [53], often used as a representative model for the Poincaré maps of quasiperiodically forced oscillators:

$$M : \begin{cases} x_{n+1} = a - x_n^2 + y_n + \varepsilon \cos 2\pi\theta_n, \\ y_{n+1} = bx_n, \\ \theta_{n+1} = \theta_n + \omega \pmod 1, \end{cases} \tag{3.2}$$

where a is the nonlinearity parameter of the unforced Hénon map, and ω and ε represent the frequency and amplitude of the quasiperiodic forcing, respectively. This quasiperiodically forced Hénon map M is invertible, because it has a nonzero constant Jacobian determinant $-b$ whose magnitude is less than unity (i.e., $b \neq 0$ and $-1 < b < 1$). Here, we fix the value of the dissipation parameter b at $b = 0.05$ and set the frequency ω to be the reciprocal of the golden mean, $\omega = (\sqrt{5} - 1)/2$. Then, using the rational approximations (rational approximations) to this quasiperiodic forcing, we investigate the intermittent route to strange nonchaotic attractors. For the inverse golden mean, its rational approximants are given by the ratios of the Fibonacci numbers, $\omega_k = F_{k-1}/F_k$, where the sequence of $\{F_k\}$ satisfies $F_{k+1} = F_k + F_{k-1}$ with $F_0 = 0$ and $F_1 = 1$. Instead of the quasiperiodically forced system, we study an infinite sequence of periodically forced systems with rational driving frequencies ω_k. We suppose that the properties of the original system M may be obtained by taking the quasiperiodic limit $k \to \infty$.

Figure 3.4(a) shows a phase diagram in the $a - \varepsilon$ plane. Each phase is characterized by both the (nontrivial) Lyapunov exponents, σ_1 and σ_2 ($\leq \sigma_1$), associated with dynamics of the variables x and y (besides the zero exponent, related to the phase variable θ of the quasiperiodic forcing) and the phase sensitivity exponent δ. The exponent δ measures the sensitivity with respect to the phase of the quasiperiodic forcing and characterizes the strangeness of an attractor [53]. A smooth torus has negative Lyapunov exponents ($\sigma_{1,2} < 0$) and has no phase sensitivity (i.e., $\delta = 0$). The region where it exists is shown in light gray and represented by T . When crossing the solid line, the smooth torus becomes unstable

and a smooth doubled torus appears in the region denoted by $2T$. On the other hand, a chaotic attractor has a positive Lyapunov exponent $\sigma_1 > 0$, and its region is shown in black. Between these regular and chaotic regions, strange nonchaotic attractors that have negative Lyapunov exponents ($\sigma_{1,2} < 0$) and positive phase sensitivity exponents ($\delta > 0$) exist in the regions shown in gray and dark gray. Due to their high phase sensitivity, strange nonchaotic attractors have a strange fractal structure. In the thin gray region [e.g., see a magnified part in Fig. 3.4(a)], intermittent strange nonchaotic attractors exist, while in the dark-gray region nonintermittent strange nonchaotic attractors, born through the mechanism of the gradual fractalization [58] or torus collision [30], exist.

A main interesting feature of the phase diagram is the existence of the "tongue" of quasiperiodic motion that penetrates into the chaotic region and separates it into upper and lower parts. This tongue lies near the terminal point (represented by the cross) of the torus doubling bifurcation curve. Upon crossing the upper boundary of the tongue, a smooth torus transforms into an intermittent strange nonchaotic attractor that exists in the thin gray region. Here we investigate this intermittent route to strange nonchaotic attractors [see the route a in Fig. 3.4(a)]. As an example, consider the case of $a = 0.96$. Figures 3.4(b) and 3.4(c) show projections of a smooth torus with $\sigma_1 = -0.077$ onto the $\theta - x$ and $x - y$ planes for $\varepsilon = 0.415$, respectively. We note that the projections are smooth invariant curves. A curve can be regarded as a cross section (Poincaré map) for the two-frequency quasiperiodic motion on a smooth torus in continuous-time dynamical systems. Hence, we call this curve a torus. However, as ε passes a threshold value ε^* ($= 0.416\,857\,986$), dynamical transition to an intermittent strange nonchaotic attractor, occupying a finite volume of the phase space, occurs. As shown in Figs. 3.4(d) and 3.4(e) for $\varepsilon = 0.416\,86$, a typical trajectory on the newly-born intermittent strange nonchaotic attractor with $\sigma_1 = -0.006$ and $\delta = 4.32$ spends most of its time near the former torus with sporadic large bursts away from it.

Using rational approximations, we search for un unstable orbit that causes the intermittent transition via a collision with the smooth (stable) torus. Thus, an invariant "ring-shaped" unstable set that is different from the smooth unstable torus is found. When crossing the dashed curve in Fig. 3.4, such a ring-shaped unstable set appears through a phase-dependent saddle-node bifurcation which has no counterpart in the unforced case. As an example, consider the rational approximation of level $k = 7$. The rational approximation

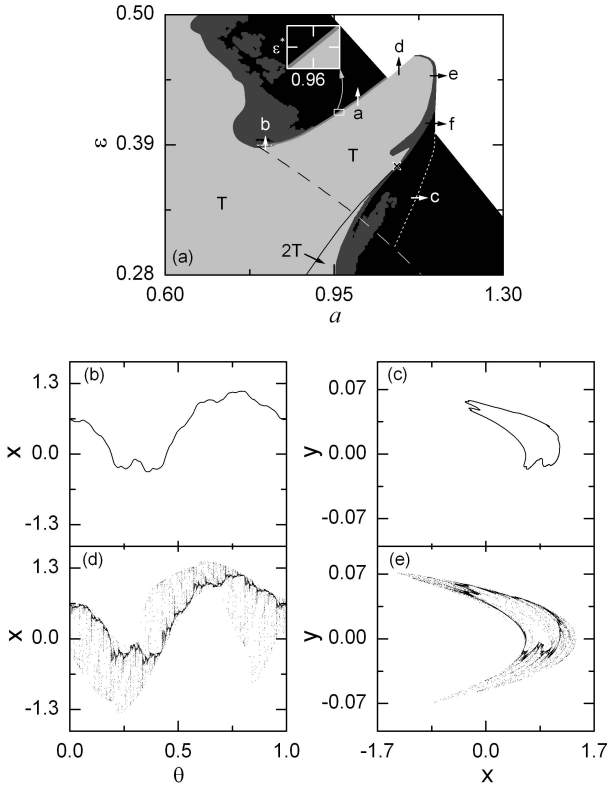

Figure 3.4: (a) Phase Diagram of the quasiperiodically forced Hénon map in the $a-\varepsilon$ plane for the case of $b = 0.05$ and $\omega = (\sqrt{5}-1)/2$. Regular, chaotic, strange nonchaotic attractor, and divergence regimes are shown in light gray, black, gray (or dark gray), and white, respectively. To show the region of existence (gray) of the intermittent strange nonchaotic attractor occurring between T (light gray) and the chaotic attractor region (black), a small box near $(a, \varepsilon) = [0.96, \varepsilon^*(= 0.416\,857\,986)]$ is magnified. Through interaction with the ring-shaped unstable set born when passing the dashed line (which is obtained for a sufficiently large level $k = 10$ of the rational approximations), typical dynamical transitions such as the intermittency (route a) and the interior (routes b and c; the dotted line is an interior crisis line) and boundary (routes d, e, and f) crises may occur. Here, the torus and the doubled torus are denoted by T and $2T$ and the solid line represents a torus doubling bifurcation curve whose terminal point is marked with the cross. Projections of a smooth torus onto (b) the $\theta - x$ and (c) $x - y$ planes for $a = 0.96$ $\varepsilon = 0.415$. In (b) and (c), the initial orbit points are $(x_0, y_0, \theta_0) = (0.8, 0.0, 0.0)$, 5×10^3 points are computed before plotting, and the next 10^4 points are plotted. Projections of a strange nonchaotic attractor onto (d) the $\theta - x$ and (e) $x - y$ planes for $a = 0.96$ $\varepsilon = 0.416\,86$. In (d) and (e), the initial orbit points are $(x_0, y_0, \theta_0) = (0.8, 0.0, 0.0)$, 5×10^3 points are computed before plotting, and the next 6×10^4 points are plotted. For other details, see the text.

to the smooth torus (denoted by a black line), composed of stable orbits with period F_7 (= 13), is shown in Fig. 3.5(a) for $a = 0.85$ and $\varepsilon = 0.3707$. We note that a ring-shaped unstable set, born via a phase-dependent saddle-node bifurcation and composed of F_7 small rings, lies near the smooth torus. At first, each ring is composed of the stable (shown in black) and unstable (shown in gray) orbits with period F_7 [see the inset in Fig. 3.5(a)]. However, as the parameters increase such rings make evolution, as shown in Fig. 3.5(b) for $a = 0.86$ and $\varepsilon = 0.375$. For fixed values of a and ε, the phase θ may be regarded as a "bifurcation parameter." As θ is changed, a chaotic attractor appears via an infinite sequence of period doubling bifurcations of stable periodic orbits in each ring, and then it disappears via a boundary crisis when it collides with the unstable F_7-periodic orbit [see the inset in Fig. 3.5(b)]. Thus, the attracting part (shown in black) of each ring is composed of the union of the originally stable F_7-periodic attractor and the higher $2^n F_7$-periodic ($n = 1, 2, \ldots$) and chaotic attractors born through the period-doubling cascade. On the other hand, the unstable part (shown in gray) of each ring consists of the union of the originally unstable F_7-periodic orbit [e.g., the upper gray line in the inset in Fig. 3.5(b)] born via a saddle-node bifurcation and the destabilized F_7-periodic orbit [e.g., the lower gray line in the inset in Fig. 3.5(b)] via a period doubling bifurcation. As the parameters are further increased, both the size and shape of the rings change, and for sufficiently large parameters, each ring is composed of a large unstable part (shown in gray) and a small attracting part (shown in black), as shown in Fig. 3.5(c) for $a = 0.96$ and $\varepsilon = 0.4$. Furthermore, new rings may appear inside or outside the "old" rings via another (phase-dependent) saddle-node bifurcation [e.g., see F_7 new small rings in Fig. 3.5(c).] With further increase in the level k of the rational approximations, the ring-shaped unstable set consists of a larger number of rings with a smaller attracting part. Hence, we believe that, in the quasiperiodic limit, the ring-shaped unstable set might become a complicated invariant unstable set composed of only unstable orbits.

In terms of the rational approximation of level 7, we now explain the mechanism for the intermittent transition occurring in Figs. 3.4(b) - 3.4(e) for $a = 0.96$. As we approach the border of the intermittent transition in the phase diagram, the ring-shaped unstable set comes closer to the smooth torus (denoted by a black curve), as shown in Fig. 3.5(c) for $\varepsilon = 0.4$ [a magnified view is given in Fig. 3.5(d)]. As ε passes a threshold value $\varepsilon_7^{(1)}$

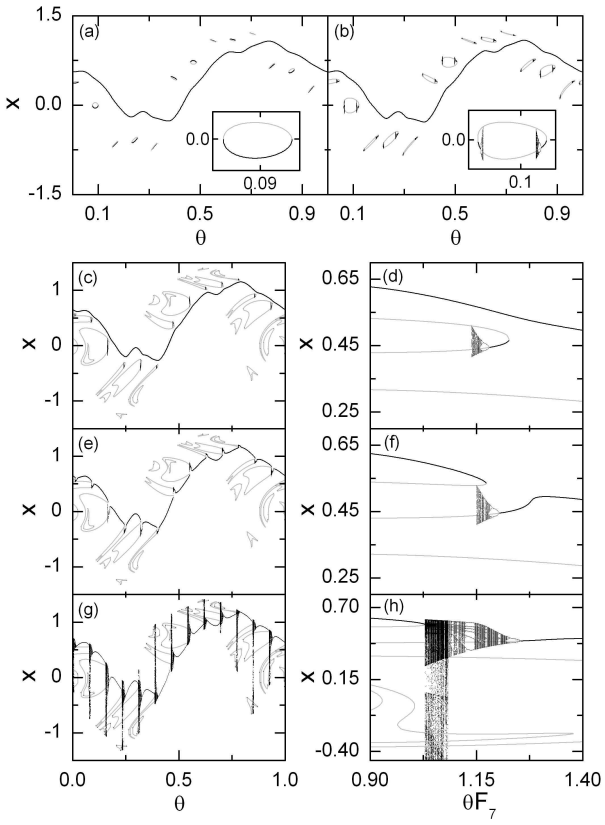

Figure 3.5: Dynamical mechanism for the intermittent route to strange nonchaotic attractors in the quasiperiodically forced Hénon map. In (a)-(h), projections of the attractor and the ring-shaped unstable set onto the $\theta - x$ plane are given in the rational approximation of level 7. A smooth torus (denoted by a black curve) and a ring-shaped unstable set [composed of F_7 (=13) rings] are shown for (a) $a = 0.85$ and $\varepsilon = 0.3707$ and (b) $a = 0.86$ and $\varepsilon = 0.375$. Each ring is composed of the attracting part (shown in black) and the unstable part (shown in gray and consisting of unstable F_7-periodic orbits). Magnified views of rings are given in insets. In (c), a ring-shaped unstable set [composed of $2F_7$ (= 26) rings] lies close to the smooth torus (denoted by a black curve) for $a = 0.96$ and $\varepsilon = 0.4$. A magnified view near $(\theta F_7, x) = (1.15, 0.45)$ is given in (d). For this case, the intermittent transition from a smooth torus to a strange nonchaotic attractor occurs through the following two procedures. First, the rational approximation to the attractor becomes nonsmooth via a phase-dependent saddle-node bifurcation, as shown in (e) [a magnified view is given in (f)] for $a = 0.96$ and $\varepsilon = 0.4015$. Second, the chaotic component in the rational approximation to the attractor becomes suddenly widened via an interior crisis, as shown in (g) [a magnified view is given in (h)] for $a = 0.96$ and $\varepsilon = 0.4045$. Thus, F_7 "gaps," filled by intermittent chaotic attractors, are formed. For more details, see the text.

($= 0.401\,035\,615$), a phase-dependent saddle-node bifurcation occurs between the smooth torus and the unstable part (shown in gray) of the ring-shaped unstable set. Then, the new attractor of the system contains the attracting part (shown in black) of the ring-shaped unstable set and becomes nonsmooth, which is shown in Fig. 3.5(e) for $\varepsilon = 0.4015$ [see a magnified view in Fig. 3.5(f)]. As ε is further increased, the chaotic component in the rational approximation to the attractor increases, and eventually for $\varepsilon_7^{(2)} = 0.403\,399\,486$, it becomes suddenly widened via an interior crisis when it collides with the nearest ring [e.g., see Fig. 3.5(g) for $\varepsilon = 0.4045$]. Then, F_7 [$= 13$] "gaps," where no attractors with period F_7 exist, are formed. A magnified gap is shown in Fig. 3.5(h). Note that this gap is filled by intermittent chaotic attractors. This rational approximation to the whole attractor consists of the union of the periodic and chaotic components. For this case, the periodic component dominates, and hence the average 1st Lyapunov exponent ($\langle\sigma_1\rangle = -0.168$) becomes negative, where $\langle\cdots\rangle$ denotes the average over the whole θ. Hence, the rational approximation to the attractor becomes nonchaotic. We note that this 7th rational approximation to the attractor in Fig. 3.5(g) resembles the (original) intermittent strange nonchaotic attractor in Fig. 3.4(d), although the level of the rational approximation is low. Thus, in the rational approximations the intermittent transition to a strange nonchaotic attractor consists of two stages: the phase-dependent saddle-node bifurcation and the interior crisis. This is in contrast to the previously-reported case in the quasiperiodically forced logistic map [66], where the intermittent transition occurs directly through only the phase-dependent saddle-node bifurcation. Increasing the level to $k = 18$, we obtain the threshold values $\varepsilon_k^{(1)}$ and $\varepsilon_k^{(2)}$ at which the phase-dependent saddle-node bifurcation and the interior crisis occur, respectively. As the level k increases, the difference $\Delta\varepsilon_k$ [$\equiv \varepsilon_k^{(2)} - \varepsilon_k^{(1)}$] tends to zero, and both sequences of $\{\varepsilon_k^{(1)}\}$ and $\{\varepsilon_k^{(2)}\}$ converge to the same quasiperiodic limit ε^* ($= 0.416\,857\,986$) in an algebraic manner, $|\Delta\varepsilon_k^{(i)}|$ [$\equiv |\varepsilon_k^{(i)} - \varepsilon^*|$] $\sim F_k^{-\alpha}$ ($i = 1, 2$), where $\alpha \simeq 2.0$, as shown in Fig. 3.6. In the quasiperiodic limit $k \to \infty$, the rational approximation to the attractor has a dense set of gaps which are filled by intermittent chaotic attractors. Consequently, an intermittent strange nonchaotic attractor, containing the whole ring-shaped unstable set, appears, as shown in Fig. 3.4(d). As ε is further increased and passes another threshold value ε^c ($= 0.416\,879$), the strange nonchaotic attractor transforms into a chaotic attractor.

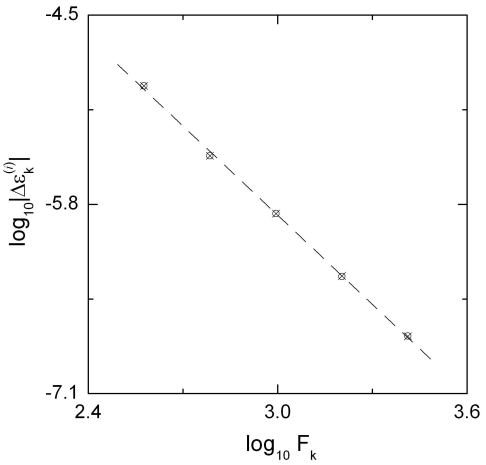

Figure 3.6: Plot of $\log_{10}|\Delta\varepsilon_k^{(i)}|$ vs. $\log_{10} F_k$ for $k = 14, \ldots, 18$ [$\Delta\varepsilon_k^{(i)} = \varepsilon_k^{(i)} - \varepsilon^*$, i=1 (circles) and 2(crosses)]. Here, $\varepsilon_k^{(1)}$ and $\varepsilon_k^{(2)}$ represent the threshold values for the saddle-node bifurcation and the interior crisis in the rational approximation of level k, respectively, and ε^* denotes the quasiperiodic limit.

As a second example, we consider the quasiperiodically forced ring map [53],

$$M : \begin{cases} x_{n+1} &= x_n + \Omega - \frac{a}{2\pi}\sin 2\pi x_n + b y_n \\ & \quad +\varepsilon\cos 2\pi\theta_n \pmod 1, \\ y_{n+1} &= b y_n - \frac{a}{2\pi}\sin 2\pi x_n, \\ \theta_{n+1} &= \theta_n + \omega \pmod 1, \end{cases} \tag{3.3}$$

where a quasiperiodic forcing of the frequency ω and amplitude ε is acted on the two-dimensional ring map with the parameters of the nonlinearity a and phase shift Ω. This quasiperiodically forced ring map is an invertible dissipative map, because it has a nonzero constant Jacobian determinant b ($b \neq 0$ and $-1 < b < 1$). (In the singular limit of $b = 0$, this map is reduced to the quasiperiodically forced circle map [54].) Here, the value of b is fixed at $b = 0.01$. This system M may be used as a model for the quasiperiodically forced pendulum, Josepson junction, and charge-density wave [95].

We consider the case of $\Omega = 0$. For this case, the quasiperiodically forced ring map has a symmetry, because it is invariant under the transformation,

$$S : \; x \to -x, \;\; y \to -y, \;\; \text{and} \;\; \theta \to \theta + 1/2. \tag{3.4}$$

Here, we set ω to be the reciprocal of the golden mean (i.e., $\omega = (\sqrt{5}-1)/2$), and investigate

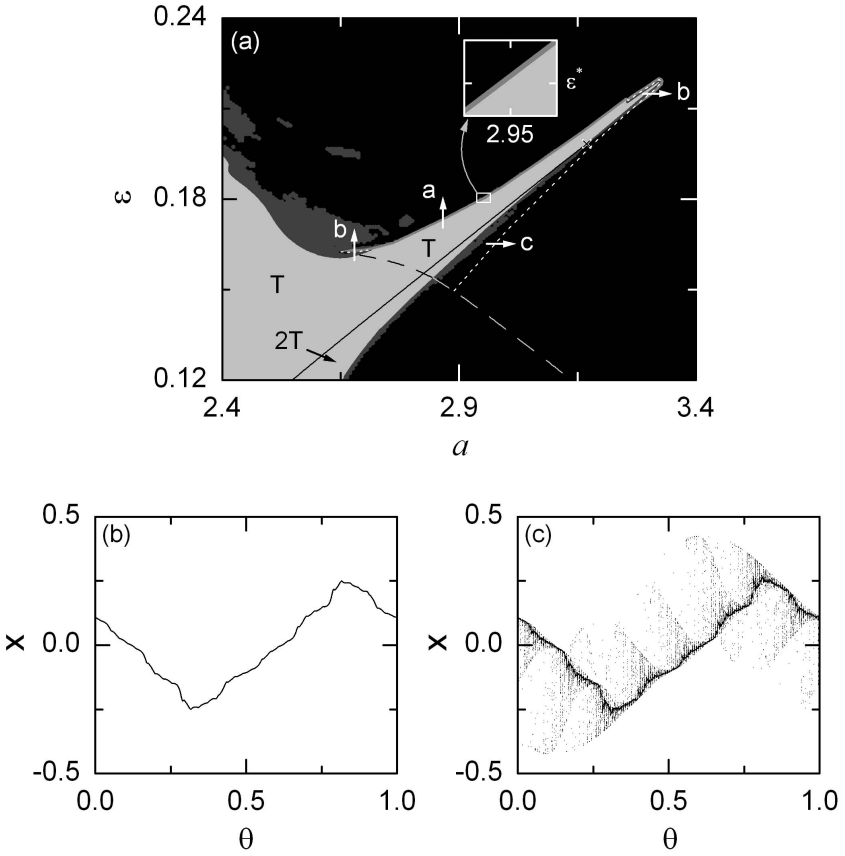

Figure 3.7: (a) Phase Diagram of the quasiperiodically forced ring map in the $a-\varepsilon$ plane for the case of $b = 0.01$ and $\omega = (\sqrt{5}-1)/2$. In the thin gray region, intermittent strange nonchaotic attractors exist, while in the dark gray region, nonintermittent strange nonchaotic attractors exist. Here all phases are symmetric. Regular, chaotic, and strange nonchaotic attractor regimes are shown in light gray, black, and gray (or dark gray), respectively. To show the region of existence (gray) of the intermittent strange nonchaotic attractor occurring between T (light gray) and the chaotic attractor region (black), a small box near $(a, \varepsilon) = [2.95, \varepsilon^*(= 0.180\,275\,991)]$ is magnified. Through interaction with the ring-shaped unstable set born when passing the dashed line, typical dynamical transitions such as the intermittency (route a) and the interior crisis (routes b and c; the dotted line is an interior crisis line) may occur. Here the torus and the doubled torus are denoted by T and $2T$ and the solid line represents a torus doubling bifurcation curve whose terminal point is marked with the cross. Projections of (b) the symmetric smooth torus for $a = 2.95$ and $\varepsilon = 0.1801$ and (c) the symmetric intermittent strange nonchaotic attractor for $a = 2.95$ and $\varepsilon = 0.180\,276$ onto the $\theta - x$ plane are shown. In (b) [(c)], the initial orbit point is $(x_0, y_0, \theta_0) = (0.0, 0.0, 0.0)$, 5×10^3 points are computed before plotting, and the next 10^4 (6×10^4) points are plotted. For other details, see the text.

the transition to intermittent strange nonchaotic attractors by using the rational approximations. Figure 3.7(a) shows a phase diagram in the $a - \varepsilon$ plane, where all phases are symmetric ones. Each dynamical phase is characterized by calculating both the nontrivial Lyapunov exponents, σ_1 and σ_2, associated with dynamics of the variables x and y and the phase sensitivity exponent δ. As in the quasiperiodically forced Hénon map, a tongue of quasiperiodic motion, penetrating into the chaotic region, lies near the terminal point (denoted by the cross) of the torus doubling bifurcation line (represented by the solid line). When crossing the upper boundary of the tongue [see the route a in Fig. 3.7(a)], a transition to an intermittent strange nonchaotic attractor occurs. As an example, we consider the case of $a = 2.95$. For $\varepsilon = 0.1801$, a symmetric smooth torus with $\sigma_1 = -0.069$ exists, as shown in Fig. 3.7(b). However, as ε passes a threshold value ε^* ($= 0.180\,275\,991$), dynamical transition to a symmetric intermittent strange nonchaotic attractor occurs [e.g., see the strange nonchaotic attractor with $\sigma_1 = -0.004$ and $\delta \simeq 20.5$ in Fig. 3.7(c) for $\varepsilon = 0.180\,276$].

We now use the rational approximation of level 7 and explain the mechanism for the intermittent route to strange nonchaotic attractors occurring for $a = 2.95$. Since the driving period F_7 ($= 13$) is an odd number, all orbits, constituting the rational approximations to the symmetric attractor and the symmetric ring-shaped unstable set, are asymmetric ones with respect to the θ-transformation in S of Eq. (3.4). However, such rational approximations are symmetric because they contain all conjugate pairs of asymmetric orbits in the whole range of θ ($0 \le \theta < 1$). This is in contrast to the case of even driving periods, where all orbits in the rational approximations are symmetric ones. Figure 3.8(a) shows that a ring-shaped unstable set, composed of $14F_7$ ($= 182$) rings, lies close to the smooth torus (denoted by a black curve) for $\varepsilon = 0.177$. In a basic interval of $\theta F_7 \in [0.2, 1.2)$, a magnified view of conjugate pairs of asymmetric orbits (the nearest orbit point conjugate to an asymmetric orbit point lying at a given θF_7 lies at $\theta F_7 + 1/2$), constituting the smooth torus and the ring-shaped unstable set, is shown in Fig. 3.8(b). As ε passes a threshold value $\varepsilon_7^{(1)}$ ($= 0.177\,196\,924$), a pair of phase-dependent saddle-node bifurcations occurs through the collision of the smooth torus and the unstable part (shown in gray) of the ring-shaped unstable set. Consequently, the rational approximation to the new attractor, containing the attracting part (shown in black) of the ring-shaped unstable set, becomes nonsmooth, as shown in Figs. 3.8(c) and 3.8(d) for $\varepsilon = 0.1775$. As ε passes another threshold value $\varepsilon_7^{(2)}$ ($= 0.177\,855\,989$), the chaotic component

in the rational approximation becomes abruptly widened via a pair of interior crises [e.g., see Fig. 3.8(e) for $\varepsilon = 0.178$]. Then, "gaps" without F_7-periodic attractors are formed, and they are filled by intermittent chaotic attractors. Figure 3.8(f) shows a conjugate pair of asymmetric gaps in a basic interval of $\theta F_7 \in [0.2, 1.2)$. Hence, the rational approximation to the whole attractor contains $2F_7$ $(= 26)$ gaps. This is in contrast to the case of the quasiperiodically forced Hénon map without symmetry, where only F_7 gaps appear through the interior crisis [see Fig. 3.5(g)]. Furthermore, the rational approximation to the whole attractor becomes nonchaotic, because its average 1st Lyapunov exponent is $\langle \sigma_1 \rangle = -0.053$. We note that this 7th rational approximation to the attractor in Fig. 3.8(e) is similar to the (original) intermittent strange nonchaotic attractor in Fig. 3.7(c), although the level of the rational approximation is low. By increasing the level to $k = 16$, we get the threshold values $\varepsilon_k^{(1)}$ and $\varepsilon_k^{(2)}$ at which the phase-dependent saddle-node bifurcation and the interior crisis occur, respectively. It is thus found that as the level k increases, both sequences of $\{\varepsilon_k^{(1)}\}$ and $\{\varepsilon_k^{(2)}\}$ converge to the same quasiperiodic limit ε^* $(= 0.180\,275\,991)$ in an algebraic way, $|\Delta\varepsilon_k^{(i)}|$ $[\equiv |\varepsilon_k^{(i)} - \varepsilon^*|] \sim F_k^{-\alpha}$ $(i = 1, 2)$, where $\alpha \simeq 2.0$. Note that the value of α is the same as that in the quasiperiodically forced Hénon map. In the quasiperiodic limit $k \to \infty$, the rational approximation to the attractor has a dense set of gaps filled by intermittent chaotic attractors. Consequently, a symmetric intermittent strange nonchaotic attractor, containing the whole ring-shaped unstable set, appears when passing the threshold value ε^*, as shown in Fig. 3.7(c). This intermittent strange nonchaotic attractor transforms into a symmetric chaotic attractor as ε passes another threshold value ε^c $(= 0.185\,276\,21)$.

As a third example, we consider the Toda oscillator with an asymmetric exponential potential [96] which is quasiperiodically forced at two incommensurate frequencies,

$$\ddot{x} + \gamma\dot{x} + e^x - 1 = a\cos\omega_1 t + \varepsilon\cos\omega_2 t, \tag{3.5}$$

where γ is the damping coefficient, a and ε represent the amplitudes of the quasiperiodic forcing, and ω $(\equiv \omega_2/\omega_1)$ is irrational. By making a normalization, $\omega_1 t \to 2\pi t$, Eq. (3.5) can be reduced to three first-order differential equations,

$$\begin{aligned} &\dot{x} = y, \\ &\dot{y} = -\tfrac{2\pi}{\omega_1}\gamma y + \tfrac{4\pi^2}{\omega_1^2}(-e^x + 1 + a\cos 2\pi t + \varepsilon\cos 2\pi\theta), \\ &\dot{\theta} = \omega \pmod 1. \end{aligned} \tag{3.6}$$

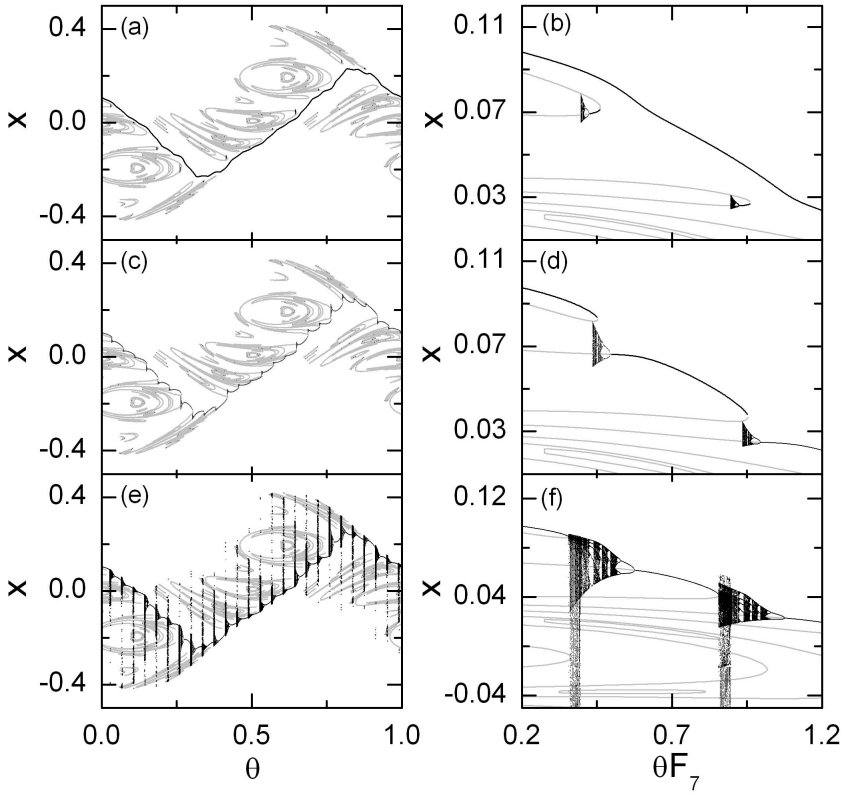

Figure 3.8: Intermittent route to strange nonchaotic attractors for $a = 2.95$ in the quasiperiodically forced ring map. In (a)-(f), projections of the attractor and the ring-shaped unstable set onto the $\theta - x$ plane are given in the rational approximation of level 7. In (a), a symmetric ring-shaped unstable set [composed of $14F_7$ $(= 182)$ rings] lies close to a symmetric smooth torus (denoted by a black curve) for $\varepsilon = 0.177$. A magnified view near $(\theta F_7, x) = (0.7, 0.07)$ is given in (b). In the rational approximation, the intermittent transition from the symmetric smooth torus to a symmetric strange nonchaotic attractor occurs through the following two stages. First, the rational approximation to the attractor becomes nonsmooth via a pair of phase-dependent saddle-node bifurcations, as shown in (c) [a magnified view is given in (d)] for $\varepsilon = 0.1775$. Second, the chaotic component in the rational approximation to the attractor becomes suddenly widened via a pair of interior crises, as shown in (e) [a magnified view is given in (f)] for $\varepsilon = 0.178$. Thus, $2F_7$ $(= 26)$ "gaps," filled by intermittent chaotic attractors, are formed. For more details, see the text.

This system may be used as a model for the quasiperiodically forced RLC circuit [97].

The phase space of the quasiperiodically forced Toda oscillator is four dimensional with coordinates x, y, θ, and t. Since the system is periodic in t, it is convenient to regard time as a circular coordinate in the phase space. Then, we consider the surface of section, the x-y-θ hypersurface at integer times (i.e., $t = n$, n: integer). The phase-space trajectory intersects the surface of section in a sequence of points. This sequence of points corresponds to a mapping on the 3D hypersurface. The map can be computed by stroboscopically sampling the orbit points $\mathbf{v}_n$ $[\equiv (x_n, y_n, \theta_n)]$ at the discrete time n. We call the transformation $\mathbf{v}_n \to \mathbf{v}_{n+1}$ the Poincaré map, and write $\mathbf{v}_{n+1} = P(\mathbf{v}_n)$. This 3D Poincaré map P has a constant Jacobian determinant of $e^{-\gamma T_1}$, where $T_1 = 2\pi/\omega_1$.

Here, we set ω to be the reciprocal of the golden mean [i.e., $\omega = (\sqrt{5} - 1)/2$)], and investigate the intermittent route to strange nonchaotic attractors in the 3D Poincaré map P for the case of $\gamma = 0.8$ and $\omega_1 = 2.0$. Figure 3.9(a) shows a phase diagram in the $a - \varepsilon$ plane. Here each dynamical phase is characterized in terms of the nontrivial Lyapunov exponents, σ_1 and σ_2 (associated with dynamics of the variables x and y), and the phase sensitivity exponent δ. As in the preceding examples, a tongue of quasiperiodic motion, penetrating into the chaotic region, exists near the terminal point (denoted by the cross) of the torus doubling bifurcation curve (represented by the solid line). When crossing the upper boundary of the tongue [see the route a in Fig. 3.9(a)], an intermittent transition to a strange nonchaotic attractor takes place. As an example, we consider the case of $a = 18$. For $\varepsilon = 0.764$, a smooth torus with $\sigma_1 = -0.043$ exists, as shown in Fig. 3.9(b). However, when passing a threshold value ε^* $(= 0.765\,139\,585)$, dynamical transition to an intermittent strange nonchaotic attractor occurs [e.g., see the strange nonchaotic attractor with $\sigma_1 = -0.004$ and $\delta \simeq 7.6$ in Fig. 3.9(c) for $\varepsilon = 0.765\,15$].

Using the rational approximation of level 7, we explain the mechanism for the intermittent transition to strange nonchaotic attractors occurring for $a = 18$. As ε is increased toward a threshold value $\varepsilon_7^{(1)}$ $(= 0.727\,986\,519)$, the ring-shaped unstable set, composed of $2F_7$ $(= 26)$ rings, comes closer to the smooth torus (denoted by a black curve), as shown in Fig. 3.10(a) for $\varepsilon = 0.715$ [a magnified view is given in Fig. 3.10(b)]. When passing the threshold value $\varepsilon_7^{(1)}$, a phase-dependent saddle-node bifurcation occurs between the smooth torus and the unstable part (shown in gray) of the ring-shaped unstable set. Then, the smooth torus is

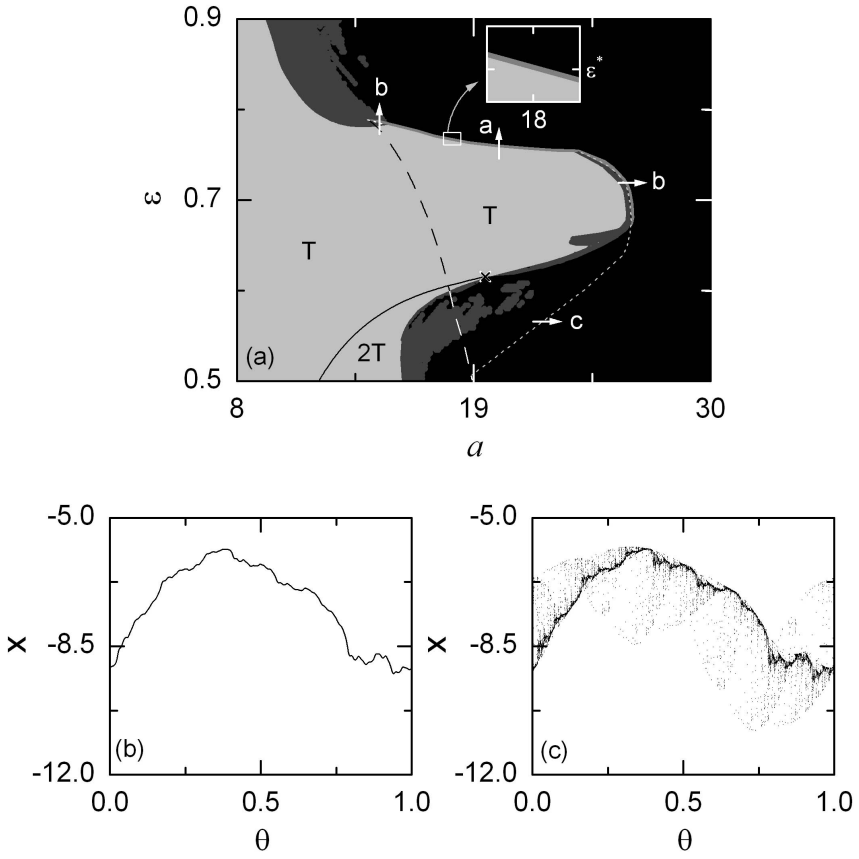

Figure 3.9: (a) Phase Diagram of the quasiperiodically forced Toda oscillator in the $a-\varepsilon$ plane for the case of $\gamma = 0.8, \omega_1 = 2.0$, and $\omega = (\sqrt{5}-1)/2$. Regular, chaotic, and strange nonchaotic attractor regimes are shown in light gray, black, and gray (or dark gray), respectively. In the thin gray region, intermittent strange nonchaotic attractors exist, while in the dark gray region, nonintermittent strange nonchaotic attractors exist. To show the region of existence (gray) of the intermittent strange nonchaotic attractor occurring between T (light gray) and the chaotic attractor region (black), a small box near $(a, \varepsilon) = [18, \varepsilon^*(= 0.765\,139\,585)]$ is magnified. Through interaction with the ring-shaped unstable set born when passing the dashed line, typical dynamical transitions such as the intermittency (route a) and the interior crisis (routes b and c; the dotted line is an interior crisis line) may occur. Here the torus and the doubled torus are denoted by T and $2T$ and the solid line represents a torus doubling bifurcation curve whose terminal point is marked with the cross. Projections of (b) the smooth torus for $a = 18$ and $\varepsilon = 0.764$ and (c) the intermittent strange nonchaotic attractor for $a = 18$ and $\varepsilon = 0.765\,15$ onto the $\theta - x$ plane are shown. In (b) [(c)], the initial orbit point is $(x_0, y_0, \theta_0) = (-8, 8, 0)$, 5×10^3 points are computed before plotting, and the next 10^4 (6×10^4) points are plotted. For other details, see the text.

broken, and a nonsmooth attractor, containing the attracting part (shown in black) of the ring-shaped unstable set, appears [e.g., see Figs. 3.10(c) and 3.10(d) for $\varepsilon = 0.729$]. As ε is further increased, the chaotic component in the rational approximation to the attractor increases, and eventually for $\varepsilon_7^{(2)} = 0.734\,049\,948$, it becomes abruptly widened via an interior crisis [e.g., see Fig. 3.10(e) for $\varepsilon = 0.74$]. Then, F_7 "gaps" without F_7-periodic attractors appear. Figure 3.10(f) shows a magnified gap, filled by intermittent chaotic attractors. Moreover, the rational approximation to the attractor is nonchaotic, because $\langle \sigma_1 \rangle = -0.102$. We note that the 7th rational approximation to the attractor in Fig. 3.10(e) resembles the (original) intermittent strange nonchaotic attractor in Fig. 3.9(c), although the level of the rational approximation is low. Increasing the level to $k = 15$, we obtain the threshold values $\varepsilon_k^{(1)}$ and $\varepsilon_k^{(2)}$ at which the phase-dependent saddle-node bifurcation and the interior crisis occur, respectively. As the level k increases, both sequences of $\{\varepsilon_k^{(1)}\}$ and $\{\varepsilon_k^{(2)}\}$ are found to converge to the same quasiperiodic limit ε^* $(= 0.765\,139\,585)$ in an algebraic way, $|\Delta\varepsilon_k^{(i)}|$ $[\equiv |\varepsilon_k^{(i)} - \varepsilon^*|] \sim F_k^{-\alpha}$ $(i = 1, 2)$, where $\alpha \simeq 2.0$. We note that the value of α is the same as that in the preceding examples within numerical accuracy. In the quasiperiodic limit $k \to \infty$, the rational approximation to the attractor has a dense set of gaps filled by intermittent chaotic attractors. As a result, an intermittent strange nonchaotic attractor, containing the whole ring-shaped unstable set, appears, as shown in Fig. 3.9(c). As ε is further increased, the value of $\langle \sigma_1 \rangle$ of the strange nonchaotic attractor increases, and eventually for $\varepsilon = \varepsilon^c$ $(= 0.765\,154)$, it becomes zero. Then, a transition to chaos occurs.

3.2 Band-Merging Route to Strange Nonchaotic Attractors

We investigate the mechanism for the band-merging route to strange nonchaotic attractors in the quasiperiodically forced logistic map as a representative model for quasiperiodically forced period-doubling systems [68]. When the smooth unstable torus loses its accessibility from the interior of the basin of an attractor, it cannot induce the "standard" band-merging transition. For this case, we use the rational approximation to the quasiperiodic forcing and show that a new type of band-merging transition occurs for a nonchaotic attractor (smooth

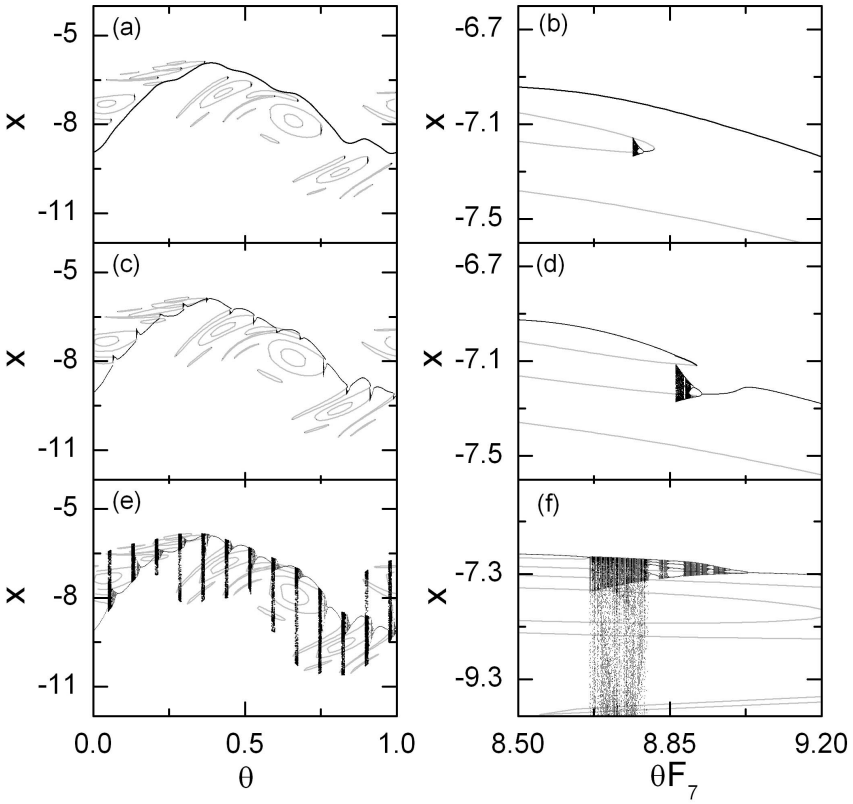

Figure 3.10: Intermittent route to strange nonchaotic attractors for $a = 18$ in the quasiperiodically forced Toda oscillator. In (a)-(f), projections of the attractor and the ring-shaped unstable set onto the $\theta - x$ plane are given in the rational approximation of level 7. In (a), the ring-shaped unstable set [composed of $2F_7$ (= 26) rings] lies close to the smooth torus (denoted by a black curve) for $\varepsilon = 0.715$. A magnified view near $(\theta F_7, x) = (8.85, -7.1)$ is given in (b). In the rational approximation, the intermittent transition from a smooth torus to a strange nonchaotic attractor occurs through the following two stages. First, the rational approximation to the attractor becomes nonsmooth via a phase-dependent saddle-node bifurcation, as shown in (c) [a magnified view is given in (d)] for $\varepsilon = 0.729$. Second, the chaotic component in the rational approximation to the attractor becomes abruptly widened via an interior crises, as shown in (e) [a magnified view is given in (f)] for $\varepsilon = 0.74$. Thus, F_7 (= 13) "gaps," filled by intermittent chaotic attractors, are formed. For more details, see the text.

torus or strange nonchaotic attractor) as well as a chaotic attractor through a collision with an invariant ring-shaped unstable set which has no counterpart in the unforced case. Particularly, a two-band smooth torus is found to transform into a single-band intermittent strange nonchaotic attractor via a new band-merging transition, which corresponds to a new mechanism for the appearance of strange nonchaotic attractors. Characterization of the intermittent strange nonchaotic attractor is made in terms of the average time between bursts and the local Lyapunov exponents. We also confirm for the universality of the band-merging route to strange nonchaotic attractors in the quasiperiodically forced Hénon map and Toda oscillator [69].

3.2.1 Band-Merging Transitions in the Quasiperiodically Forced Logistic Map

We study band-merging transitions in the quasiperiodically forced logistic map M, which is often used as a representative model for the quasiperiodically forced period-doubling systems:

$$M : \begin{cases} x_{n+1} = (a + \varepsilon \cos 2\pi\theta_n) x_n (1 - x_n), \\ \theta_{n+1} = \theta_n + \omega \pmod 1, \end{cases} \tag{3.7}$$

where $x \in [0, 1]$, $\theta \in S^1$, a is the nonlinearity parameter of the logistic map, and ω and ε represent the frequency and amplitude of the quasiperiodic forcing, respectively. This quasiperiodically forced logistic map M is noninvertible, because its Jacobian determinant becomes zero along the critical curve, $L_0 = \{x = 0.5,\ \theta \in [0, 1)\}$. Critical curves of rank k, L_k $(k = 1, 2, \ldots)$, are then given by the images of L_0, [i.e., $L_k = M^k(L_0)$; M^k is the kth iterate of M]. Segments of these critical curves can be used to define a bounded trapping region of the phase space, called an "absorbing area," inside which, upon entering, trajectories are henceforth confined [82].

Here, we set the frequency to be the reciprocal of the golden mean, $\omega = (\sqrt{5} - 1)/2$. For the inverse golden mean, its rational approximants are given by the ratios of the Fibonacci numbers, $\omega_k = F_{k-1}/F_k$, where the sequence of $\{F_k\}$ satisfies $F_{k+1} = F_k + F_{k-1}$ with $F_0 = 0$ and $F_1 = 1$. Instead of the quasiperiodically forced system, we study an infinite sequence of periodically forced systems with rational driving frequencies ω_k. We assume that the properties of the original system M may be obtained by taking the quasiperiodic limit $k \to$

∞. Using this technique, the mechanism for the band-merging transitions is investigated.

Figure 3.11(a) shows a phase diagram in the $a - \varepsilon$ plane. Each phase is characterized by the Lyapunov exponent σ_x in the x-direction and the phase sensitivity exponent δ. The exponent δ measures the sensitivity with respect to the phase of the quasiperiodic forcing and characterizes the strangeness of an attractor in a quasiperiodically forced system [53]. A smooth torus with two bands which is born via a (first-order) torus doubling bifurcation of its parent torus with a single band exists in the region denoted by $2T$ and shown in light gray. It has a negative Lyapunov exponent ($\sigma_x < 0$) and no phase sensitivity ($\delta = 0$). When crossing the solid line (corresponding to a second-order torus doubling bifurcation line), the two-band torus becomes unstable and bifurcates to a four-band torus which exists in the region denoted by $4T$. Chaotic attractors with positive Lyapunov exponents ($\sigma_x > 0$) exist in the region shown in black. Between these regular and chaotic regions, strange nonchaotic attractors that have negative Lyapunov exponents ($\sigma_x < 0$) and high phase sensitivity ($\delta > 0$) exist in the region shown in gray. Because of their high phase sensitivity, these strange nonchaotic attractors have fractal structure [53]. A main interesting feature of the phase diagram is the existence of a second-order "tongue" that penetrates into the chaotic region. This tongue lies near the terminal point (denoted by the cross) of the second-order torus doubling bifurcation curve, as in the case of the main (first-order) tongue that exists near the terminal point of the first-order torus doubling bifurcation line [e.g., see Fig. 1(a) in [66]]. For a clear view of the second-order tongue, the rectangular region in Fig. 3.11(a) is rotated and magnified in Fig. 3.11(b), using the new parameters, s_1 and s_2, defined by $s_1 = \cos(27^\circ)(a - 3.48) - \sin(27^\circ)(\varepsilon - 0.12)$ and $s_2 = \sin(27^\circ)(a - 3.48) + \cos(27^\circ)(\varepsilon - 0.12)$. Near this tongue, rich dynamical transitions such as band-merging transition (routes A, B, and C), intermittency (route a), and interior crisis (route b) occur through collision with an invariant ring-shaped unstable set which has no counterpart in the unforced case. Here, we are interested in the band-merging transitions, which occur when crossing the white solid curve in Fig. 3.11.

We first consider a band-merging transition of a chaotic attractor which occurs along the route α ($\varepsilon = a - 3.55$) in Fig. 3.11(a). For this case, it is convenient to investigate the band-merging transition in M^2 (i.e., the second iterate of M). For $a = 3.596$ and $\varepsilon = 0.046$, there exists a two-band chaotic attractor with $\sigma_x = 0.159$ in the original map M. This

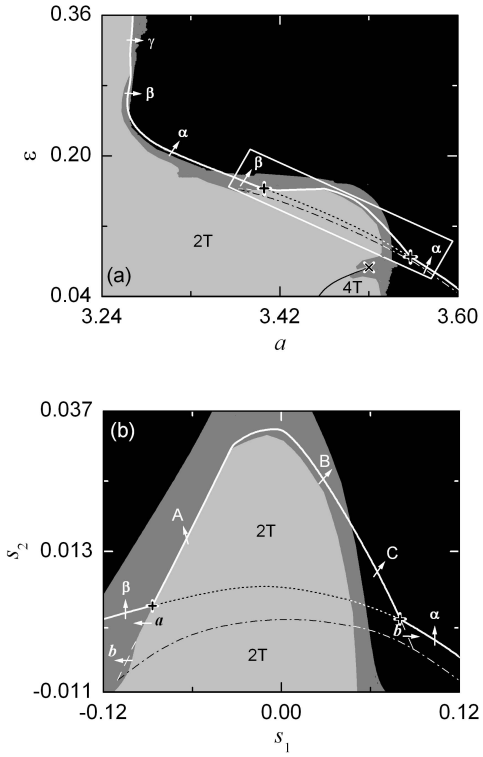

Figure 3.11: (a) Phase Diagram near the second-order tongue in the $a - \varepsilon$ plane. Regular, chaotic, and strange nonchaotic attractor regimes are shown in light gray, black, and gray, respectively. For the case of regular attractor, tori with two and four bands exist in the regions denoted by $2T$ and $4T$, respectively. A second-order "tongue" that penetrates into the chaotic region lies near the terminal point (marked with the cross) of the second-order torus doubling bifurcation curve represented by the solid line. Through collision with the smooth unstable torus, standard band-merging transitions of a chaotic attractor, strange nonchaotic attractor, and smooth torus occur along the routes α, β, and γ, respectively. For a clear view of the tongue, the rectangular region is rotated and magnified in (b), using the new parameters s_1 [$\equiv \cos(27°)(a - 3.48) - \sin(27°)(\varepsilon - 0.12)$] and s_2 [$\equiv \sin(27°)(a - 3.48) + \cos(27°)(\varepsilon - 0.12)$]. A new type of dynamical transitions such as band-merging transition (routes A, B, and C), intermittency (route a), and interior crisis (route b) occur through collision with a ring-shaped unstable set born when passing the dash-dotted line. As the dotted line is crossed, a basin boundary metamorphosis occurs, and then the smooth torus becomes inaccessible from the interior of the basin of the attractor. Note that the band-merging transition curve, denoted by the white solid curve, is not differentiable at the two vertices, denoted by the pluses (+).

chaotic attractor with two bands turns into a pair of conjugate chaotic attractors in M^2, which is denoted by black dots and bounded by the critical curves L_k ($k = 1, \ldots, 8$) in Fig. 3.12(a). The basins of the upper and lower chaotic attractors are shown in light gray and gray, respectively. A smooth unstable torus (denoted by the dashed line) lies on a basin boundary. As the parameters a and ε increase, the conjugate chaotic attractors become closer. Eventually, at a threshold value $(a, \varepsilon) = (3.600\,998, 0.050\,998)$, they contact the smooth unstable torus simultaneously, and merge to form a single chaotic attractor (i.e., an attractor-merging crisis occurs). Thus, for $a = 3.603$ and $\varepsilon = 0.053$, a single-band chaotic attractor with $\sigma_x = 0.196$ appears in M, as shown in Fig. 3.12(b). This band-merging transition corresponds to a natural generalization of the band-merging transition occurring for the unforced case ($\varepsilon = 0$). Hence, we call it the "standard" band-merging transition.

As ε is increased from zero, the standard band-merging transition curve in the $a - \varepsilon$ plane continues smoothly. However, at a lower vertex $(a_l^*, \varepsilon_l^*) \simeq (3.552, 0.085)$ [denoted by a plus (+) in Fig. 3.11(a)], the standard band-merging transition curve ceases and a new type of band-merging transition curve begins by making a sharp turning. Hence, the band-merging transition curve is not differentiable at the vertex. For this case, beyond the vertex the standard band-merging transition curve is smoothly transformed into a curve of a basin boundary metamorphosis line denoted by a dotted line, while the new band-merging transition curve joins smoothly with an interior crisis line denoted by a dashed line at the vertex [see Fig. 3.11(b)]. As the basin boundary metamorphosis line is passed, the basin boundary abruptly jumps in size [78], and when crossing the interior crisis line, a sudden widening of an attractor (without band merging) occurs. Note that these double (band-merging and interior) crises plus a basin boundary metamorphosis take place simultaneously at the vertex [98].

We consider a smooth doubled torus with two bands in M, which exists below the basin boundary metamorphosis line. This two-band torus is transformed into a pair of conjugate single-band tori in M^2. Figure 3.12(c) shows the conjugate tori (denoted by heavy black lines) inside their absorbing areas bounded by the critical curves L_k ($k = 1, \ldots, 8$) for $a = 3.46$ and $\varepsilon = 0.11$. The basins of the upper and lower tori are shown in light gray and gray, respectively. However, when passing the basin boundary metamorphosis line, the absorbing areas become broken up through collision with the unstable parent torus (denoted

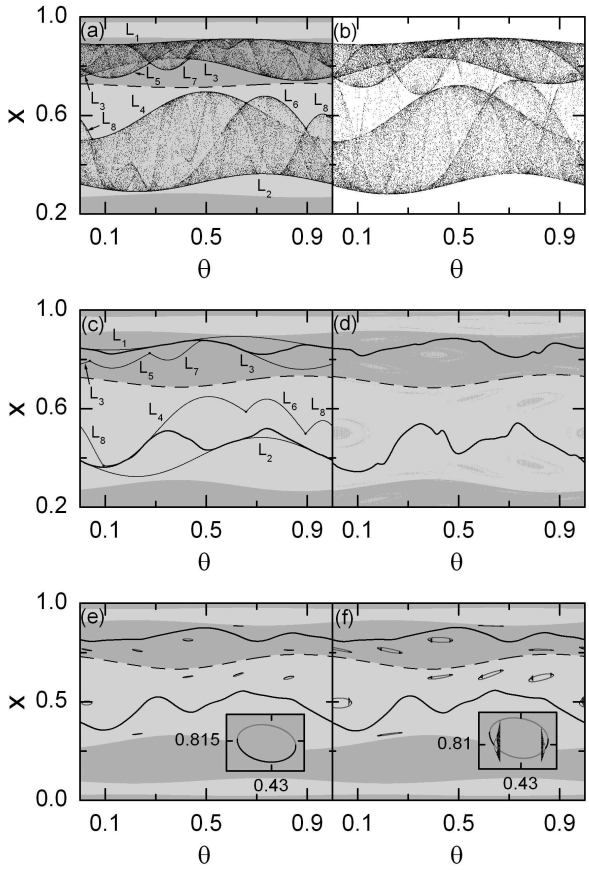

Figure 3.12: (a) and (b) Standard band-merging transition of a chaotic attractor. A two-band chaotic attractor in M turns into a pair of conjugate chaotic attractors in M^2. Such chaotic attractors, denoted by black dots and bounded by the critical curves L_k $(k = 1, \ldots, 8)$, are shown in (a) for $a = 3.596$ and $\varepsilon = 0.046$. The basins of the upper and lower chaotic attractors are shown in light gray and gray, respectively. Through collision with the unstable smooth torus (denoted by a dashed line), the chaotic attractors merge to form a single chaotic attractor, as shown in (b) for $a = 3.603$ and $\varepsilon = 0.053$. (c) and (d) Basin boundary metamorphosis in M^2. (c) A pair of conjugate tori (denoted by heavy black lines) exists inside their absorbing areas bounded by L_k $(k = 1, \ldots, 8)$ for $a = 3.46$ and $\varepsilon = 0.11$. (d) The basin of each torus contains "holes" of other basin of the counterpart for $a = 3.48$ and $\varepsilon = 0.13$ after breakup of the absorbing area. (e) and (f) Appearance of ring-shaped unstable sets in the rational approximation of level 5 in M^2. A pair of conjugate ring-shaped unstable sets exists inside the basins of smooth tori (denoted by a black curve) for (e) $a = 3.396$ and $\varepsilon = 0.146$ and (f) $a = 3.4$ and $\varepsilon = 0.15$. Each ring-shaped unstable set is composed of F_5 $(= 5)$ small rings. Magnified views of a ring are given in the insets. Note that each ring consists of the unstable part (composed of unstable orbits with the forcing period F_5 and shown in dark gray) and the attracting part (shown in black).

by the dashed line) on a basin boundary. Then, the basin of each torus becomes complex, because it contains "holes" of other basin of the counterpart, as shown in Fig. 3.12(d) for $a = 3.48$ and $\varepsilon = 0.13$. Due to this basin boundary metamorphosis, the unstable parent torus becomes inaccessible from the interior of the basins of the upper and lower tori, and hence it cannot induce any band-merging transition. For this case, using the rational approximations to the quasiperiodic forcing, we locate an invariant ring-shaped unstable set that causes a new type of band-merging transition. When passing the dash-dotted line in Fig. 3.11, a pair of conjugate ring-shaped unstable sets is born via phase-dependent saddle-node bifurcations in M^2 [66]. This bifurcation has no counterpart in the unforced case. As an example, in the rational approximation of level $k = 5$ we explain the structure of the ring-shaped unstable set. As shown in Fig. 3.12(e) for $a = 3.396$ and $\varepsilon = 0.146$, the rational approximation to each ring-shaped unstable set, consisting of F_5 $(= 5)$ small rings, exists in the basin of the rational approximation to each smooth torus (denoted by a black curve and composed of stable orbits with period F_5). At first, each ring is composed of the stable (shown in black) and unstable (shown in dark gray) orbits with the forcing period F_5 [see the inset in Fig. 3.12(e)]. However, as the parameters a and ε are increased, these rings evolve, and then each ring consists of a large unstable part (shown in dark gray) and a small attracting part (shown in black) [see the inset in Fig. 3.12(f)]. With increase in the level k of the rational approximation, each ring-shaped unstable set becomes composed of a larger number of rings with a smaller attracting part. Hence, we believe that, in the quasiperiodic limit, the ring-shaped unstable set might become a complicated invariant unstable set consisting of only unstable orbits. Through a collision with this ring-shaped unstable set which has no counterpart in the unforced case, a new type of band-merging transition occurs, as will be shown below.

As ε is further increased, both the new band-merging transition curve and the basin boundary metamorphosis line cease simultaneously at the upper double-crisis vertex (denoted by a plus) $(a_u^*, \varepsilon_u^*) \simeq (3.404, 0.163)$ in Fig. 3.11(a). Then, the standard band-merging transition line, which is connected smoothly with the basin boundary metamorphosis line at the upper vertex, begins again by making an angle. Along the routes α, β, and γ beyond the upper vertex, standard band-merging transitions of a chaotic attractor, strange nonchaotic attractor, and smooth torus occur, respectively, through a collision with the smooth unstable torus. On the other hand, the new band-merging transition curve transforms smoothly to

a curve of intermittency at the upper vertex. When passing the intermittency line [route a in Fig. 3.11(b)], a transition from a smooth two-band torus to an intermittent two-band strange nonchaotic attractor occurs through collision with a ring-shaped unstable set [66]. As in the case of interior crisis [route b Fig. 3.11(b)], the size of the attractor abruptly increases (without band merging). Hereafter, we will investigate the new band-merging transitions which occur along the routes A, B, and C crossing the segment bounded by the two double-crisis vertices [see Fig. 3.11(b)]. A new band-merging transition is found to take place for a nonchaotic attractor [smooth torus (route A) and strange nonchaotic attractor (route B)] as well as a chaotic attractor (route C) through a collision with a ring-shaped unstable set. Particularly, a single-band strange nonchaotic attractor appears as a result of the new band-merging transition of a two-band smooth torus.

We now fix the value of a at $a = 3.43$ and study the band-merging transition from a two-band torus to a single-band intermittent strange nonchaotic attractor by varying ε along the route A. A two-band torus in the original map M is transformed into a pair of conjugate tori in M^2. Figure 3.13(a) shows a pair of upper and lower tori (denoted by black curves) for $\varepsilon = 0.161$, whose basins are shown in light gray and gray, respectively. For this case, the basin of each smooth torus contains holes of other basin of the counterpart. Hence, the smooth unstable torus (denoted by the dashed line) is not accessible from the interior of the basins of the conjugate (attracting) tori. As the parameter ε increases, conjugate tori and holes become closer. Eventually, for $\varepsilon = \varepsilon^*$ $(= 0.161\,323\,479)$ an attractor-merging crisis of the conjugate tori occurs through a collision with a hole boundary, and then for $\varepsilon = 0.163$, a single-band intermittent strange nonchaotic attractor with $\sigma_x = -0.019$ and $\delta = 10.8$ appears in M, as shown in Fig. 3.13(b). Using the rational approximation of level $k = 8$, we investigate the mechanism for the band-merging transition of the smooth torus. Figure 3.13(c) shows conjugate tori (denoted by black lines), conjugate ring-shaped unstable sets (represented by dark gray lines), and holes (shown in gray and light gray inside the basins of the upper and lower tori, respectively) in M^2 for $\varepsilon = 0.1597$. The rational approximations to the smooth torus and the ring-shaped unstable set are composed of stable and unstable orbits with period F_8 $(= 21)$, respectively. For this case, some part of each ring-shaped unstable set (denoted by dark gray curves) lies on a hole boundary (e.g., see a magnified view in Fig. 3.13(d), where holes in the light gray basin are represented by gray dots). With

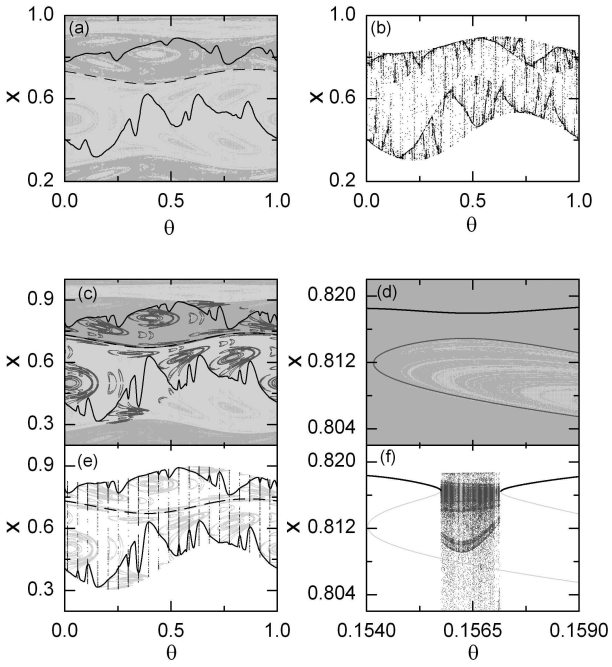

Figure 3.13: Band-merging transition of a two-band torus for $a = 3.43$. There exists a pair of conjugate tori in M^2, which are denoted by black lines in (a) for $\varepsilon = 0.161$. The basins of the upper and lower tori are shown in light gray and gray, respectively. Each basin is complex, because it contains holes of other basin of the counterpart. Through a collision with a hole boundary, the conjugate tori merge into a single-band strange nonchaotic attractor, as shown in (b) for $\varepsilon = 0.163$. (c)-(f) Analysis of the mechanism for the band-merging transition of the two-band torus for $a = 3.43$, using the rational approximation of level 8. In (c), the eight rational approximation to the conjugate tori and ring-shaped unstable sets are plotted in M^2 for $\varepsilon = 0.1597$. For this case, the ring-shaped unstable sets (represented by dark gray curves), some part of which exists on a hole boundary, lie close to the smooth tori (denoted by black lines) (e.g., see a magnified view in (d), where holes in the light gray basin are denoted by gray dots). Through collision between the smooth tori and the ring-shaped unstable sets, F_8 (= 21) "gaps," filled by single-band intermittent chaotic attractors denoted by black dots, are formed, as shown in (e) for $\varepsilon = 0.15976$. For a clear view, a magnified gap is given in (f). In (e) and (f), attractors (denoted by black dots) and ring-shaped unstable sets (represented by gray curves) are plotted in the original map M.

increase in ε, the conjugate tori and ring-shaped unstable sets become closer, and eventually, for $\varepsilon = \varepsilon_8^*$ ($= 0.159\,750\,121$) a pair of phase-dependent saddle-node bifurcations occurs through collision between the conjugate tori and ring-shaped unstable sets. Then, F_8 ($= 21$) "gaps," where no orbits with period F_8 exist, are formed in the whole range of θ, as shown in Fig. 3.13(e) for $\varepsilon = 0.15976$. In these gaps, single-band intermittent chaotic attractors (denoted by black dots) appear (i.e., saddle-node bifurcations induce attractor-merging crises in the gaps) [for a clear view, a magnified gap is given in Fig. 3.13(f)]. Thus, the rational approximation to the whole attractor in the original map M becomes composed of the union of the two-band periodic component and the single-band intermittent chaotic component. Since the periodic component is dominant, the average Lyapunov exponent ($\langle \sigma_x \rangle = -0.105$) is negative, where $\langle \cdots \rangle$ denotes the average over the whole θ. Hence, the (partially-merged) 8th rational approximation to the attractor in Fig. 3.13(e) becomes nonchaotic, and resembles the single-band strange nonchaotic attractor in Fig. 3.13(b), although the level $k = 8$ is low. By increasing the level of the rational approximation to $k = 16$, we study the band-merging transition of the two-band torus. It is thus found that the threshold value ε_k^*, at which the phase-dependent saddle-node bifurcation of level k (inducing attractor-merging crises in the gaps) occurs, converges to the quasiperiodic limit ε^* ($= 0.161\,323\,479$) in an algebraic manner, $|\Delta\varepsilon_k| \sim F_k^{-\alpha}$, where $\Delta\varepsilon_k = \varepsilon_k^* - \varepsilon^*$ and $\alpha \simeq 2.0$. As the level k of the rational approximation increases, the number of gaps, where phase-dependent attractor-merging crises occur, becomes larger, and eventually in the quasiperiodic limit, the rational approximation to the attractor has a dense set of gaps, filled by single-band intermittent chaotic attractors. Consequently, an intermittent single-band strange nonchaotic attractor, containing the ring-shaped unstable set, appears, as shown in Fig. 3.13(b). We note that this transition from a two-band torus to a single-band intermittent strange nonchaotic attractor corresponds to a new mechanism for the appearance of strange nonchaotic attractors.

The intermittent strange nonchaotic attractor, born via an attractor-merging crisis [29], may be characterized in terms of the average time between bursts and the local Lyapunov exponents [60, 61, 62]. A typical trajectory of the second iterate of Eq. (3.7) (i.e., M^2) spends a long stretch of time in the vicinity of one of the two former attractors (i.e., smooth tori), then it bursts out from this region and comes close to the same or other former tori where it remains again for some time interval, and so on. In this way the trajectory irregularly

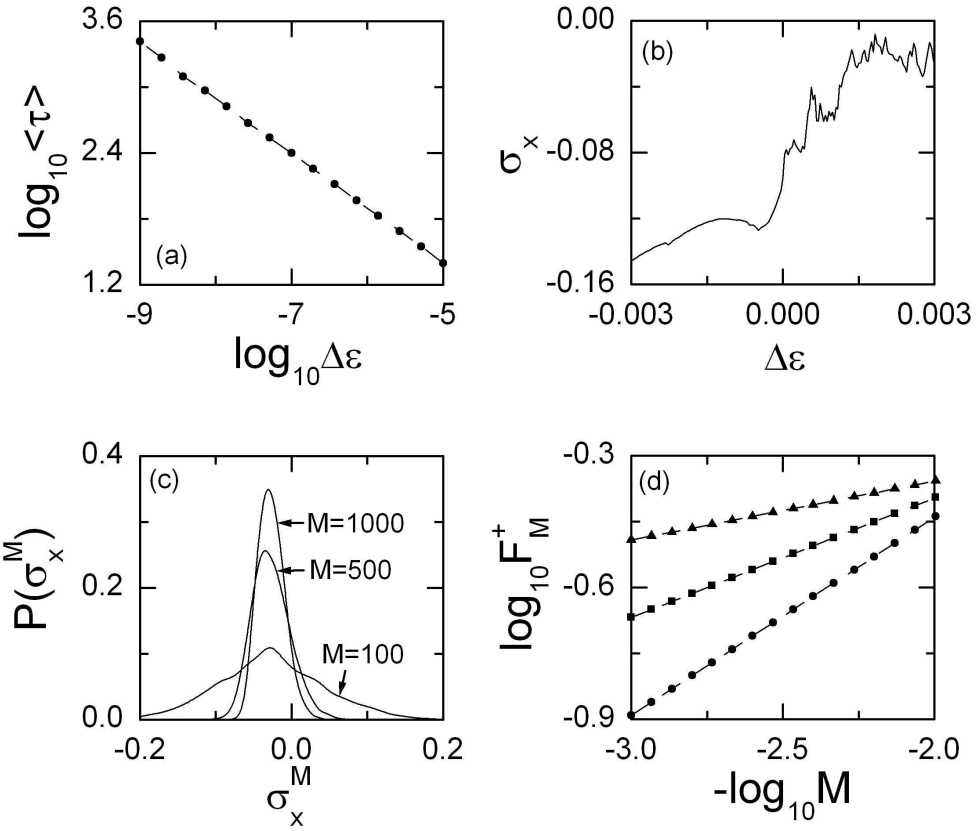

Figure 3.14: (a) Plot of $\log_{10}\langle\tau\rangle$ ($\langle\tau\rangle$ is the average time between bursts) versus $\log_{10}\Delta\varepsilon$ ($\Delta\varepsilon = \varepsilon - \varepsilon^*$) for $a = 3.43$. The data are well fitted with the straight line with the slope $\gamma = 0.5 \pm 0.002$. (b) Plot of σ_x versus $\Delta\varepsilon$ for $a = 3.43$. We note that abrupt change in σ_x near the transition point. (c) Three probability distributions $P(\sigma_x^M)$ of the local M-time Lyapunov exponents for $M = 100$, 500, and 1000 when $a = 3.43$ and $\varepsilon = 0.163$. (d) Plots of $\log_{10} F_M^+$ (F_M^+: fraction of the positive local Lyapunov exponents) versus $-\log_{10} M$. Note that the three plots for $\varepsilon = 0.163$ (circles), 0.165 (squares), and 0.1667 (triangles) are well fitted with the straight lines with the slopes $\eta = 0.45$, 0.27, and 0.13, respectively. Hence F_M^+ decays with some power η.

jumps between the two former tori. For this case, the characteristic time τ is the average over a long trajectory of the time between bursts (i.e., jumps) [29]. As shown in Fig. 3.14(a) for $a = 3.43$, the average value of τ exhibits a power-law scaling behavior,

$$\langle \tau \rangle \sim (\varepsilon - \varepsilon^*)^{-\gamma}, \quad \gamma = 0.5 \pm 0.002. \tag{3.8}$$

The scaling exponent γ is the same as that for the case of the intermittent route to strange nonchaotic attractors occurring near the main tongue of the quasiperiodically forced logistic map [60]. Since the dynamical mechanisms for the appearance of intermittent strange nonchaotic attractors near the main tongue [66] and the second-order tongue (in the present case) are the same (i.e., an intermittent strange nonchaotic attractor appears via a phase-dependent saddle-node bifurcation between a smooth torus and a ring-shaped unstable set), the intermittent strange nonchaotic attractors for both cases seem to exhibit the same scaling behaviors. Figure 3.14(b) shows the plot of the Lyapunov exponent σ_x versus $\Delta\varepsilon$ $(= \varepsilon - \varepsilon^*)$. We note that σ_x abruptly increases during the transition from torus to strange nonchaotic attractor, which is similar to the case of the intermittent route to strange nonchaotic attractor [60]. We also discuss the distribution of local (M-time) Lyapunov exponents σ_x^M, causing the sensitivity of the strange nonchaotic attractor with respect to the phase θ of the quasiperiodic forcing [53]. As an example, we consider the case of $a = 3.43$ and $\varepsilon = 0.163$ and obtain the probability distribution $P(\sigma_x^M)$ of local (M-time) Lyapunov exponents σ_x^M by taking a long trajectory dividing it into segments of length M and calculating σ_x^M in each segment. For $M = 100$, 500, and 1000, $P(\sigma_x^M)$'s are shown in Fig. 3.14(c). In the limit $M \to \infty$, $P(\sigma_x^M)$ approaches the delta distribution $\delta(\sigma_x^M - \sigma_x)$, where σ_x $(= -0.019)$ is just the usual averaged Lyapunov exponent. However, we note that the distribution $P(\sigma_x^M)$ has a significant positive tail which does not vanish even for large M. To quantify this slow decay of the positive tail, we define the fraction of positive local Lyapunov exponents as

$$F_M^+ = \int_0^\infty P(\sigma_x^M) d\sigma_x^M. \tag{3.9}$$

These fractions F_M^+'s are plotted for $\varepsilon = 0.163$, 0.165, and 0.1667 in Fig. 3.14(d). Note that for each value of ε, the fraction F_M^+ exhibits a power-law decay,

$$F_M^+ \sim M^{-\eta}. \tag{3.10}$$

Here the values of the exponent η decreases as ε increases. Consequently, a trajectory on any strange nonchaotic attractor has segments of arbitrarily long M that have positive local Lyapunov exponents, and thus it has a phase sensitivity, inducing the strangeness of the strange nonchaotic attractor. As shown in Fig. 3.14(d), as ε increases the value of F_M^+ becomes larger. Hence, the degree of the phase sensitivity of the strange nonchaotic attractor increases.

When crossing the remaining part of the new band-merging transition curve along the route B (C) in Fig. 3.11(b), a transition from a two-band strange nonchaotic attractor (chaotic attractor) into a single-band one occurs via a collision with a ring-shaped unstable set. We fix the value of ε at $\varepsilon = 0.1305$ and investigate the band-merging transition of a two-band strange nonchaotic attractor by varying a along the route B. For $a = 3.5153$, there exists a two-band strange nonchaotic attractor with $\sigma_x = -0.027$ and $\delta = 1.752$ in the original map M. This two-band strange nonchaotic attractor is transformed into a pair of conjugate strange nonchaotic attractors in M^2, which is denoted by black dots in Fig. 3.15(a). The basins of the upper and lower strange nonchaotic attractors are shown in light gray and gray, respectively. For this case, the unstable smooth torus (denoted by a dashed line) is not accessible from the interior of the basins of the conjugate strange nonchaotic attractors, because the basin of each strange nonchaotic attractor contains holes of other basin of the counterpart. As a is increased, conjugate strange nonchaotic attractors and holes become closer. Eventually, an attractor-merging crisis of the conjugate strange nonchaotic attractors occurs for $a = a^*(= 3.515\,342\,763)$ through a collision with a hole boundary, and then for $a = 3.5157$, a single-band strange nonchaotic attractor with $\sigma_x = -0.013$ and $\delta = 3.734$ appears in M, as shown in Fig. 3.15(b). As in the case of the strange nonchaotic attractor, band-merging transition of a chaotic attractor also occurs along the route C through a collision with a hole boundary. For example, at a fixed value of $\varepsilon = 0.105$, we consider a two-band chaotic attractor with $\sigma_x = 0.023$ in M for $a = 3.535$. This two-band chaotic attractor turns into a pair of conjugate single-band chaotic attractors in M^2, which is represented by black dots in Fig. 3.15(c). An attractor-merging crisis of the upper and lower chaotic attractors takes place when passing a threshold value of $a = 3.538\,034\,276$, and then for $a = 3.545$, a single-band chaotic attractor with $\sigma_x = 0.077$ appears in M, as shown in Fig. 3.15(d). Since the mechanism for the band-merging transition of the

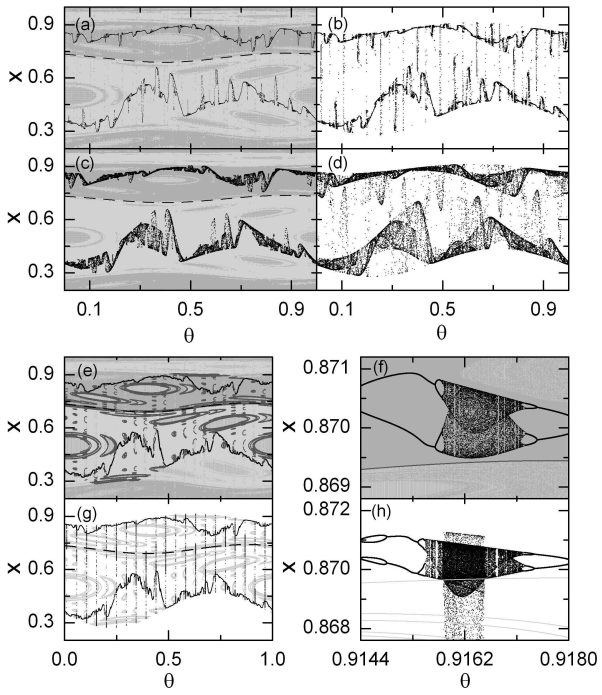

Figure 3.15: (a) and (b) band-merging transition of a two-band strange nonchaotic attractor for a fixed value of $\varepsilon = 0.1305$. A pair of conjugate strange nonchaotic attractors in M^2 is represented by black dots in (a) for $a = 3.5153$. The basins of the upper and lower strange nonchaotic attractors are shown in light gray and gray, respectively. Due to a collision with a hole boundary, the conjugate strange nonchaotic attractors merge to form a single-band strange nonchaotic attractor, as shown in (b) for $a = 3.5157$. (c) and (d) band-merging transition of a two-band chaotic attractor for a fixed value of $\varepsilon = 0.105$. A pair of conjugate chaotic attractors in M^2 is denoted by black dots in (c) for $a = 3.535$. The basins of the upper and lower chaotic attractors are shown in light gray and gray, respectively. Because of a collision with a hole boundary, the upper and lower chaotic attractors merge to form a single-band chaotic attractor, as shown in (d) for $a = 3.545$. (e)-(h) Investigation of the mechanism for the band-merging transition of the strange nonchaotic attractor in the rational approximation of level $k = 8$ for $\varepsilon = 0.1305$. The rational approximations to the conjugate strange nonchaotic attractors and the conjugate ring-shaped unstable sets in M^2 are denoted by black dots and dark gray curves, respectively, in (e) for $a = 3.5224$. Some part of the ring-shaped unstable set, represented by dark gray lines, lies on a hole boundary (e.g., see a magnified view in (f), where holes in the light gray basin are denotde by gray dots). Through collision between the chaotic components of the rational approximations to the conjugate strange nonchaotic attractors and the conjugate ring-shaped unstable sets, F_8 $(= 21)$ "gaps," filled by single-band intermittent chaotic attractors, are formed, as shown in (g) for $a = 3.5229$, [for a clear view, see a magnified gap in (h)]. In (g) and (h), attractors (denoted by black dots) and ring-shaped unstable sets (represented by gray curves) are plotted in the original map M.

chaotic attractor is the same as that for the case of the strange nonchaotic attractor, it is sufficient to consider only the case of the strange nonchaotic attractor for presentation of the mechanism for the band-merging transition. Hence, using the rational approximation of level $k = 8$, we investigate the mechanism for the band-merging transition of the strange nonchaotic attractor along the route B for $\varepsilon = 0.1305$. Figures 3.15(e) and 3.15(f) show the rational approximations to the conjugate strange nonchaotic attractors (denoted by black dots) and conjugate ring-shaped unstable sets (represented by dark gray curves) for $a = 3.5224$. For this case, the rational approximation to a strange nonchaotic attractor is composed of periodic and chaotic components, and some part of the ring-shaped unstable set (denoted by dark gray lines) lies on a hole boundary (e.g., see a magnified view in Fig. 3.15(f), where holes in the light gray basin are denoted by gray dots). As a is increased, the chaotic components of the rational approximations to the conjugate strange nonchaotic attractors and the conjugate ring-shaped unstable sets on the hole boundary become closer. Eventually, for $a = a_8^*$ $(= 3.522\,675\,762)$, they make a collision and then a phase-dependent attractor-merging crisis occurs. Thus, F_8 $(= 21)$ "gaps," filled by single-band intermittent chaotic attractors (represented by black dots), are formed in the whole range of θ, as shown in Fig. 3.15(g) for $a = 3.5229$ [for a clear view, a magnified gap is given in Fig. 3.15(h)]. This (partially-merged) rational approximation to the attractor, composed of the union of the periodic and chaotic components, has a negative average Lyapunov exponent ($\langle\sigma_x\rangle = -0.046$ in M), because its periodic component is dominant. Hence, the 8th rational approximation to the attractor in Fig. 3.15(g) becomes nonchaotic, and is similar to the single-band strange nonchaotic attractor in Fig. 3.15(b). Increasing the level of the rational approximation to $k = 16$, we find that the threshold value a_k^*, at which the phase-dependent attractor-merging crisis of level k occurs, converges to the quasiperiodic limit a^* $(= 3.515\,342\,763)$ in an algebraic manner, $|\Delta a_k| \sim F_k^{-\alpha}$, where $\Delta a_k = a_k^* - a^*$ and $\alpha \simeq 2.8$. In the quasiperiodic limit $k \to \infty$, there appear a dense set of gaps, filled by single-band intermittent chaotic attractors, in the rational approximation to the attractor. Consequently, when passing the threshold value a^* along the route B, a transition from a two-band strange nonchaotic attractor to an intermittent single-band strange nonchaotic attractor, containing the ring-shaped unstable set, occurs.

3.2.2 Universality for the Band-Merging Route to Strange Nonchaotic Attractors

We consider the quasiperiodically forced Hénon map, which is a representative model for the quasiperiodically forced period-doubling systems:

$$M : \begin{cases} x_{n+1} = a - x_n^2 + y_n + \varepsilon \cos 2\pi\theta_n, \\ y_{n+1} = bx_n, \\ \theta_{n+1} = \theta_n + \omega \pmod 1, \end{cases} \tag{3.11}$$

where a is the nonlinearity parameter of the unforced Hénon map, and ω and ε represent the frequency and amplitude of the quasiperiodic forcing, respectively. This quasiperiodically forced Hénon map M is invertible, because it has a nonzero constant Jacobian determinant $-b$ whose magnitude is less than unity (i.e., $b \neq 0$ and $-1 < b < 1$). Here, we fix the value of the dissipation parameter b at $b = 0.05$, and set the frequency ω to be the reciprocal of the golden mean, $\omega = (\sqrt{5} - 1)/2$. Then, using the rational approximation to this quasiperiodic forcing, we investigate the dynamical mechanism for the band-merging route to intermittent strange nonchaotic attractors. For the inverse golden mean, its rational approximants are given by the ratios of the Fibonacci numbers, $\omega_k = F_{k-1}/F_k$, where the sequence of $\{F_k\}$ satisfies $F_{k+1} = F_k + F_{k-1}$ with $F_0 = 0$ and $F_1 = 1$. Instead of the quasiperiodically forced system, we study an infinite sequence of periodically forced systems with rational driving frequencies ω_k, and suppose that the properties of the original system M may be obtained by taking the quasiperiodic limit $k \to \infty$.

Figure 3.16(a) shows a phase diagram in the $a - \varepsilon$ plane. Each phase is characterized by the (nontrivial) Lyapunov exponents, σ_1 and σ_2 ($\leq \sigma_1$), associated with dynamics of the variables x and y (besides the zero exponent, connected to the phase variable θ of the quasiperiodic forcing) as well as the phase sensitivity exponent δ. The exponent δ measures the sensitivity with respect to the phase of the quasiperiodic forcing and characterizes the strangeness of an attractor [53]. A two-band smooth torus, which is born via a first-order torus-doubling bifurcation of its parent torus with a single band, exists in the region represented by $2T$ and shown in light gray. It has negative Lyapunov exponents ($\sigma_{1,2} < 0$) and no phase sensitivity ($\delta = 0$). When crossing the solid line (corresponding to a second-order torus-doubling bifurcation line), the two-band smooth torus becomes unstable and bifurcates

to a four-band smooth torus which exists in the region denoted by $4T$. On the other hand, a chaotic attractor with a positive Lyapunov exponent ($\sigma_1 > 0$) exists in the region shown in black. Between these regular and chaotic regions, strange nonchaotic attractors that have negative Lyapunov exponents ($\sigma_{1,2} < 0$) and high phase sensitivity ($\delta > 0$) exist in the region shown in gray. Because of their high phase sensitivity, these strange nonchaotic attractors have fractal structure [53]. A main interesting feature of the phase diagram is the existence of a second-order "tongue" that penetrates into the chaotic region. This tongue lies near the terminal point (denoted by the cross) of the second-order torus-doubling bifurcation curve, as in the case of the main (first-order) tongue that exists near the terminal point of the first-order torus-doubling bifurcation line (e.g., see Fig. 1(a) in [66]).

When passing the white solid line in Fig. 3.16(a), a two-band attractor (smooth torus, strange nonchaotic attractor, or chaotic attractor) transforms into a single-band attractor. We note that the band-merging curve loses its differentiability at the two vertices denoted by the pluses (+). A new type of band-merging transition occurs along the routes A, B, and C crossing the segment bounded by the two vertices. This new band merging is in contrast to the "standard" band merging which takes place on the remaining part of the band-merging curve when a two-band attractor collides with the smooth unstable torus, which is developed from the unstable fixed point for the unforced case. (The band-merging transition in [30] corresponds to the standard transition.) For the case of new band merging, due to a basin boundary metamorphosis [78], the smooth unstable torus becomes inaccessible from the interior of the basin of the attractor, and hence it cannot induce any band merging. For this case, through a collision with a ring-shaped unstable set which has no counterpart for the unforced case, a band-merging transition occurs for a nonchaotic attractor [smooth torus (route A) or strange nonchaotic attractor (route B)] as well as a chaotic attractor (route C). Particularly, a two-band smooth torus transforms into a single-band intermittent strange nonchaotic attractor along the route A, which corresponds to a new mechanism for the appearance of strange nonchaotic attractors. Here, we are interested in this kind of band-merging route to intermittent strange nonchaotic attractors.

As an example, we consider the case of $a = 1.17$ and study the band-merging transition from a two-band torus to a single-band intermittent strange nonchaotic attractor by varying ε along the route A. It is convenient to investigate such a band-merging transition in

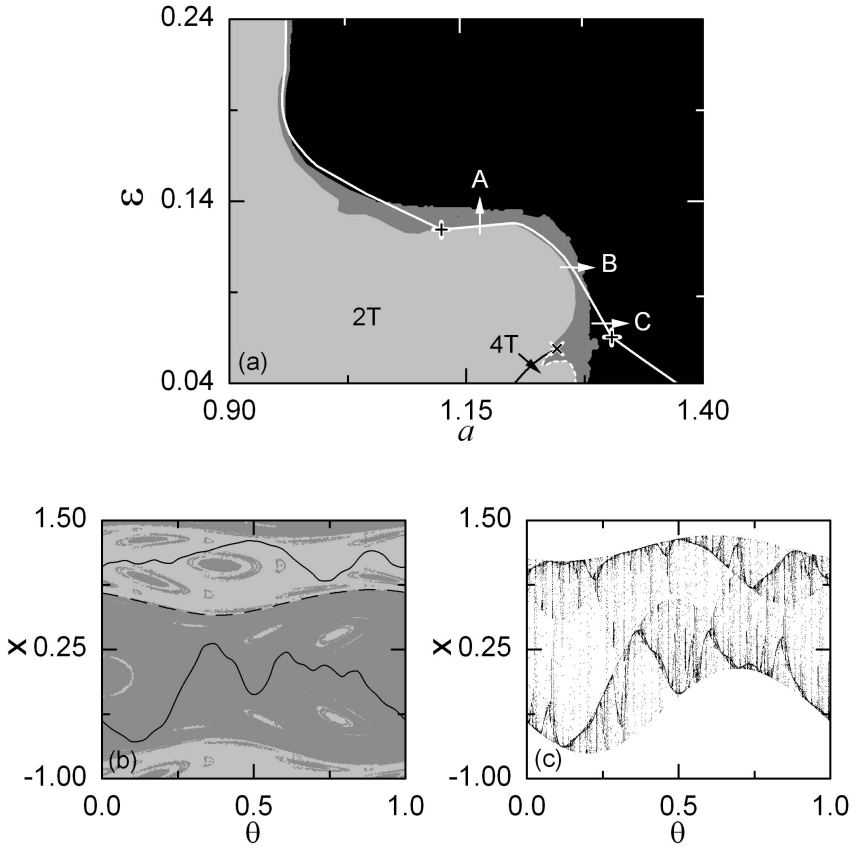

Figure 3.16: (a) Phase Diagram of the quasiperiodically forced Hénon map M in the $a-\varepsilon$ plane for the case of $b = 0.05$ and $\omega = (\sqrt{5}-1)/2$. Regular, chaotic, and strange nonchaotic attractor regimes are shown in light gray, black, and gray, respectively. For the case of regular attractor, tori with two and four bands exist in the regions denoted by $2T$ and $4T$, respectively. When crossing the white solid curve, a two-band attractor is transformed into a single-band attractor; a transition from a four-band attractor to a two-band attractor occurs when passing the white dashed curve. Particularly, a band-merging transition to an intermittent strange nonchaotic attractor takes place along the route A. In (b) and (c), projections of the attractors and the smooth unstable torus (represented by a dashed curve) onto the $\theta - x$ plane and the 2D slices with $y = 0.005$ of the basins of the attractors are given for $a = 1.17$. There exists a pair of conjugate tori in M^2, which are denoted by black curves in (b) for $\varepsilon = 0.12$. The basins of the upper and lower tori are shown in light gray and gray, respectively. Through a collision with a hole boundary, the conjugate tori merge into a single-band intermittent strange nonchaotic attractor in M, as shown in (c) for $\varepsilon = 0.127$.

M^2 (i.e., the second iterate of the original map M). A two-band smooth torus in M is transformed into a pair of conjugate tori in M^2. Figure 3.16(b) shows a pair of upper and lower tori (denoted by black curves) for $\varepsilon = 0.12$, whose basins are shown in light gray and gray, respectively. For this case, the basin of each smooth torus contains "holes" of other basin of the counterpart. Hence, the smooth unstable torus (denoted by the dashed line) on a basin boundary is not accessible from the interior of the basins of the conjugate attracting tori, and hence it cannot induce any band-merging transition. For this case of a basin boundary metamorphosis, conjugate tori and holes become closer as the parameter ε increases. Eventually, for $\varepsilon = \varepsilon^*$ ($= 0.126\,662\,718$) an attractor-merging crisis occurs for the conjugate tori via a collision with a hole boundary, and then a single-band intermittent strange nonchaotic attractor appears in the original map M. As shown in Fig. 3.16(c) for $\varepsilon = 0.127$, a typical trajectory on the newly-born intermittent strange nonchaotic attractor with $\sigma_1 \simeq -0.029$ and $\delta \simeq 4.60$ spends most of its time near the former two-band torus with sporadic large bursts away from it.

Such a band-merging transition to an intermittent strange nonchaotic attractor takes place through a collision with a ring-shaped unstable set on a hole boundary, as will be shown below. Using the rational approximation, the ring-shaped unstable set which has no counterpart in the unforced case was first discovered in the study on the intermittent route to strange nonchaotic attractors [66]. As the system parameters vary, both the size and the shape of rings, constituting the unstable set, are changed. Furthermore, as the level of the rational approximation increases, the ring-shaped unstable set consists of a large number of rings, and hence it becomes a complicated unstable set. (For details on the structure and evolution of the ring-shaped unstable set, refer to Fig. 2 of Ref. [66].)

In terms of the rational approximation of level 8, we now explain the mechanism for the band-merging route to intermittent strange nonchaotic attractors occurring in Figs. 3.16(b)-3.16(c) for $a = 1.17$. Figure 3.17(a) shows conjugate tori (denoted by black curves), conjugate ring-shaped unstable sets (represented by dark gray curves), and holes (shown in gray and light gray inside the basins of the upper and lower tori, respectively) in M^2 for $\varepsilon = 0.125$. The rational approximations to the conjugate smooth tori and ring-shaped unstable sets are composed of stable and unstable orbits with period F_8 ($= 21$) in M^2, respectively. For this case, some part of each ring-shaped unstable set (denoted by dark gray curves) lies on

a hole boundary (e.g., see a magnified view in Fig. 3.17(b), where holes in the light gray basin are represented by gray dots). With increase in ε, the conjugate tori and ring-shaped unstable sets become closer, and eventually, for $\varepsilon = \varepsilon_8^*$ ($= 0.125\,669\,395$) a pair of phase-dependent saddle-node bifurcations occurs for the conjugate stable and unstable F_8-periodic orbits through collision between the conjugate tori and ring-shaped unstable sets. Then, F_8 ($= 21$) "gaps," where no orbits with period F_8 exist, are formed in the whole range of θ, as shown in Fig. 3.17(c) for $\varepsilon = 0.1257$ [e.g., see a magnified gap in Fig. 3.17(d)]. In these gaps, single-band intermittent chaotic attractors (denoted by black dots) appear (i.e., saddle-node bifurcations induce attractor-merging crises in the gaps). Thus, the rational approximation to the whole attractor in the original map M becomes composed of the union of the two-band periodic component and the single-band intermittent chaotic component. Since the periodic component is dominant, its average Lyapunov exponent ($\langle\sigma_1\rangle \simeq -0.098$) is negative, where $\langle\cdots\rangle$ denotes the average over the whole θ. Hence, the partially-merged 8th rational approximation to the attractor in Fig. 3.17(c) becomes nonchaotic, and resembles the single-band strange nonchaotic attractor in Fig. 3.16(c), although the level $k = 8$ is low. By increasing the level of the rational approximation to $k = 18$, we study the band-merging transition of the two-band torus. It is thus found that the threshold value ε_k^*, at which the phase-dependent saddle-node bifurcation of level k (inducing the attractor-merging crises in the gaps) occurs, converges to the quasiperiodic limit ε^* ($= 0.126\,662\,718$) in an algebraic manner, $|\Delta\varepsilon_k| \sim F_k^{-\alpha}$, where $\Delta\varepsilon_k = \varepsilon_k^* - \varepsilon^*$ and $\alpha \simeq 2.0$, as shown in Fig. 3.17(e). As the level k of the rational approximation increases, the number of gaps, where phase-dependent attractor-merging crises occur, becomes larger, and eventually in the quasiperiodic limit, the rational approximation to the attractor has a dense set of gaps, filled by single-band intermittent chaotic attractors. Consequently, an intermittent single-band strange nonchaotic attractor, containing the ring-shaped unstable set, appears, as shown in Fig. 3.16(c). We also note that this band-merging transition results in the truncation of the torus-doubling cascade.

To confirm the above mechanism for the band-merging transition, we also study the Toda oscillator with an asymmetric exponential potential which is quasiperiodically forced at two

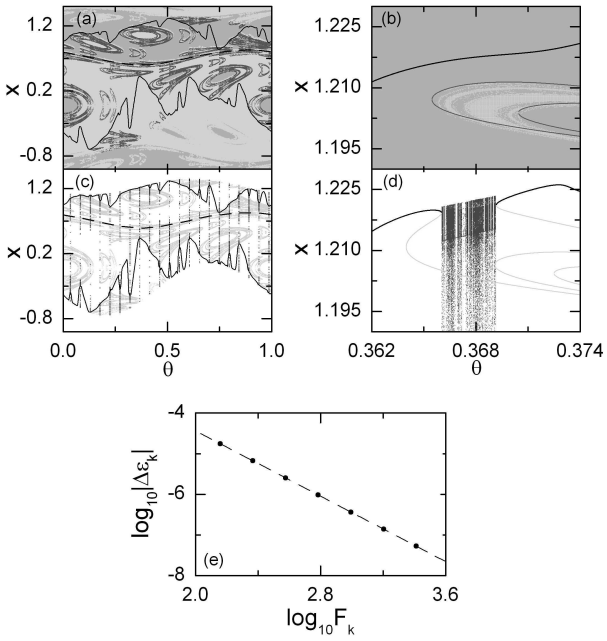

Figure 3.17: Dynamical mechanism for the transition from a two-band smooth torus to a single-band intermittent strange nonchaotic attractor for $a = 1.17$ in the quasiperiodically forced Hénon map M. In (a)-(d), projections of the attractors, the ring-shaped unstable sets, and the smooth unstable torus (denoted by a dashed curve) onto the $\theta - x$ plane and the 2D slices with $y = 0.005$ of the basins of the attractors are given in the rational approximation of level 8. (a) and (b) Eighth rational approximation to the conjugate smooth tori and ring-shaped unstable sets for $\varepsilon = 0.125$ in M^2. The basins of the upper and lower tori, denoted by black curves, are shown in light gray and gray, respectively. The conjugate ring-shaped unstable sets, represented by dark gray curves, lie close to the smooth tori (e.g., see a magnified view in (b), where holes in the light gray basin are denoted by gray dots). (c) and (d) Eighth rational approximation to the single-band intermittent strange nonchaotic attractor for $\varepsilon = 0.1257$ in M. The attractors and ring-shaped unstable sets are shown in black and gray, respectively. The rational approximation to the strange nonchaotic attractor is composed of the union of the two-band periodic component and the single-band intermittent chaotic component, where the latter occupies the F_8 $(= 21)$ gaps in θ. For a clear view, a magnified gap is given in (d). (e) Plot of $\log_{10}|\Delta\varepsilon_k^*|$ vs. $\log_{10} F_k$ for $k = 12, \ldots, 18$ $[\Delta\varepsilon_k^* = \varepsilon_k^* - \varepsilon^*]$. Here, ε_k^* (denoted by solid circles) represents the threshold value for the saddle-node bifurcation (inducing the attractor-merging crises in the gaps) in the rational approximation of level k, and ε^* denotes the quasiperiodic limit.

incommensurate frequencies [67],

$$\ddot{x} + \gamma\dot{x} + e^x - 1 = a\cos\omega_1 t + \varepsilon\cos\omega_2 t, \tag{3.12}$$

where γ is the damping coefficient, a and ε represent the amplitudes of the quasiperiodic forcing, and ω ($\equiv \omega_2/\omega_1$) is irrational. By making a normalization, $\omega_1 t \to 2\pi t$, Eq. (3.12) can be reduced to three first-order differential equations,

$$\begin{aligned} \dot{x} &= y, \\ \dot{y} &= -\tfrac{2\pi}{\omega_1}\gamma y + \tfrac{4\pi^2}{\omega_1^2}(-e^x + 1 + a\cos 2\pi t + \varepsilon\cos 2\pi\theta), \\ \dot{\theta} &= \omega \pmod 1. \end{aligned} \tag{3.13}$$

By stroboscopically sampling the orbit points (x_n, y_n, θ_n) at the discrete time n,we obtain the 3D Poincaré map P with a constant Jacobian determinant of $e^{-\gamma T_1}$, where $T_1 = 2\pi/\omega_1$. Here, we set ω to be the reciprocal of the golden mean [i.e., $\omega = (\sqrt{5}-1)/2$)], and investigate the band-merging route to intermittent strange nonchaotic attractors in the 3D Poincaré map P for the case of $\gamma = 0.8$ and $\omega_1 = 2.0$. Figure 3.18(a) shows a phase diagram in the $a - \varepsilon$ plane. As in the case of the quasiperiosically forced Hénon map, a band-merging transition from a two-band smooth torus to a single-band intermittent strange nonchaotic attractor occurs when passing the white solid curve along the route A. As an example, we consider the case of $a = 27$. Figure 3.18(b) shows a two-band smooth torus in the Poincaré map P for $\varepsilon = 0.21$. When passing a threshold value $\varepsilon = \varepsilon^*$ ($= 0.242\,953\,437$), such a two-band torus transforms into a single-band intermittent strange nonchaotic attractor (e.g., see the newly-born intermittent strange nonchaotic attractor with $\sigma_1 \simeq -0.051$ and $\delta \simeq 6.2$ in Fig. 3.18(c) for $\varepsilon = 0.244$).

Using the rational approximation of level 8, we explain the mechanism for the band-merging transition to intermittent strange nonchaotic attractors occurring in Figs. 3.18(b)-3.18(c) for $a = 27$. In P^2 (i.e., the second iterate of the Poincaré map P), there exists a pair of conjugate smooth tori denoted by black curves, as shown in Fig. 3.18(d) for $\varepsilon = 0.207$. We note that conjugate ring-shaped unstable sets, represented by gray curves, lie close to the conjugate smooth tori. For this case, the smooth unstable torus, denoted by a black dashed line, is inaccessible from the interior of the basins of the conjugate smooth tori, and hence it cannot induce any band-merging transition. As ε is increased, the conjugate tori and ring-shaped unstable sets become closer. Eventually, when passing the threshold value

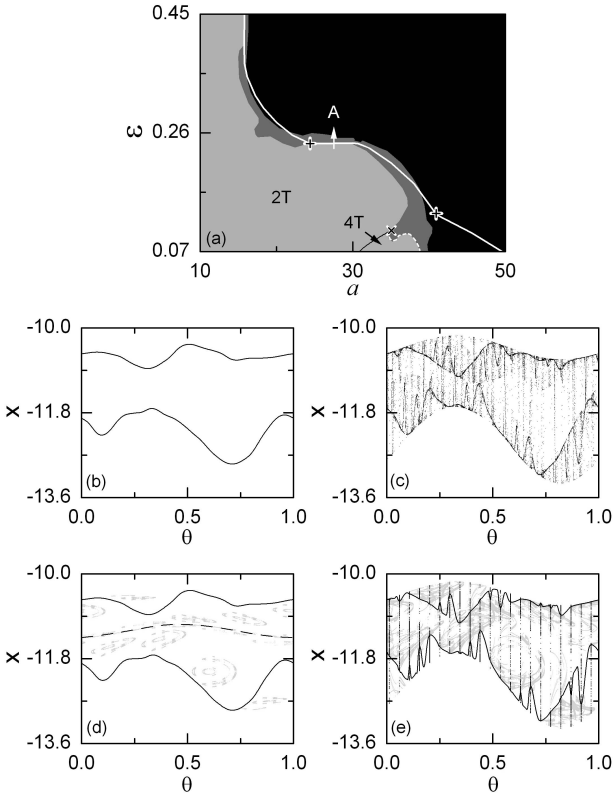

Figure 3.18: (a) Phase Diagram of the quasiperiodically forced Toda oscillator in the $a-\varepsilon$ plane for the case of $\gamma = 0.8, \omega_1 = 2.0$, and $\omega = (\sqrt{5}-1)/2$. Symbols and colors represent the same things as in Fig. 3.16(a). (b) and (c) Band-merging route to an intermittent strange nonchaotic attractor for $a = 27$ in the Poincaré map P. In (b) and (c), projections of the two-band smooth torus and the single-band intermittent strange nonchaotic attractor onto the $\theta - x$ plane are given for $\varepsilon = 0.21$ and 0.244, respectively. (d) and (e) Mechanism for the transition from a two-band smooth torus to a single-band intermittent strange nonchaotic attractor for $a = 27$ in the rational approximation of level 8. In the second iterate of the Poincaré map P (i.e., P^2), projections of the conjugate tori (denoted by black solid curves), ring-shaped unstable sets (represented by gray curves), and the unstable smooth torus (denoted by a dashed curve) onto the $\theta - x$ plane are given in (d) for $\varepsilon = 0.207$. Through collision between the conjugate tori and ring-shaped unstable sets, F_8 (= 21) "gaps," filled by single-band intermittent chaotic attractors denoted by black dots, appear in the whole range of θ, as shown in (e) for $\varepsilon = 0.2409$. In (e), projections of the attractors (denoted by black dots) and the ring-shaped unstable sets (represented by gray curves) are plotted in the Poincaré map P.

ε_8^* (= 0.240 831 592), a pair of phase-dependent saddle-node bifurcations occurs through collision between the conjugate tori and ring-shaped unstable sets. Then, F_8 (= 21) "gaps" without F_8-periodic attractors appear in the whole range of θ, as shown in Fig. 3.18(e) for $\varepsilon = 0.2409$. In these gaps, single-band intermittent chaotic attractors (denoted by black dots) appear. Thus, the rational approximation to the whole attractor in the Poincaré map P becomes composed of the union of the two-band periodic component and the single-band intermittent chaotic component. This partially-merged 8th rational approximation to the attractor in Fig. 3.18(e) becomes nonchaotic because $\langle \sigma_1 \rangle \simeq -0.112$, and it resembles the single-band intermittent strange nonchaotic attractor in Fig. 3.18(c), although the level $k = 8$ is low. Increasing the level of the rational approximation to $k = 18$, we obtain the threshold value ε_k^*, at which the phase-dependent saddle-node bifurcation of level k (mediating the attractor-merging crises in the gaps) occurs. As the level k increases, the sequence $\{\varepsilon_k^*\}$ is found to converge to the quasiperiodic limit ε^* (= 0.242 953 437) in an algebraic manner, $|\Delta\varepsilon_k| \sim F_k^{-\alpha}$, where $\Delta\varepsilon_k = \varepsilon_k^* - \varepsilon^*$ and $\alpha \simeq 2.0$. In the quasiperiodic limit $k \to \infty$, the rational approximation to the attractor has a dense set of gaps, filled by single-band intermittent chaotic attractors. As a result, an intermittent single-band strange nonchaotic attractor, containing the ring-shaped unstable set, appears, as shown in Fig. 3.18(c). In addition to the birth of strange nonchaotic attractors, such a band-merging transition induces the truncation of the torus-doubling sequence.

3.3 Boundary Crises in Quasiperiodically Forced Systems

We investigate the mechanism for boundary crises in the quasiperiodically logistic map [70]. For small quasiperiodic forcing ε, a chaotic attractor disappears suddenly via a "standard" boundary crisis when it collides with the smooth unstable torus. However, when passing a threshold value of ε, a basin boundary metamorphosis occurs, and then the smooth unstable torus is no longer accessible from the interior of the basin of the attractor. For this case, using the rational approximations to the quasiperiodic forcing, it is shown that a nonchaotic attractor (smooth torus or strange nonchaotic attractor) as well as a chaotic attractor is

destroyed abruptly through a new type of boundary crisis when it collides with an invariant "ring-shaped" unstable set which has no counterpart in the unforced case. The universality for the boundary crises is also confirmed in the quasiperiodically forced Hénon map [71].

3.3.1 Boundary Crises in the Quasiperiodically Forced Logistic Map

We study the mechanism for the boundary crisis in the quasiperiodically forced logistic map M, often used as a representative model for the quasiperiodically forced period-doubling systems:

$$M : \begin{cases} x_{n+1} = a - x_n^2 + \varepsilon \cos 2\pi\theta_n, \\ \theta_{n+1} = \theta_n + \omega \pmod 1, \end{cases} \tag{3.14}$$

where $x \in [0,1]$, $\theta \in S^1$, a is the nonlinearity parameter of the logistic map, and ω and ε represent the frequency and amplitude of the quasiperiodic forcing, respectively. This quasiperiodically forced logistic map M is noninvertible, because its Jacobian determinant becomes zero along the critical curve, $L_0 = \{x = 0,\ \theta \in [0,1)\}$. Critical curves of rank k, L_k $(k = 1, 2, \ldots)$, are then given by the images of L_0, [i.e., $L_k = M^k(L_0)$]. Segments of these critical curves can be used to define a bounded trapping region of the phase space, called an "absorbing area," inside which, upon entering, trajectories are henceforth confined [82].

Here, we set the frequency to be the reciprocal of the golden mean, $\omega = (\sqrt{5} - 1)/2$, and then investigate the boundary crisis using the rational approximations. For the inverse golden mean, its rational approximants are given by the ratios of the Fibonacci numbers, $\omega_k = F_{k-1}/F_k$, where the sequence of $\{F_k\}$ satisfies $F_{k+1} = F_k + F_{k-1}$ with $F_0 = 0$ and $F_1 = 1$. Instead of the quasiperiodically forced system, we study an infinite sequence of periodically forced systems with rational driving frequencies ω_k. We suppose that the properties of the original system M may be obtained by taking the quasiperiodic limit $k \to \infty$.

Figure 3.19 shows a phase diagram in the $a - \varepsilon$ plane. Each phase is characterized by both the Lyapunov exponent σ_x in the x-direction and the phase sensitivity exponent δ. The exponent δ measures the sensitivity with respect to the phase of the quasiperiodic forcing and characterizes the strangeness of an attractor in a quasiperiodically driven system [53]. A smooth torus has a negative Lyapunov exponent and no phase sensitivity ($\delta = 0$). Its region

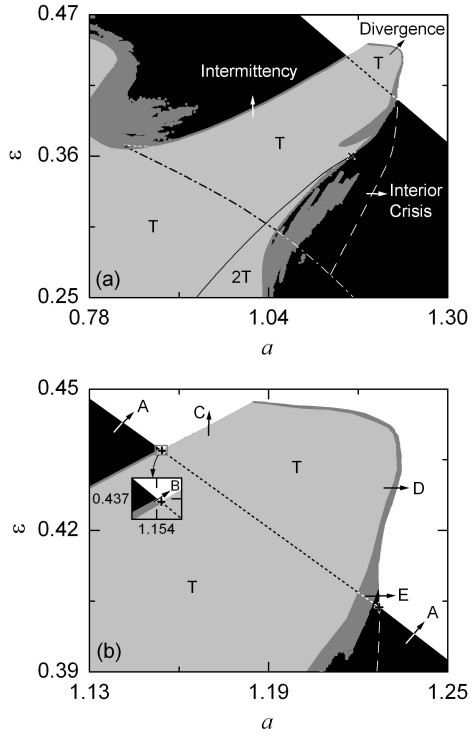

Figure 3.19: (a) Phase Diagram in the $a - \varepsilon$ plane. Regular, chaotic, strange nonchaotic attractor, and divergence regimes are shown in light gray, black, gray, and white, respectively. For the case of regular attractor, a torus and a doubled torus exist in the regions denoted by T and $2T$, respectively. We note the existence of a "tongue" of quasiperiodic motion near the terminal point (marked with the cross) of the torus doubling bifurcation curve represented by the solid line. In this tongue, typical dynamical transitions such as the intermittency, interior crisis (occurring when passing the dashed line) and boundary crisis may occur through interaction with the ring-shaped unstable set born when passing the dash-dotted line. When passing the dotted line, a basin boundary metamorphosis occurs, and then the smooth unstable torus becomes inaccessible from the basin of the attractor. (b) boundary crises leading to divergence. A sudden destruction of a chaotic attractor (strange nonchaotic attractor) occurs via a "standard" boundary crisis along the route A (B) when it collides with the smooth unstable torus. On the other hand, through collision with a ring-shaped unstable set, a new type of boundary crises, which cause the abrupt destruction of the smooth torus, strange nonchaotic attractor, and chaotic attractors, occur along the routes C, D, and E, respectively. Hence, the boundary crisis curve is not differentiable at the two double-crisis vertices, denoted by the plus. A small box near the upper double-crisis vertex is magnified. For other details, see the text.

is denoted by T and shown in light gray. When crossing the solid line, the smooth torus becomes unstable and bifurcates to a smooth doubled torus in the region denoted by $2T$. On the other hand, chaotic attractors have positive Lyapunov exponents and its region is shown in black. Between these regular and chaotic regions, strange nonchaotic attractors that have negative Lyapunov exponents and high phase sensitivity ($\delta > 0$) exist in the region shown in gray. Due to their high phase sensitivity, these strange nonchaotic attractors have fractal structure. This phase diagram is typical for quasiperiodically forced period-doubling systems [60, 61, 62, 63, 64, 66]. Note that its main interesting feature is the existence of the "tongue" of quasiperiodic motion that penetrates into the chaotic region and separates it into upper and lower parts. We also note that this tongue lies near the terminal point (denoted by the cross) of the torus doubling bifurcation curve. In this tongue, rich dynamical transitions such as intermittency, interior crisis, and boundary crisis occur. Here, we are interested in the boundary crisis inducing divergence that occurs in the region shown in white.

We first consider a boundary crisis occurring along the route A ($\varepsilon = 0.5a - 0.28$) in Fig. 3.19(b). A chaotic attractor, bounded by the critical curves L_k ($k = 1, \ldots, 4$), is given in Fig. 3.20(a) for $a = 1.19$ and $\varepsilon = 0.315$, and its basin is shown in gray. As the parameters a and ε increase, the chaotic attractor and a smooth unstable torus (denoted by a dashed line) on the basin boundary become closer [see Fig. 3.20(b)]. Eventually, when passing the threshold value $(a, \varepsilon) = (1.298\,618, 0.369\,309)$, a sudden destruction of the chaotic attractor occurs through a collision with the smooth unstable torus which is developed from the unstable fixed point of the (unforced) logistic map. This boundary crisis corresponds to a natural generalization of the boundary crisis occurring for the unforced case ($\varepsilon = 0$). Hence, we call it the "standard" boundary crisis.

As a and ε are increased, the standard boundary crisis line continues smoothly. However, at a lower vertex $(a_l^*, \varepsilon_l^*) \simeq (1.227, 0.404)$ [denoted by a plus (+) in Fig. 3.19(b)], the standard boundary crisis line ends and a new kind of boundary crisis curve begins by making a sharp turning. Hence, the boundary crisis curve loses its differentiability at the vertex. For this case, the standard boundary crisis line is continued smoothly beyond the vertex as a curve of a basin metamorphosis line denoted by a dotted line, and the new boundary crisis curve joins smoothly with an interior crisis curve denoted by a dashed line at the vertex [see Fig. 3.19(b)]. When passing the basin boundary metamorphosis line, the basin boundary

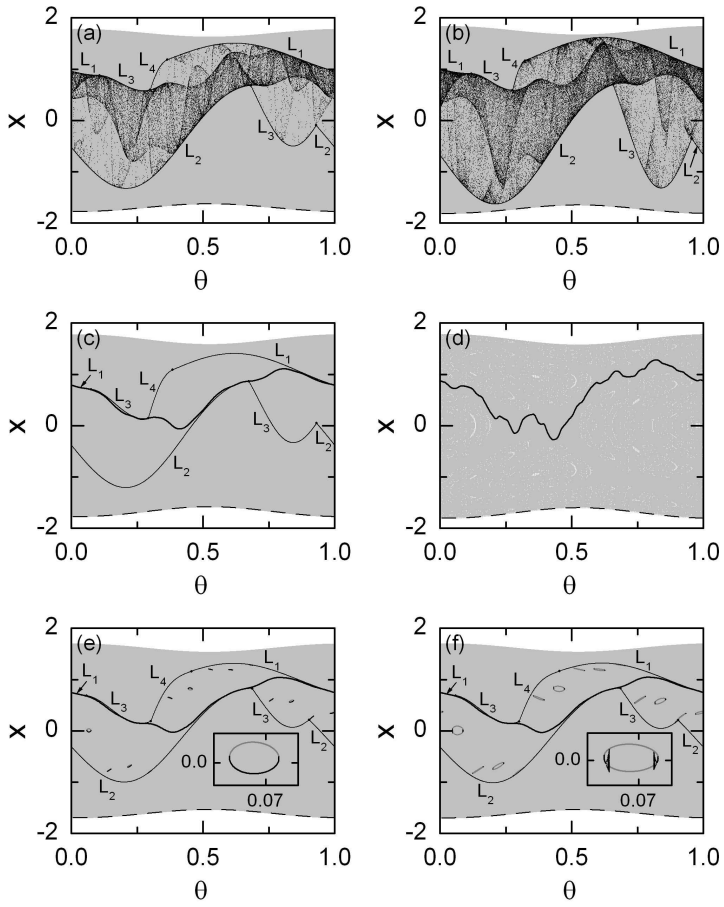

Figure 3.20: (a) and (b) Standard boundary crisis of a chaotic attractor. Chaotic attractors bounded by the critical curves L_k ($k = 1, \ldots, 4$) and their basins of attraction are denoted by black dots and shown in gray, respectively for (a) $a = 1.19$ and $\varepsilon = 0.315$ and (b) $a = 1.265$ and $\varepsilon = 0.3525$. Here the dashed line represents a smooth unstable torus on the basin boundary. (c) and (d) Basin boundary metamorphosis. (c) A smooth torus (denoted by a heavy black curve) exists inside the absorbing area bounded by the critical curves L_k ($k = 1, \ldots, 4$) for $a = 1.05$ and $\varepsilon = 0.355$. (d) "Holes" (denoted by white dots), leading to divergence, appear inside the basin (shown in gray) of the smooth torus (denoted by a heavy black curve) for $a = 1.187$ and $\varepsilon = 0.4235$ after breakup of the absorbing area. (e) and (f) Appearance of a ring-shaped unstable set in the rational approximation of level 7. A smooth torus (denoted by a heavy black curve) and a ring-shaped unstable set exist inside the absorbing area bounded by the critical curves L_k ($k = 1, \ldots, 4$) for (e) $a = 0.989$ and $\varepsilon = 0.3245$ and (f) $a = 0.993$ and $\varepsilon = 0.3265$. A ring-shaped unstable set is composed of F_7 ($= 13$) small rings. Magnified views of a ring are given in the insets. Note that each ring consists of the unstable part (composed of unstable orbits with the forcing period F_7 and shown in dark gray) and the attracting part (denoted by black dots). For more details, see the text.

suddenly jumps in size [78], and as the interior crisis curve is crossed, abrupt widening of an attractor occurs [64]. Note that these double (boundary and interior) crises plus a basin boundary metamorphosis occur simultaneously at the vertex [98].

Below the basin boundary metamorphosis line in the tongue, a smooth torus (denoted by a heavy black curve) exists inside an absorbing area bounded by the critical curves L_k ($k = 1, \ldots, 4$) [e.g., see Fig. 3.20(c) for $a = 1.05$ and $\varepsilon = 0.355$]. However, as the basin boundary metamorphosis line is crossed, the absorbing area becomes broken up through collision with the smooth unstable torus (denoted by the dashed line), and then "holes (denoted by white dots)," leading to divergence, appear inside the basin of the smooth attracting torus [see Fig. 3.20(d)] [78]. As a consequence of this basin boundary metamorphosis, the smooth unstable torus becomes inaccessible from the interior of basin of the smooth attracting torus, and hence it cannot induce any boundary crisis. For this case, using the rational approximations to the quasiperiodic forcing, we locate an invariant ring-shaped unstable set that causes a new type of boundary crisis through a collision with the smooth (attracting) torus. When passing the dash-dotted line in Fig. 3.19(a), such a ring-shaped unstable set is born via a phase-dependent saddle-node bifurcation [66]. This bifurcation has no counterpart in the unforced case. As an example, we consider the rational approximation of level $k = 7$ and explain the structure of the ring-shaped unstable set. As shown in Fig. 3.20(e) for $a = 0.989$ and $\varepsilon = 0.3245$, the rational approximation to the smooth torus (denoted by a heavy black line), composed of stable orbits with period F_7 (= 13), exists inside an absorbing area bounded by segments of the critical curves L_k ($k = 1, \ldots, 4$). We also note that a ring-shaped unstable set, consisting of F_7 small rings, lies inside the absorbing area. At first, each ring consists of the stable (shown in black) and unstable (shown in dark gray) orbits with the forcing period F_7 [see the inset in Fig. 3.20(e)]. However, as the parameters a and ε increase, such rings evolve, and thus each ring becomes composed of a large unstable part (shown in dark gray) and a small attracting part (denoted by black dots) [see the inset in Fig. 3.20(f)]. As the level k of the rational approximation increases, the ring-shaped unstable set consists of a larger number of rings with a smaller attracting part. Hence, we believe that, in the quasiperiodic limit, the ring-shaped unstable set might become a complicated invariant unstable set composed of only unstable orbits. Through a collision with this ring-shaped unstable set which has no counterpart in the unforced case, a new type of boundary

crisis occurs, as will be seen below.

With further increase in a and ε, both the new boundary crisis curve and the basin boundary metamorphosis line end simultaneously at the upper double-crisis vertex (denoted by a plus) $(a_u^*, \varepsilon_u^*) \simeq (1.154, 0.437)$ in Fig. 3.19(b). Then, the standard boundary crisis line, which joins smoothly with the basin boundary metamorphosis line at the upper vertex, starts again by making an angle. Along the routes A and B beyond the upper vertex, standard boundary crises of the chaotic attractor and strange nonchaotic attractor occur, respectively. On the other hand, the new boundary crisis curve turns smoothly into a curve of intermittency at the upper vertex. When passing the intermittency line, a transition from a smooth torus to an intermittent strange nonchaotic attractor occurs through collision with a ring-shaped unstable set [66]. As in the case of interior crisis, the size of the attractor abruptly increases. Hereafter, we will study new type of boundary crises which occur along the routes C, D, and E crossing the segment bounded by the lower and upper double-crisis vertices [see Fig. 3.19(b)]. A nonchaotic attractor [smooth torus (route C) or strange nonchaotic attractor (route D)] as well as a chaotic attractor (route E) is found to be abruptly destroyed through a new boundary crisis when it collides with a ring-shaped unstable set.

We now fix the value of a at $a = 1.18$ and investigate the boundary crisis of a smooth torus by varying ε along the route C. Figure 3.21(a) shows a smooth torus (denoted by black curve) whose basin is shown in gray for $\varepsilon = 0.43$. Due to the existence of holes (shown in white), leading to divergence, the smooth unstable torus (denoted by the dashed line) is not accessible from the interior of the basin of the smooth attracting torus. As the parameter ε increases, the smooth torus and holes become closer, as shown in Fig. 3.21(b) for $\varepsilon = 0.445$. Eventually, the smooth (attracting) torus is abruptly destructed via a boundary crisis when it collides with the hole boundary for $\varepsilon = \varepsilon^* (= 0.445\,567\,905)$. Using the rational approximation of level $k = 7$, we investigate the mechanism for the boundary crisis of the smooth torus. Figure 3.21(c) shows the smooth torus (denoted by a black line), the ring-shaped unstable set (represented by dark gray curves), and holes (shown in white) for $\varepsilon = 0.427$. The rational approximations to the smooth torus and the ring-shaped unstable set are composed of stable and unstable orbits with period F_7 $(= 13)$, respectively. For this case, the ring-shaped unstable set is close to the smooth torus. However, it does not lie on any hole boundary [e.g., see a magnified view in Fig. 3.21(d)]. As the parameter ε increases,

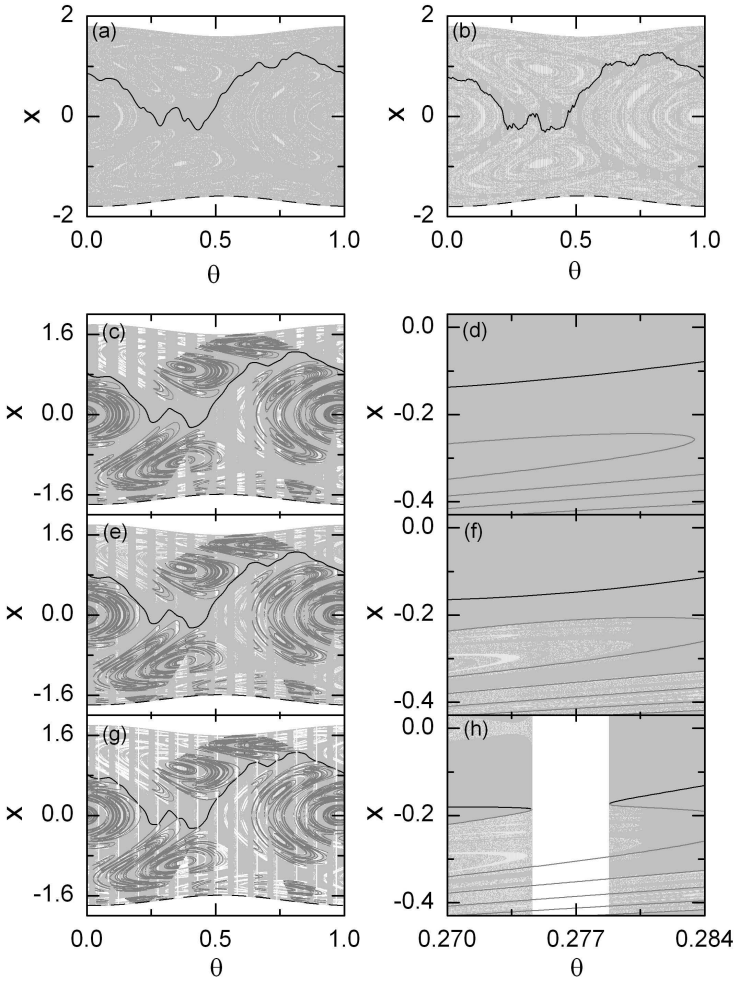

Figure 3.21: (a) and (b) boundary crisis of a smooth torus along the route C for $a = 1.18$. (a) Smooth torus (denoted by a black curve) and its basin (shown in gray) for $\varepsilon = 0.43$. The unstable smooth torus (denoted by a dashed line) is not accessible from the interior of the basin of the stable smooth torus because of the existence of holes (denoted by white dots). (b) Smooth torus and holes just before the boundary crisis for $\varepsilon = 0.445$. (c)-(h) Analysis of the mechanism for the boundary crisisof the smooth torus in the rational approximation of level 7 for $a = 1.18$. Magnified views near $(\theta, x) = (0.277, -0.2)$ in (c), (e), and (g) are given in (d), (f), and (h), respectively. Here, the smooth torus whose basin is shown in gray, a ring-shaped unstable set, and holes are shown in black, dark gray, and white dots, respectively. In (c) and (d) for $\varepsilon = 0.427$, a ring-shaped unstable set lies close to the smooth torus. In (e) and (f) for $\varepsilon = 0.43$, some part of the ring-shaped unstable set lies on a hole boundary [e.g., see a magnified view in (f)]. For $\varepsilon = \varepsilon_7^*$ $(= 0.430\,854\,479)$, a boundary crisis occurs via phase-dependent saddle-node bifurcations between the smooth torus and the ring-shaped unstable set on the hole boundary. Then, F_7 $(= 13)$ "gaps," where divergence occurs, are formed, as shown in (g) for $\varepsilon = 0.4309$, [e.g., see a magnified gap in (h)].

the size of holes increases and new holes appear. Then, some part of the ring-shaped unstable set lies on a hole boundary, as shown in Figs. 3.21(e) and 3.21(f). With further increases in ε, the smooth torus and the ring-shaped unstable set on the hole boundary become closer, and eventually, for $\varepsilon = \varepsilon_7^*$ ($= 0.430\,854\,479$) a phase-dependent saddle-node bifurcation occurs through a collision between the smooth torus and the ring-shaped unstable set. Then, "gaps," where the former attractor (i.e., the stable F_7-periodic orbits) no longer exists and almost all trajectories go to the infinity, are formed, as shown in Fig. 3.21(g) [e.g., see a magnified gap in Fig. 3.21(h)]. As a result, a "partially-destroyed" torus with F_7 ($= 13$) gaps, where divergence occurs, is left. By increasing the level of the rational approximation to $k = 19$, we study the boundary crisis of the smooth torus. It is thus found that the threshold value ε_k^*, at which the phase-dependent saddle-node bifurcation of level k (inducing the phase-dependent boundary crises in the gaps) occurs, converges to the quasiperiodic limit ε^* ($= 0.445\,567\,905$) in an algebraic manner, $|\Delta\varepsilon_k| \sim F_k^{-\alpha}$, where $\Delta\varepsilon_k = \varepsilon_k^* - \varepsilon^*$ and $\alpha \simeq 2.01$. As the level k of the rational approximation increases, the number of gaps, where divergence takes place, becomes larger, and eventually in the quasiperiodic limit, a boundary crisis occurs in a dense set of gaps covering the whole θ-range. Consequently, the whole smooth torus disappears suddenly via a new type of boundary crisis when it collides with the ring-shaped unstable set.

When crossing the remaining part of the new boundary crisis curve along the routes D and E in Fig. 2.30(b), a strange nonchaotic attractor and a chaotic attractor are destructed abruptly through a collision with a ring-shaped unstable set, respectively. For a fixed value of $\varepsilon = 0.43$, a smooth torus is transformed into a strange nonchaotic attractor via gradual fractalization [58] when passing a threshold value of $a = 1.231\,592$. Figure 3.22(a) shows a strange nonchaotic attractor (denoted by black dots) with $\sigma_x = -0.038$ and $\delta = 1.077$ for $a = 1.2327$. Due to the existence of holes (shown in white), the smooth unstable torus (represented by a dashed line) is inaccessible from the interior of the basin of the strange nonchaotic attractor. As a passes another threshold value a^* ($= 1.232\,722\,002$), the strange nonchaotic attractor is destroyed abruptly via a boundary crisis when it collides with a hole boundary. As in the case of the strange nonchaotic attractor, boundary crisis of a chaotic attractor also occurs along the route E through a collision with a hole boundary. For example, at a fixed value of $\varepsilon = 0.405$, consider a chaotic attractor with $\sigma_x = 0.006$

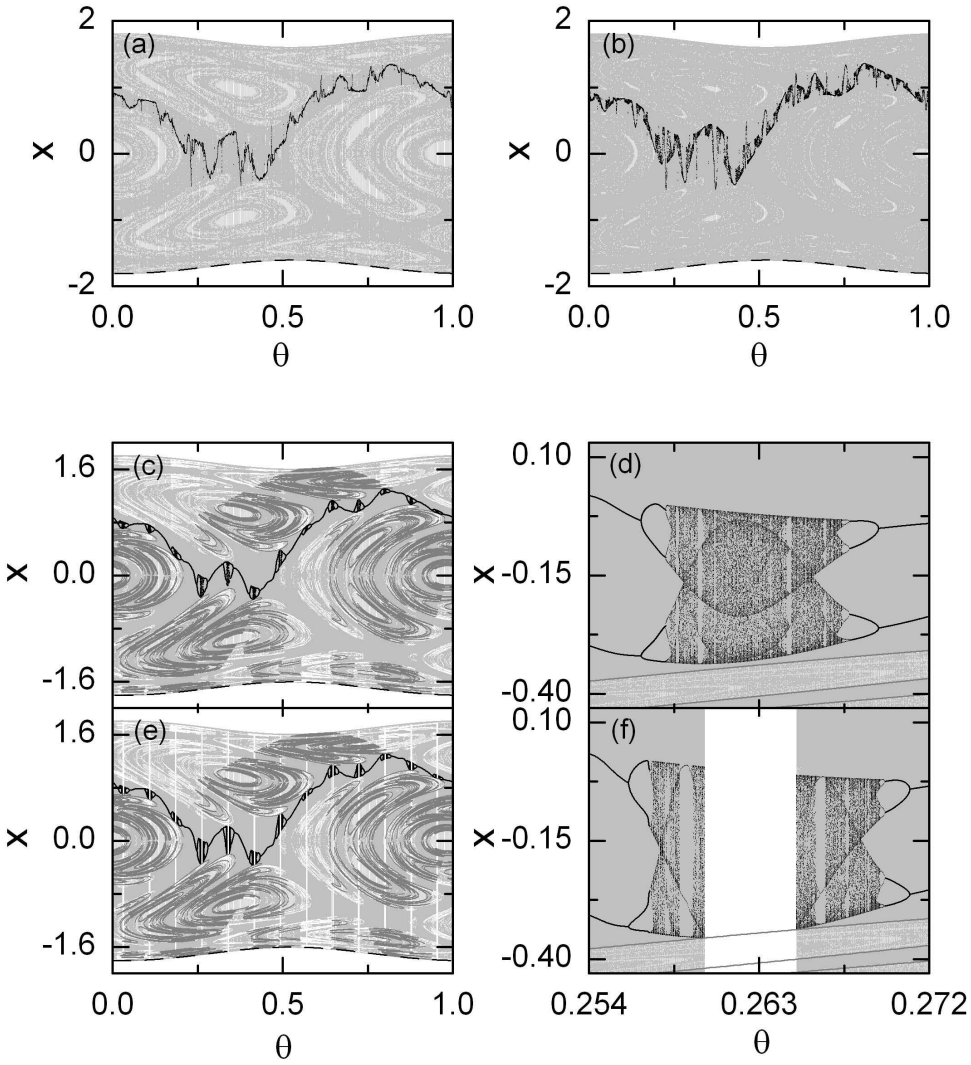

Figure 3.22: (a) a strange nonchaotic attractor with $\sigma_x = -0.038$ and $\delta = 1.077$ and (b) a chaotic attractor $\sigma_x = 0.006$ are denoted by black dots for $(a, \varepsilon) = (1.2327, 0.43)$ and $(1.227, 0.405)$, respectively. These attractors whose basins are shown in gray lie close to holes (represented by white dots), leading to divergence. (c)-(f) Investigation of the mechanism for the boundary crisis of the strange nonchaotic attractor along the route D in the rational approximation of level $k = 7$ for $\varepsilon = 0.43$. The rational approximations to the strange nonchaotic attractor and the ring-shaped unstable set are denoted by black and dark gray dots, respectively, in (c) for $a = 1.207$ and $\varepsilon = 0.43$. Some part of the ring-shaped unstable set lies on a hole boundary (shown in white) [e.g., see a magnified view in (d)]. For $a = a_7^*$ $(= 1.208\,945\,689)$, a boundary crisis occurs through a collision between the chaotic component of the rational approximation to the strange nonchaotic attractor and the ring-shaped unstable set on the hole boundary. Then, F_7 $(= 13)$ "gaps," where divergence takes place, are formed as shown in (e) for $a = 1.21$, [e.g., see a magnified gap in (f)].

shown in Fig. 3.22(b) for $a = 1.227$. Sudden destruction of the chaotic attractor takes place when passing a threshold value of $a = 1.227\,030\,014$. For this case, the mechanism for the boundary crisis of the chaotic attractor is the same as that for the case of the strange nonchaotic attractor. Hence, it is sufficient to consider only the case of the strange nonchaotic attractor for presentation of the mechanism for the boundary crisis. Using the rational approximation of level $k = 7$, we investigate the mechanism for the boundary crisis of the strange nonchaotic attractor along the route D for $\varepsilon = 0.43$. Figures 3.22(c) and 3.22 (d) show the rational approximations to the strange nonchaotic attractor (denoted by black dots) and the ring-shaped unstable set (shown in dark gray). Unlike the case of the smooth torus, the rational approximation to the strange nonchaotic attractor consists of the periodic and chaotic components. Since the periodic component is dominant, the average Lyapunov exponent ($\langle\sigma_x\rangle = -0.109$) is negative, where $\langle\cdots\rangle$ denotes the average over the whole θ. Note that some of the ring-shaped unstable set lies on a hole boundary (shown in white) [e.g., see a magnified view in Fig. 3.22(d)]. As a is increased, the chaotic component of the rational approximation to the strange nonchaotic attractor and the ring-shaped unstable set on the hole boundary become closer. Eventually, for $a = a_7^*$ ($= 1.208\,945\,689$), they make a collision and then a phase-dependent boundary crisis occurs. Thus, F_7 ($= 13$) gaps, where divergence occurs, are formed in the whole range of θ, as shown in Fig. 3.22(e) for $a = 1.21$ [e.g., see a magnified gap in Fig. 3.22(f)]. As a result, the strange nonchaotic attractor becomes destroyed partially in gaps. By increasing the level of the rational approximation to $k = 19$, we study the boundary crisis of the strange nonchaotic attractor. It is thus found that the threshold value a_k^*, at which the phase-dependent boundary crisis of level k occurs, converges to the quasiperiodic limit a^* ($= 1.232\,722\,002$) in an algebraic manner, $|\Delta a_k| \sim F_k^{-\alpha}$, where $\Delta a_k = a_k^* - a^*$ and $\alpha \simeq 2.67$. As the level k of the rational approximation increases, more and more gaps, where divergence takes place, appear, and eventually in the quasiperiodic limit, a boundary crisis occurs in a dense set of gaps covering the whole θ-range. Hence, the whole strange nonchaotic attractor is destroyed abruptly through a new type of boundary crisis when it collides with the ring-shaped unstable set.

3.3.2 Universality for the Boundary Crises

We investigate the dynamical origin for the new boundary crisis in the quasiperiodically forced Hénon map M, often used as a representative model for the Poincaré map of quasiperiodically forced oscillators:

$$M : \begin{cases} x_{n+1} = a - x_n^2 + y_n + \varepsilon \cos 2\pi\theta_n, \\ y_{n+1} = bx_n, \\ \theta_{n+1} = \theta_n + \omega \pmod 1, \end{cases} \tag{3.15}$$

where a is the nonlinearity parameter of the unforced Hénon map, and ω and ε represent the frequency and amplitude of the quasiperiodic forcing, respectively. This quasiperiodically forced Hénon map M is invertible because it has a nonzero constant Jacobian determinant $-b$ whose magnitude is less than unity (i.e., $b \neq 0$ and $-1 < b < 1$). Here we fix the value of the dissipation parameter b at $b = 0.05$.

We set the frequency ω to be the reciprocal of the golden mean, $\omega = (\sqrt{5} - 1)/2$. Then, using the rational approximation to this quasiperiodic forcing, we investigate the mechanism for the boundary crisis. For the inverse golden mean, its rational approximants are given by the ratios of the Fibonacci numbers, $\omega_k = F_{k-1}/F_k$, where the sequence of $\{F_k\}$ satisfies $F_{k+1} = F_k + F_{k-1}$ with $F_0 = 0$ and $F_1 = 1$. Instead of the quasiperiodically forced system, we study an infinite sequence of periodically forced systems with rational driving frequencies ω_k. We assume that the properties of the original system M may be obtained by taking the quasiperiodic limit $k \to \infty$.

Figure 3.23 shows a phase diagram in the $a - \varepsilon$ plane. Each phase is characterized by the (nontrivial) Lyapunov exponents, σ_1 and σ_2 ($\leq \sigma_1$), associated with the dynamics of the variables x and y (besides the zero exponent connected to the phase variable θ of the quasiperiodic forcing), as well as the phase sensitivity exponent δ. The exponent δ measures the sensitivity with respect to the phase of the quasiperiodic forcing and characterizes the strangeness of an attractor [53]. A smooth torus has negative Lyapunov exponents ($\sigma_{1,2} < 0$) and has no phase sensitivity (i.e., $\delta = 0$). Its region is denoted by T and is shown in light gray. On the other hand, a chaotic attractor has a positive Lyapunov exponent $\sigma_1 > 0$, and its region is shown in black. Between these regular and chaotic regions, strange nonchaotic attractors that have negative Lyapunov exponents ($\sigma_{1,2} < 0$) and positive phase sensitivity

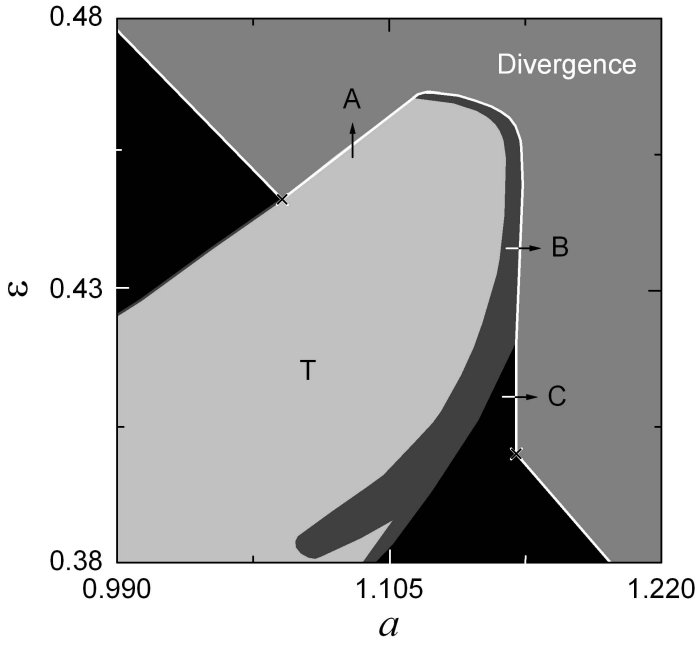

Figure 3.23: Phase diagram in the $a - \varepsilon$ plane for the case of $b = 0.05$ and $\omega = (\sqrt{5} - 1)/2$. Regular, chaotic, strange nonchaotic attractor, and divergence regions are shown in light gray, black, dark gray, and gray, respectively. A nonchaotic attractor [smooth torus (route A) or strange nonchaotic attractor (route B)], as well as a chaotic attractor (route C), is suddenly destroyed when passing the white solid curve. For other details, see the text.

exponents ($\delta > 0$) exist in the regions shown in dark gray. Due to their high phase sensitivity, strange nonchaotic attractors are observed to have a strange fractal structure.

The attractors (smooth torus, strange nonchaotic attractor, and chaotic attractor) are abruptly destroyed via a boundary crisis inducing divergence (which occurs in the region shown in gray) when crossing the white solid curve in Fig. 3.23. We note that the boundary crisis curve loses its differentiability at the two vertices denoted by the crosses. A new type of boundary crisis occurs along the routes A, B, and C crossing the segment bounded by the two vertices. The new boundary crisis is in contrast to the standard boundary crisis which takes place for a chaotic attractor via a collision with the smooth unstable torus, which is developed from the unstable fixed point for the unforced case, on the remaining part of the boundary crisis curve. For the case of new boundary crisis, the smooth unstable torus becomes inaccessible from the interior of the basin of the attractor; hence, it cannot

induce any boundary crisis. Through a collision with a new kind of ring-shaped unstable set, a nonchaotic attractor [smooth torus (route A) or strange nonchaotic attractor (route B)], as well as a chaotic attractor (route C), is suddenly destroyed. Using the rational approximation, such a ring-shaped unstable set, which has no counterpart in the unforced case, was first discovered in our previous study on the intermittent route to strange nonchaotic attractors [66, 67]. It appears via a phase-dependent saddle-node bifurcation. As the system parameters vary, both the sizes and the shapes of the rings constituting the unstable set are changed. Furthermore, as the level of the rational approximation increases, the ring-shaped unstable set consists of a large number of rings; hence, it becomes a complicated unstable set. (For details on the structure and the evolution of the ring-shaped unstable set, refer to Fig. 2 of Ref. [66].)

We fix the value of a at $a = 1.09$ and investigate the boundary crisis of a smooth torus by varying ε along the route A. Figure 3.24(a) shows a smooth torus (denoted by a black curve) whose basin is shown in gray for $\varepsilon = 0.435$. We note that holes (shown in white), leading to divergence, exist inside the basin of the smooth attracting torus. Hence, the smooth unstable torus (denoted by the dashed line) is not accessible from the interior of the basin of the smooth attracting torus; hence, it cannot induce any boundary crisis. As the parameter ε increases, the smooth torus and holes become closer, as shown in Fig. 3.24(b) for $\varepsilon = 0.44$. Eventually, the smooth (attracting) torus is abruptly destroyed via a boundary crisis when it collides with the hole boundary for $\varepsilon = \varepsilon^*(= 0.457\,113\,401)$. Using the rational approximation of level $k = 7$, we explain the mechanism for the boundary crisis of the smooth torus. Figure 3.24(c) shows the smooth torus (denoted by a black line), the ring-shaped unstable set (represented by dark gray dots), and holes (shown in white) for $\varepsilon = 0.434$. The rational approximations to the smooth torus and the ring-shaped unstable set are composed of stable and unstable orbits, respectively, with period F_7 (= 13). For this case, the ring-shaped unstable set is close to the smooth torus. However, it does not lie on any hole boundary [e.g., see a magnified view in Fig. 3.24(d)]. As the parameter ε increases, the size of the holes increases, and new holes appear. Then, some part of the ring-shaped unstable set lies on a hole boundary. With further increases in ε, the smooth torus and the ring-shaped unstable set on the hole boundary become closer, and eventually, for $\varepsilon = \varepsilon_7^*$ $(= 0.441\,629\,146)$, a phase-dependent saddle-node bifurcation occurs through a

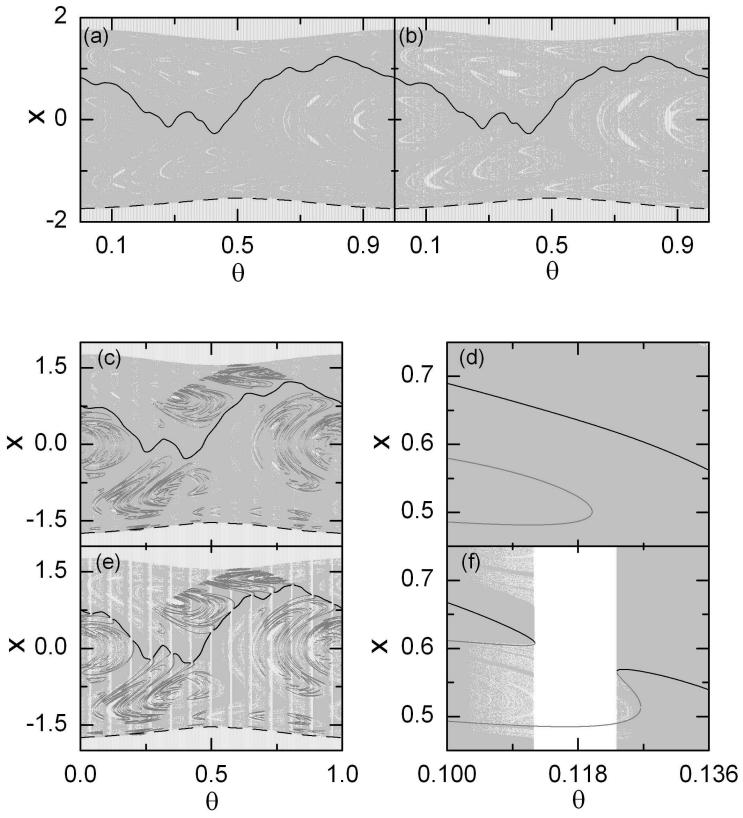

Figure 3.24: In (a)-(f), projections of the attractor, the ring-shaped unstable set, and the smooth unstable torus onto the $\theta - x$ plane and the 2D slice with $y = 0$ of the basin are given. (a) and (b) boundary crisis of a smooth torus along the route A for $a = 1.09$. (a) Smooth torus (denoted by a black line) and its basin (shown in gray) for $\varepsilon = 0.435$. The unstable smooth torus (denoted by a dashed line) is not accessible from the interior of the basin of the smooth attracting torus because of the existence of holes (denoted by white dots). (b) Smooth torus and holes just before the boundary crisis for $\varepsilon = 0.44$. (c)-(f) Analysis of the mechanism for the boundary crisis of the smooth torus in the rational approximation of level 7 for $a = 1.09$. Magnified views near $(\theta, x) = (0.118, 0.6)$ in (c) and (e) are given in (d) and (f), respectively. Here, the smooth torus whose basin is shown in gray, a ring-shaped unstable set, and holes are denoted by black, dark gray, and white dots, respectively. In (c) and (d) for $\varepsilon = 0.434$, a ring-shaped unstable set lies close to the smooth torus. For $\varepsilon = \varepsilon_7^*$ $(= 0.441\,629\,146)$, a boundary crisis occurs via phase-dependent saddle-node bifurcations between the smooth torus and the ring-shaped unstable set on the hole boundary. Then, F_7 $(= 13)$ "gaps," where divergence occurs, are formed, as shown in (e) for $\varepsilon = 0.442$, [e.g., see a magnified gap in (f)].

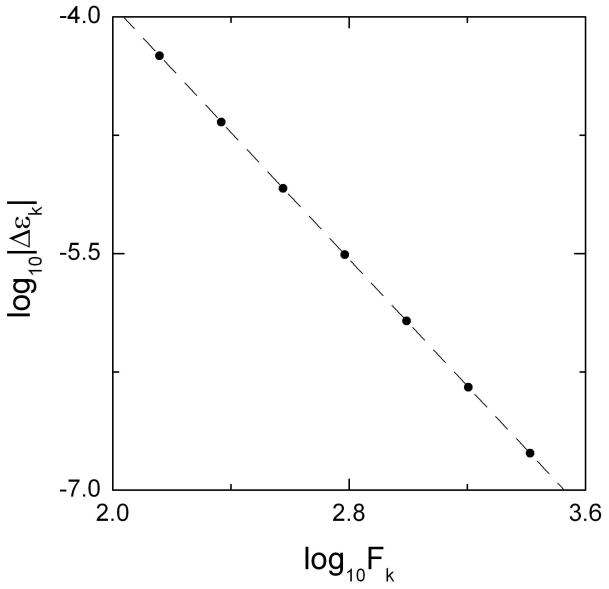

Figure 3.25: Plot of $\log_{10}|\Delta\varepsilon_k^*|$ vs. $\log_{10} F_k$ for $k = 12, \ldots, 18$ [$\Delta\varepsilon_k^* = \varepsilon_k^* - \varepsilon^*$]. Here, ε_k^* (denoted by solid circles) represents the threshold value for the saddle-node bifurcation in the rational approximation of level k, and ε^* denotes the quasiperiodic limit.

collision between the smooth torus and the ring-shaped unstable set. Then, "gaps," where the former attractor (i.e., the stable F_7-periodic orbits) no longer exists and almost all trajectories go to the infinity, are formed, as shown in Fig. 3.24(e) for $\varepsilon = 0.442$ [e.g., see a magnified gap in Fig. 3.24(f)]. As a result, a "partially-destroyed" torus with F_7 (= 13) gaps, where divergence occurs, is left. By increasing the level of the rational approximation to $k = 18$, we study the boundary crisis of the smooth torus, and the threshold value ε_k^*, at which the phase-dependent saddle-node bifurcation of level k occurs, is found to converge to the quasiperiodic limit ε^* (= 0.457 113 401) in an algebraic manner: $|\Delta\varepsilon_k| \sim F_k^{-\alpha}$, where $\Delta\varepsilon_k = \varepsilon_k^* - \varepsilon^*$ and $\alpha \simeq 2.01$, as shown in Fig. 3.25. With an increase in the level k of the rational approximation, the number of gaps where divergences take place becomes larger, and eventually in the quasiperiodic limit, a boundary crisis occurs in a dense set of gaps covering the whole θ-range. Consequently, the whole smooth torus disappears suddenly via a new type of boundary crisis when it collides with the ring-shaped unstable set. In a similar way, a strange nonchaotic attractor and a chaotic attractor are also destroyed suddenly through a collision with a ring-shaped unstable set when passing the boundary crisis curve along the routes B and C, respectively.

Chapter 4

Conclusion

Recently, much attention has been paid to the study of the synchronization in coupled chaotic systems because of its potential applications. The quasiperiodically forced systems have also attracted much attention due to typical appearance of strange nonchaotic attractors as intermediate states between order and chaos. In this thesis, we have studied both the chaos synchronization and the dynamical transitions in quasiperiodically forced systems.

For the case of chaos synchronization, the loss of chaos synchronization has been investigated by varying a coupling parameter in two coupled chaotic systems. The transverse stability of the synchronized chaotic attractor is intimately connected with transverse bifurcations of periodic saddles embedded in the synchronized chaotic attractor. If all periodic saddles are transversely stable, the synchronized chaotic attractor becomes strongly stable because there are no burstings from the invariant synchronization subspace. However, as the coupling parameter passes a threshold value, a transition from strong to weak synchronization has been found to occur in asymmetrically coupled chaotic systems when a periodic saddle first loses its transverse stability via a transcritical bifurcation. We note that this bifurcation mechanism is different from that in symmetrically coupled chaotic systems. As a result of the first transcritical bifurcation, the basin of attraction becomes globally riddled with a dense set of holes belonging to the basin of another attractor [11, 12]. This riddled basin is a fat fractal with a positive measure. The measure of the basin riddling and the fine scaled riddling of the fat fractal have been characterized in terms of the divergence and uncertainty exponents, respectively, and thus typical power-law scaling has been

found. Furthermore, we have investigated how the asymmetry of coupling affects the bifurcation mechanism for the loss of synchronous chaos by varying the asymmetry parameter α [13]. The bifurcation effects for small α are similar to those in the symmetric-coupling case ($\alpha = 0$). However, as α increases, they change qualitatively, and eventually become similar to those in the unidirectionally coupled case ($\alpha = 1$).

A weakly stable synchronized chaotic attractor becomes very sensitive with respect to the variation of the parameter mismatching and the noise intensity [20], because of local transverse repulsion of periodic repellers embedded in the synchronized chaotic attractor. We have first introduced a new quantifier, called the parameter sensitivity exponent, to measure the parameter sensitivity of the weakly stable synchronized chaotic attractor in two coupled 1D maps [19]. As the local transverse repulsion of the periodic repellers strengthens, the value of the parameter sensitivity exponent increases. In terms of these parameter sensitivity exponents, we have characterized the effect of the parameter mismatching on both the intermittent bursting and the basin riddling occurring in the regime of weak synchronization. It has thus been found that the scaling exponent for the average time spending near the diagonal for both the bubbling and riddling cases is given by the reciprocal of the parameter sensitivity exponent. As in the parameter-mismatching case, we have introduced the noise sensitivity exponent to measure the noise sensitivity of the synchronized chaotic attractor, and characterized the effect of noise on weak synchronization [21]. For the case of bounded noise, the values of the noise sensitivity exponent have been found to be the same as those of the parameter sensitivity exponent. Consequently, both the parameter mismatch and the noise have the same effect on the scaling behavior of the average characteristic time. Similar results have also been obtained in two coupled multidimensional invertible systems such as the coupled Hénon maps and coupled pendula [22].

As the coupling parameter is further changed and passes another threshold value, the synchronized chaotic attractor loses its transverse stability and then a complete desynchronization occurs via a blowout bifurcation. We are interested in the type of asynchronous attractors, exhibiting on-off intermittency, born via a supercritical blowout bifurcation. Here, we consider two coupled 1D maps with a parameter α tuning the degree of asymmetry of coupling, and have investigated the dynamical origin for the appearance of asynchronous hyperchaotic and chaotic attractors through blowout bifurcations. Depending on the value of

α, asynchronous hyperchaos or chaos occurs. Through decomposition of a typical trajectory on the asynchronous intermittent attractor into the laminar and bursting components, its type may be determined via competition between the laminar and bursting components [38]. An asynchronous hyperchaotic (chaotic) attractor has been found to appear when its bursting (laminar) component is dominant. These results have also been confirmed in coupled multidimensional invertible systems.

Similar idea has been used to study the mechanism for the partial synchronization which may occur in three or more coupled systems [47]. We consider three coupled 1D maps with a parameter p tuning the symmetry of the coupling from the unidirectional coupling ($p = 0$) to the symmetric coupling ($p = 1/3$), and have investigated the dynamical mechanism for the occurrence of the partial synchronization by varying the parameter p. For this case, a two-cluster state, exhibiting on-off intermittency, appears on an invariant subspace via a supercritical blowout bifurcation of the synchronized chaotic attractor on the diagonal. When the newly-born two cluster state is transversely stable, partial synchronization occurs on the invariant plane. Such transverse stability of the intermittent two-cluster state has also been found to be determined through competition between its laminar and bursting components. When the transverse strength of the laminar component is larger than that of the bursting component, the two-cluster state becomes transversely stable, and hence partial synchronization takes place. Similar results have also been obtained in three coupled multidimensional invertible systems.

As a second main topic, we have studied the dynamical transitions in quasiperiodically forced systems driven at two incommensurate frequencies. In particular, we are interested in the dynamical routes to strange nonchaotic attractors which exhibit properties of regular as well as chaotic attractors.

Intermittent strange nonchaotic attractors appear typically in quasiperiodically forced period-doubling systems. As a representative model we consider the quasiperiodically forced logistic map. As a parameter passes a threshold value, a smooth torus transforms to an intermittent strange nonchaotic attractor. Using the rational approximation to the quasiperiodic forcing, we have investigated the mechanism for the intermittent route to strange nonchaotic attractors [66]. It has thus been found that a transition to an intermittent strange nonchaotic attractor occurs via a phase-dependent saddle-node bifurcation when a smooth torus collides

with a new type of ring-shaped unstable set which has no counterpart in the unforced case. The universality for this intermittent route to strange nonchaotic attractors has also been confirmed in multidimensional invertible systems such as the quasiperiodically forced Hénon map, ring map, and Toda Oscillator [67].

In the quasiperiodically forced logistic map, we have shown that the newly-found ring-shaped unstable sets which have no counterparts in the unforced case play a central role because they also induce other typical transitions such as band-merging, boundary, and interior crises. A new type of band-merging transition has been found to occur for a nonchaotic attractor (torus or strange nonchaotic attractor) as well as a chaotic attractor through collision with the ring-shaped unstable set [68]. For the case of a smooth two-band torus, an intermittent single-band strange nonchaotic attractor appears via the new band-merging transition. This corresponds to a new mechanism for the birth of strange nonchaotic attractors. We note that such a band-merging transition is a direct cause for the truncation of the torus-doubling sequence. This new type of band-merging route to strange nonchaotic attractors is also observed in the multidimensional invertible systems [69]. Furthermore, in the quasiperiodically forced logistic map a nonchaotic attractor (torus, strange nonchaotic attractor) as well as a chaotic attractor has been found to disappear suddenly through a new type of boundary crisis when it collides with a ring-shaped unstable set on the basin boundary [70]. The mechanism for such a new kind of boundary crisis has also been confirmed in the quasiperiodically forced Hénon map [71].

Finally, we discuss our future research associated with the results obtained in this thesis. We consider an ensemble of globally coupled systems where each subsystem is coupled to all others with equal strength. For the sufficiently strong coupling, a fully synchronized state exists. However, as the coupling parameter is decreased, clustering states appear [46, 99]. The dynamical routes to clusters and scaling will be investigated in an ensemble of globally coupled period-doubling systems. Furthermore, we are interested in the onset of coherence in an ensemble of globally coupled noisy period-doubling systems. As the coupling parameter increases from zero and passes a threshold value, a transition from an incoherent state with a zero mean field to a coherent state with a macroscopic mean field occurs [100]. Scaling associated with onset of coherence will be particularly investigated. Next, we study the dynamical behaviors of quasiperiodically forced neural systems. In

addition to the regular and chaotic attractors, strange nonchaotic attractors may appear typically in quasiperiodically forced systems. Hence, complex neural signals may be chaotic or strange nonchaotic in the presence of quasiperiodic forcing. Mechanism for the occurrence of strange nonchaotic firing (beating or bursting) will be investigated in the quasiperiodically forced Hodgkin-Huxley [101], FitzHugh-Nagumo [102], Morris-Lecar [103], and Hindmarsh-Rose models [104].

Bibliography

[1] E. N. Lorentz, J. Atmos. Sci. **20**, 130 (1963).

[2] H. Fujisaka and T. Yamada, Prog. Theor. Phys. **69**, 32 (1983); A. S. Pikovsky, Z. Phys. B: Condens. Matter **50**, 149 (1984);L. M. Pecora and T. L. Carroll, Phys. Rev. Lett. **64**, 821 (1990).

[3] K. M. Cuomo and A. V. Oppenheim, Phys. Rev. Lett. **71**, 65 (1993).

[4] L. Kocarev, K. S. Halle, K. Eckert, L. O. Chua, and U. Parlitz, Int. J. Bifurcation Chaos Appl. Sci. Eng. **2**, 973 (1992); L. Kocarev and U. Parlitz, Phys. Rev. Lett. **74**, 5028 (1995); N. F. Rulkov, Chaos **6**, 262 (1996).

[5] P. Ashwin, J. Buescu, and I. Stewart, Nonlinearity **9**, 703 (1996).

[6] B. R. Hunt and E. Ott, Phys. Rev. Lett. **76**, 2254 (1996); Phys. Rev. E **54**, 328 (1996).

[7] Y.-C. Lai, C. Grebogi, J. A. Yorke, and S. C. Venkataramani, Phys. Rev. Lett. **77**, 55 (1996).

[8] V. Astakhov, A. Shabunin, T. Kapitaniak, and V. Anishchenko, Phys. Rev. Lett. **79**, 1014 (1997).

[9] Yu. L. Maistrenko, V. L. Maistrenko, A. Popovich, and E. Mosekilde, Phys. Rev. E **57**, 2713 (1998); **60**, 2817 (1999).

[10] O. Popovych, Yu. L. Maistrenko, E. Moskilde, A. Pikovsly, and J. Kurhts, Phys. Lett. A **275**, 401 (2002); Phys. Rev. E **63**, 036201 (2001).

[11] S.-Y. Kim and W. Lim, Phys. Rev. E **63**, 026217 (2001).

[12] S.-Y. Kim and W. Lim, Prog. Thoer. Phys. **105**, 187 (2001); W. Lim, S.-Y. Kim, and Y. Kim, J. Korean Phys. Soc. 38, 532 (2001).

[13] S.-Y. Kim and W. Lim, Phys. Rev. E **64**, 016211 (2001).

[14] W. Lim and S.-Y. Kim, J. Korean Phys. Soc. 43, 193-201 (2003).

[15] P. Ashwin, J. Buescu, and I. Stewart, Phys. Lett. A **193**, 126 (1994); J. F. Heagy, T. L. Carroll, and L. M. Pecora, Phys. Rev. E **52**, 1253 (1995); D. J. Gauthier and J. C. Bienfang, Phys. Rev. Lett. **77**, 1751 (1996); V. Ashtakhov, M. Hasler, T. Kapitaniak, V. Shabunin, and V. Anishchenko, Phys. Rev. E **58**, 5620 (1998); S. Yanchuk, Y. Maistrenko, B. Lading, and E. Mosekilde, Int. J. Bifurcation Chaos Appl. Sci. Eng. **10**, 2629 (2000); S.-Y. Kim and W. Lim, J. Phys. A **36**, 6951 (2003).

[16] C. Venkataramani, B. R. Hunt, and E. Ott, Phys. Rev. E **54**, 1346 (1996); S. C. Venkataramani, B. R. Hunt, E. Ott, D. J. Gauthier, and J. C. Bienfang, Phys. Rev. Lett. **77**, 5361 (1996); A. V. Zimin, B. R. Hunt, and E. Ott, Phys. Rev. E **67**, 016204 (2003).

[17] J. C. Alexander, J. A. Yorke, Z. You, and I. Kan, Int. J. Bifurcation Chaos Appl. Sci. Eng. **2**, 795 (1992); E. Ott, J. C. Sommerer, J. C. Alexander, I. Kan, and J. A. Yorke, Phys. Rev. Lett. **71**, 4134 (1993); J. C. Sommerer and E. Ott, Nature (London) **365**, 136 (1993); E. Ott, J. C. Alexander, I. Kan, J. C. Sommerer, and J. A. Yorke, Physica D **76**, 384 (1994); J. F. Heagy, T. L. Carroll, and L. M. Pecora, Phys. Rev. Lett. **73**, 3528 (1994).

[18] E. Ott, J. C. Sommerer, J. C. Alexander, I. Kan, and J. A. Yorke, Phys. Rev. Lett. **71**, 4134 (1993); E. Ott, J. C. Alexander, I. Kan, J. C. Sommerer, and J. A. Yorke, Physica D **76**, 384 (1994); J. F. Heagy, T. L. Caroll, and L. M. Pecora, Phys. Rev. Lett. **73**, 3528 (1994).

[19] A. Jalnine and S.-Y. Kim, Phys. Rev. E **65**, 026210 (2002); S.-Y. Kim, A. Jalnine, W. Lim, and S. P. Kuznetsov, Applied Nonlinear Dynamics. 11, 81 (2003).

[20] S.-Y. Kim, W. Lim, and Y. Kim, Prog. Theor. Phys. **107**, 239 (2002).

[21] S.-Y. Kim, W. Lim, A. Jalnine, and S. Kuznetsov, Phys. Rev. E **67**, 016217 (2003).

[22] W. Lim and S.-Y. Kim, J. Phys. A **37**, 8233 (2004); ; W. Lim and S.-Y. Kim, J. Korean Phys. Soc. 45, 287 (2004).

[23] E. Ott and J. C. Sommerer. Phy. Lett. A **188**, 39 (1994).

[24] P. Ashwin, P. J. Aston, and M. Nicol, Physica D **111**, 81 (1998).

[25] Y. Nagai and Y.-C. Lai, Phys. Rev. E **55**, R1251 (1997); *ibid* **56**, 4031 (1997).

[26] P. Glendinning, Phys. Lett. A **264**, 303 (1999).

[27] A. S. Pikovsky and P. Grassberger, J. Phys. A **24**, 4587 (1991); A. S. Pikovsky, Phys. Lett. A **165**, 33 (1992).

[28] H. Fujisaka and T. Yamada, Prog. Theor. Phys. **74**, 918 (1985); **75**, 1087 (1986); H. Fujisaka, H. Ishii, M. Inoue, and T. Yamada, *ibid.* **76**, 1198 (1986).

[29] L. Yu, E. Ott, and Q. Chen, Phys. Rev. Lett. **65**, 2935 (1990); Physica D **53**, 102 (1992).

[30] N. Platt, E. A. Spiegel, and C. Tresser, Phys. Rev. Lett. **70**, 279 (1993); J. F. Heagy, N. Platt, and S. M. Hammel, Phys. Rev. E **49**, 1140 (1994); N. Platt, S. M. Hammel, and J. F. Heagy, Phys. Rev. Lett. **72**, 3498 (1994).

[31] S. C. Venkataramani, T. M. Antonsen, E. Ott, and J. C. Sommerer, Physica D **96**, 66 (1996).

[32] M. Ding and W. Yang, Phys. Rev. E **56**, 4009 (1997).

[33] H. L. Yang and E. J. Ding, Phys. Rev. E **50**, R3295 (1994).

[34] A. Čenys and H. Lustfeld, J. Phys. A **29**, 11 (1996).

[35] D. Marthaler, D. Armbruster, Y.-C. Lai, and E. Kostelich, Phys. Rev. E **64**, 016220 (2001).

[36] M. de Sousa Vieira, A. J. Lichtenberg, and M. A. Lieberman, Phys. Rev. A **46**, R7359 (1992).

[37] T. Kapitaniak, Phys. Rev. E **47**, R2975 (1993); T. Kapitaniak and L. O. Chua, Int. J. Bifurcation Chaos Appl. Sci. Eng. **4**, 477 (1994).

[38] S.-Y. Kim, W. Lim, E. Ott, and B. Hunt, Phys. Rev. E **68**, 066203 (2003); W. Lim and S.-Y. Kim, J. Korean Phys. Soc. 43, 202 (2003).

[39] S.-Y. Kim and K. Lee, Phys. Rev. E **54**, 1237 (1996); S.-Y. Kim and W. Lim, *ibid.* **63**, 036223 (2001).

[40] K. Pyragas, Phys. Rev. E **54**, R4508 (1996).

[41] M. S. Vieira and A. J. Lichtenberg, Phys. Rev. E **56**, R3741 (1997).

[42] M. Hasler, Yu. Maistrenko, and O. Popovych, Phys. Rev. E **58**, 6843 (1998); Yu Maistrenko, O. Popovych, and M. Hasler, Int. J. Bifurcation Chaos Appl. Sci. Eng. **10**, 179 (2000); A. V. Taborov, Yu. Maistrenko, and E. Mosekilde, Int. J. Bifurcation Chaos Appl. Sci. Eng. **10**, 1051 (2000); S. Yanchuk, Yu. Maistrenko, and E. Mosekilde, Chaos **13**, 388 (2003).

[43] M. Inoue, T. Kawazoe, Y. Nishi, and M. Nagadome, Phys. Lett. A **249**, 69 (1998).

[44] Y. Zing, G. Hu, H. A. Cerdera, S. Chen, T. Braun, and Y. Yao, Phys. Rev. E **63**, 026211 (2001).

[45] N. Tsukamoto, S. Miyazaki, and H. Fujisaka, Phys. Rev. E **67**, 016212 (2003).

[46] K. Kaneko, Phys. Rev. Lett. **63**, 219 (1989); Physica D **41**, 137 (1990).

[47] W. Lim and S.-Y. Kim, Phys. Rev. E **71**, 035221 (2005); J. Korean Phys. Soc. **46**, 638 (2005).

[48] A. Prasad, S. S. Negi and R. Ramaswamy, Int. J. Bif. Chaos **11**, 291 (2001).

[49] C. Grebogi, E. Ott, S. Pelikan, and J. A. Yorke, Physica D **13**, 261 (1984).

[50] F. J. Romeiras and E. Ott, Phys. Rev. A **35**, 4404 (1987); M. Ding, C. Grebogi, and E. Ott, Phys. Rev. A **39**, 2593 (1989).

[51] T. Kapitaniak, E. Ponce, and T. Wojewoda, J. Phys. A **23**, L383 (1990).

[52] J. F. Heagy and S. M. Hammel, Physica D **70**, 140 (1994)

[53] A. S. Pikovsky and U. Feudel, Chaos **5**, 253 (1995).

[54] U. Feudel, J. Kurths, A. S. Pikovsky, Physica D **88**, 176 (1995); U. Feudel, C. Grebogi, and E. Ott, Phys. Rep. **290**, 11 (1997).

[55] O. Sosnovtseva, U. Feudel, J. Kurths, and A. Pikovsky, Phys. Lett. A **218**, 255 (1996).

[56] S. P. Kuznetsov, A. S. Pikovsky, and U. Feudel, Phys. Rev. E **51**, R1629 (1995); S. Kuznetsov, U. Feudel, and A. Pikovsky, Phys. Rev. E **57**, 1585 (1998); S. Kuznetsov, E. Neumann, A. Pikovsky, and I. Sataev, Phys. Rev. E **62**, 1995 (2000). S. P. Kuznetsov, Phys. Rev. E **65**, 066209 (2002).

[57] P. R. Chastell, P. A. Glendinning, and J. Stark, Phys. Lett. A **200**, 17 (1995); H. Osinga, J. Wiersig, P. Glendinning, and U. Feudel, Int. J. Bif. Chaos **11**, 3085 (2001); B. R. Hunt and E. Ott, Phys. Rev. Lett. **87**, 254101 (2001).

[58] T. Nishikawa and K. Kaneko, Phys. Rev. E **54**, 6114 (1996); S. Datta, R. Ramaswamy, and A. Prasad, Phys. Rev. E **70**, 046203 (2004).

[59] T. Yalçınkaya and Y.-C. Lai, Phys. Rev. Lett. **77**, 5039 (1996).

[60] A. Prasad, V. Mehra, and R. Ramaswamy, Phys. Rev. Lett. **79**, 4127 (1997); Phys. Rev. E **57**, 1576 (1998).

[61] A. Witt, U. Feudel, and A. Pikovsky, Physica D **109**, 180 (1997).

[62] A. Venkatesan, K. Murali, M. Lakshmanan, Phys. Lett. A **259**, 246 (1999); A. Venkatesan, M. Lakshmanan, A. Prasad and R. Ramaswamy, Phys. Rev. E **61**, 3641 (2000); A. Venkatesan and M. Lakshmanan, Phys. Rev. E **63**, 026219 (2001).

[63] S. S. Negi, A. Prasad, and R. Ramaswamy, Physica D **145**, 1 (2000).

[64] H. M. Osinga and U. Feudel, Physica D **141**, 54 (2000).

[65] B.R. Hunt and E. Ott, Phys. Rev. Lett. **87**, 254101 (2001); J.-W. Kim, S.-Y. Kim, B. Hunt, and E. Ott, Phys. Rev. E **67**, 036211 (2003).

[66] S.-Y. Kim, W. Lim, and E. Ott, Phys. Rev. E **67**, 056203 (2003); S.-Y. Kim, W. Lim, and A. Jalnine, Applied Nonlinear Dynamics. 11, 55 (2003).

[67] S.-Y. Kim and W. Lim, J. Phys. A **37**, 6477 (2004); W. Lim and S.-Y. Kim, J. Korean Phys. Soc. 44, 514-517 (2004).

[68] W. Lim and S.-Y. Kim, Phys. Lett. A **335**, 383 (2005).

[69] W. Lim and S.-Y. Kim (unpublished).

[70] S.-Y. Kim and W. Lim, Phys. Lett. A **334**, 160 (2005).

[71] W. Lim and S.-Y. Kim, J. Korean Phys. Soc. **46**, 642 (2005).

[72] W. L. Ditto, M. L. Spano, H. T. Savage, S. N. Rauseo, J. Heagy, and E. Ott, Phys. Rev. Lett. **65**, 533 (1990); T. Zhou, F. Moss, and A. Bulsara, Phys. Rev. A **45**, 5394 (1992); W. X. Ding, H. Deutsch, A. Dinklage, and C. Wilke, Phys. Rev. E **55**, 3769 (1997); T. Yang and K. Bilimgut, Phys. Lett. A **236**, 494 (1997); B. P. Bezruchko, S. P. Kuznetsov, and Y. P. Seleznev, Phys. Rev. E **62**, 7828 (2000).

[73] A. Bondeson, E. Ott, and T. M. Antonsen, Phys. Rev. Lett. **55**, 2103 (1985); J. A. Ketoja and I. I. Satija, Physica D **109**, 70 (1997).

[74] C.-S. Zhou and T.-L. Chen, Europhys. Lett. **38**, 261 (1997); R. Ramaswamy, Phys. Rev. E **56**, 7294 (1997).

[75] E. Ott, *Chaos in Dynamical Systems* (Cambridge Univ. Press, Cambridge, 2002).

[76] M. J. Feigenbaum, J. Stat. Phys. **19**, 25 (1978).

[77] E. N. Lorentz, Ann. N. Y. Acad. Sci. **357**, 282 (1980).

[78] C. Grebogi, E. Ott, and J. A. Yorke, Phys. Rev. Lett. **56**, 1011 (1986); Physica D **24**, 243 (1987); U. Feudel, A. Witt, Y.-C. Lai, and C. Grebogi, Phys. Rev. E **58**, 3060 (1998).

[79] C. Grebogi, E. Ott, and J. A. Yorke, Phys. Rev. Lett. **48**, 1507 (1982); Physica D **7**, 181 (1983).

[80] C. Grebogi, E. Ott, F. Romeiras, and J. A. Yorke, Phys. Rev. A **36**, 5365 (1987); C. Grebogi, E. Ott, and J. A. Yorke, Phys. Rev. Lett. **57**, 1284 (1986).

[81] C. Jeffries and J. Perez, Phys. Rev. A **27**, 601 (1983); S. D. Brorson, D. Dewey, and P. S. Linsay, Phys. Rev. A **28**, 1201 (1983); H. Ikezi, J. S. degrassie, and T. H. Jensen, Phys. Rev. A **28**, 1207 (1983); R. W. Rollins and E. R. Hunt, Phys. Rev. A **29**, 3327 (1984); E. G. Gwinn and R. M. Westervelt, Phys. Rev. Lett. **54**, 1613 (1985); M. Iansiti, Q. Hu, R. M. westervely, and M. Tinkham, Phys. Rev. Lett. **55**, 746 (1985); D. Dangoisse, P. Glorieux, and D. Hennequin, Phys. Rev. Rett. **57**, 2657 (1986); W. L. Ditto, S. Rauseo, R. Cawley, C. Grebogi, G.-H. Hsu, E. Kostelich, E. Ott, H. T. Savage, R. Segnan, M. L. Spano, and J. A. Yorke, Phys. Rev. Lett. **63**, 923 (1989); J. C. Sommerer, W. L. Ditto, C. Grebogi, E. Ott, and M. L. Spano, Phys. Lett. A **153**, 105 (1991).

[82] C. Mira, L. Gardini, A. Barugola, and J.-C. Cathala, *Chaotic Dynamics in Two-Dimensional Noninvertible Maps* (World Scientific, Singapore, 1996); R. H. Abraham, L. Gardini, and C. Mira, *Chaos in Discrete Dynamical systems* (Springer, New York, 1997).

[83] J. D. Farmer, Phys. Rev. Lett. **55**, 351 (1985).

[84] Yu. L. Maistrenko, V. L. Maistrenko, A. Popovich, and E. Mosekilde, Phys. Rev. Lett. **80**, 1638 (1998); G.-I. Bischi and L. Gardini, Phys. Rev. E **58**, 5710 (1998).

[85] J. Guckenheimer and P. Holmes, *Nonlinear Oscillations, Dynamical Systems, and Bifurcations of Vector Fields* (Springer, New York, 1983), p. 149.

[86] C. Grebogi, E. Ott, and J. A. Yorke, Phys. Rev. Lett. **50**, 935 (1983); Erg. Th. Dyna. Sys. **5**, 341 (1985).

[87] S.-Y. Kim and H. Kook, Phys. Rev. A **48**, 785 (1993).

[88] W. Lim and S.-Y. Kim, J. Korean Phys. Soc. **44**, 510 (2004).

[89] D. V. Ramana Reddy, A. Sen, and G. L. Johnston, Phys. Rev. Lett. **80**, 5109 (1998).

[90] K. Wiesenfeld, P. Colet, S. H. Strogatz, Phys. Rev. Lett. **76**, 404 (1996).

[91] C. S. Peskin, *Mathematical Aspects of Heart Physiology* (Courant Institute of Mathematical Sciences, New York, 1975).

[92] J. Buck, Q. Rev. Biol. **63**, 265 (1988).

[93] T. J. Walker, Science **166**, 891 (1969).

[94] A. Wolf, J. B. Swift, H. L. Swinney, and J. A. Vastano, Physica D **16**, 285 (1985); G. Benettin, L. Galgani, A. Giorgilli, and J.-M. Strelcyn, Meccanica **15**, 9 (1980); A. J. Lichtenberg and M. A. Lieberman, *Regular and Stochastic Motion* (Springer-Verlag, New York, 1983), p. 283.

[95] T. Bohr, P. Bak, M. H. Jensen, Phys. Rev. A **30**, 1970 (1984).

[96] M. Toda, Phys. Rep. **18**, 1 (1975).

[97] T. Klinker, W. Meyer-Ilse, and W. Lauterborn, Phys. Lett. A **101**, 371 (1984); T. Kurz and W. Lauterborn, Phys. Rev. A **37**, 1029 (1988).

[98] J. A. Gallas, C. Grebogi, and J. A. Yorke, Phys. Rev. Lett. **71**, 1359 (1993); H. B. Stewart, Y. Ueda, C. Grebogi, and J. A. Yorke, Phys. Rev. Lett. **75**, 2478 (1995).

[99] O. Popovych, Yu. Maistrenko, and E. Mosekilde, Phys. Rev. E **64**, 026205 (2001); Phys. Lett. A **302**, 171 (2002).

[100] A. S. Pikovsky, M. G. Rosenblum, and J. Kurths, Europhys. Lett. **34**, 165 (1996); D. Topaj, W.-H, Kye, and A. Pikovsky, Phys. Rev. Lett. **87**, 074101 (2001); H. Sakaguchi, Phys. Rev. E **61**, 7212 (2000); E. Ott, P. So, E. Barreto, and T. Antosen, Physics D **173**, 29 (2002); S.-J. Paik and E. Ott, Phys. Rev. E **69**, 066210 (2004).

[101] A.L. Hodgkin and A.F. Huxley, J. Physiol. **117**, 500 (1952).

[102] R. FitzHugh, Biophys. J. **1**, 445 (1961); J.S. Nagumo, S. Arimoto, and S. Yoshizawa, Proc. IRE **50**, 2061 (1961).

[103] C. Morris and H. Lecar, Biophys. J. **35**, 193 (1981).

[104] J.L. Hindmarsh and R.M. Rose, Proc. Ro. Soc. London Ser. B **221**, 87 (1984); ibid. **225**, 161 (1985).

결합 혼돈계와 준주기 구동계의 동역학적 거동: 동기화와 이상한 비혼돈 끌개

초록

결합 혼돈계에서 동기화(synchronization)는 비밀통신과 같은 실제적인 응용 때문에 최근에 심도있게 연구되는 주제이다. 그리고, 이상한 비혼돈 끌개(strange nonchaotic attractor)의 존재 때문에 준주기 구동계 연구에도 많은 관심이 집중되어 지고 있다. 본 논문에서는 이러한 혼돈 동기화와 이상한 비혼돈 끌개가 출현하는 동역학적 전이에 대해서 공부하고자 한다.

첫 번째로, 혼돈계 두 개가 비대칭으로 결합된 계에서 동기화를 잃어가는 과정에 관심이 있다. 결합 맺음변수를 바꿔가면서, 동기화 부분공간에 가로지르는 섭동에 대한 동기화된 혼돈 끌개의 안정성을 탐구한다. 동기화된 혼돈 끌개에 묻혀 있는 모든 주기 말안장점(periodic saddles)들이 가로 안정하면, 동기화 부분공간으로부터 어떤 파열(bursting)도 없는 고질의 "강한 동기화"가 생기게 된다. 결합 맺음변수가 변하면서 문턱값(threshold value)을 지나게 되면, 어떤 말안장 고정점(fixed point)이 처음으로 관통 쌍갈림(transcritical bifurcation)을 통해서 가로 불안정해진다. 그러면, 동기화 부분공간으로부터 파열이 일어나고, 저질의 "약한 동기화"가 생기게 된다. 이 경우에, 동기화된 혼돈 끌개의 유인 영역(basin of attraction)이 다른 끌개(또는 무한대)의 유인 영역에 속하는 구멍들로 빽빽하게 채워지게 된다. 이 구멍난 유인 영역을 발산과 불확실성 지수로 특성화 한다. 이러한 약하게 안정한 동기화된 혼돈 끌개는 현실 상황에서 피할 수 없는 맺음변수 불일치와 잡음에 매우 민감하게 된다. 그러한 민감도를 정량적으로 측정하기 위해서 맺음변수와 잡음 민감지수를 도입한다. 이러한 지수들로 약한 동기화 경우에 일어나는 간헐적인 파열과 유인영역 구멍내기에 미치는 맺음변수 불일치와 잡음 효과를 특성화한다. 결합 매개변수를 더 바꾸어 가면, 동기화된 혼돈 끌개는 점점 더 약하게 안정되고, 궁극적으로는 또 다른 문턱값을 지날 때 폭발 쌍갈림(blowout bifurcation)을 통해서 가로 불안정해진다. 그 결과, 완전 비동기화가 일어나게 된다. 그렇게 해서 초임계 폭발 쌍갈림(supercritical blowout bifurcation)을 통해서 두 번째 리아프노프 지수가 양 또는 음인 비동기화된 초혼돈 또는 혼돈 끌개가 나타난다. 새롭게 태어난 간헐성 거동을 보이는 비동기화된 끌개의 유형은 라미나(laminar)와 파열 성분의 경쟁을 통해서 결정할 수가 있다. 그러나, 세개 이상 결합된 계에서는 완전 비동기화에 추가해서 (구성원 일부분만 동기화된) 부분 동기화가 동기

화된 혼돈 끌개의 폭발쌍갈림을 통해서 일어날 수가 있다. 세 개의 혼돈계로 구성된 결합계에서 부분 동기화의 발생에 대한 동역학적 메커니즘을 탐구한다. 이 경우에 초임계 폭발쌍갈림을 통해서 불변 평면 위에 간헐성 거동을 보이는 두 클러스터 상태(two-cluster state)가 나타난다. 새롭게 태어난 두 클러스터 상태가 가로 안정하면, 불변 평면 위에 부분 동기화가 일어나게 된다. 간헐적인 두 클러스터 상태의 가로 안정성은 또한 라미나와 파열 성분의 경쟁을 통해서 결정할 수가 있다.

두 번째로, 준주기 구동계의 동역학적 거동을 공부한다. 특히, 이상한 비혼돈 끌개의 탄생에 관심이 있다. 준주기 힘에 대한 유리 근사(rational approximation)를 사용해서 이상한 비혼돈 끌개의 출현에 대한 메커니즘을 탐구한다. 그렇게 해서, 매끄러운 토러스(torus)가 (비구동계에는 없는) 새로운 형태의 반지모양의 불안정한 궤도와 충돌할 때 간헐성 또는 밴드 융합(band merging) 메커니즘을 통해서 간헐적인 이상한 비혼돈 끌개가 나타남을 발견했다. 이러한 간헐적인 이상한 비혼돈 끌개를 파열들 사이의 평균 시간과 국소 리아프노프 지수로 특성화 한다. 게다가, 토러스, 이상한 비혼돈 끌개, 또는 혼돈 끌개가 유인 영역 경계에 놓인 반지 모양의 불안정 궤도와 충돌하면, 새로운 경계 고비(boundary crisis)를 통해서 갑자기 사라지게 된다.